

ABSTRACT

DAUBERT, JAMES STEVEN. Atomic Layer Deposition for Electrochemical Applications: Energy Storage and Corrosion Protection. (Under the direction of Gregory N. Parsons.)

Atomic layer deposition (ALD) is a vapor phase thin film deposition technique that is capable of depositing ultrathin, conformal films with sub-nanometer thickness control. ALD utilizes a binary self-limiting surface reaction, where the gas-phase precursors infiltrate and form coatings over complex substrate geometries. A wide array of materials can be deposited using ALD, including materials that are of interest in electrochemical systems. This work focuses on the application of ultrathin coatings deposited using ALD to modify electrochemical systems, including improving the performance of supercapacitors and preventing metal from corroding.

We first show that ALD of vanadium oxide is a viable means to add pseudocapacitive layers to porous carbon electrodes. Capacitance and electrochemical impedance analysis of subsequently constructed electrochemical capacitors showed improved charge storage for the ALD coated electrodes, but the extent of improvement depended on initial pore structure. By comparing the pseudocapacitive performance of ALD V_2O_5 in micro-, meso- and macroporous carbon electrodes, we describe fundamental limits to ALD in very fine pores for pseudocapacitance charge storage. Comparing experimental trends with an ALD coating model, we find that the thermal V_2O_5 ALD process using vanadium triisopropoxide (VTIP) and water is uniformly deposited into pores only when the pore diameter exceeds a critical diameter of 13 Å. To understand the ALD coating limits, the pores of the carbon electrodes were modeled as a series of connected tubes, and the volume of V_2O_5 deposited determined experimentally was compared to the calculated deposition limit. Pores below this critical diameter with sealed and decreased the accessible volume for V_2O_5 deposition by more than half, decreasing the maximum energy density. The effect of the pore sealing by the ALD process on the capacitive response of the activated carbon based electrodes is also studied. This work highlights the intrinsic capabilities and limitations of coating microporous materials using ALD.

We then show that Kevlar®, poly(p-phenylene terephthalamide) (PPTA), yarns can be modified for use as flexible supercapacitor electrodes by coating them with a nanometer-scale

film of conductive platinum metal and pseudocapacitive V_2O_5 using ALD. The PPTA yarns were incorporated into a solid state supercapacitor through the use of a polyvinyl alcohol/lithium chloride gel electrolyte. This work describes how ALD metal and metal oxide can be combined to add double layer and pseudocapacitive charge storage to mechanically robust PPTA creating unique multifunctional electronic fabric device systems.

Finally, we demonstrate that ALD is a viable means to add corrosion protection to copper metal. Ultrathin films of Al_2O_3 , TiO_2 , ZnO , HfO_2 , and ZrO_2 were deposited on copper metal using ALD and their corrosion protection properties were measured using electrochemical impedance spectroscopy (EIS) and linear sweep voltammetry (LSV). Analysis of films of each metal oxide demonstrated low electrochemical porosity and provided enhanced corrosion protection. Films of Al_2O_3 or HfO_2 provided the highest level of initial corrosion protection, but films of HfO_2 exhibited the best coating quality after extended exposure. This is the first reported instance of using ultrathin films of HfO_2 or ZrO_2 produced with ALD for corrosion protection, and both are promising materials for corrosion protection.

© Copyright 2017 James Steven Daubert
All Rights Reserved

Atomic Layer Deposition for Electrochemical Applications: Energy Storage and Corrosion
Protection

by
James Steven Daubert

A dissertation submitted to the Graduate Faculty of
North Carolina State University
in partial fulfillment of the
requirements for the degree of
Doctor of Philosophy

Chemical Engineering

Raleigh, North Carolina
2017

APPROVED BY:

Dr. Gregory N. Parsons
Committee Chair

Dr. Peter S. Fedkiw

Dr. Michael D. Dickey

Dr. Elizabeth C. Dickey

Dr. Xiangwu Zhang

Dr. Veronica Augustyn

BIOGRAPHY

James Daubert was born in Morristown, New Jersey, to Steven and Marianne Daubert. He is the oldest of three children and has a sister, Alicia, and brother, Christopher. He grew up in Lincroft, New Jersey, where he attended Middletown High School South. After graduating from high school in 2006, he attended Cornell University in Ithaca, New York, where he studied chemical engineering. While at Cornell he co-oped at ExxonMobil in Beaumont, Texas, where he worked in both the refinery and the chemical plant. James was a member for the Cornell 100+ MPG team, where he designed a built a HVAC system for a high efficiency automobile. During his time at Cornell, he met and began dating Tracy Cheung. Upon graduation in 2010 with his B.S. in chemical engineering he went to work for Eastern Research Group in Chantilly, Virginia, where he provided technical support for the U.S. Environmental Protection Agency. He then entered the Ph.D. program in chemical engineering at North Carolina State University in 2012. He first worked with Wesley Henderson studying the properties of lithium ion battery electrolytes before joining Gregory Parsons's group in November 2013. While in the Parsons Group, he has researched improving electrochemical systems using ultrathin coatings deposited using atomic layer deposition. He recently married Tracy in November 2016, and he is excited for everything the world has in store for them.

ACKNOWLEDGMENTS

I would like to thank my advisor Dr. Gregory Parsons for his help, mentorship, advice, and support over the years. I would also like to thank all past and present Parsons Group members that have helped me during my time at NC State. You all have always been there to lend a helping hand in lab, brainstorm ideas in the office, and hang out with in the lobby.

I am also thankful for all of the support and opportunities my family has given me my entire life by always allowing me to pursue my interests and goals. Lastly, I would like to thank my wife, Tracy. You are always there to support me, love me, and push me to be a better man.

TABLE OF CONTENTS

LIST OF TABLES	vii
LIST OF FIGURES	viii
CHAPTER 1. Introduction.....	1
1.1 Atomic Layer Deposition.....	1
1.2 Electrochemical Capacitors.....	2
1.3 Pseudocapacitance.....	5
1.4 Flexible Electrochemical Capacitors and Pseudocapacitors	8
1.5 Summary of Results Integrating Pseudocapacitive Materials into Electrochemical Capacitors.....	10
1.6 Metal Corrosion.....	11
1.7 Summary of Results Protecting Metal Using ALD Thin Films	13
1.8 References	15
CHAPTER 2. Experimental.....	28
2.1 Atomic Layer Deposition (ALD).....	28
2.2 Quartz Crystal Microbalance (QCM).....	28
2.3 Ellipsometry	29
2.4 X-ray Reflectivity (XRR).....	29
2.5 X-ray Diffraction (XRD).....	29
2.6 X-ray photoelectron spectroscopy (XPS).....	29
2.7 Fourier Transform Infrared (FTIR) Spectroscopy	30
2.8 Raman Spectroscopy	30
2.9 Scanning Electron Microscopy (SEM)	31
2.10 Energy Filtered Transmission Electron Microscopy (EFTEM).....	31
2.11 Atomic Force Microscopy (AFM)	31
2.12 Gas Adsorption.....	32
2.13 Tensile Strength.....	32
2.14 Cyclic Voltammetry (CV).....	32
2.15 Galvanostatic Charging and Discharging.....	33
2.16 Electrochemical Impedance Spectroscopy (EIS).....	33

2.17	Linear Sweep Voltammetry (LSV)	35
2.18	References	37
CHAPTER 3. Effect of Meso- and Micro-Porosity in Carbon Electrodes on Atomic Layer Deposition of Pseudocapacitive V ₂ O ₅ for High Performance Supercapacitors.....		
3.1	Abstract	39
3.2	Introduction	39
3.3	Experimental Section	42
3.4	Results	47
3.5	Discussion	60
3.6	Conclusions	63
3.7	Supporting Information	64
3.8	Acknowledgments	64
3.9	References	65
CHAPTER 4. Intrinsic Limitations of Atomic Layer Deposition for Pseudocapacitive Metal Oxides in Porous Electrochemical Capacitor Electrodes.....		
4.1	Abstract	71
4.2	Introduction	71
4.3	Experimental Section	74
4.4	Results	76
4.5	Discussion	88
4.6	Conclusions	94
4.7	Acknowledgments	94
4.8	References	95
CHAPTER 5. Kevlar®-Based Supercapacitor Fibers with Conformal Pseudocapacitive Metal Oxide and Metal formed by ALD.....		
5.1	Abstract	102
5.2	Introduction	102
5.3	Experimental Section	106
5.4	Results	109
5.5	Discussion	117
5.6	Conclusions	119

5.7	Acknowledgments	120
5.8	References	121
CHAPTER 6. Corrosion Protection of Copper Using Al ₂ O ₃ , TiO ₂ , ZnO, HfO ₂ , and ZrO ₂ Atomic Layer Deposition.....		127
6.1	Abstract	128
6.2	Introduction	128
6.3	Experimental Section	130
6.4	Results	133
6.5	Discussion	146
6.6	Conclusions	152
6.7	Acknowledgments	152
6.8	References	153
APPENDICES		158
APPENDIX A: Supporting Information for Chapter 3. Effect of Meso- and Micro-Porosity in Carbon Electrodes on Atomic Layer Deposition of Pseudocapacitive V ₂ O ₅ for High Performance Supercapacitors.....		159
A.1	Figures.....	160
A.2	References	167
APPENDIX B. Co-Authored Publications		168
B.1	Solvate Structures and Spectroscopic Characterization of LiTFSI Electrolytes....	168
B.2	Electrolyte Solvation and Ionic Association VI. Acetonitrile-Lithium Salt Mixtures: Highly Associated Salts Revisited*	169

LIST OF TABLES

Table 4.1. The experimental and maximum capacities of the carbons studied when coated with V_2O_5 . ^a	89
Table 5.1. Reported areal capacitance for various fiber-based supercapacitors.	103
Table 5.2. Areal capacitance of varying thickness V_2O_5 films on PPTA electrodes at 2 mV s^{-1}	114
Table 6.1. Corrosion properties of Al_2O_3 films on varying thickness on copper obtained from LSV.	136
Table 6.2. Corrosion properties of ~50 nm ALD films on copper obtained from LSV.	139
Table 6.3. Comparison of reported values obtained from LSV and EIS measurements of copper.	147
Table 6.4. Summary of reported results obtained from LSV and EIS measurements of Al_2O_3 coated copper.	147
Table 6.5. Fitted Equivalent Circuit Model Parameters of ~50 nm ALD Films on Copper.	150

LIST OF FIGURES

Figure 1.1. An ALD deposition cycle showing the deposition of TiO ₂ films from TiCl ₄ and H ₂ O. Figure adopted. ¹⁴	2
Figure 1.2. A Ragone plot showing the specific power versus specific energy comparison of common electrical energy-storage devices. Figure reproduced. ¹⁵	3
Figure 1.3. Schematic of two different charge storage mechanisms via (a) electrochemical double-layer capacitance (EDLC) or (b) redox reactions based pseudocapacitance. Figure reproduced. ¹⁵	4
Figure 2.1. (a) Nyquist plot of a V ₂ O ₅ coated supercapacitor, and (b) Bode plot of Al ₂ O ₃ coated copper with both the measured values and the calculated values from the fitted equivalent circuit shown inset.	34
Figure 2.2. Polarization curve of copper that was coated with Al ₂ O ₃ with i_{corr} , E_{corr} , b_c , and b_a labeled.	35
Figure 3.1. FTIR spectra of (a) G60 and (b) Supra powders treated with 15 M HNO ₃ at varying temperatures. Effect of acid treatment on the pore distribution of (c) G60 and (d) Supra powders and a comparison of the microporosity and mesoporosity (inset).....	48
Figure 3.2. QCM measurements for three ALD cycles of V ₂ O ₅ films deposited at 150°C with a VTIP/N ₂ /H ₂ O/N ₂ = 8/100/2/100 dosing sequence. Left (red) arrow indicates VTIP dose, and the right (blue) arrow indicates H ₂ O dose. The growth during the entire run is shown in the inset.	49
Figure 3.3. (a) Increase in the vanadium content of G60 powder coated with 125 cycles of V ₂ O ₅ ALD at 175°C as measured with EDS; (b) SEM image of untreated G60 coated with V ₂ O ₅ ; and (c) conformal distribution of vanadium measured with EDS. SEM images highlighting the loss in fine porosity of (d) untreated G60; (e) after acid treatment; and (f) subsequent coating with V ₂ O ₅ ALD.....	51
Figure 3.4. FTIR spectra of (a) G60 and (b) Supra powder that was treated with 15 M HNO ₃ that was boiled off and then coated with varying number of V ₂ O ₅ ALD cycles at 150°C. Effect of ALD coatings on the pore distribution of (c) G60 and (d) Supra powder and a comparison of the microporosity and mesoporosity (inset).	52
Figure 3.5. EFTEM micrographs of two sites (left and right) of G60 treated with boiled off HNO ₃ and coated with 1000 cycles of V ₂ O ₅ ALD: (a) zero-loss; (b) carbon; (c) vanadium; and (d) composite carbon and vanadium.	54
Figure 3.6. Cyclic voltammetry scans of V ₂ O ₅ ALD coated (a) G60 and (b) Supra electrodes at 20 mV/s in 1 M KCl.at a 10 μm length scale (Figure 3.3(b)). Figure 3.3(d), (e) and (f) show	

SEM images of the untreated G60, G60 after nitric acid boiled off, and after coating with 125 cycles of V_2O_5 ALD at 175°C , respectively. The dark features present in the untreated carbon become less distinct upon acid treatment, and even less visible after ALD treatment, consistent with a loss in porosity after each step.55

Figure 3.7. (a) The effect of V_2O_5 ALD on capacitor energy storage of G60 and Supra electrodes; (b) weight gain as a function of ALD cycles; and (c) the specific capacitance exhibited by the V_2O_556

Figure 3.8. (a) G60 electrodes after V_2O_5 ALD coatings average current as a function of cyclic voltammetry scan rate; and (b) the specific capacitance versus scan rate^{-1/2}.58

Figure 3.9. Long term performance of V_2O_5 coated G60 electrodes charged/discharged from 0.0 to 0.8 V at a rate of 5 A/g(capacitor).59

Figure 3.10. (a) Nyquist plot of EIS measurements of V_2O_5 ALD coated G60 electrodes; (b) equivalent circuit used to model EIS data; (c) calculated ESR values; and (d) Warburg admittances.60

Figure 3.11. Comparison of the pore distribution and the porosity of the G60 and Supra carbon that had been treated with HNO_3 at 100°C from which the electrodes were constructed. Dimensions of a VTIP molecule (inset).61

Figure 4.1. Illustration of a carbon particle (a) as formed; and (b) after being coated with pseudocapacitive material using ALD. After coating, the image highlights pores that are uncoated and sealed, pores that are partially filled and sealed, and pores that are internally coated. (c) A representative model for a carbon particle pore, depicted as a series of narrowing tubes coated with ALD. The coated, partially sealed and fully sealed portions are indicated in both (b) and (c).77

Figure 4.2. (a) Nitrogen isotherms and (b) cumulative pore volume of the carbon powders studied. The label “AC” corresponds to different activated carbons, and “CB” is a porous carbon black powder.79

Figure 4.3. V_2O_5 volume gains of electrodes constructed from (a) micro-AC, (b) meso-AC, (c) macro-AC, and (d) macro-CB that were coated with varying thicknesses of V_2O_5 ALD. The dashed curves are the modeled volume gains with “no pore sealing” (representing the maximum amount of V_2O_5 based on the carbon’s pore volume), and the “13 Å pore sealing” indicating the modeled V_2O_5 volume gain from depositing only in pores > 13 Å in diameter. Note: the macro-CB does not have any pores < 13 Å in diameter.81

Figure 4.4. Cyclic voltammograms at 2mV/s of electrodes constructed out of micro-AC and coated with 26 Å of V_2O_5 ALD that were annealed at temperatures between 200°C and 300°C82

Figure 4.5. (a) XPS scans of V 2p _{3/2} and O 1s peaks, (b) XRD pattern, and (c) Raman spectra of V ₂ O ₅ ALD as deposited at 150°C and after annealing under air at 300°C.....	84
Figure 4.6. Cyclic voltammograms of (a) micro-AC, (b) meso-AC, (c) macro-AC, and (d) macro-CB electrodes coated with varying thicknesses of V ₂ O ₅ ALD at 2 mV/s.	86
Figure 4.7. Capacity of (a) micro-AC, (b) meso-AC, (c) macro-AC, and (d) macro-CB electrodes that were cycled between 2-4 V vs. Li/Li ⁺ at scan rates of 1 - 200 mV/s.....	87
Figure 4.8. The normalized capacity of (a) macro-AC electrodes and (b) macro-CB electrodes with varying amounts of V ₂ O ₅ deposited on them as a function of cyclic voltammetry scan rate. The normalized capacity of ALD V ₂ O ₅ deposited directly on the stainless steel current collector is provided for comparison.	91
Figure 4.9. (a) Linearization of eqn. 4.4 for macro-CB +43 Å V ₂ O ₅ at 3 V. (b) Cyclic voltammogram of macro-CB +43 Å V ₂ O ₅ scanned at 5 mV/s, the current response calculated from eqn. 4.4, and the capacitive capacity of the electrode. (c) The capacitive capacity, which does not vary with scan rate, of the macro-CB and macro-AC electrodes as a function of V ₂ O ₅ thickness.....	93
Figure 5.1. Schematic of PPTA supercapacitor construction and testing.....	110
Figure 5.2. SEM image of individual PPTA fibers after coating with (a) ALD Pt; and (b) combined ALD Pt/V ₂ O ₅ . Fibers were knotted after ALD coating. Arrows indicate some evidence for minor sheer-related cracking of the ALD Pt and V ₂ O ₅ in panels a and b, respectively.	111
Figure 5.3. Tensile strength of PPTA, PPTA coated with Pt, and PPTA coated with Pt and V ₂ O ₅	112
Figure 5.4. PPTA based supercapacitors were tested in (a) a single yarn in a 3-electrode configuration with a H ₂ O-KCl electrolyte; (b) a two-electrode configuration with two yarns in a PVA-LiCl gel electrolyte and a separator; and (c) a twisted pair of PPTA/Pt/V ₂ O ₅ yarns coated with PVA-LiCl.	113
Figure 5.5. Cyclic voltammetry scans of V ₂ O ₅ /Pt/PPTA supercapacitor yarns at 2 mV s ⁻¹ in (a) H ₂ O-KCl; and (b) PVA-LiCl. Panel (c) shows results for a twisted pair of PPTA/Pt/V ₂ O ₅ yarns in PVA-LiCl.....	114
Figure 5.6. A summary of the areal capacitance as a function of cyclic voltammetry scan rate in (a) H ₂ O-KCl, (b) PVA-LiCl. Panel (c) shows results for a twisted pair of PPTA/Pt/V ₂ O ₅ yarns in PVA-LiCl.	116
Figure 5.7. Nyquist plots of (a) PPTA coated with 11 nm of V ₂ O ₅ , and (b) zoomed in view of the same data.....	117

Figure 6.1. (a) Polarization curve and (b) Bode plot of bare copper and Al ₂ O ₃ coatings of varying thickness on copper with impedance shown as closed squares and phase angle shown with open circles.	135
Figure 6.2. Bode plots for (a) TiO ₂ and (b) ZnO films of varying thickness compared to uncoated copper with impedance shown as closed squares and phase angle shown with open circles. (c) Impedance at 10 mHz for bare copper and Al ₂ O ₃ , TiO ₂ , and ZnO films of varying thickness, and (d) phase angle at 100 Hz.	136
Figure 6.3. AFM images showing morphological differences between (a) bare Cu, (b) Al ₂ O ₃ , (c) TiO ₂ , (d) ZnO, (e) HfO ₂ , and (f) ZrO ₂ films.	138
Figure 6.4. Polarization curves of ~50 nm films of Al ₂ O ₃ , TiO ₂ , ZnO, HfO ₂ , and ZrO ₂ on copper.	139
Figure 6.5. (a) Bode plot of ~50 nm films of Al ₂ O ₃ , TiO ₂ , ZnO, HfO ₂ , and ZrO ₂ on copper with impedance shown as closed squares and phase angle shown with open circles, and (b) impedance at 10 mHz and phase at 100 Hz of the films.	140
Figure 6.6. Bode plots of (a) uncoated copper and ~50 nm films of (b) Al ₂ O ₃ , (c) TiO ₂ , (d) ZnO, (e) HfO ₂ , and (f) ZrO ₂ on copper aged in 0.1 M NaCl for up to 90 h with impedance shown as closed squares and phase angle shown with open circles.	142
Figure 6.7. The (a) relative impedance at 10 mHz and (b) relative phase angle at 100 Hz of ~50 nm Al ₂ O ₃ , TiO ₂ , ZnO, HfO ₂ , ZrO ₂ films on copper, and bare copper compared to the starting impedance and phase angle, respectively, during aging up to 90 h in electrolyte.	143
Figure 6.8. AFM images showing morphological differences in the surfaces of the (a) bare copper, (b) Al ₂ O ₃ coated copper, and (c) HfO ₂ coated copper after a 21 day exposure to 0.1 M NaCl.	144
Figure 6.9. (a) Bode plots of bare copper, Al ₂ O ₃ coated copper, and HfO ₂ coated copper after a 21 day exposure to 0.1 M NaCl with impedance shown as closed squares and phase angle shown with open circles, and (b) a comparison of the impedance at 10 mHz and phase at 100 Hz of the films before and after the extended exposure.	145
Figure 6.10. (a) Diagram of the test setup; and (b) the equivalent circuit used to model the impedance results.	150
Figure 6.11. Polarization resistance of ~50 nm films during exposure to 0.1 M NaCl solution calculated from model fitting parameters.	151
Figure A.1. Comparison of G60 electrodes in a measured using cyclic voltammetry in a 3-electrode and 2-electrode configuration. There is no significant difference in the performance of the electrodes.	160

Figure A.2. Elemental analysis by EDS of (a) G60 and (b) Supra carbon shows more oxygen in the carbon after the acid treatment consistent with the IR results.160

Figure A.3. Raman spectra of (a) G60 and (b) Supra. (c) Band fitting for untreated G60 is shown; and (d) the comparison of the peaks is shown for all samples. The carbon powders were measured with a Raman spectrometer after different acid treatments to identify the disorder (D) and graphitic (G) nature of the powder.¹ The deconvolution of the Raman spectra shows that for the G60 powder, the high temperature acid treatment tends to decrease the relative intensity of the D-band (i.e. increasing graphic structure) whereas the Supra shows a relative increase in the D-band. However, these changes are small, and we do not see significant trends in electrode performance for these changes in D- and G- mode intensity.....161

Figure A.4. (a) V₂O₅ growth per cycle at varying temperatures; and (b) growth with cycle number at 150°C. Film thickness was determined from ellipsometry. The ALD temperature window and growth rate are consistent with previous reports.²162

Figure A.5. (a) XPS and (b) XRD (b) of 400 Å vanadium oxide films deposited at 175°C on Si indicate the vanadium oxide deposited is amorphous V₂O₅.³⁻⁶162

Figure A.6. Mass gain of (a) G60 and (b) Supra powder that was treated with boiling nitric acid as a function of ALD cycles of V₂O₅ at 150°C and the corresponding thickness of V₂O₅ measured on monitor Si wafers. The resulting linear increase in mass gain fits for G60 carbon fits in the with the linear film growth seen on monitor silicon wafers. Similar trends were also seen for the limited number of Supra powder coated. The G60 and Supra carbons displayed different mass gains after similar number of ALD cycles. The variation could be a result of the Supra carbon powder that was coated having a surface area that was only about 1/3 of that of the G60 carbon powder that was coated. We would expect different carbon powders to have a linear mass gain as well, but with a different slope, which would vary as a result of different pore size distribution and surface area of the carbons.163

Figure A.7. Effect of acid treatment on capacitance measured in a 3-electrode cell on (a) G60 and (b) Supra in 1 M KCl reported at a scan rate of 200 mV/s.164

Figure A.8. Columbic efficiency of V₂O₅ coated G60 electrodes as a function of ALD cycles charged/discharged from 0.0 to 0.8 V at a rate of 5 A/g(capacitor).165

Figure A.9. EIS model results of G60 electrodes coated with V₂O₅. (a) specific capacitance and (b) specific capacitance of deposited V₂O₅.....165

Figure A.10. Current response during cyclic voltammetry from either capacitive processes (varies with v) or diffusion processes (varies with $v^{-1/2}$) in the G60 EC coated with V₂O₅ ALD: (a) 0 cycles; (b) 75 cycles; (c) 200 cycles; and (d) 1000 cycles according to the relationship $i(V) = k_1v + k_2v^{1/2}$, where k_1 and k_2 are constants at a particular sweep rate. The capacitive current (dashed line) represents 67 to 93% of the total current (solid line).^{7,8}166

CHAPTER 1. Introduction

1.1 Atomic Layer Deposition

Atomic layer deposition (ALD) is a vapor phase thin film deposition technique based on sequential, self-limiting surface half-reactions that are capable of conformally coating highly porous 3D structures with nanoscale precision. The vapor phase chemicals, or precursors, are introduced into a low vacuum, temperature controlled reactor separately with saturating doses where they perform a self-limiting reaction with the surface sites on the substrate as shown in the cartoon in Figure 1.1. Any excess precursor is then purged from the reactor. Since the precursors are introduced sequentially they are unable to interact in the gas phase, thus leading to a self limiting reaction. The half-reactions can be repeated for a predetermined number of cycles to achieve a controlled thickness based. ALD is advantageous over other coating techniques, because it has no line-of-sight requirement, and thickness control that cannot be matched by other vapor-phase deposition techniques.

Many different metal oxides, metals, and conductive polymers have been deposited using ALD, including conductive metals such as Pt and W; pseudocapacitive materials for energy storage such as RuO_2 , MnO , V_2O_5 , NiO , Fe_2O_3 , Co_3O_4 , and the polymer PEDOT; and dielectrics of interest for corrosion protection such as Al_2O_3 , TiO_2 , ZnO , HfO_2 and ZrO_2 .¹⁻¹³

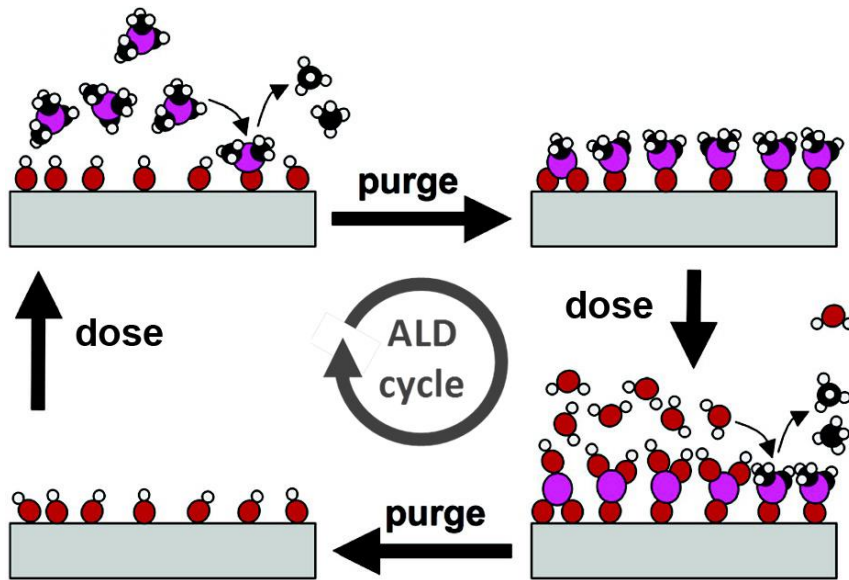


Figure 1.1. An ALD deposition cycle showing the deposition of TiO_2 films from TiCl_4 and H_2O . Figure adopted.¹⁴

1.2 Electrochemical Capacitors

Electrochemical capacitors are an emerging set of electrical energy-storage devices, whose position on the energy versus power spectrum fills the gap between the high power density of conventional solid-state electrostatic capacitors and the high energy density of batteries. Instead of storing charge on the electrode surface in an electric field, as capacitors do, or storing energy in the bulk electrodes with electrochemical reactions, as batteries do, electrochemical capacitors physically store charge at the electrode/electrolyte interface. This charge storage mechanism results in electrochemical capacitors having specific power and specific energy densities that are in between electrostatic capacitors and batteries, as shown on the Ragone plot in Figure 1.2.

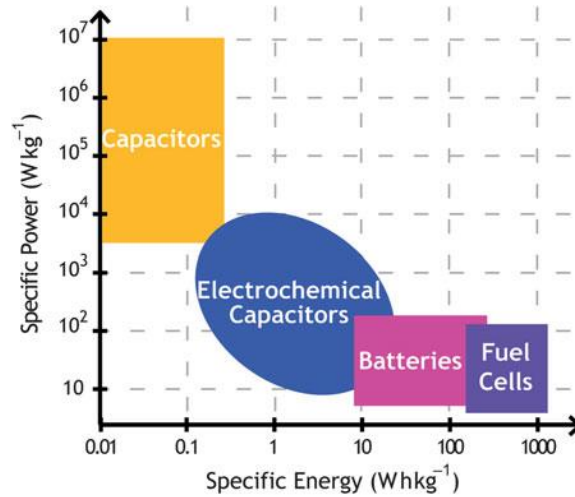


Figure 1.2. A Ragone plot showing the specific power versus specific energy comparison of common electrical energy-storage devices. Figure reproduced.¹⁵

Electrochemical capacitors consist of high surface area, microporous electrodes immersed in an electrolyte as shown in Figure 1.3a. Commercially available electrochemical capacitors are constructed using activated carbons with surface areas ranging between 700-2200 m²/g(carbon), which leads to an effective capacitance in the range from 5-40 μF/cm² (or 70-200 F/g).¹⁵⁻¹⁹ Electrochemical capacitors are capable of power densities of ~15 kW/kg compared to 2 kW/kg for Li-ion batteries, but electrochemical capacitors only have an energy density of 5-8 Wh/kg compared to 180 Wh/kg for Li-ion batteries.^{15,17,18}

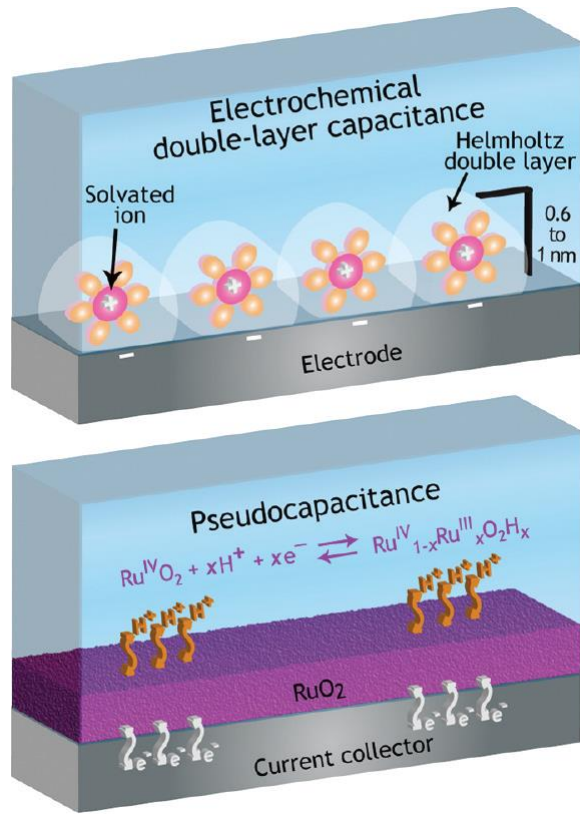


Figure 1.3. Schematic of two different charge storage mechanisms via (a) electrochemical double-layer capacitance (EDLC) or (b) redox reactions based pseudocapacitance. Figure reproduced.¹⁵

While a Ragone plot allows one to quickly compare the energy and power density of an electrical energy-storage devices, it does not include important characteristics, such as cycle life, energy efficiency, and self-discharge. Storing energy at the interface results in electrochemical capacitors being capable of being cycled for hundreds of thousands of cycles, unlike batteries, which suffer from a relatively short cycle life.

The energy density of an electrochemical capacitor (E) is related to the capacitance (C) and operating voltage (V) through the relationship shown in equation 1.1.

$$E = \frac{1}{2} C V^2 \tag{1.1}$$

Electrochemical capacitors can be constructed using either aqueous based or organic based electrolytes. Electrochemical capacitors constructed with aqueous electrolytes are typically limited to an operating voltage of ~ 1 V due to the small (1.23 V) electrochemical stability window of water, and use acids, bases, or salts (i.e. H_2SO_4 , KOH , or KCl) to achieve a high conductivity (~ 1 S/cm).¹⁷ Electrochemical capacitors can also use organic based electrolytes, such as acetonitrile or propylene carbonate, and use highly dissociated salts, the most common being the quaternary ammonium salt tetraethylammonium tetrafluoroborate (TEA-BF_4), and can operate up to ~ 2.7 V.¹⁷ The three-fold increase in voltage between aqueous and organic based electrolytes results in an order of magnitude (eqn. 1.1) increase in the energy density.

In order to make electrochemical capacitors economical for the widespread adoption in electrified vehicles and to add the energy storage capacity needed for the Smart Grid, where both high power output and energy density is needed, the energy density of electrochemical capacitors needs to be increased.^{17,18,20-24} While there has been considerable work investigating the use of nanostructured carbons to increase the capacitance, the energy density will not be able to approach that of batteries without the addition of a new charge storage mechanism.

1.3 Pseudocapacitance

A promising approach to enhancing energy storage of electrochemical capacitors is to add Faradaic charge storage mechanisms, fast and reversible redox reactions that occur near the electrode's surface, known as "pseudocapacitance," as shown in Figure 1.3b.^{17,18,25} There are multiple metal oxides, metal nitrides, and conductive polymers that demonstrate pseudocapacitance, the best-known being ruthenium oxide.

Ruthenium oxide is used in multiple forms, from nanocrystalline to disordered hydrous, in acidic aqueous electrolytes, and have obtained capacitances of 200-1200 F/g.^{15,25} The pseudocapacitive storage mechanism appears to work best in aqueous systems, and the electrochemical capacitors should only be tested where they are stable on a Pourbaix diagram.^{15,26} Due to the high cost of ruthenium oxide, however, there has been a search for cheaper oxides.

While pseudocapacitance can increase charge storage by up to two orders of magnitude, the Faradaic processes can slow charge transfer rates and reduce electrode stability.¹⁸ Pseudocapacitor electrodes are commonly made entirely of metal oxide or a composite of carbon and metal oxide powders.^{26,27} These electrodes often suffer from electrical resistance and poor stability (similar to batteries), therefore failing to maximize their energy storage capacity.²⁶ Pseudocapacitive electrodes constructed using hybrid nanostructured materials can avoid these shortcomings.^{25,26} To design and build nanostructured electrochemical capacitors, it is important to understand the structure-property relationships of both the carbon substrate/pseudocapacitive material and the pseudocapacitive material/electrolyte junctions. Pseudocapacitive thin films yield specific capacitances 2 to 5 times larger than the same material in powder form,¹⁵ and conformal coatings add negligible volume and footprint to the electrode. However, the pseudocapacitive loading needs to be controlled in order to avoid “clogging” of the pores and decreasing net capacitance.²⁸ One way to carefully control the addition of thin films of pseudocapacitive material to electrodes is with ALD.

Multiple ALD materials have been studied to add pseudocapacitance to electrochemical capacitors. Ruthenium oxide ALD has been used to coat: carbon nanotubes (CNTs) that were then electrochemical oxidized and achieved a capacitance of 644 F/g;^{29,30} plasma treated CNTs that demonstrated a six-fold increase in capacitance;³¹ tobacco mosaic virus to create a pseudocapacitor;³² and rGO defects to produce a capacitance of 1100 F/gRuO₂.³³ Vanadium oxide, with its high pseudocapacitance has also been deposited on: CNTs to achieve a capacitance of 600 F/g (1550 F/gV₂O₅);³⁴ indium tin oxide (ITO) nanocrystal scaffolds that showed 2 nm V₂O₅ coatings perform better than 7 nm coatings;³⁵ and carbon onions, which had a large mass loading due to their external surface area.³⁶ Titanium oxide ALD has also been frequently used to add pseudocapacitance with: graphene powders coated with TiO₂ having a capacitance of 84 F/g³⁷ or 98 F/g when an ALD Al₂O₃ seed layer was used;³⁸ CNTs coated with a seed layer of Al₂O₃ and TiO₂ demonstrating a capacitance of 135 F/g;³⁸ vertically aligned CNTs coated with TiO₂ exhibiting a capacitance of 73 F/g or 1364 F/gTiO₂;³⁹ and graphene nanosheets coated with ALD TiO₂ and annealed with NH₃ forming TiN cathodes for

asymmetric supercapacitors.⁴⁰ Some other pseudocapacitive oxides deposited by ALD have included Fe₂O₃ on CNTs integrated into graphene foam for asymmetric supercapacitors anodes;⁴¹ NiO on nanoporous graphene that achieved a capacitance of 1000 F/g (1900 F/gNiO);⁴² and Co₃O₄ on carbon cloth coated with CNTs.¹³

Non-pseudocapacitive ALD films have also been used to aid in the fabrication of pseudocapacitor electrodes. While Al₂O₃ is not pseudocapacitive it has been used to fabricate pseudocapacitors. Alumina ALD has been used: to encapsulate activated carbon with Al₂O₃ to allow higher voltages and increase capacitance;⁴³ as a sacrificial layer for nanotubes that displayed a two to four fold increase in capacitance;⁴⁴ for forming carbon nanoflakes from glucose with a sacrificial Al₂O₃ layer;⁴⁵ and to coat carbon nanoflakes to allow the growth of Ni_xCo_(1-x)O nanonets.⁴⁶ Platinum metal nanotubes deposited using ALD in alumina arrays have also been used to aid the electrodeposition of pseudocapacitive MnO₂.⁴⁷

In order to coat complex materials using ALD an understanding of the complex network of the nanometer scale pores is necessary. Multiple groups have worked to develop a model for the diffusion and reaction of ALD precursors into small pores, focusing on parameters including the saturation dose,⁴⁸ and exposure time,^{49,50} diffusion coefficient,^{51,52} and reactor pressure.⁵³ Most of the models, however, focus on coating pores and particles that are micron scale, and not nanometer scale. Only a few groups have experimental examined the limits of how deep and small a pore that ALD can be used to coat on the nanometer scale. Knez, et al. coated tobacco mosaic virus, with its well defined tubular structure with TiO₂ using titanium tetraisopropyl oxide and found the inner hole of the virus was sealed off with an inner uncoated pore that was 1.0-1.5 nm in diameter.⁵⁴ Work of V₂O₅ ALD on carbon materials has shown that the V₂O₅ mass gain remains linear with increasing ALD cycles on carbon onions that consist of external surface area, but begins to saturate between 100 and 200 ALD cycles on activated carbon with large interior surface area.³⁶

One additional concern that arises when pseudocapacitive materials are used to modify electrochemical capacitors, is that the material will not exhibit pseudocapacitance, with its

constant capacitance over its voltage window, but rather become battery-like with sharp, well defined, redox peaks.^{55,56}

1.4 Flexible Electrochemical Capacitors and Pseudocapacitors

The development of flexible/stretchable electronics or “smart textiles” has spurred interest in developing flexible supercapacitors that are capable of powering the electronics and can be used in the same form factor.^{57–59} Flexible supercapacitors can be classified as either electrochemical double layer capacitors, or pseudocapacitors. In order to achieve widespread adoption to power smart textiles, devices must have high areal capacitance, incorporate a robust current collector that maintains performance under repeated stress, be solid state to avoid the limitations of liquid electrolytes, and be formed from known fiber materials to simplify fabrication.

The efforts to produce flexible supercapacitors can be categorized by the type of current collectors used: flexible metal cores, carbon-based fibers, or the modification of traditional textile fibers or yarns. Within yarns, charge storage layers can be built into each fiber or be added to the external yarn surface after spinning. Capacitance values are typically normalized by the lateral electrode area, i.e. the external cylindrical surface area of the fiber or yarn structure. It is important to note, however, that the normalized capacitance will often depend on the yarn construction, i.e. fiber density, diameter and number of fibers in the yarn, and capacitive contribution from each fiber, making direct comparison difficult. Similar problems arise when normalizing by fiber volume, length or geometric area (i.e. the exposed size of a fabric “patch”).^{13,60,61} Comparisons based on mass or specific surface area are difficult, because active mass fraction is small and the specific surface area is difficult to quantify. To boost the capacitance per unit lateral area, researchers work to create fibers containing high surface area components⁶¹ or with high surface area nanostructured finishes,^{13,60,62,63} where the electrochemically active surface area can significantly exceed the lateral surface area.

Reports show that stainless steel,^{60,64,65,12} gold,⁶⁶ titanium,⁶⁷ or platinum⁶⁸ wire metal cores can be coated with various forms of carbon^{64,66} to form electrochemical double layer capacitors, or

with pseudocapacitive TiO₂ nanotubes,⁶⁷ polyaniline (PANI),^{65,68} Fe₂O₃,¹² and MnO₂⁶⁰ to create supercapacitors. Many flexible supercapacitors utilize gel electrolytes formed by mixing polyvinyl alcohol (PVA) with ionic materials such as H₃PO₄,^{60,61,63,64,12,66-78} H₂SO₄,⁷⁹⁻⁸¹ KOH,⁸²⁻⁸⁴ or LiCl.⁸⁵⁻⁸⁷

Carbon-based fibers or cloth are often treated to increase the available specific surface area and increase conductivity as the basis for increasing the double-layer capacitance.^{61,70,71,74,79,88,89} Wet-spun rGO/CNT yarns have exhibited an areal capacitance of up to 177 mF cm⁻².⁶¹ Conductive polymers are also incorporated into the carbon materials to add pseudocapacitance.^{69,72,77,80,81} Researchers have studied pseudocapacitive metal oxides including Co₃O₄,^{13,73} RuO₂,⁸³ and MnO₂,^{75,76,82,85,86,90} added to carbon-based fibers. The metal oxides are often incorporated into the fibers using liquid phase processes (i.e. electrodeposition, hydrothermal/solvothermal, sol-gel, spray deposition, or electroless),²⁴ but vapor phase processes (i.e. atomic layer deposition, ALD) can also be used to address issues of interfacial and surface chemistry at nanometer scale.⁹¹ Using ALD Co₃O₄, carbon cloth modified with carbon nanotubes has produced estimated charge storage density of 66 mF cm⁻² on the carbon cloth when tested in a basic electrolyte.¹³ While flexible supercapacitors with carbon cores are able to provide high areal capacitance, the carbon fibers have not been commercialized for use in textiles.

Textile substrates are interesting for ALD because of its ability to coat the high aspect ratio materials at low processing temperatures.^{92,93} ALD has been used to make textiles, such as nylon and polypropylene, conductive through the deposition of ZnO, W, or Pt.^{10,94-96}

A few researchers have explored capacitors formed directly on traditional textile fabrics, including cotton, lycra,⁹⁷ or Kevlar®. This approach offers unique opportunity to couple supercapacitor fabrication methodology with textile manufacturing. Double-layer capacitors have been formed by interweaving cotton with steel wires,⁹⁸ and cotton-based pseudocapacitors can be formed by the addition of active NiO and reduced graphene oxide.⁸⁷ An areal capacitance of 1490 mF cm⁻² was reported for 0.3 mm thick cotton threads that were

coated with high surface area CNTs, pseudocapacitive MnO₂ nanostructures, and polypyrrole.⁶²

Kevlar®, or poly(p-phenylene terephthalamide) (PPTA), is particularly interesting because of its use in ballistic protection.^{99,100} Charge storage capacity has been added to PPTA fabrics by dip-coating the fabric in carbon nanotube ink,⁷⁸ and by sputter-coating with gold followed by hydrothermal growth of ZnO. The highest reported areal capacitance for PPTA based supercapacitors of 2.4 mF cm⁻² was achieved using ZnO structures on PPTA fibers wound with Au-coated plastic wire.⁶³ While ALD has previously been studied on PPTA,¹⁰¹ no previous reports show integration of pseudocapacitive ALD materials on PPTA textiles.

1.5 Summary of Results Integrating Pseudocapacitive Materials into Electrochemical Capacitors

In chapter 3 we hypothesized that ALD can be used to form a nanoscale pseudocapacitive layer on porous carbon electrodes to enhance charge storage while maintaining low equivalent series electrical resistances and high cycle life. We embarked on a fundamental study of ALD growth on activated carbon powders, including structural investigations of how surface chemistry affects ALD nucleation and layer uniformity, and the subsequent effects on electrochemical performance, including pseudocapacitance, power delivery, and long-term cycle stability of the ALD layer. We found that ALD of V₂O₅ is a viable means to add pseudocapacitive layers to porous carbon electrodes, but capacitance and electrochemical impedance analysis showed the extent of improvement depended on initial pore structure. The ALD of V₂O₅ onto mesoporous carbon increased the capacitance by up to 46% after 75 ALD cycles, and obtained a maximum pseudocapacitance of 540 F/g(V₂O₅) after 25 ALD cycles, while maintaining low electrical resistance, high columbic efficiency, and a high cycle life. However, adding V₂O₅ ALD to microporous carbons with pore diameters of <11 Å showed far less improvement, likely due to “blocking off” of the micropores and reducing the accessible surface area. Results show that ALD is a viable means to construct high-performance supercapacitors from activated

carbon, but a clear understanding of carbon electrode pore structure, layer conformality, and layer thickness are necessary to fully optimize performance.

In chapter 4 multiple types of carbon powder, with different pore volume and pore distribution, have been fabricated into electrochemical capacitors electrodes and coated with V_2O_5 films of varying thickness using ALD. The effect of the pore structure on the V_2O_5 deposition has been thoroughly analyzed and modeled. The energy density of activated carbon electrodes with both micropores and macropores increased by 144%, while the capacity of electrodes constructed out of carbon black with only macropores increased more than 40-fold. The pores of the carbon electrodes were modeled as a series of connected tubes, and the experimental volumes of V_2O_5 deposited was compared to the theoretical deposition limit. The V_2O_5 ALD process appears to be unable to deposit in pores that are below a critical diameter of 13 Å. Pores below this critical diameter were sealed and decreased the accessible volume for V_2O_5 deposition by more than half, decreasing the maximum energy density. The effect of the pore sealing by the ALD process on the capacitive response of the activated carbon based electrodes is also studied. This work highlights the capabilities and limitations of coating microporous materials using ALD.

In chapter 5 we report an integrated conductor/pseudocapacitor (Pt/ V_2O_5) ALD approach to form PPTA-based supercapacitors using a solid PVA-LiCl gel electrolyte. The PPTA yarns were incorporated into a solid state supercapacitor through the use of a polyvinyl alcohol/lithium chloride gel electrolyte. Pseudocapacitive V_2O_5 films 11 nm thick provided up to a 5x increase in areal capacitance (18.4 mF cm^{-2}) over the Pt-only coated PPTA. Thicker films of V_2O_5 and wrapping the electrodes together into a single yarn resulted in decreased areal capacitance due to charge-transfer limitations. The work describes how ALD metal and metal oxide can be combined to add double layer and pseudocapacitive charge storage to mechanically robust PPTA creating unique multifunctional electronic fabric device systems.

1.6 Metal Corrosion

Copper is a common metal widely used in applications such as plumbing and heat exchangers.^{102–107} While copper has a reasonable resistance to corrosion in liquid water, there

is a finite corrosion rate, which decreases the life of the materials. The rate of copper corrosion is dependent on the water's temperature, pH, and solutes.^{104,105,107–110} The application of barrier coatings on copper is one method to reduce corrosion. There are many well-studied methods for applying corrosion protective coatings including chemical vapor deposition (CVD),^{111,112} self-assembled monolayers,¹¹³ organic azoles,¹¹⁴ polymers,¹¹⁵ plasma,¹¹⁶ and electrochemical deposition.¹¹⁷ Recently, several groups have explored atomic layer deposition (ALD) as a means to form various metal oxide corrosion protection layers. For example, ALD Al₂O₃, TiO₂, and ZnO have been studied to protect metals including copper and stainless steel.^{118–132} In general, while the ALD coatings have been found to provide corrosion protection, the magnitude of corrosion protection has varied significantly between the reported results, in part due to differences in initial surface preparation. For example, Chai, et al. reported ALD Al₂O₃ layers 29.4 nm thick on mechanically and chemically polished copper and has corrosion currents as low as 0.03 $\mu\text{A}/\text{cm}^2$ and an impedance of $2 \times 10^6 \Omega/\text{cm}^2$ at 10 mHz.^{128,129} In another report, Mirhashemihaghighi, et al. deposited ALD Al₂O₃ layers 50 nm thick on mechanically polished and electropolished copper and found corrosion currents of $8 \times 10^{-5} \mu\text{A}/\text{cm}^2$ and impedances of $1 \times 10^8 \Omega/\text{cm}^2$.¹³⁰ The differences indicate that carefully polishing a copper surface can improve the corrosion protection of ALD coatings.

Alumina is the most readily studied ALD thin film for corrosion protection, because it has been shown to nucleate well on metals giving rise to low porosity that prevents the solution from accessing the metal.^{121–131,133} When copper is coated with Al₂O₃ barrier coatings and exposed to aqueous NaCl solution, the corrosion rate is markedly decreased compared to uncoated material, and the surface retains its original visual appearance.^{124,125,128–130} The long term corrosion protection of Al₂O₃ coatings, however, is known to be inhibited by its dissolution into water.^{121,123,127,133}

Titanium dioxide is also studied as a corrosion protection layer of metals.^{119–121,126,127,133} Titanium dioxide coatings deposited by ALD have been found to decrease the corrosion rate as well as shift the corrosion potential to be more positive than the base metal, indicating it provides corrosion resistance,^{119,120} and ALD TiO₂ has also been shown to prevent corrosion

in alkaline conditions.¹³⁴ Titanium dioxide ALD, however, has issues during film nucleation on copper leading to high porosity and poor long term corrosion resistance.¹²⁷ The grain boundaries present in crystalline TiO₂ are also susceptible to species diffusion, which promote surface corrosion.¹²¹

Relatively thick ZnO coatings on copper have also been shown to decrease corrosion current density.¹³⁵ ZnO deposited by ALD does not etch in alkaline conditions,¹³⁶ but suffers from dissolution in purified water.¹²⁷

Atomic layer deposition is also advantageous because it provides direct means to form laminated metal oxide films. For example, laminates of Al₂O₃ and TiO₂ have been studied on copper and stainless steel to combine the corrosion resistance of the TiO₂ and the low porosity of the Al₂O₃,^{118,121,127} and these structures show slower dissolution in water and improved corrosion protection and for copper compared to the single oxides.

Thin films of HfO₂ and ZrO₂ have been widely investigated for electronic dielectric applications, and some research teams have studied their capacity for surface corrosion protection, because of their strong dielectric properties. HfO₂ coatings have been shown to increase the impedance, indicating corrosion protection.^{137,138} ZrO₂ coatings are also of interest for corrosion protection, because they have been shown to increase the polarization potential, decrease the corrosion current density, and increase the impedance.^{139,140} The corrosion resistance of ALD HfO₂ and ZrO₂, however, have not been reported in detail.

1.7 Summary of Results Protecting Metal Using ALD Thin Films

In chapter 6, we used ALD to coat clean copper with a series of metal oxides including Al₂O₃, TiO₂, ZnO, HfO₂ and ZrO₂, and use atomic force microscopy (AFM) to examine the physical properties of the ~50 nm thick films, and electrochemical impedance spectroscopy (EIS) and linear sweep voltammetry (LSV) to characterize the corrosion barrier properties. Analysis of films of each metal oxide demonstrated low electrochemical porosity and provided enhanced corrosion protection from aqueous NaCl solution. The surface pre-treatment and roughness

was found to affect the extent of the corrosion protection. Films of Al_2O_3 or HfO_2 provided the highest level of initial corrosion protection, but films of HfO_2 exhibited the best coating quality after extended exposure. It is the first reported instance of using ultrathin films of HfO_2 or ZrO_2 produced with ALD for corrosion protection, and both are promising materials for corrosion protection.

1.8 References

- (1) Atanasov, S. E.; Losego, M. D.; Gong, B.; Sachet, E.; Maria, J.-P.; Williams, P. S.; Parsons, G. N. Highly Conductive and Conformal Poly(3,4-Ethylenedioxythiophene) (PEDOT) Thin Films via Oxidative Molecular Layer Deposition. *Chem. Mater.* **2014**, *26*, 3471–3478.
- (2) Badot, J. C.; Ribes, S.; Yousfi, E. B.; Vivier, V.; Pereira-Ramos, J. P.; Baffier, N.; Lincot, D. Atomic Layer Epitaxy of Vanadium Oxide Thin Films and Electrochemical Behavior in Presence of Lithium Ions. *Electrochem. Solid-State Lett.* **2000**, *3*, 485–488.
- (3) Kalanyan, B.; Losego, M. D.; Oldham, C. J.; Parsons, G. N. Low-Temperature Atomic Layer Deposition of Tungsten Using Tungsten Hexafluoride and Highly-Diluted Silane in Argon. *Chem. Vap. Deposition* **2013**, *19*, 161–166.
- (4) Burton, B. B.; Fabreguette, F. H.; George, S. M. Atomic Layer Deposition of MnO Using Bis(ethylcyclopentadienyl)manganese and H₂O. *Thin Solid Films* **2009**, *517*, 5658–5665.
- (5) Groner, M. D.; Fabreguette, F. H.; Elam, J. W.; George, S. M. Low-Temperature Al₂O₃ Atomic Layer Deposition. *Chem. Mater.* **2004**, *16*, 639–645.
- (6) Kwon, O.-K.; Kim, J.-H.; Park, H.-S.; Kang, S.-W. Atomic Layer Deposition of Ruthenium Thin Films for Copper Glue Layer. *J. Electrochem. Soc.* **2004**, *151*, G109–G112.
- (7) Lujala, V.; Skarp, J.; Tammenmaa, M.; Suntola, T. Atomic Layer Epitaxy Growth of Doped Zinc Oxide Thin Films from Organometals. *Appl. Surf. Sci.* **1994**, *82–83*, 34–40.
- (8) Ritala, M.; Leskela, M.; Niinisto, L.; Haussalo, P.; Niinist, L. Titanium Isopropoxide as a Precursor in Atomic Layer Epitaxy of Titanium Dioxide Thin Films. *Chem. Mater.* **1993**, *5*, 1174–1181.
- (9) Guan, C.; Wang, Y.; Hu, Y.; Liu, J.; Ho, K. H.; Zhao, W.; Fan, Z.; Shen, Z.; Zhang, H.; Wang, J. Conformally Deposited NiO on a Hierarchical Carbon Support for High-Power and Durable Asymmetric Supercapacitors. *J. Mater. Chem. A* **2015**, *3*, 23283–23288.
- (10) Mundy, J. Z.; Shafiefarhood, A.; Li, F.; Khan, S. A.; Parsons, G. N. Low Temperature Platinum Atomic Layer Deposition on Nylon-6 for Highly Conductive and Catalytic Fiber Mats. *J. Vac. Sci. Technol. A* **2016**, *34*, 01A152.

- (11) Hausmann, D. M.; Kim, E.; Becker, J.; Gordon, R. G. Atomic Layer Deposition of Hafnium and Zirconium Oxides Using Metal Amide Precursors. *Chem. Mater.* **2002**, *14*, 4350–4358.
- (12) Huang, Y.; Huang, Y.; Zhu, M.; Meng, W.; Pei, Z.; Liu, C.; Hu, H.; Zhi, C. Magnetic-Assisted, Self-Healable, Yarn-Based Supercapacitor. *ACS Nano* **2015**, *9*, 6242–6251.
- (13) Guan, C.; Qian, X.; Wang, X.; Cao, Y.; Zhang, Q.; Li, A.; Wang, J. Atomic Layer Deposition of Co_3O_4 on Carbon Nanotubes/carbon Cloth for High-Capacitance and Ultrastable Supercapacitor Electrode. *Nanotechnology* **2015**, *26*, 94001.
- (14) Peng, Q.; Sun, X.-Y.; Spagnola, J. C.; Hyde, G. K.; Spontak, R. J.; Parsons, G. N. Atomic Layer Deposition on Electrospun Polymer Fibers as a Direct Route to Al_2O_3 Microtubes with Precise Wall Thickness Control. *Nano Lett.* **2007**, *7*, 719–722.
- (15) Long, J. W.; Bélanger, D.; Brousse, T.; Sugimoto, W.; Sassin, M. B.; Crosnier, O. Asymmetric Electrochemical Capacitors—Stretching the Limits of Aqueous Electrolytes. *MRS Bull.* **2011**, *36*, 513–522.
- (16) Pandolfo, A. G.; Hollenkamp, A. F. Carbon Properties and Their Role in Supercapacitors. *J. Power Sources* **2006**, *157*, 11–27.
- (17) Béguin, F.; Presser, V.; Balducci, A.; Frackowiak, E. Carbons and Electrolytes for Advanced Supercapacitors. *Adv. Mater.* **2014**, *26*, 2219–2251, 2283.
- (18) Simon, P.; Gogotsi, Y. Materials for Electrochemical Capacitors. *Nat. Mater.* **2008**, *7*, 845–854.
- (19) Gu, W.; Yushin, G. Review of Nanostructured Carbon Materials for Electrochemical Capacitor Applications: Advantages and Limitations of Activated Carbon, Carbide-Derived Carbon, Zeolite-Templated Carbon, Carbon Aerogels, Carbon Nanotubes, Onion-like Carbon, and Graphene. *WIREs Energy Env.* **2014**, *3*, 424–473.
- (20) Goodenough, J. B.; Abruna, H. D.; Buchanan, M. V. *Basic Research Needs for Electrical Energy Storage*; 2007.
- (21) Augustyn, V.; Simon, P.; Dunn, B. Pseudocapacitive Oxide Materials for High-Rate Electrochemical Energy Storage. *Energy Environ. Sci.* **2014**, *7*, 1597.
- (22) Yan, Y.; Li, B.; Guo, W.; Pang, H.; Xue, H. Vanadium Based Materials as Electrode Materials for High Performance Supercapacitors. *J. Power Sources* **2016**, *329*, 148–169.

- (23) Lokhande, V. C.; Lokhande, A. C.; Lokhande, C. D.; Kim, J. H.; Ji, T. Supercapacitive Composite Metal Oxide Electrodes Formed with Carbon, Metal Oxides and Conducting Polymers. *J. Alloys Compd.* **2016**.
- (24) Li, B.; Zheng, M.; Xue, H.; Pang, H. High Performance Electrochemical Capacitor Materials Focusing on Nickel Based Materials. *Inorg. Chem. Front.* **2016**, 3, 175–202.
- (25) Yu, G.; Xie, X.; Pan, L.; Bao, Z.; Cui, Y. Hybrid Nanostructured Materials for High-Performance Electrochemical Capacitors. *Nano Energy* **2013**, 2, 213–234.
- (26) Sassin, M. B.; Chervin, C. N.; Rolison, D. R.; Long, J. W. Redox Deposition of Nanoscale Metal Oxides on Carbon for Next-Generation Electrochemical Capacitors. *Acc. Chem. Res.* **2013**, 46, 1062–1074.
- (27) Lu, M.; Beguin, F.; Frackowiak, E. *Supercapacitors: Materials, Systems and Applications*; 2013.
- (28) Peng, Y.; Chen, Z.; Wen, J.; Xiao, Q.; Weng, D.; He, S.; Geng, H.; Lu, Y. Hierarchical Manganese Oxide/Carbon Nanocomposites for Supercapacitor Electrodes. *Nano Res.* **2011**, 4, 216–225.
- (29) Warren, R.; Sammoura, F.; Tounsi, F.; Sanghadasa, M.; Lin, L. Highly Active Ruthenium Oxide Coating via ALD and Electrochemical Activation in Supercapacitor Applications. *J. Mater. Chem. A* **2015**, 3, 15568–15575.
- (30) Warren, R.; Sammoura, F.; Kozinda, A.; Lin, L. ALD Ruthenium Oxide-Carbon Nanotube Electrodes for Supercapacitor Applications. In; 2014; pp. 167–170.
- (31) Woo Kim, J.; Kim, B.; Won Park, S.; Kim, W.; Hyung Shim, J. Atomic Layer Deposition of Ruthenium on Plasma-Treated Vertically Aligned Carbon Nanotubes for High-Performance Ultracapacitors. *Nanotechnology* **2014**, 25, 435404.
- (32) Gnerlich, M.; Pomerantseva, E.; Gregorczyk, K.; Ketchum, D.; Rubloff, G.; Ghodssi, R. Solid Flexible Electrochemical Supercapacitor Using Tobacco Mosaic Virus Nanostructures and ALD Ruthenium Oxide. *J. Micromechanics Microengineering* **2013**, 23, 114014.
- (33) Yang, F.; Zhang, L.; Zuzuarregui, A.; Gregorczyk, K.; Li, L.; Beltrán, M.; Tollan, C.; Brede, J.; Rogero, C.; Chuvilin, A.; Knez, M. Functionalization of Defect Sites in Graphene with RuO₂ for High Capacitive Performance. *ACS Appl. Mater. Interfaces* **2015**, 7, 20513–20519.
- (34) Boukhalifa, S.; Evanoff, K.; Yushin, G. Atomic Layer Deposition of Vanadium Oxide on Carbon Nanotubes for High-Power Supercapacitor Electrodes. *Energy Environ. Sci.* **2012**, 5, 6872–6879.

- (35) Rauda, I. E.; Augustyn, V.; Saldarriaga-Lopez, L. C.; Chen, X.; Schelhas, L. T.; Rubloff, G. W.; Dunn, B.; Tolbert, S. H. Nanostructured Pseudocapacitors Based on Atomic Layer Deposition of V_2O_5 onto Conductive Nanocrystal-Based Mesoporous ITO Scaffolds. *Adv. Funct. Mater.* **2014**, *24*, 6717–6728.
- (36) Fleischmann, S.; Jäckel, N.; Zeiger, M.; Krüner, B.; Grobelsek, I.; Formanek, P.; Choudhury, S.; Weingarh, D.; Presser, V. Enhanced Electrochemical Energy Storage by Nanoscopic Decoration of Endohedral and Exohedral Carbon with Vanadium Oxide via Atomic Layer Deposition. *Chem. Mater.* **2016**, *28*, 2802–2813.
- (37) Sun, X.; Xie, M.; Wang, G.; Sun, H.; Cavanagh, A. S.; Travis, J. J.; George, S. M.; Lian, J. Atomic Layer Deposition of TiO_2 on Graphene for Supercapacitors. *J. Electrochem. Soc.* **2012**, *159*, A364–A369.
- (38) Sun, X.; Xie, M.; Travis, J. J.; Wang, G.; Sun, H.; Lian, J.; George, S. M. Pseudocapacitance of Amorphous TiO_2 Thin Films Anchored to Graphene and Carbon Nanotubes Using Atomic Layer Deposition. *J. Phys. Chem. C* **2013**, *117*, 22497–22508.
- (39) Fisher, R. A.; Watt, M. R.; Konjeti, R.; Ready, W. J. Atomic Layer Deposition of Titanium Oxide for Pseudocapacitive Functionalization of Vertically-Aligned Carbon Nanotube Supercapacitor Electrodes. *ECS J. Solid State Sci. Technol.* **2014**, *4*, M1–M5.
- (40) Zhu, C.; Yang, P.; Chao, D.; Wang, X.; Zhang, X.; Chen, S.; Tay, B. K.; Huang, H.; Zhang, H.; Mai, W.; Fan, H. All Metal Nitrides Solid-State Asymmetric Supercapacitors. *Adv. Mater.* **2015**, *27*, 4566–4571.
- (41) Guan, C.; Liu, J.; Wang, Y.; Mao, L.; Fan, Z.; Shen, Z.; Zhang, H.; Wang, J. Iron Oxide-Decorated Carbon for Supercapacitor Anodes with Ultrahigh Energy Density and Outstanding Cycling Stability. *ACS Nano* **2015**, *9*, 5198–5207.
- (42) Chen, C.; Chen, C.; Huang, P.; Duan, F.; Zhao, S.; Li, P.; Fan, J.; Song, W.; Qin, Y. NiO/nanoporous Graphene Composites with Excellent Supercapacitive Performance Produced by Atomic Layer Deposition. *Nanotechnology* **2014**, *25*, 504001.
- (43) Hong, K.; Cho, M.; Kim, S. O. Atomic Layer Deposition Encapsulated Activated Carbon Electrodes for High Voltage Stable Supercapacitors. *ACS Appl. Mater. Interfaces* **2015**, *7*, 1899–1906.
- (44) Guan, C.; Xia, X.; Meng, N.; Zeng, Z.; Cao, X.; Soci, C.; Zhang, H.; Fan, H. J. Hollow Core–shell Nanostructure Supercapacitor Electrodes: Gap Matters. *Energy Environ. Sci.* **2012**, *5*, 9085.

- (45) Guan, C.; Zeng, Z.; Li, X.; Cao, X.; Fan, Y.; Xia, X.; Pan, G.; Zhang, H.; Fan, H. J. Atomic-Layer-Deposition-Assisted Formation of Carbon Nanoflakes on Metal Oxides and Energy Storage Application. *Small* **2014**, *10*, 300–307.
- (46) Guan, C.; Wang, Y.; Zacharias, M.; Wang, J.; Fan, H. J. Atomic-Layer-Deposition Alumina Induced Carbon on Porous Ni_(x)Co_(1-x)O Nanonets for Enhanced Pseudocapacitive and Li-Ion Storage Performance. *Nanotechnology* **2015**, *26*, 14001.
- (47) Wen, L.; Mi, Y.; Wang, C.; Fang, Y.; Grote, F.; Zhao, H.; Zhou, M.; Lei, Y. Cost-Effective Atomic Layer Deposition Synthesis of Pt Nanotube Arrays: Application for High Performance Supercapacitor. *Small* **2014**, *10*, 3162–3168.
- (48) Gordon, R. G.; Hausmann, D.; Kim, E.; Shepard, J. A Kinetic Model for Step Coverage by Atomic Layer Deposition in Narrow Holes or Trenches. *Chem. Vap. Deposition*. **2003**, *9*, 73–78.
- (49) Yanguas-Gil, A.; Elam, J. W. Self-Limited Reaction-Diffusion in Nanostructured Substrates: Surface Coverage Dynamics and Analytic Approximations to ALD Saturation Times. *Chem. Vap. Deposition*. **2012**, *18*, 46–52.
- (50) Elam, J. W.; Routkevitch, D.; Mardilovich, P. P.; George, S. M. Conformal Coating on Ultrahigh-Aspect-Ratio Nanopores of Anodic Alumina by Atomic Layer Deposition. *Chem. Mater.* **2003**, *15*, 3507–3517.
- (51) Keuter, T.; Menzler, N. H.; Mauer, G.; Vondahlen, F.; Vaßen, R.; Buchkremer, H. P. Modeling Precursor Diffusion and Reaction of Atomic Layer Deposition in Porous Structures. *J. Vac. Sci. Technol. A*. **2015**, *33*, 01A104.
- (52) Fiorentino, G.; Vollebregt, S.; Tichelaar, F. D.; Ishihara, R.; Sarro, P. M. Impact of the Atomic Layer Deposition Precursors Diffusion on Solid-State Carbon Nanotube Based Supercapacitors Performances. *Nanotechnology* **2015**, *26*, 64002.
- (53) Poodt, P.; Marnett, A.; Schulpen, J.; Kessels, W. M. M. (Erwin); Roozeboom, F. Effect of Reactor Pressure on the Conformal Coating inside Porous Substrates by Atomic Layer Deposition. *J. Vac. Sci. Technol. A*. **2017**, *35*, 21502.
- (54) Knez, M.; Kadri, A.; Wege, C.; Gösele, U.; Jeske, H.; Nielsch, K. Atomic Layer Deposition on Biological Macromolecules: Metal Oxide Coating of Tobacco Mosaic Virus and Ferritin. *Nano Lett.* **2006**, *6*, 1172–1177.
- (55) Brousse, T.; Belanger, D.; Long, J. W. To Be or Not To Be Pseudocapacitive? *J. Electrochem. Soc.* **2015**, *162*, A5185–A5189.
- (56) Simon, P.; Gogotsi, Y.; Dunn, B. Where Do Batteries End and Supercapacitors Begin? *Science (80-.)*. **2014**, *343*, 1210–1211.

- (57) Cai, X.; Peng, M.; Yu, X.; Fu, Y.; Zou, D. Flexible Planar/fiber-Architected Supercapacitors for Wearable Energy Storage. *J. Mater. Chem. C* **2014**, *2*, 1184–1200.
- (58) Yu, D.; Qian, Q.; Wei, L.; Jiang, W.; Goh, K.; Wei, J.; Zhang, J.; Chen, Y. Emergence of Fiber Supercapacitors. *Chem. Soc. Rev.* **2015**, *44*, 647–662.
- (59) Yang, P.; Mai, W. Flexible Solid-State Electrochemical Supercapacitors. *Nano Energy* **2014**, *8*, 274–290.
- (60) Huang, Y.; Hu, H.; Huang, Y.; Zhu, M.; Meng, W.; Liu, C.; Pei, Z.; Hao, C.; Wang, Z.; Zhi, C. From Industrially Weavable and Knittable Highly Conductive Yarns to Large Wearable Energy Storage Textiles. *ACS Nano* **2015**, *9*, 4766–4775.
- (61) Kou, L.; Huang, T.; Zheng, B.; Han, Y.; Zhao, X.; Gopalsamy, K.; Sun, H.; Gao, C. Coaxial Wet-Spun Yarn Supercapacitors for High-Energy Density and Safe Wearable Electronics. *Nat. Commun.* **2014**, *5*, 3754.
- (62) Liu, N.; Ma, W.; Tao, J.; Zhang, X.; Su, J.; Li, L.; Yang, C.; Gao, Y.; Golberg, D.; Bando, Y. Cable-Type Supercapacitors of Three-Dimensional Cotton Thread Based Multi-Grade Nanostructures for Wearable Energy Storage. *Adv. Mater.* **2013**, *25*, 4925–4931.
- (63) Bae, J.; Song, M. K.; Park, Y. J.; Kim, J. M.; Liu, M.; Wang, Z. L. Fiber Supercapacitors Made of Nanowire-Fiber Hybrid Structures for Wearable/Flexible Energy Storage. *Angew. Chemie Int. Ed.* **2011**, *50*, 1683–1687.
- (64) Harrison, D.; Qiu, F.; Fyson, J.; Xu, Y.; Evans, P.; Southee, D. A Coaxial Single Fibre Supercapacitor for Energy Storage. *Phys. Chem. Chem. Phys.* **2013**, *15*, 12215–12219.
- (65) Fu, Y.; Wu, H.; Ye, S.; Cai, X.; Yu, X.; Hou, S.; Kafafy, H.; Zou, D. Integrated Power Fiber for Energy Conversion and Storage. *Energy Environ. Sci.* **2013**, *6*, 805–812.
- (66) Li, Y.; Sheng, K.; Yuan, W.; Shi, G. A High-Performance Flexible Fibre-Shaped Electrochemical Capacitor Based on Electrochemically Reduced Graphene Oxide. *Chem. Commun.* **2013**, *49*, 291–293.
- (67) Chen, T.; Qiu, L.; Yang, Z.; Cai, Z.; Ren, J.; Li, H.; Lin, H.; Sun, X.; Peng, H. An Integrated “Energy Wire” for Both Photoelectric Conversion and Energy Storage. *Angew. Chemie Int. Ed.* **2012**, *51*, 11977–11980.
- (68) Zhang, D.; Miao, M.; Niu, H.; Wei, Z. Core-Spun Carbon Nanotube Yarn Supercapacitors for Wearable Electronic Textiles. *ACS Nano* **2014**, *8*, 4571–4579.

- (69) Cai, Z.; Li, L.; Ren, J.; Qiu, L.; Lin, H.; Peng, H. Flexible, Weavable and Efficient Microsupercapacitor Wires Based on Polyaniline Composite Fibers Incorporated with Aligned Carbon Nanotubes. *J. Mater. Chem. A* **2013**, *1*, 258–261.
- (70) Chen, X.; Qiu, L.; Ren, J.; Guan, G.; Lin, H.; Zhang, Z.; Chen, P.; Wang, Y.; Peng, H. Novel Electric Double-Layer Capacitor with a Coaxial Fiber Structure. *Adv. Mater.* **2013**, *25*, 6436–6441.
- (71) Le, V. T.; Kim, H.; Ghosh, A.; Kim, J.; Chang, J.; Vu, Q. A.; Pham, D. T.; Lee, J.-H.; Kim, S.-W.; Lee, Y. H. Coaxial Fiber Supercapacitor Using All-Carbon Material Electrodes. *ACS Nano* **2013**, *7*, 5940–5947.
- (72) Lee, J. A.; Shin, M. K.; Kim, S. H.; Cho, H. U.; Spinks, G. M.; Wallace, G. G.; Lima, M. D.; Lepró, X.; Kozlov, M. E.; Baughman, R. H.; Kim, S. J. Ultrafast Charge and Discharge Biscrolled Yarn Supercapacitors for Textiles and Microdevices. *Nat. Commun.* **2013**, *4*, 1970.
- (73) Liu, B.; Tan, D.; Wang, X.; Chen, D.; Shen, G. Flexible, Planar-Integrated, All-Solid-State Fiber Supercapacitors with an Enhanced Distributed-Capacitance Effect. *Small* **2013**, *9*, 1998–2004.
- (74) Ren, J.; Bai, W.; Guan, G.; Zhang, Y.; Peng, H. Flexible and Weaveable Capacitor Wire Based on a Carbon Nanocomposite Fiber. *Adv. Mater.* **2013**, *25*, 5965–5970.
- (75) Ren, J.; Li, L.; Chen, C.; Chen, X.; Cai, Z.; Qiu, L.; Wang, Y.; Zhu, X.; Peng, H. Twisting Carbon Nanotube Fibers for Both Wire-Shaped Micro-Supercapacitor and Micro-Battery. *Adv. Mater.* **2013**, *25*, 1155–1159.
- (76) Xiao, X.; Li, T.; Yang, P.; Gao, Y.; Jin, H.; Ni, W.; Zhan, W.; Zhang, X.; Cao, Y.; Zhong, J.; Gong, L.; Yen, W.; Mai, W.; Chen, J.; Huo, K.; Chueh, Y.; Wang, Z.; Zhou, J. Fiber-Based All-Solid-State Flexible Supercapacitors for Self-Powered Systems. *ACS Nano* **2012**, *6*, 9200–9206.
- (77) Yu, D.; Goh, K.; Wang, H.; Wei, L.; Jiang, W.; Zhang, Q.; Dai, L.; Chen, Y. Scalable Synthesis of Hierarchically Structured Carbon Nanotube–graphene Fibres for Capacitive Energy Storage. *Nat. Nanotechnol.* **2014**, *9*, 555–562.
- (78) Gao, Y.; Sim, K.; Sun, S.; Chen, Z.; Song, J.; Yu, C. Crack-Insensitive Wearable Electronics Enabled Through High-Strength Kevlar Fabrics. *IEEE Trans. Components, Packag. Manuf. Technol.* **2015**, *5*, 1230–1236.
- (79) Meng, Y.; Zhao, Y.; Hu, C.; Cheng, H.; Hu, Y.; Zhang, Z.; Shi, G.; Qu, L. All-Graphene Core-Sheath Microfibers for All-Solid-State, Stretchable Fibriform Supercapacitors and Wearable Electronic Textiles. *Adv. Mater.* **2013**, *25*, 2326–2331.

- (80) Meng, Q.; Wang, K.; Guo, W.; Fang, J.; Wei, Z.; She, X. Thread-like Supercapacitors Based on One-Step Spun Nanocomposite Yarns. *Small* **2014**, *10*, 3187–3193.
- (81) Wang, K.; Meng, Q.; Zhang, Y.; Wei, Z.; Miao, M. High-Performance Two-Ply Yarn Supercapacitors Based on Carbon Nanotubes and Polyaniline Nanowire Arrays. *Adv. Mater.* **2013**, *25*, 1494–1498.
- (82) Xu, P.; Wei, B.; Cao, Z.; Zheng, J.; Gong, K.; Li, F.; Yu, J.; Li, Q.; Lu, W.; Byun, J.-H.; Kim, B.-S.; Yan, Y.; Chou, T.-W. Stretchable Wire-Shaped Asymmetric Supercapacitors Based on Pristine and MnO₂ Coated Carbon Nanotube Fibers. *ACS Nano* **2015**, *9*, 6088–6096.
- (83) Xu, J.; Wang, Q.; Wang, X.; Xiang, Q.; Liang, B.; Chen, D.; Shen, G. Flexible Asymmetric Supercapacitors Based upon Co₉S₈ Nanorod//Co₃O₄@RuO₂ Nanosheet Arrays on Carbon Cloth. *ACS Nano* **2013**, *7*, 5453–5462.
- (84) Pang, H.; Zhang, Y.; Lai, W.-Y.; Hu, Z.; Huang, W. Lamellar K₂Co₃(P₂O₇)₂·2H₂O Nanocrystal Whiskers: High-Performance Flexible All-Solid-State Asymmetric Micro-Supercapacitors via Inkjet Printing. *Nano Energy* **2015**, *15*, 303–312.
- (85) Lu, X.; Yu, M.; Wang, G.; Zhai, T.; Xie, S.; Ling, Y.; Tong, Y.; Li, Y. H-TiO₂@MnO₂//H-TiO₂@C Core-Shell Nanowires for High Performance and Flexible Asymmetric Supercapacitors. *Adv. Mater.* **2013**, *25*, 267–272.
- (86) Yang, P.; Xiao, X.; Li, Y.; Ding, Y.; Qiang, P.; Tan, X.; Mai, W.; Lin, Z.; Wu, W.; Li, T.; Jin, H.; Liu, P.; Zhou, J.; Wong, C.; Wang, Z. Hydrogenated ZnO Core–Shell Nanocables for Flexible Supercapacitors and Self-Powered Systems. *ACS Nano* **2013**, *7*, 2617–2626.
- (87) Liu, L.; Yu, Y.; Yan, C.; Li, K.; Zheng, Z. Wearable Energy-Dense and Power-Dense Supercapacitor Yarns Enabled by Scalable Graphene–metallic Textile Composite Electrodes. *Nat. Commun.* **2015**, *6*, 7260.
- (88) Fu, Y.; Cai, X.; Wu, H.; Lv, Z.; Hou, S.; Peng, M.; Yu, X.; Zou, D. Fiber Supercapacitors Utilizing Pen Ink for Flexible/Wearable Energy Storage. *Adv. Mater.* **2012**, *24*, 5713–5718.
- (89) Chen, Z.; Qin, Y.; Weng, D.; Xiao, Q.; Peng, Y.; Wang, X.; Li, H.; Wei, F.; Lu, Y. Design and Synthesis of Hierarchical Nanowire Composites for Electrochemical Energy Storage. *Adv. Funct. Mater.* **2009**, *19*, 3420–3426.
- (90) Yu, D.; Goh, K.; Zhang, Q.; Wei, L.; Wang, H.; Jiang, W.; Chen, Y. Controlled Functionalization of Carbonaceous Fibers for Asymmetric Solid-State Micro-Supercapacitors with High Volumetric Energy Density. *Adv. Mater.* **2014**, *26*, 6790–6797.

- (91) Guan, C.; Wang, J. Recent Development of Advanced Electrode Materials by Atomic Layer Deposition for Electrochemical Energy Storage. *Adv. Sci.* **2016**.
- (92) Brozena, A. H.; Oldham, C. J.; Parsons, G. N. Atomic Layer Deposition on Polymer Fibers and Fabrics for Multifunctional and Electronic Textiles. *J. Vac. Sci. Technol. A* **2016**, *34*, 10801.
- (93) Parsons, G. N.; Atanasov, S. E.; Dandley, E. C.; Devine, C. K.; Gong, B.; Jur, J. S.; Lee, K.; Oldham, C. J.; Peng, Q.; Spagnola, J. C.; Williams, P. S. Mechanisms and Reactions during Atomic Layer Deposition on Polymers. *Coord. Chem. Rev.* **2013**, *257*, 3323–3331.
- (94) Kalanyan, B.; Oldham, C. J.; Sweet, W. J.; Parsons, G. N. Highly Conductive and Flexible Nylon-6 Nonwoven Fiber Mats Formed Using Tungsten Atomic Layer Deposition. *ACS Appl. Mater. Interfaces* **2013**, *5*, 5253–5259.
- (95) Sweet, W. J.; Jur, J. S.; Parsons, G. N. Bi-Layer Al₂O₃/ZnO Atomic Layer Deposition for Controllable Conductive Coatings on Polypropylene Nonwoven Fiber Mats. *J. Appl. Phys.* **2013**, *113*, 194303.
- (96) Sweet, W. J.; Oldham, C. J.; Parsons, G. N. Conductivity and Touch-Sensor Application for Atomic Layer Deposition ZnO and Al:ZnO on Nylon Nonwoven Fiber Mats. *J. Vac. Sci. Technol. A* **2015**, *33*, 01A117.
- (97) Yue, B.; Wang, C.; Ding, X.; Wallace, G. G. Polypyrrole Coated Nylon Lycra Fabric as Stretchable Electrode for Supercapacitor Applications. *Electrochim. Acta* **2012**, *68*, 18–24.
- (98) Jost, K.; Durkin, D. P.; Haverhals, L. M.; Brown, E. K.; Langenstein, M.; De Long, H. C.; Trulove, P. C.; Gogotsi, Y.; Dion, G. Natural Fiber Welded Electrode Yarns for Knittable Textile Supercapacitors. *Adv. Energy Mater.* **2015**, *5*, 1401286.
- (99) Jacobs, M. J. N.; Van Dingenen, J. L. J. Ballistic Protection Mechanisms in Personal Armour. *J. Mater. Sci.* **2001**, *36*, 3137–3142.
- (100) Lee, Y. S.; Wetzel, E. D.; Wagner, N. J. The Ballistic Impact Characteristics of Kevlar Woven Fabrics Impregnated with a Colloidal Shear Thickening Fluid. *J. Mater. Sci.* **2003**, *38*, 2825–2833.
- (101) Atanasov, S. E.; Oldham, C. J.; Slusarski, K. A.; Taggart-Scarff, J.; Sherman, S. A.; Senecal, K. J.; Filocamo, S. F.; McAllister, Q. P.; Wetzel, E. D.; Parsons, G. N. Improved Cut-Resistance of Kevlar® Using Controlled Interface Reactions during Atomic Layer Deposition of Ultrathin (<50 Å) Inorganic Coatings. *J. Mater. Chem. A* **2014**, *2*, 17371–17379.

- (102) Lee, S.-H.; Kim, J.-G.; Koo, J.-Y. Investigation of Pitting Corrosion of a Copper Tube in a Heating System. *Eng. Fail. Anal.* **2010**, *17*, 1424–1435.
- (103) Lu, B.; Meng, W. J.; Mei, F. Experimental Investigation of Cu-Based, Double-Layered, Microchannel Heat Exchangers. *J. Micromechanics Microengineering* **2013**, *23*, 35017.
- (104) Sobue, K.; Sugahara, A.; Nakata, T.; Imai, H.; Magaino, S. Effect of Free Carbon Dioxide on Corrosion Behavior of Copper in Simulated Water. *Surf. Coat. Technol.* **2003**, *169–170*, 662–665.
- (105) Boulay, N.; Edwards, M. Role of Temperature, Chlorine, and Organic Matter in Copper Corrosion by-Product Release in Soft Water. *Water Res.* **2001**, *35*, 683–690.
- (106) Armanious, A.; Johannsen, K. Alternative Methods for Copper Corrosion Studies in Household Plumbing Systems. *Mater. Corros.* **2012**, *63*, 438–444.
- (107) Farooqi, O. E.; Asce, M.; Loganathan, G. V.; Edwards, M. A.; Bosch, D.; Lee, J.; Scardina, P. Copper Pinhole Failures: Plumbing Susceptibility and Management. *J. Water Resour. Plan. Manag.* **2009**, *135*, 227–236.
- (108) Jeon, B.; Sankaranarayanan, S. K. R. S.; van Duin, A. C. T.; Ramanathan, S. Atomistic Insights into Aqueous Corrosion of Copper. *J. Chem. Phys.* **2011**, *134*, 234706.
- (109) Pehkonen, S. O.; Palit, A.; Zhang, X. Effect of Specific Water Quality Parameters on Copper Corrosion. *Corrosion* **2002**, *58*, 156–165.
- (110) Feng, Y.; Siow, K.-S.; Teo, W.-K.; Tan, K.-L.; Hsieh, A.-K. Corrosion Mechanisms and Products of Copper in Aqueous Solutions at Various pH Values. *Corrosion* **1997**, *53*, 389–398.
- (111) Lau, K. H.; Sanjurjo, A.; Wood, B. J. Aluminum and Alumina Coatings on Copper by Chemical Vapor Deposition in Fluidized Bed Reactors. *Surf. Coat. Technol.* **1992**, *54–55*, 234–240.
- (112) Sanjurjo, A.; Wood, B. J.; Lau, K. H.; Tong, G. T.; Choi, D. K.; McKubre, M. C. H.; Song, H. K.; Church, N. Titanium-Based Coatings on Copper by Chemical Vapor Deposition in Fluidized Bed Reactors. *Surf. Coat. Technol.* **1991**, *49*, 110–115.
- (113) Yamamoto, Y.; Nishihara, H.; Aramaki, K. Self-Assembled Layers of Alkanethiols on Copper for Protection Against Corrosion. *J. Electrochem. Soc.* **1993**, *140*, 436–443.
- (114) Brusic, V.; Frisch, M. A.; Eldridge, B. N.; Novak, F. P.; Kaufman, F. B.; Rush, B. M.; Frankel, G. S. Copper Corrosion With and Without Inhibitors. *J. Electrochem. Soc.* **1991**, *138*, 2253–2259.

- (115) Tallman, D. E.; Spinks, G.; Dominis, A.; Wallace, G. G. Electroactive Conducting Polymers for Corrosion Control. *J. Solid State Electrochem.* **2002**, *6*, 73–84.
- (116) Lin, Y.; Yasuda, H. Effect of Plasma Polymer Deposition Methods on Copper Corrosion Protection. *J. Appl. Polym. Sci.* **1996**, *60*, 543–555.
- (117) Patil, S.; Sainkar, S. R.; Patil, P. P. Poly(o-Anisidine) Coatings on Copper: Synthesis, Characterization and Evaluation of Corrosion Protection Performance. *Appl. Surf. Sci.* **2004**, *225*, 204–216.
- (118) Marin, E.; Lanzutti, A.; Guzman, L.; Fedrizzi, L. Corrosion Protection of AISI 316 Stainless Steel by ALD Alumina/titania Nanometric Coatings. *J. Coatings Technol. Res.* **2011**, *8*, 655–659.
- (119) Shan, C. X.; Hou, X.; Choy, K.-L. Corrosion Resistance of TiO₂ Films Grown on Stainless Steel by Atomic Layer Deposition. *Surf. Coat. Technol.* **2008**, *202*, 2399–2402.
- (120) Shan, C. X.; Hou, X.; Choy, K.-L.; Choquet, P. Improvement in Corrosion Resistance of CrN Coated Stainless Steel by Conformal TiO₂ Deposition. *Surf. Coat. Technol.* **2008**, *202*, 2147–2151.
- (121) Matero, R.; Ritala, M.; Leskelä, M.; Salo, T.; Aromaa, J.; Forsén, O. Atomic Layer Deposited Thin Films for Corrosion Protection. *Le J. Phys. IV* **1999**, *9*, 1340–1344.
- (122) Potts, S. E.; Schmalz, L.; Fenker, M.; Díaz, B.; Światowska, J.; Maurice, V.; Seyeux, A.; Marcus, P.; Radnóczy, G.; Tóth, L.; Kessels, W. M. M. Ultra-Thin Aluminium Oxide Films Deposited by Plasma-Enhanced Atomic Layer Deposition for Corrosion Protection. *J. Electrochem. Soc.* **2011**, *158*, C132–C138.
- (123) Díaz, B.; Härkönen, E.; Maurice, V.; Światowska, J.; Seyeux, A.; Ritala, M.; Marcus, P. Failure Mechanism of Thin Al₂O₃ Coatings Grown by Atomic Layer Deposition for Corrosion Protection of Carbon Steel. *Electrochim. Acta* **2011**, *56*, 9609–9618.
- (124) Díaz, B.; Światowska, J.; Maurice, V.; Seyeux, A.; Normand, B.; Härkönen, E.; Ritala, M.; Marcus, P. Electrochemical and Time-of-Flight Secondary Ion Mass Spectrometry Analysis of Ultra-Thin Metal Oxide (Al₂O₃ and Ta₂O₅) Coatings Deposited by Atomic Layer Deposition on Stainless Steel. *Electrochim. Acta* **2011**, *56*, 10516–10523.
- (125) Díaz, B.; Härkönen, E.; Światowska, J.; Maurice, V.; Seyeux, A.; Marcus, P.; Ritala, M. Low-Temperature Atomic Layer Deposition of Al₂O₃ Thin Coatings for Corrosion Protection of Steel: Surface and Electrochemical Analysis. *Corros. Sci.* **2011**, *53*, 2168–2175.

- (126) Marin, E.; Lanzutti, A.; Paussa, L.; Guzman, L.; Fedrizzi, L. Long Term Performance of Atomic Layer Deposition Coatings for Corrosion Protection of Stainless Steel. *Mater. Corros.* **2015**, *66*, 907–914.
- (127) Abdulagatov, A. I.; Yan, Y.; Cooper, J. R.; Zhang, Y.; Gibbs, Z. M.; Cavanagh, A. S.; Yang, R. G.; Lee, Y. C.; George, S. M. Al₂O₃ and TiO₂ Atomic Layer Deposition on Copper for Water Corrosion Resistance. *ACS Appl. Mater. Interfaces* **2011**, *3*, 4593–4601.
- (128) Chai, Z.; Li, J.; Lu, X.; He, D. Use of Electrochemical Measurements to Investigate the Porosity of Ultra-Thin Al₂O₃ Films Prepared by Atomic Layer Deposition. *RSC Adv.* **2014**, *4*, 39365–39371.
- (129) Chai, Z.; Liu, Y.; Li, J.; Lu, X.; He, D. Ultra-Thin Al₂O₃ Films Grown by Atomic Layer Deposition for Corrosion Protection of Copper. *RSC Adv.* **2014**, *4*, 50503–50509.
- (130) Mirhashemihaghighi, S.; Swiatowska, J.; Maurice, V.; Seyeux, A.; Klein, L. H.; Harkonen, E.; Ritala, M.; Marcus, P. Electrochemical and Surface Analysis of the Corrosion Protection of Copper by Nanometer-Thick Alumina Coatings Prepared by Atomic Layer Deposition. *J. Electrochem. Soc.* **2015**, *162*, C377–C384.
- (131) Mirhashemihaghighi, S.; Światowska, J.; Maurice, V.; Seyeux, A.; Zanna, S.; Salmi, E.; Ritala, M.; Marcus, P. Corrosion Protection of Aluminium by Ultra-Thin Atomic Layer Deposited Alumina Coatings. *Corros. Sci.* **2016**, *106*, 16–24.
- (132) Mirhashemihaghighi, S.; Światowska, J.; Maurice, V.; Seyeux, A.; Klein, L. H.; Salmi, E.; Ritala, M.; Marcus, P. Interfacial Native Oxide Effects on the Corrosion Protection of Copper Coated with ALD Alumina. *Electrochim. Acta* **2016**, *193*, 7–15.
- (133) Correa, G. C.; Bao, B.; Strandwitz, N. C. Chemical Stability of Titania and Alumina Thin Films Formed by Atomic Layer Deposition. *ACS Appl. Mater. Interfaces* **2015**, *7*, 14816–14821.
- (134) Hu, S.; Shaner, M. R.; Beardslee, J. A.; Lichterman, M.; Brunshwig, B. S.; Lewis, N. S. Amorphous TiO₂ Coatings Stabilize Si, GaAs, and GaP Photoanodes for Efficient Water Oxidation. *Science*. **2014**, *344*, 1005–1009.
- (135) Spathis, P.; Poullos, I. The Corrosion and Photocorrosion of Zinc and Zinc Oxide Coatings. *Corros. Sci.* **1995**, *37*, 673–680.
- (136) Sun, K. G.; Li, Y. V.; Saint John, D. B.; Jackson, T. N. pH-Controlled Selective Etching of Al₂O₃ over ZnO. *ACS Appl. Mater. Interfaces* **2014**, *6*, 7028–7031.
- (137) Esplandiu, M. J.; Patrino, E. M.; Macagno, V. A. Characterization of Hafnium Anodic Oxide Films: An AC Impedance Investigation. *Electrochim. Acta* **1995**, *40*, 809–815.

- (138) Badawy, W. a.; Al-Kharafi, F. M. Electrochemical Behaviour of Naturally Passivated Hafnium in Aqueous Solutions of Different pH. *J. Mater. Sci.* **1999**, *34*, 2483–2491.
- (139) Li, H.; Liang, K.; Mei, L.; Gu, S.; Wang, S. Corrosion Protection of Mild Steel by Zirconia Sol-Gel Coatings. *J. Mater. Sci. Lett.* **2001**, *20*, 1081–1083.
- (140) Li, Q.; Zhong, X.; Hu, J.; Kang, W. Preparation and Corrosion Resistance Studies of Zirconia Coating on Fluorinated AZ91D Magnesium Alloy. *Prog. Org. Coat.* **2008**, *63*, 222–227.

CHAPTER 2. Experimental

2.1 Atomic Layer Deposition (ALD)

Atomic layer deposition for the growth of thin films was performed in a custom-built viscous flow-tube reactor. The reactant carrier and purge gas was ultrahigh-purity nitrogen (99.999%, Arc3) that was further purified using a Gatekeeper inert gas purifier (rated to <100 parts per trillion H₂O and O₂, Entegris) before flowing into the reactor. The reactor consisted of a stainless steel tube 10 cm in diameter connected to gas inlet and pumping ports by conflat flanges. A resistively heated jacket surrounding the system was used to achieve the desired temperature. A controlled temperature gradient was maintained along the entire gas flow path to prevent precursor condensation. The flowrate in the reactor during gas purge cycles was 100 standard cubic centimeters per minute (sccm) and the working pressure was 1 Torr. A typical ALD cycle consisted of a 0.5 s ALD precursor dose, a 30 s N₂ purge, a 0.5 s H₂O dose, and a 30 s N₂ purge. A set number of ALD cycles was performed based off a pre-measure growth rate to obtain a film of the desired thickness. The purge gas flowrate, chamber pressure, reactor temperature, and precursor exposure sequence were controlled and monitored with a LabVIEW interface.

2.2 Quartz Crystal Microbalance (QCM)

The ALD reactor was equipped with an *in-situ* QCM sensor to monitor mass uptake during the precursor exposures. The QCM measurements were performed *in-situ* on unpolished gold faced quartz crystals (Inficon) with a 6 MHz oscillation frequency. The QCM crystal was mounted in the QCM housing and positioned in the ALD chamber at the center deposition site. Small changes in mass during the ALD process were quantified by measuring changes in the resonance frequency of the crystal. The sensor head was modified to allow inert gas flow (~10 sccm) to the backside of the QCM crystal to locally prevent film deposition and protect the electrical contacts. A film thickness monitor (Maxtek TM-400) recorded the mass change using a LabVIEW program.

2.3 Ellipsometry

To determine the metal oxide film thickness deposited during each ALD run a planar silicon wafer was included in the reactor and analyzed using spectroscopic ellipsometry (J.A. Woollam Co. alpha-SE, using the CompleteEASE data analysis software package). A polarized light source with wavelengths from 380-900 nm was shone on the silicon at an angle of incidence of 70° and changes in the polarization were detected using a charge coupled device and fit to an optical model to determine the film thickness and refractive index. A native SiO₂ layer of 20 Å, as measured for each silicon wafer, was also included in the optical model. The thickness of the ALD films are accurate within ±10%.

2.4 X-ray Reflectivity (XRR)

Metal ALD film thickness data were obtained by analyzing silicon wafers that were included in the ALD reactor during film growth with XRR (Rigaku SmartLab diffractometer equipped with a Cu K α source). A monochromatic x-ray beam was shone on the surface of the coated silicon from 0-5° and the reflected x-ray intensities was measured using an x-ray detector. The resulting critical angle and reflections were modeled using the Panalytical X'pert Reflectivity software package to determine the thickness of the metal films.

2.5 X-ray Diffraction (XRD)

The crystalline structure of the ALD films were assessed with x-ray diffraction using a Rigaku SmartLab and Panalytical Empyrean with a Cu K α source. A x-ray beam was shone on the sample with a 2 θ from 10-60° and diffracted, based on the sample's lattice spacing, towards a detector that converted the beam intensity into a count rate. The resulting diffraction pattern was compared to previously reported patterns to determine the crystal structure of the film.

2.6 X-ray photoelectron spectroscopy (XPS)

X-ray photoelectron spectroscopy (SPECS System with a PHOIBOS 150 Analyzer) was used to analyze the atomic composition and chemical state of the ALD thin films. The samples were

irradiated with x-rays that caused core electrons to be ejected from the surface atoms. The kinetic energy of the ejected electrons were measured with an electron energy analyzer. The binding energy, which is unique for each element, of the electrons was then deduced from the measured kinetic energy of the electron and the known x-ray energy. The resulting spectra was calibrated based on the carbon 1s peak normalized at 284.5 eV. The resulting binding energy for each element was compared to previously reported values to determine the oxidation state of each element and the chemical composition of the film.

2.7 Fourier Transform Infrared (FTIR) Spectroscopy

Sample composition was analyzed using FTIR spectroscopy. Infrared radiation was passed through the samples and the transmitted radiation was measured by a detector. The wavelengths that were absorbed by the sample related to the specific energies of the vibrational and rotational modes that cause a dipole moment in the chemical functional groups present in the sample. FTIR spectroscopy was performed with a ThermoNicolet 6700 IR bench with a deuterated triglycine sulfate detector operated in transmission mode with 200 scans at 4 cm^{-1} resolution. The sample was mixed with potassium bromide (FTIR grade, Sigma Aldrich) to be less than 0.5 wt.% sample, and pressed into pellets that were dried at 140°C to remove any absorbed water before collecting spectra.^{1,2} The collected spectra were compared to previously reported spectra to determine the functional groups that were present in the sample.

2.8 Raman Spectroscopy

The composition of samples were also measured using Raman spectroscopy. Raman spectra was collected using either a Horiba-Jobin Yvon LabRAM HR VIS confocal microscope with a 632 nm laser source or a WITEC confocal Raman alpha300 M microscope system with a 532 nm laser source. Both spectrometers were calibrated using the crystalline silicon peak at 520.7 cm^{-1} . The back scattered radiation of the monochromatic laser bouncing off the sample passed through a filter, which allowed only wavelengths that shifted in energy to pass through. The back scattered radiation that passed through was associated with symmetric vibrational and rotational modes that caused a change in the polarizability of the molecule. The collected

spectra were compared to previously reported spectra to determine the functional groups that were present in the sample.

2.9 Scanning Electron Microscopy (SEM)

High resolution images of samples were collected using SEM. The images were produced by focusing a beam of electrons on the sample and collecting the electrons and x-rays that were ejected from the sample and converting the resulting information into an image of the sample. SEM images were taken with either a JEOL 6010LA with an energy-dispersive X-ray spectroscopy (EDS) attachment, or a FEI Verios 460L.

2.10 Energy Filtered Transmission Electron Microscopy (EFTEM)

Elemental mapping of samples was conducted using EFTEM. A very thin sample was exposed to a focused electron beam and only electrons that passed through the sample with a specific kinetic energy. The kinetic energy loss of the electrons was associated with specific elements and were used to form an image. For example, the carbon signal was filtered using the K1 edge ($E = 284$ eV) and the vanadium signal was filtered using the L2,3 edge ($E = 521$ eV & $E = 513$ eV). EFTEM data was acquired on a JEOL-2010F S/TEM with Gatan® GIF 200 at 200 kV.

2.11 Atomic Force Microscopy (AFM)

Atomic Force Microscopy was conducted using a Digital Instruments Dimension 3000, with a Nanoscope IIIa controller and vibration shielded hood for surface topography analysis. Imaging was performed in intermittent contact mode with a silicon cantilever and tip. The cantilever was attached to a support to maintain it above the surface of the sample and was oscillated up and down near its resonance frequency using a piezoelectric element. A laser was directed at the end of the cantilever where the tip was located and changes in the vertical position of the tip due to atomic interactions with the surface of the sample was measured using a photodiode. The tip was scanned along the surface of the sample to create a 3-D image of the material. Image analysis was performed using built-in software functions to calculate the root-mean-square roughness (rms) of $1 \mu\text{m}^2$ sites.

2.12 Gas Adsorption

The surface area and pore sizes of samples were measured using gas adsorption using a Quantachrome Autosorb-1C. Samples ($\sim 10 \text{ m}^2$) were degassed at 150°C for more than 4 h before measurement. The samples were cooled to 77 K (the temperature of liquid nitrogen) and the amount of nitrogen gas that was adsorbed by the sample at different pressures was precisely measured. The measurements consisted of either 20 adsorption and 20 desorption points between 0.05 and 0.995 P/P_0 to determine the pore size distribution, or 11 adsorption points between 0.05 and 0.3 P/P_0 to determine the surface area. Pore sizes distributions were calculated in the AS1Win software package using either the nonlocal density functional theory (DFT) method with the slit pore quenched solid state function theory (QSDFT) carbon equilibrium transition kernel using nitrogen absorption and desorption curves or a Barrett-Joyner-Halenda (BJH) desorption analysis. Surface area measurements were also conducted in the AS1Win software package using Brunauer-Emmett-Teller (BET) theory.

2.13 Tensile Strength

The tensile strength, or the resistance to breaking under tension, of yarns was measured using an MTS Q-Test/5 Universal Testing Machine equipped with a 1000 lb load cell. Per ASTM D7269-08, pneumatic bollard-type clamps were used with 60 psi to prevent yarn slippage. A gauge length of 10 in was used with a crosshead speed of 5 in per min. A U.S. Testing Twist Tester was used to insert 3 twists per in into each yarn.

2.14 Cyclic Voltammetry (CV)

Electrochemical measurements were conducted using a BioLogic VMP3 potentiostat.

Cyclic voltammograms of supercapacitor electrodes were collected to study their electrochemical charge storage mechanisms and to quantify their charge storage capacity. The CVs were collected by changing the applied voltage against a reference electrode at scan rates between 1 mV s^{-1} and 2000 mV s^{-1} and recording the current response. The electrodes were measured in either a three-electrode or symmetric two-electrode configuration. The three-

electrode setup with an aqueous electrode consisted of the working sample electrode, a platinum counter electrode, and a Ag/AgCl reference electrode. When a nonaqueous electrolyte was used the counter electrode was lithium metal and the pseudo-reference electrode was a separate lithium metal electrode. The electrode's capacitance ($C_{electrode}$) was calculated according to:

$$C_{electrode} = \frac{1}{\frac{dv}{dt} m (V_{high} - V_{low})} \frac{1}{2} \left\{ \int_{V_{low}}^{V_{high}} I(V) dV - \int_{V_{high}}^{V_{low}} I(V) dV \right\} \quad 2.1$$

where dv/dt is the scan rate, m is the mass of the electrode, V_{high} and V_{low} are the limits of the sweep, and $I(V)$ is the total current. The limits of the sweep were selected based on the electrolyte being used and the properties of the electrode being tested.

When cyclic voltammograms were collected in the symmetric configuration, the parallel electrodes ($C_{electrode}$) are considered to contribute equally to the measured cell capacitance (C_{cell}). The electrode capacitance is then given as:

$$C_{electrode} = 2 C_{cell} \quad 2.2$$

2.15 Galvanostatic Charging and Discharging

Charge-discharge cycles of the electrodes at currents of 0.1-10 A/g were performed to calculate the energy density of power density of the supercapacitor electrode. The capacitance of the electrodes were calculated according to:

$$C_{electrode} = \frac{I}{m \frac{-dV}{dt}} \quad 2.3$$

where I is the current, and dV/dt is the discharge rate.

2.16 Electrochemical Impedance Spectroscopy (EIS)

Electrochemical impedance spectroscopy was performed to quantify the dielectric properties of the supercapacitor electrodes and the coated copper samples. The EIS measurements were

collected by applying an alternating potential perturbation at varying frequencies and measuring the resulting current to determine the impedance and phase shift. An alternating potential of 10 mV was applied over the frequency range 100 kHz to 10 mHz with 10 points collected per decade, 2 periods between each frequency measurement, and 2 measurements per frequency. The EIS data was then modeled using equivalent circuit models consisting of resistors, capacitors, and inductors based on different physical components of the systems. Curve fitting of the equivalent circuit model to determine the values of the circuit components was performed using the ZSimpWin 3.21 software package. The sample was visualized using either a Nyquist plot or Bode plot. Figure 2.1(a) shows the Nyquist plot along with the model that was fitted to the results of a supercapacitor, and Figure 2.1(b) shows the Bode plot along with the model that was fitted to the results of copper coated with Al_2O_3 .

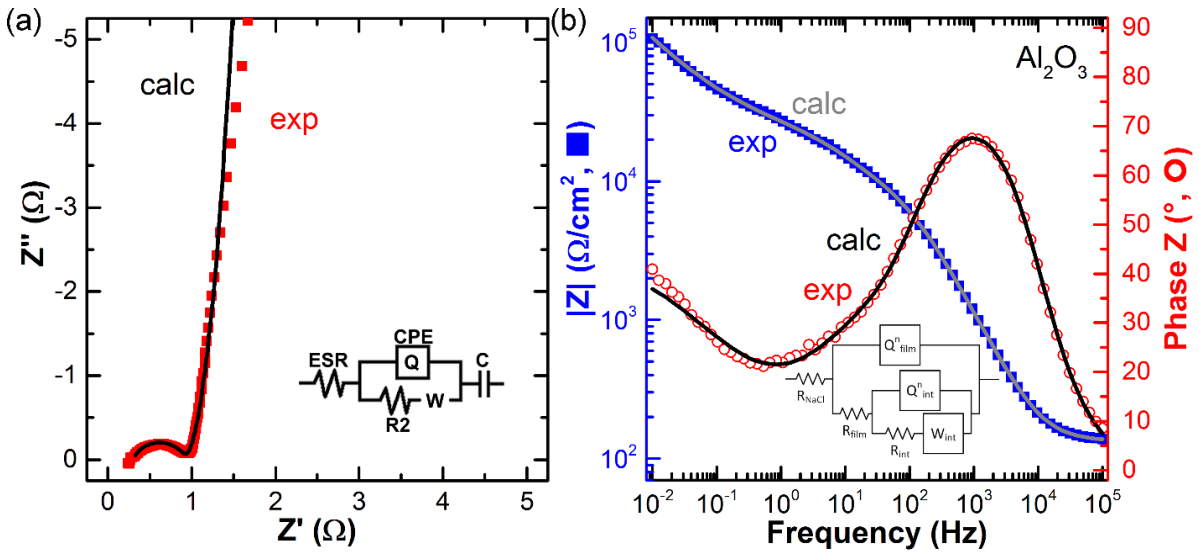


Figure 2.1. (a) Nyquist plot of a V_2O_5 coated supercapacitor, and (b) Bode plot of Al_2O_3 coated copper with both the measured values and the calculated values from the fitted equivalent circuit shown inset.

2.17 Linear Sweep Voltammetry (LSV)

Corrosion polarization curves of the coated copper samples was obtained by using LSV to calculated the corrosion potentials, corrosion currents, polarization resistances, and porosities. The LSV data was collected at a rate of 1 mV/s from -0.8 to 0.5 V versus a Ag/AgCl reference electrode. A sample polarization curve for copper coated with Al₂O₃ is shown in Figure 2.2.

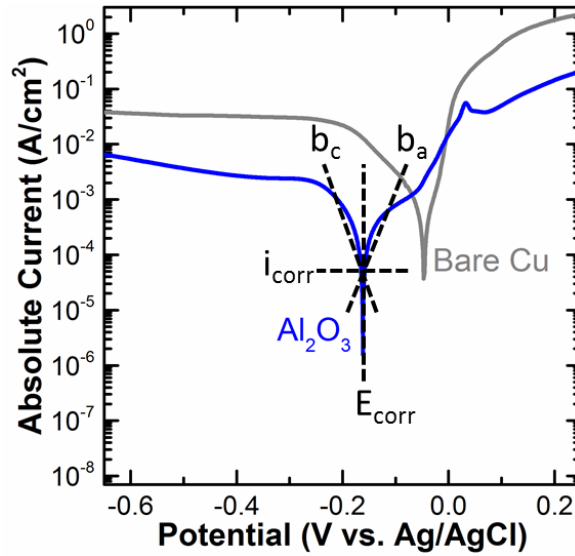


Figure 2.2. Polarization curve of copper that was coated with Al₂O₃ with i_{corr} , E_{corr} , b_c , and b_a labeled.

b_a and b_c are the slopes of the anodic and cathodic branches of the polarization plot, and the i_{corr} and E_{corr} and the current and potential were b_a and b_c intersect.

The polarization resistances were calculated using the Stern-Geary equation:³⁻⁵

$$R_p = \frac{b_a b_c}{i_{corr} \ln(10)(b_a + b_c)} \quad 2.4$$

The electrochemical porosity of coatings were calculated by using equation 2.5:³⁻⁵

$$P = \left(\frac{R_{p \text{ bare}}}{R_{p \text{ ALD}}} \right) \times 10^{-\left(\frac{\Delta E_{\text{corr}}}{b_a} \right)} \times 100 \quad 2.5$$

Where ΔE_{corr} is the difference in the corrosion potentials from the polarization curve. Because this value is determined by the magnitude of the polarization resistance, the net electrochemical porosity can be ascribed to ion transport through a continuous solid film, or due to charge flow through gaps or pinholes in the coating. Due to the variation in the measurements used in the calculation of the polarization resistances, the reported electrochemical porosities vary by $\pm 50\%$.

2.18 References

- (1) Moreno-Castilla, C.; Ferro-García, M. a.; Joly, J. P.; Bautista-Toledo, I.; Carrasco-Marín, F.; Rivera-Utrilla, J.; Carrasco-Marín, F.; Rivera-Utrilla, J. Activated Carbon Surface Modifications by Nitric Acid, Hydrogen Peroxide, and Ammonium Peroxydisulfate Treatments. *Langmuir* **1995**, *11*, 4386–4392.
- (2) Domingo-García, M.; López Garzón, F. J.; Pérez-Mendoza, M. J. On the Characterization of Chemical Surface Groups of Carbon Materials. *J. Colloid Interface Sci.* **2002**, *248*, 116–122.
- (3) Chai, Z.; Li, J.; Lu, X.; He, D. Use of Electrochemical Measurements to Investigate the Porosity of Ultra-Thin Al₂O₃ Films Prepared by Atomic Layer Deposition. *RSC Adv.* **2014**, *4*, 39365–39371.
- (4) Díaz, B.; Härkönen, E.; Światowska, J.; Maurice, V.; Seyeux, A.; Marcus, P.; Ritala, M. Low-Temperature Atomic Layer Deposition of Al₂O₃ Thin Coatings for Corrosion Protection of Steel: Surface and Electrochemical Analysis. *Corros. Sci.* **2011**, *53*, 2168–2175.
- (5) Mirhashemihaghighi, S.; Swiatowska, J.; Maurice, V.; Seyeux, A.; Klein, L. H.; Harkonen, E.; Ritala, M.; Marcus, P. Electrochemical and Surface Analysis of the Corrosion Protection of Copper by Nanometer-Thick Alumina Coatings Prepared by Atomic Layer Deposition. *J. Electrochem. Soc.* **2015**, *162*, C377–C384.

CHAPTER 3. Effect of Meso- and Micro-Porosity in Carbon Electrodes on Atomic Layer Deposition of Pseudocapacitive V₂O₅ for High Performance Supercapacitors

This chapter is based on a manuscript published as:

Daubert, J. S.; Lewis, N. P.; Gotsch, H. N.; Mundy, J. Z.; Monroe, D. N.; Dickey, E. C.; Losego, M. D.; Parsons, G. N. Effect of Meso- and Micro-Porosity in Carbon Electrodes on Atomic Layer Deposition of Pseudocapacitive V₂O₅ for High Performance Supercapacitors. *Chem. Mater.* **2015**, *27*, 6524–6534.

3.1 Abstract

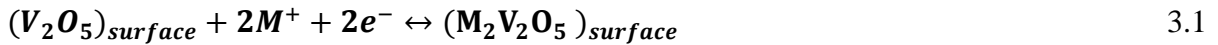
Atomic layer deposition (ALD) of vanadium oxide is a viable means to add pseudocapacitive layers to porous carbon electrodes. Two commercial activated carbon materials with different surface areas and pore structures were acid treated and coated by V_2O_5 ALD using vanadium triisopropoxide and water at 150°C . The V_2O_5 ALD process was characterized at various temperatures to confirm saturated ALD growth conditions. Capacitance and electrochemical impedance analysis of subsequently constructed electrochemical capacitors (ECs) showed improved charge storage for the ALD coated electrodes, but the extent of improvement depended on initial pore structure. The ALD of V_2O_5 onto mesoporous carbon increased the capacitance by up to 46% after 75 ALD cycles, and obtained a maximum pseudocapacitance of $540\text{ F/g}(V_2O_5)$ after 25 ALD cycles, while maintaining low electrical resistance, high columbic efficiency, and a high cycle life. However, adding V_2O_5 ALD to microporous carbons with pore diameters of $< 11\text{ \AA}$ showed far less improvement, likely due to “blocking off” of the micropores and reducing the accessible surface area. Results show that ALD is a viable means to construct high-performance supercapacitors from activated carbon which is the basis for commercial products, and a clear understanding of carbon electrode pore structure, layer conformality, and layer thickness are necessary to fully optimize performance.

3.2 Introduction

Electrochemical capacitors (ECs), or supercapacitors, store significantly higher energy per unit volume than electrostatic capacitors and deliver a higher power density than typical batteries. This combination of attributes make ECs promising for energy management in electrified vehicles and Smart Grid applications.¹⁻⁴ Charge is stored physically in the electrical double layer of an EC at the electrode/electrolyte interface. Commercially available ECs are constructed using activated carbons with surface areas ranging between 700 and 2200 $\text{m}^2/\text{g}(\text{carbon})$, which leads to an effective capacitance in the range from 5 to $40\text{ }\mu\text{F}/\text{cm}^2$ (or 70-200 F/g).^{2,3,5-7} Improved charge and energy storage density are needed, however, to expand commercial market potential. One approach is to include an additional Faradaic, or

“pseudocapacitive,” charge storage layer, where fast and reversible redox reactions can occur near the electrode’s surface, allowing additional charge to be stored.^{2,3,8}

Ruthenium oxide is the most well-studied pseudocapacitive material, and can exhibit specific capacitances of 200-1200 F/g(RuO₂).^{5,8} Here we investigate the less expensive and less explored pseudocapacitive material, vanadium oxide.⁹⁻²³ Our particular focus is on understanding how ALD can modify commonly used supercapacitor materials and structures (i.e. activated carbon) to improve overall function and performance. Pseudocapacitive vanadium oxide can be viewed as a reaction where monovalent electrolyte cations (M⁺) intercalate into the V₂O₅ on the cathode while preserving the oxide structure.^{9,23,24}



A pseudocapacitive layer on the anode could also allow anion intercalation for some electrolytes.^{4,25}

In order to minimize the distance required for the M⁺ cation to diffuse into V₂O₅, the electrode design targets a uniform thin oxide film dispersed over a large surface area that is readily contacted and accessed by the electrolyte solution. If each vanadium-center in the V₂O₅ participates in a 1 electron transfer (reaction 3.1), then the V₂O₅ can store a theoretical maximum of 1060 C/g(V₂O₅). (Note: we differentiate between “per gram of pseudocapacitive material”, /g(V₂O₅) and “per gram of total electrode weight” /g(electrode).) The corresponding maximum theoretical capacitance of the V₂O₅ is then defined by the potential window in which the electron transfer occurs. A 1.2 V window (the stable window of H₂O) leads to a maximum theoretical capacitance of 883 F/g(V₂O₅). The faradaic reaction of vanadium in reaction 3.1 does not generally produce a redox peak on cyclic voltammetry scans because in the amorphous V₂O₅ the intercalation of the monovalent cations does not cause a shift in the oxide bond structure over the continuous potential range of surface storage sites.⁹

Previous reports using nanoporous vanadium oxide prepared by sol-gel methods led to specific capacitance values as high as 214 F/g(V₂O₅),¹³ and vanadium oxide powders with a surface

area of 41 m²/g showed up to 262 F/g(V₂O₅).¹⁰ Thin films of V₂O₅ deposited on self-standing carbon nanofiber paper had specific capacitance of up to 1308 F/g(V₂O₅).¹⁹ Previous reports of V₂O₅ deposited using ALD show good capacitance density, up to 1550 F/g(V₂O₅), but substrates were limited to carbon nanotubes, and the overall capacitance of the electrodes was 600 F/g(electrode).¹² The capacitances higher than 883 F/g(V₂O₅) may result from the reduction of the vanadium oxide through multiple oxidation states, although this possibility was not directly discussed.^{12,19} In this work, we address the challenge of depositing V₂O₅ on high-surface area activated carbon powders that are used commercially to construct ECs. The goal of this study is to attain both high specific pseudocapacitance (F/g(metal oxide)) and overall capacitance (F/g(electrode)) through ALD of V₂O₅ into porous carbon electrodes.

While pseudocapacitance can increase charge storage by up to 2 orders of magnitude, the Faradaic processes can slow charge transfer rates and reduce electrode stability.³ Pseudocapacitor electrodes are commonly made entirely of metal oxide or a composite of carbon and metal oxide powders.^{26,27} These electrodes often suffer from electrical resistance and poor stability (similar to batteries), therefore failing to maximize their energy storage capacity.²⁷ Pseudocapacitive electrodes constructed using hybrid nanostructured materials can avoid these shortcomings.^{8,27} To design and build nanostructured ECs, it is important to understand the structure-property relationships of both the carbon substrate/pseudocapacitive material and the pseudocapacitive material/electrolyte junctions. Pseudocapacitive thin films yield specific capacitances 2 to 5 times larger than the same material in powder form,⁵ and conformal coatings add negligible volume and footprint to the electrode. However, the pseudocapacitive loading needs to be controlled in order to avoid “clogging” of the pores and decreasing net capacitance.²⁸

For this work, we hypothesize that ALD can be used to form a highly conformal nanoscale pseudocapacitive layer on porous carbon electrodes to enhance charge storage while maintaining low equivalent series electrical resistances and high cycle life. ALD utilizes a binary self-limiting surface reaction, where the gas-phase precursors infiltrate and form coatings over complex substrate geometries. This attribute of ALD makes it well suited to form

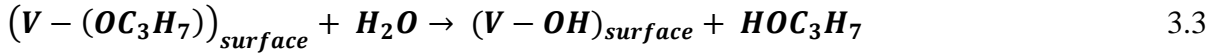
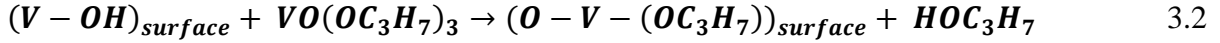
conformal pseudocapacitive layers on complex meso- and microporous conductive substrates. We therefore embarked on a fundamental study of ALD growth on activated carbon powders, including structural investigations of how surface chemistry affects ALD nucleation and layer uniformity, and the subsequent effects on electrochemical performance, including pseudocapacitance, power delivery, and long-term cycle stability of the ALD layer.

3.3 Experimental Section

Carbon powder and electrode preparation. Two different activated carbon powders were used for the electrodes, Darco G60 (G60) and DLC Supra 50 (Supra), both obtained from Norit. G60 is a common mesoporous activated carbon having both mesoporosity and microporosity (nominally 820 m²/g). Supra is predominantly microporous with an ultrahigh surface area (nominally 1560 m²/g). To modify the surface functional groups, the activated carbon powder was treated in 15 M HNO₃ (trace metal, Fisher Scientific) at a ratio of 10 mL of acid per gram of carbon. The carbon/acid dispersion was heated for 60 min on a hot plate at 60°C, 100°C, or 120°C (i.e., boiled acid off).²⁹ The treated carbon powder was then vacuum filtered and rinsed with deionized water before being dried under vacuum overnight at 120°C. The acid treatment was intended to affect the surface chemistry of the carbon to aid in the nucleation of the ALD precursors on the surface of the powders. We also predicted the acid treatment would aid in electrode wetting, by making it hydrophilic, and increase charge storage, by adding pseudocapacitive oxygen heteroatoms.

To form capacitor electrodes, the acid-treated carbon powder (without ALD layers) was mixed with 5 wt.% acetylene carbon black (99.9%, Alfa Aesar) to increase the electrode conductivity, along with 10 wt.% polyvinylidene fluoride (PVDF) (Sigma Aldrich) as an electrode binder. The mixture was dissolved into 1-methyl-2-pyrrolidinone (NMP) (99.5%, Sigma Aldrich) to form a slurry which was cast (~200 μm thick) onto nickel foil current collectors using a doctor blade. The electrodes were then dried at 120°C for 6 h under vacuum to evaporate the NMP. The finished electrode area was ~1×1 cm² with a mass of ~4 mg.

ALD coating and planar thin film characterization. The carbon electrodes were coated with V_2O_5 using previously reported processes.^{12,30–34} The ALD process used vanadium triisopropoxide (VTIP) (96%, Alfa Aesar) and H_2O (reagent grade, Ricco Chemical) as the coreactants and is described by the following chemical half-reactions:



ALD growth was conducted between 75 and 250°C in a custom-built viscous flow-tube ALD reactor. The reactant carrier and purge gas was ultrahigh-purity nitrogen (99.999%, Machine & Welding Supply) that was further purified using a Gatekeeper inert gas purifier (rated to <100 parts per trillion H_2O and O_2 , Entegris) before flowing into the reactor. The reactor consisted of a stainless steel tube 10 cm in diameter connected to gas inlet and pumping ports by conflat flanges. A resistively heated jacket surrounding the system was used to achieve the desired temperature. A controlled temperature gradient was maintained along the entire gas flow path to prevent precursor condensation. The H_2O was kept at room temperature (~25°C) and the VTIP was kept at 45°C (vapor pressure of ~0.29 Torr).³⁴ The working pressure in the reactor during gas purge cycles was ~1 Torr. A typical ALD cycle consisted of dosing VTIP, followed by closing the inlet and outlet valves to the reactor to allow the precursors to diffuse through the carbon, before purging with nitrogen, dosing of water, closing the valves to allow the water precursor to diffuse, and then purging with nitrogen before the next VTIP dose for the subsequent cycle. The VTIP dosing time is split between the prep and dose steps. During the 2 s prep step, the bypass valve is closed and the outlet valve opened to pull a slight vacuum on the setup. After the prep step, the inlet valve is opened and nitrogen is bubbled into the VTIP to volatilize the VTIP and deliver it into the reactor. One ALD cycle (VTIP dose/hold/ N_2 purge/ H_2O dose /hold/ N_2 purge) has a timing interval of 6/60/100/0.2/60/100 s, and the number of cycles was varied depending on the desired thickness of the thin film coating. This approach has been used previously to coat carbon nanotubes using ALD.³⁵

To determine the V₂O₅ growth rate, each ALD run included a planar silicon wafer, and the film thickness was measured after each run using spectroscopic ellipsometry (J.A. Woollam Co. alpha-SE, using the CompleteEASE data analysis software package). As discussed below, the ALD growth rate of V₂O₅ on silicon wafers was determined to be 0.2-0.3 Å per cycle between 125 and 175°C, consistent with previous studies.³⁰ Optical constants for V₂O₅ were determined by fitting SE data from 100 cycles of ALD to a Cauchy model. A native SiO₂ layer of 20 Å, as measured for each wafer, was also included in the optical model.

The reactor was equipped with an *in-situ* quartz crystal microbalance (QCM) sensor to monitor mass uptake during the precursor exposures. The QCM measurements were performed *in-situ* on unpolished gold faced quartz crystals (Inficon) with a 6 MHz oscillation frequency.

The QCM crystal was mounted to the QCM housing using conductive silver epoxy and positioned in the reaction chamber at the center deposition site. The sensor head was modified to allow inert gas flow (~10 standard cubic centimeters per minute, sccm) to the backside of the QCM crystal to locally prevent film deposition and protect the electrical contacts. A film thickness monitor (Maxtek TM-400) recorded the mass change using a LabVIEW program.

X-ray diffraction (XRD) (Rigaku SmartLab and Panalytical Empyrean) was used to assess crystalline structure (Cu K α source, 1.54 Å) of the ALD films. X-ray photoelectron spectroscopy (XPS) (SPECS System with PHOIBOS 150 Analyzer) was used to analyze the composition of the thin films. The spectra was calibrated based on the carbon 1s peak normalized at 284.5 eV.

Uncoated and ALD-coated carbon powder characterization. Carbon powder composition was analyzed using transmission FTIR spectroscopy. FTIR was performed with a ThermoNicolet 6700 IR bench with a deuterated triglycine sulfate detector operated in transmission mode with 200 scans at 4 cm⁻¹ resolution. The carbon powder was mixed with potassium bromide (FTIR grade, Sigma Aldrich) to be less than 0.5 wt.% carbon, and pressed into pellets that were dried at 140°C to remove any absorbed water before collecting spectra.^{29,36} Raman spectra were collected using a Horiba-Jobin Yvon LabRAM HR VIS

confocal microscope with a 632 nm laser source. The spectrometer was calibrated using the crystalline silicon peak at 520.7 cm^{-1} .

Pore sizes were measured using a Quantachrome Autosorb-1C. Carbon powder (~50 mg) was degassed at 150°C for more than 4 h before measurement. Pore sizes distributions were calculated in the AS1Win software package using the nonlocal density functional theory (DFT) method with the slit pore QSDFT carbon equilibrium transition kernel using nitrogen absorption and desorption curves within the P/P_0 range of 0.05-1. Scanning electron microscope (SEM) images were taken with either a JEOL 6010LA with an energy-dispersive X-ray spectroscopy (EDS) attachment or FEI Verios 460L. Energy filtered transmission electron microscopy (EFTEM) data was acquired on a JEOL-2010F S/TEM with Gatan GIF 200 at 200 kV. The carbon signal was filtered using the K1 edge ($E = 284 \text{ eV}$) and the vanadium signal was filtered using the L2,3 edge ($E = 521 \text{ eV}$ & $E = 513 \text{ eV}$).

Capacitor electrical characterization. Carbon electrodes were constructed on nickel foil current collectors (99%, Alfa Aesar). Capacitors were tested in a 1 M potassium chloride (KCl) aqueous electrolyte (Arcos).

Three-electrode measurements were conducted in an enclosed glass cell degassed with nitrogen. The counter electrode was Pt mesh of approximately 5 cm^2 , and the reference electrode was Ag/AgCl. Symmetric two-electrode measurements to understand electrode behavior were conducted to examine the effect of the ALD coating on electrode performance. The two electrode measurements were conducted using a Teflon cell with two electrodes separated by a $150 \mu\text{m}$ thick 55% cellulose / 45% polyester blend wipe (TechniCloth II from Texwipe) in a beaker of electrolyte. Prior to cell assembly, electrodes and separator were wetted with electrolyte. Measurements were performed on the entire cell. A comparison highlighting the similar performance of G60 electrodes measured in a three-electrode and two-electrode configuration are presented in Figure A.1. Pseudocapacitive materials are often studied in a three-electrode configuration.^{9-11,13,18,19,21,23} Asymmetric electrodes permit pairing two different electrode materials, and with a nonaqueous electrolyte can expand the operating

potential window to optimize the capacitor energy density.^{23,37,38} Symmetric electrodes are also used for material analysis.^{12,39-41} In a symmetric configuration, the pseudocapacitive material on both electrodes can optimize the total charge per unit capacitor mass. For small anions, intercalation pseudocapacitance of the V₂O₅ is expected to provide equal contributions to the overall capacitance both electrodes.

Voltammograms were recorded using either a Princeton Applied Research VersaStat3F potentiostat or a Pine Research Instrumentation WaveNow potentiostat. Twenty five sweeps were first recorded for each electrode at a scan rate of 200 mV/s to condition the electrode(s), then five sweeps were recorded at a scan rate of 20 mV/s with the fifth sweep reported. In the symmetric configuration, the parallel electrodes ($C_{electrode}$) are considered to contribute equally to the measured cell capacitance (C_{cell}). The electrode capacitance is then given as:

$$C_{electrode} = 2 C_{cell} = \frac{2}{\frac{dv}{dt} m (V_{high} - V_{low})} \frac{1}{2} \left\{ \int_{V_{low}}^{V_{high}} I(V) dV - \int_{V_{high}}^{V_{low}} I(V) dV \right\} \quad 3.4$$

where dv/dt is the scan rate, m is the mass of each electrode in a symmetric cell, V_{high} and V_{low} are the limits of the sweep, and $I(V)$ is the total current.

Electrochemical impedance spectroscopy (EIS) data was recorded using a Princeton Applied Research VersaStat3F potentiostat. EIS was measured at the open circuit DC potential with a 10 mV amplitude AC from 100 kHz to 100 mHz. Charge-discharge cycles were performed in a two-electrode configuration using a Pine Research Instrumentation WaveNow galvanostat. 10000 charge/discharge cycles were performed at 5 A/g(capacitor) with every 1000th cycle reported. The capacitance was calculated according to:

$$C_{electrode} = 2 C_{cell} = \frac{2I}{m \frac{-dV}{dt}} \quad 3.5$$

where I is the current, and dV/dt is the discharge rate.

3.4 Results

Chemical and physical analysis of acid treated activated carbon. Initially we investigated the acid treatment of activated carbons to determine how surface-bound oxide groups affect ALD nucleation and growth. FTIR spectra acid collected from coated and uncoated G60 and Supra carbons are shown in Figure 3.1 (a) and (b), respectively. Before treatment, features near $1100\text{-}1300\text{ cm}^{-1}$ and 1570 cm^{-1} correspond to combined C-O and O-H modes and a HOC=O mode respectively. On both substrates, the nitric treatment leads to increased intensity of the existing modes, and a new feature near 1720 cm^{-1} related to additional C=O bonds.^{29,36,42-45} Energy Dispersive X-ray (EDS) elemental analysis (Figure A.2) also shows increased oxygen concentration after acid treatment, consistent with the IR results.

Figure 3.1 (c) and (d) shows pore size distribution from N_2 absorption for the G60 and Supra activated carbon, respectively. The pore distributions show $\partial S(r)$ peaks for pore widths near 10 \AA (micropores) and 30 \AA (mesopores). Integrating these peaks provides estimated surface areas for each type of porosity. The untreated Supra shows fewer mesopores ($70\text{ m}^2/\text{g}$) and more than twice the number of micropores ($1340\text{ m}^2/\text{g}$) of untreated G60 ($120\text{ m}^2/\text{g}$ mesopores and $450\text{ m}^2/\text{g}$ micropores). Acid treating the G60 tends to increase the surface area of the micropores. Acid treating Supra leads to an overall decrease in surface area. The graphitic nature of the carbon was examined using Raman spectroscopy and results (Figure A.3) indicates a small increase in graphitic content after acid treatment.

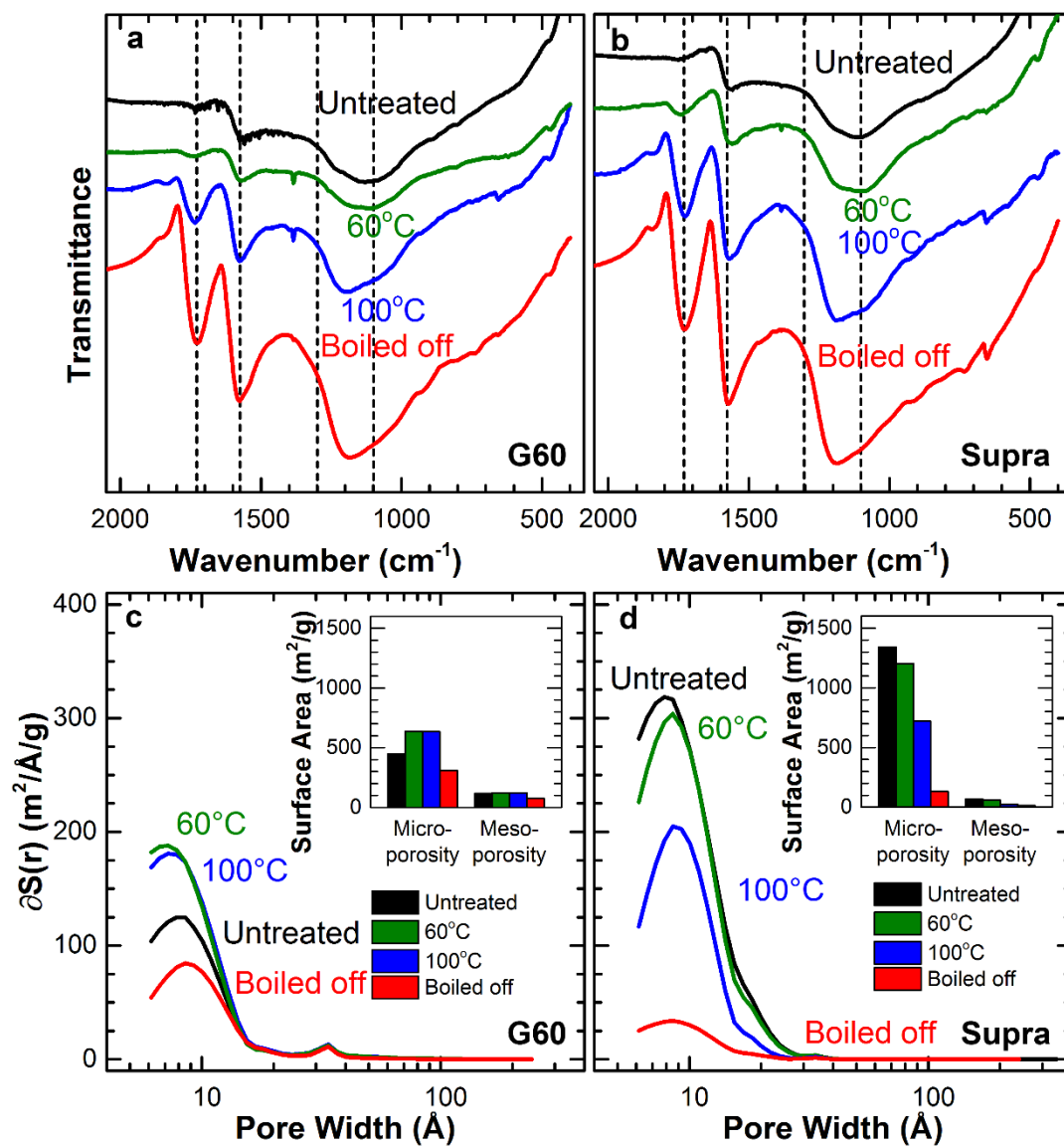


Figure 3.1. FTIR spectra of (a) G60 and (b) Supra powders treated with 15 M HNO₃ at varying temperatures. Effect of acid treatment on the pore distribution of (c) G60 and (d) Supra powders and a comparison of the microporosity and mesoporosity (inset).

ALD of V₂O₅ on planar substrates. The V₂O₅ ALD process was characterized between 75°C and 250°C on planar substrates and showed a stable growth rate (0.2-0.3 Å/cycle) in the ALD window (between 125°C and 175 °C) (Figure A.4).

The vanadium oxide ALD process was characterized using *in-situ* quartz crystal microbalance (QCM) and representative results collected at 150°C are shown in Figure 3.2. The QCM shows a mass increase during the VTIP dose, followed by a slow decrease during the purge cycle. Mass is then lost during the water dose, consistent with surface isopropoxide groups being replaced by hydroxide groups, releasing isopropanol as a by-product (reaction 3.3, above). The net mass gain per cycle at this temperature is 16 ng/cm/cycle.

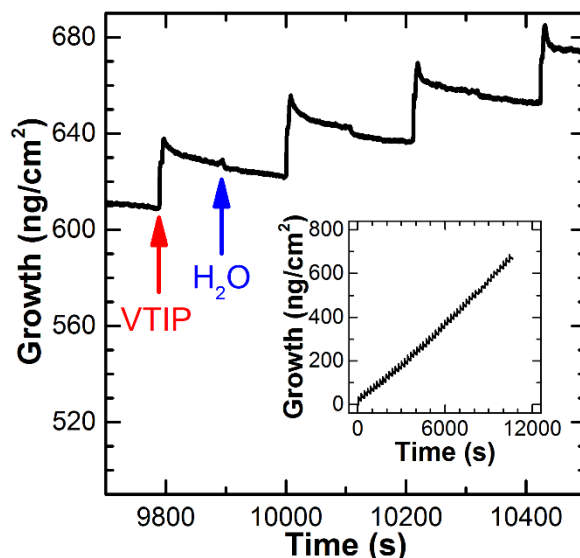


Figure 3.2. QCM measurements for three ALD cycles of V_2O_5 films deposited at 150°C with a VTIP/ N_2 / H_2O / N_2 = 8/100/2/100 dosing sequence. Left (red) arrow indicates VTIP dose, and the right (blue) arrow indicates H_2O dose. The growth during the entire run is shown in the inset.

Vanadium oxide ALD films on silicon were also characterized by XRD and XPS (Figure A.5). XRD data shows no evidence of crystalline diffraction. XPS indicates that the vanadium is oxidized to the 5+ oxidation state, consistent with amorphous V_2O_5 .^{12,46-48} Films deposited from 1000 ALD cycles were orange colored to the naked eye, consistent with V^{5+} . We expect the films deposited on the carbon powder to have the same oxidation state and amorphous structure.

Chemical and physical analysis of ALD coated activated carbon. We coated carbon powder using 125 cycles of V_2O_5 ALD at 175°C and analyzed elemental content by EDS (Figure 3.3(a)). Compared to the as-received carbon, the acid-treated carbon shows a larger vanadium signal, consistent with improved nucleation on the oxidized carbon. After ALD, SEM and related EDS images show uniform vanadium distribution on the outer surface of the G60 carbon following the boiled off nitric acid treatment, G60 and Supra carbon were coated with 50 to 1000 cycles of ALD V_2O_5 and measured by transmission FTIR (Figure 3.4 (a) and (b)). The ALD coating leads to a new band at 1000 cm^{-1} ascribed to the $V=O$ bond in amorphous vanadium oxide.^{47,49} The strength of the $V=O$ band grows with increasing number of ALD cycles, indicating more V_2O_5 on the carbon, consistent with the measured mass gain (Figure A.6). Figure 3.4 (c) and (d) shows the pore distribution of the G60 and Supra after acid treatment and after 100 and 500 cycles of V_2O_5 ALD at 150°C . For these ALD runs, the V_2O_5 on planar silicon was 20 and 100 \AA , respectively. The coated carbon powder showed decreases in the ∂S peaks near both 10 \AA and 30 \AA , indicating a decrease in surface area. On the G60, 500 ALD cycles decreased the microporous and mesoporous surface area by 55% and 45% respectively. On the Supra, the ALD process removed nearly all (99%) of the microporous surface area, while the mesoporous surface area decreased by 45%, similar to the G60. The constriction of the surface pores is visible in SEM images where G60 is coated with 125 cycles of V_2O_5 at 175°C (Figure 3.3 (f)).

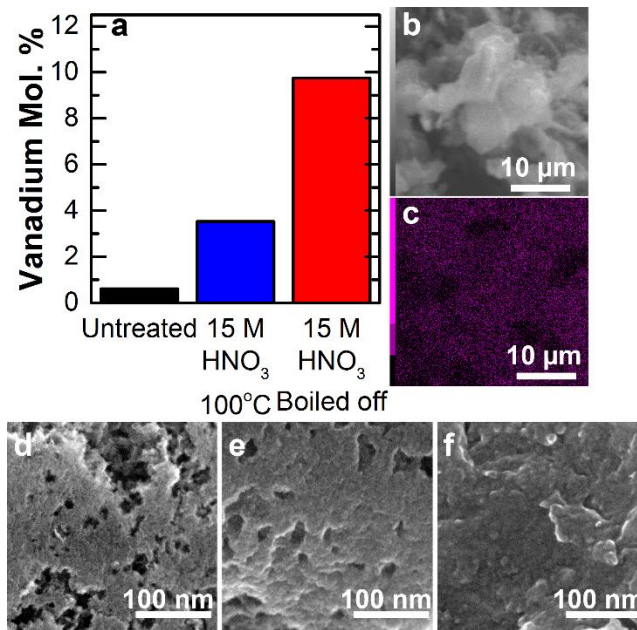


Figure 3.3. (a) Increase in the vanadium content of G60 powder coated with 125 cycles of V₂O₅ ALD at 175°C as measured with EDS; (b) SEM image of untreated G60 coated with V₂O₅; and (c) conformal distribution of vanadium measured with EDS. SEM images highlighting the loss in fine porosity of (d) untreated G60; (e) after acid treatment; and (f) subsequent coating with V₂O₅ ALD.

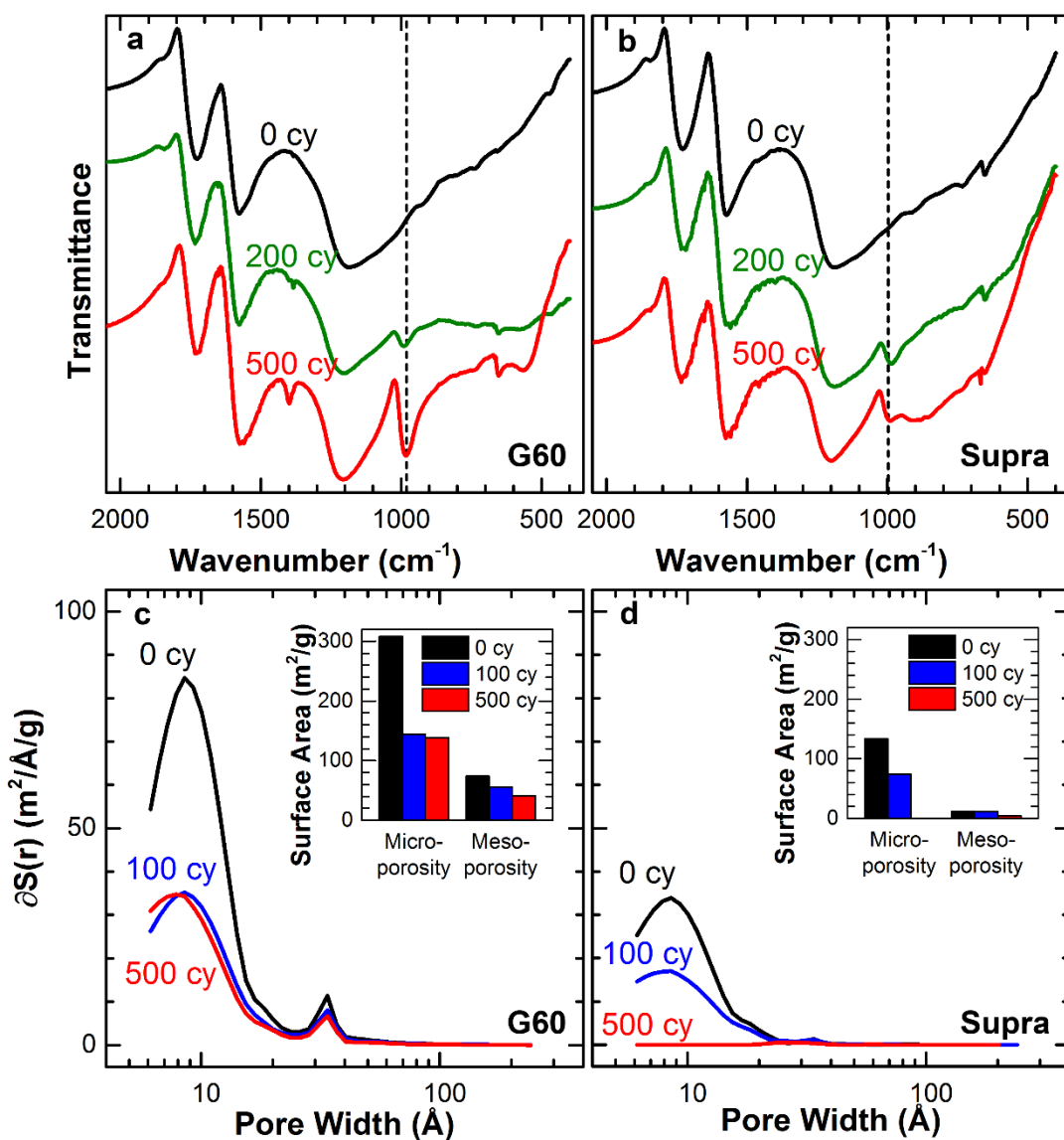


Figure 3.4. FTIR spectra of (a) G60 and (b) Supra powder that was treated with 15 M HNO_3 that was boiled off and then coated with varying number of V_2O_5 ALD cycles at 150°C . Effect of ALD coatings on the pore distribution of (c) G60 and (d) Supra powder and a comparison of the microporosity and mesoporosity (inset).

G60 powder coated with 1000 cycles of V_2O_5 ALD at 150°C was analyzed using EFTEM. Two locations imaged by EFTEM are shown in Figure 3.5. At both sites, the vanadium filtered micrograph suggests some coating nonuniformity. However, on these porous substrates, we

expect a higher vanadium intensity emanating from the pore sites. The bright signal in the lower part of the image 5(b), for example, likely coincides with V_2O_5 in the carbon pores. Locally dense carbon will also reduce the relative V signal, even for a uniform ALD coating. To test this further, we also used EFTEM to analyze G60 powder coated with thinner V_2O_5 layers (75 cycles at 150°C). For these samples, we found a small electron energy loss signal for the vanadium relative to the carbon, making it difficult to map the vanadium. A small vanadium signal is expected from a uniform V_2O_5 film, further consistent with our interpretation of a uniform V_2O_5 ALD layer on the G60 powder.

Electrochemical analysis of acid treated and ALD coated activated carbon. EC electrodes fabricated from acid-treated carbon and ALD-modified carbon were measured using cyclic voltammetry in a 3 electrode cell using 1 M KCl as an electrolyte (Figure A.7).⁵⁰ Comparing different acid treatments, without ALD, the electrodes treated at 100°C in nitric acid showed the largest increase (270%) in capacitance, likely due to pseudocapacitance from oxygen heteroatoms evident in the FTIR spectra above. Boiling off the acid leads to a decreased surface area, which negatively impacts the capacitance. Therefore, the 100°C acid treatment was used for the ALD coated electrode experiments.

The V_2O_5 ALD was performed at 150°C for a range of cycle numbers. Ideally, performing ALD on the as-formed electrodes maintains the electrode conductivity while adding more capacitive charge storage. The electrodes were tested in a symmetric 2-cell configuration. On the G60 electrodes the ALD coating increased the capacitance to 120 F/g(electrode) (a 46% increase over the acid treated activated carbon) after 75 ALD cycles (Figure 3.6 (a)). Further coating led to a net capacitance decrease, likely due to the pores in the carbon filling with V_2O_5 and reducing the available surface area for charge storage. After ALD, the Supra electrodes showed a minimal increase in charge storage after 200 ALD cycles, before decreasing with additional ALD cycles (Figure 3.6 (b)). A comparison of the specific capacitance is shown in (Figure 3.7(a)).

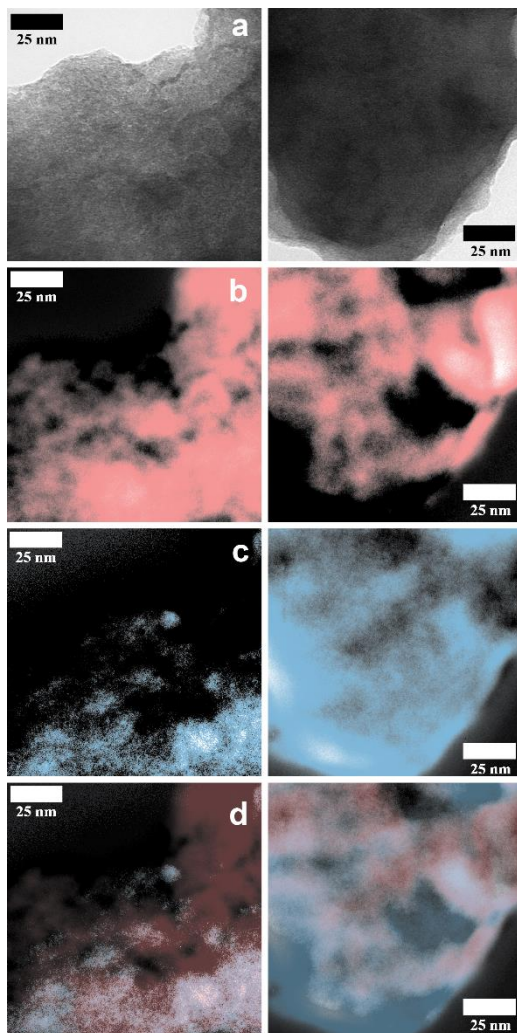


Figure 3.5. EFTEM micrographs of two sites (left and right) of G60 treated with boiled off HNO_3 and coated with 1000 cycles of V_2O_5 ALD: (a) zero-loss; (b) carbon; (c) vanadium; and (d) composite carbon and vanadium.

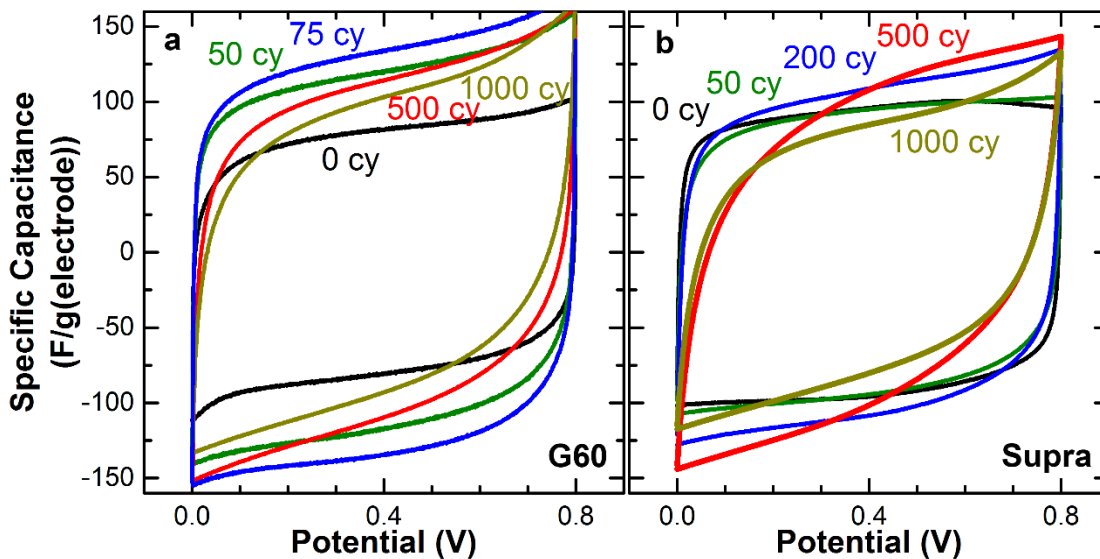


Figure 3.6. Cyclic voltammetry scans of V_2O_5 ALD coated (a) G60 and (b) Supra electrodes at 20 mV/s in 1 M KCl at a 10 μm length scale (Figure 3.3(b)). Figure 3.3(d), (e) and (f) show SEM images of the untreated G60, G60 after nitric acid boiled off, and after coating with 125 cycles of V_2O_5 ALD at 175°C, respectively. The dark features present in the untreated carbon become less distinct upon acid treatment, and even less visible after ALD treatment, consistent with a loss in porosity after each step.

The mass change after the ALD coating on the G60 electrodes and Supra electrodes are shown in Figure 3.7(a) and compared to the thickness measured on silicon wafers coated during the same ALD runs, and Figure 3.7(b) shows the results. The film thickness increases linearly with ALD cycles. The mass gain of the G60 electrodes initially increases quickly followed by a slower increase after ~100 ALD cycles, as expected for a porous substrate. Further ALD cycles can access less area, leading to a smaller increase in mass uptake. This is consistent with results in Figure 3.4 showing that 100 cycles of V_2O_5 on G60 degrades the mesopore surface area. The mass gain of the Supra electrodes was slower than the G60 electrodes, and remained linear, indicating the V_2O_5 deposited around the porous structure.

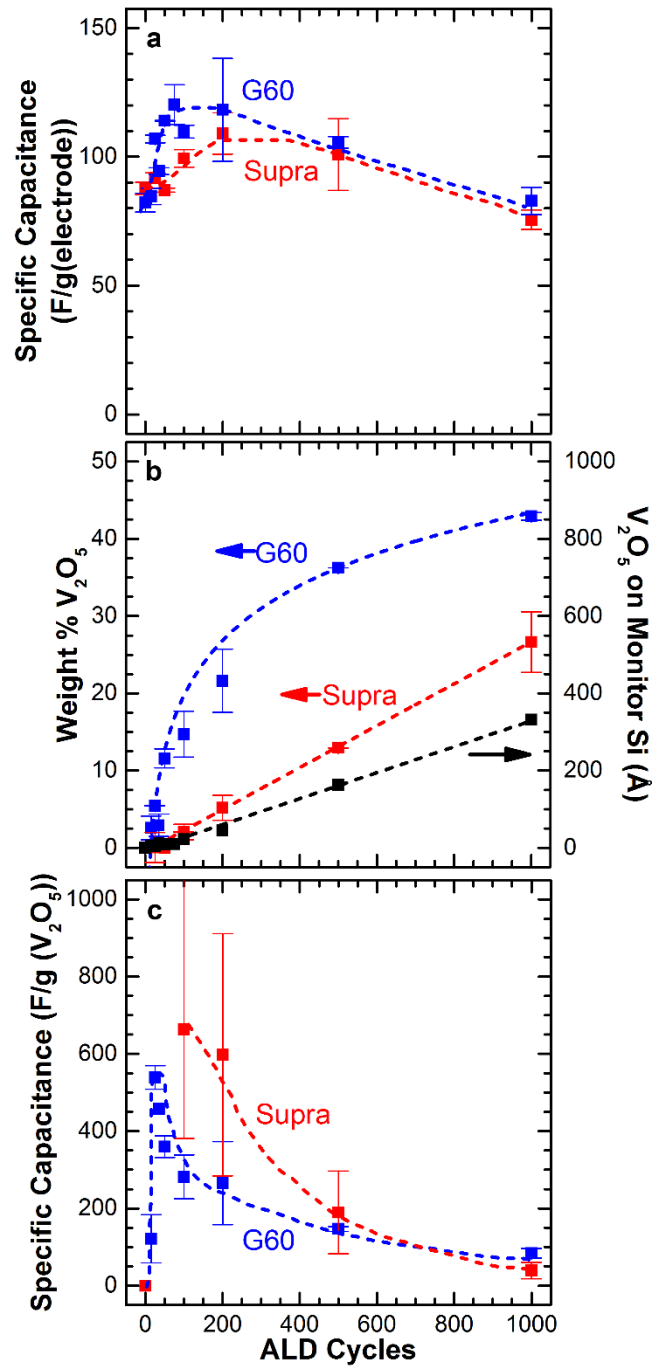


Figure 3.7. (a) The effect of V_2O_5 ALD on capacitor energy storage of G60 and Supra electrodes; (b) weight gain as a function of ALD cycles; and (c) the specific capacitance exhibited by the V_2O_5 .

Using the measured mass change, we calculated the specific capacitance of the V_2O_5 ($F/g(V_2O_5)$) on the electrodes (Figure 3.7 (c)). The V_2O_5 initially showed an increasing capacitance with increasing ALD cycles, exhibiting a maximum capacitance of $540 F/g(V_2O_5)$ after 25 ALD cycles, before decreasing to $84 F/g(V_2O_5)$ after 1000 ALD cycles on the G60 electrodes. The V_2O_5 deposited on the Supra electrodes showed high specific capacitances after 100 and 200 ALD cycles, but the margin of error in the V_2O_5 mass gain leads to a large margin of error in the calculated V_2O_5 specific capacitance. Therefore the V_2O_5 deposited on the Supra should not be interpreted as having a higher specific capacitance than the V_2O_5 deposited on G60 after an equivalent number of ALD cycles. After 500 to 1000 ALD cycles the V_2O_5 demonstrates similar specific capacitances on both the G60 and Supra electrodes.

The average current and specific capacitance of the G60 electrodes coated with V_2O_5 ALD were measured as a function of cyclic voltammetry scan rate (Figure 3.8 (a) and (b)). At both slow (< 50 mV/s) and fast (> 50 mV/s) discharge rates, the G60 electrode with 200 or less ALD cycles showed larger capacitance than uncoated electrodes. For the thickest ALD layers studied (1000 cycles) the specific capacitance only improved for the slowest scan rates (1 mV/s).

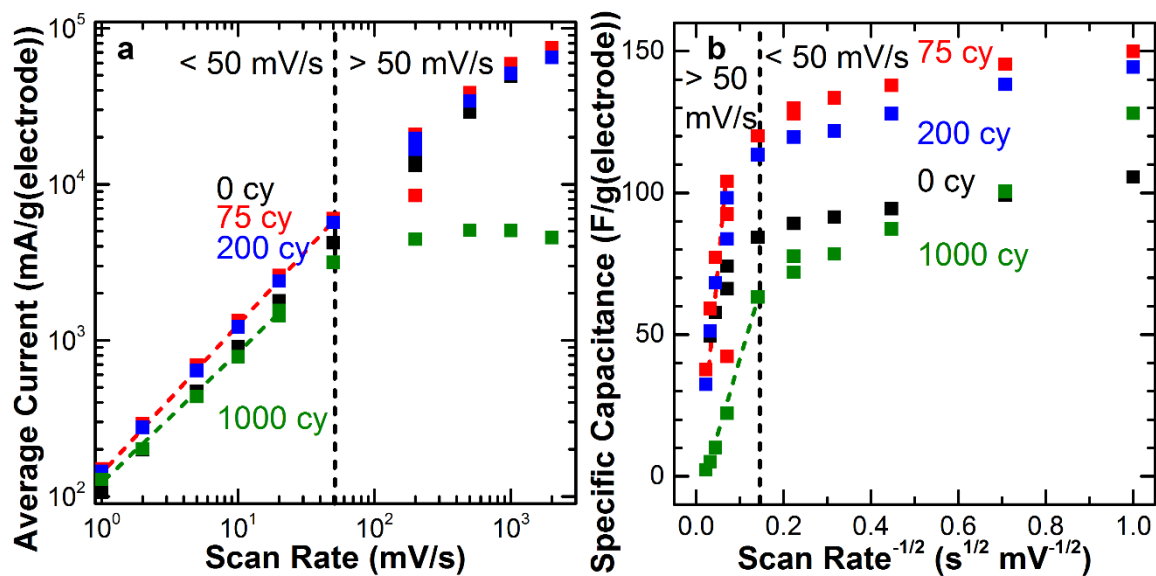


Figure 3.8. (a) G60 electrodes after V₂O₅ ALD coatings average current as a function of cyclic voltammetry scan rate; and (b) the specific capacitance versus scan rate^{-1/2}.

The coulombic efficiency of the G60 ECs was measured using galvanostatic cycling (Figure A.8). The ECs maintained high coulombic efficiency after the introduction of the pseudocapacitive V₂O₅. The G60 ECs were cycled for 10000 charge-discharge cycles at 5 A/g(capacitor) to measure the long-term stability of the V₂O₅ coatings (Figure 3.9). The electrodes displayed a long-term performance similar to that of the uncoated electrodes with the electrode coated with 75 cycles of ALD experiencing an 11% capacitance loss over 10000 cycles, compared to 12% for the uncoated electrode.

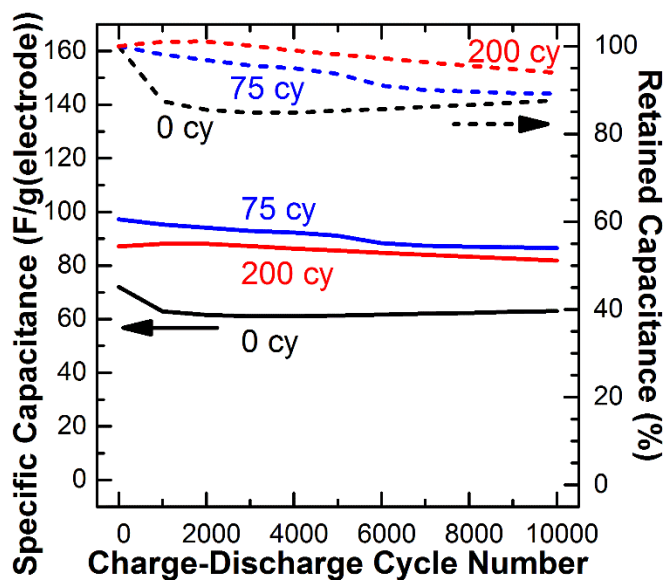


Figure 3.9. Long term performance of V_2O_5 coated G60 electrodes charged/discharged from 0.0 to 0.8 V at a rate of 5 A/g(capacitor).

The G60 electrodes were measured with electrochemical impedance spectroscopy (EIS) (Figure 3.10). The equivalent circuit used to model the EIS data is presented in Figure 3.10 (b). The results show that the equivalent series resistance (ESR) is small and is maintained after ALD (Figure 3.10 (c)), confirming that the conductivity of the carbon was not degraded by the ALD coating. The ECs with 500 or more ALD cycles experience a decreasing slope in the Nyquist plot at low frequencies caused by a decreasing Warburg admittance ((Figure 3.10 (d)), which corresponds to a decrease in ideality and an increase in diffusion limited behavior, consistent with the nonideality of the cyclic voltammetry scans (Figure 3.6 (a)) and reduced surface area from the ALD coating (Figure 3.4 (d)).²⁶ Finally, the modeled capacitances follow trends seen from the cyclic voltammograms (Figure A.9 (a) and (b)), with the capacitance initially increasing with low numbers of ALD cycles before decreasing after many ALD cycles.

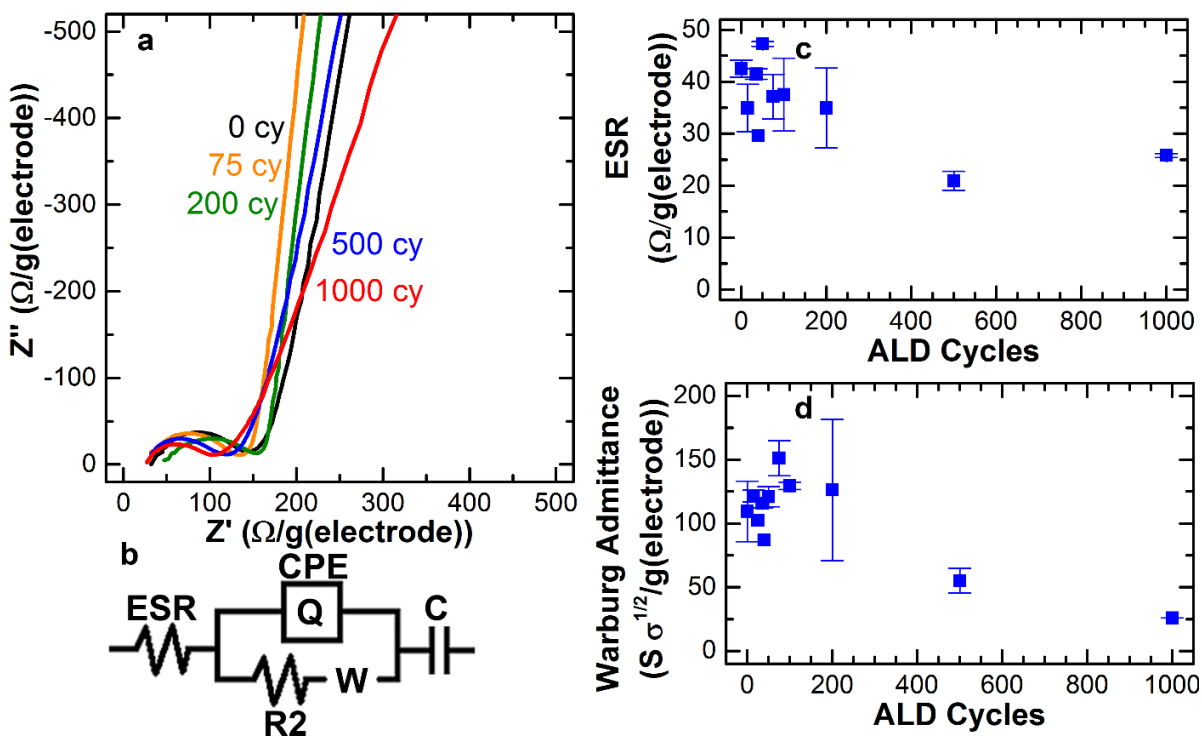


Figure 3.10. (a) Nyquist plot of EIS measurements of V_2O_5 ALD coated G60 electrodes; (b) equivalent circuit used to model EIS data; (c) calculated ESR values; and (d) Warburg admittances.

3.5 Discussion

The overall goal of our work is to understand mechanisms to improve charge storage capacity on micro- and mesoporous electrodes using conformal pseudocapacitive layers. Pseudocapacitive V_2O_5 formed by ALD on chemically-modified G60 carbon shows up to 46% increased performance under the best conditions studied, whereas ALD on the Supra carbon was less effective. To understand this trend we can compare the physical structure of the starting carbon and the ALD coated carbon with the electrochemical performance of the electrodes.

For both the G60 and Supra carbon, the nitric acid treatment aided in the nucleation of the ALD precursors, leading to improved vanadium loading (Figure 3.3), but the treatment also

produced some decrease in overall surface area. The difference in the starting structure of the two carbon materials gives insight into the ALD process. As shown in Figure 3.11, the surface area in the Supra carbon results mostly from micropores, whereas the G60 is mostly mesoporous. The improved capacitance for the ALD on the G60 suggests better ALD coating on the mesopores compared to the micropores in the Supra. The mean micropore size in the Supra is ~ 11 Å, similar to the longest dimension of the VTIP molecule (9.6 Å, Figure 3.11 inset).

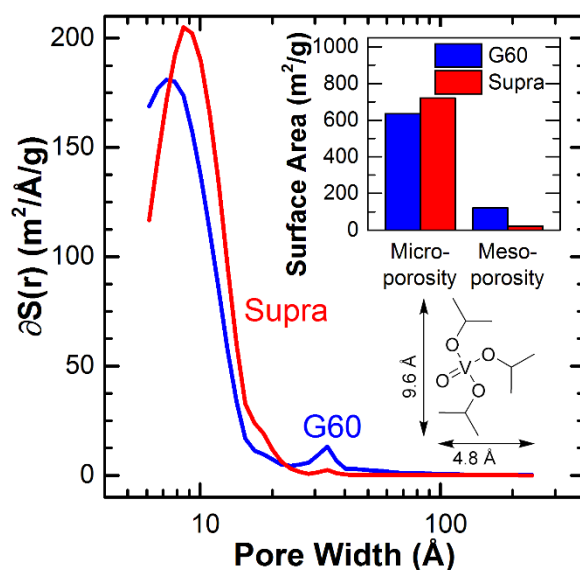


Figure 3.11. Comparison of the pore distribution and the porosity of the G60 and Supra carbon that had been treated with HNO_3 at 100°C from which the electrodes were constructed. Dimensions of a VTIP molecule (inset).

The combination of the electrochemical and physical results suggest that the micropores are physically restraining the ALD precursor from effectively entering and coating the pores. Subsequent V_2O_5 ALD near the pore opening would block the pores, thus decreasing double layer capacitance. In this scenario, the V_2O_5 coating on the microporous Supra adds minimal mass due to small amount of available accessible for deposition. The V_2O_5 adds

pseudocapacitance but decreases the accessible pores and double layer capacitance, leading to only a minimal change in overall capacitance at low ALD cycles. Also, the cyclic voltammetry scans for the ALD-coated Supra were less rectangular, i.e. more diffusion controlled, consistent with some pore blocking, whereas the scans on the ALD-coated G60 maintained a rectangular shape, consistent with good capacitance performance up to ~500 ALD cycles.

A thicker V_2O_5 layer can increase total charge capacity, whereas a thinner V_2O_5 layer requires shorter charge diffusion times and thus enables quicker faradaic charge storage. Slower discharge rates will lead to a larger total measured capacitance. The effect of layer thickness and charging rates can be understood in terms of electrolytic ion storage on the oxide surface versus diffusion and storage in the oxide bulk. The current, i , is expected to vary with the scan rate, ν , following a power law relation

$$i = a \nu^b \quad (3.6)$$

where a and b are adjustable parameters. Charge stored on the surface, i.e. non-Faradaic, responds linearly with the scan rate ($b = 1$), whereas Faradaic bulk charge storage must diffuse under applied voltage, so it responds non-

linearly with scan rate ($b \sim 0.5$).⁵¹⁻⁵⁴ If the charge is stored on the surface the average current will vary linearly with scan rate on a logarithmic plot (Figure 3.8 (a)), and if the charge is diffusion controlled the specific capacitance will vary linearly with the inverse square root of the scan rate (Figure 3.8 (b)). The uncoated G60 EC and the G60 EC coated with 75 cycles of V_2O_5 ALD display surface controlled current at scan rates of 50 mV/s or less (linear portion in Figure 3.8 (a)) and diffusion controlled current at scan rates of 200 mV/s or greater (linear portion of Figure 3.8 (b)). The G60 EC coated with 1000 cycles of V_2O_5 ALD only displays surface controlled current at scan rates of 20 mV/s or less (linear portion in Figure 3.8 (a)) and diffusion controlled current at scan rates of 50 mV/s or greater (linear portion of Figure 3.8 (b)). Quantifying the current that arises from either diffusion processes (varies with $\nu^{-1/2}$) and capacitive processes (varies with ν) results in G60 EC coated with 75 cycles of V_2O_5 ALD having 91% capacitive current at 20 mV/s versus the G60 EC coated with 1000 cycles of V_2O_5

ALD having 67% capacitive current (Figure A.10), consistent with the 1000 cycles of V_2O_5 ALD making the EC more diffusion controlled.^{20,55}

The G60 electrodes coated with 75 and 200 cycles of V_2O_5 ALD maintained a high specific capacitance after having been cycled for 10000 charge/discharge cycles at 5 A/g(capacitor). This is the longest lifespan that had been reported for V_2O_5 ECs.^{9,12,19,56,57}

3.6 Conclusions

Vanadium oxide ALD can create pseudocapacitive layers that improve electrochemical charge storage capacity on micro- and mesoporous carbon electrodes constructed from commercially available activated carbon materials. Pretreating carbon powders with acid increased the oxygen content and oxygenated functional surface groups, introducing pseudocapacitance and helping promote V_2O_5 ALD nucleation, but it led to some decrease in electrode surface area and pore volume. X-ray diffraction showed that the ALD V_2O_5 is amorphous, while XPS confirmed that vanadium is in the 5+ oxidation state.

Adding 75 ALD cycles of V_2O_5 to the mesoporous G60 led to a 46% increase in specific capacitance and maintained high columbic efficiency, low ESR, and good long-term performance over 10000 charge/discharge cycles (89% capacitance retention). The V_2O_5 exhibited a maximum pseudocapacitance of 540 F/g(V_2O_5) after 25 ALD cycles. Adding ALD V_2O_5 onto microporous Supra electrodes showed only small changes in capacitance. The differences in electrochemical performance are ascribed to differences in the ALD process in meso- and microporous substrates. Microporous substrates inhibit precursor diffusion, and micropores near in size to the ALD precursor are not as well coated as larger mesopores. Therefore, alternate ALD materials or precursors could be useful to create very high capacity pseudocapacitor using high surface area micro- and mesoporous conductive electrodes constructed from activated carbon used as a basis in commercial products for highly reliable future energy and power storage applications.

3.7 Supporting Information

Additional information pertaining to EDS, Raman, ALD, XRD, XPS, CV, and EIS is included in Appendix A1.

3.8 Acknowledgments

This material is based upon work supported by the Center for Dielectrics and Piezoelectrics I/UCRC under the National Science Foundation Grant Nos.: IIP 1361503 and 136157. J.S.D. acknowledges support from the U.S. Dept. of Education under the GAANN Fellowship program. N.P.L. acknowledges support from the U.S. National Science Foundation Research Experiences for Undergraduates site on Advanced Materials for Environmental Sustainability (Grant No. EEC-1156762). M.D.L. acknowledges support from Georgia Tech startup funds. The authors acknowledge the NCSU Analytical Instrumentation facility for access to the x-ray diffraction and electron microscopy facilities.

3.9 References

- (1) Goodenough, J. B.; Abruña, H. D.; Buchanan, M. V. *Basic Research Needs for Electrical Energy Storage*; 2007.
- (2) Béguin, F.; Presser, V.; Balducci, A.; Frackowiak, E. Carbons and Electrolytes for Advanced Supercapacitors. *Adv. Mater.* **2014**, *26*, 2219–2251, 2283.
- (3) Simon, P.; Gogotsi, Y. Materials for Electrochemical Capacitors. *Nat. Mater.* **2008**, *7*, 845–854.
- (4) Augustyn, V.; Simon, P.; Dunn, B. Pseudocapacitive Oxide Materials for High-Rate Electrochemical Energy Storage. *Energy Environ. Sci.* **2014**, *7*, 1597–1614.
- (5) Long, J. W.; Bélanger, D.; Brousse, T.; Sugimoto, W.; Sassin, M. B.; Crosnier, O. Asymmetric Electrochemical Capacitors—Stretching the Limits of Aqueous Electrolytes. *MRS Bull.* **2011**, *36*, 513–522.
- (6) Pandolfo, A. G.; Hollenkamp, A. F. Carbon Properties and Their Role in Supercapacitors. *J. Power Sources* **2006**, *157*, 11–27.
- (7) Gu, W.; Yushin, G. Review of Nanostructured Carbon Materials for Electrochemical Capacitor Applications: Advantages and Limitations of Activated Carbon, Carbide-Derived Carbon, Zeolite-Templated Carbon, Carbon Aerogels, Carbon Nanotubes, Onion-like Carbon, and Graphene. *WIREs Energy Env.* **2014**, *3*, 424–473.
- (8) Yu, G.; Xie, X.; Pan, L.; Bao, Z.; Cui, Y. Hybrid Nanostructured Materials for High-Performance Electrochemical Capacitors. *Nano Energy* **2013**, *2*, 213–234.
- (9) Engstrom, A. M.; Doyle, F. M. Exploring the Cycle Behavior of Electrodeposited Vanadium Oxide Electrochemical Capacitor Electrodes in Various Aqueous Environments. *J. Power Sources* **2013**, *228*, 120–131.
- (10) Lao, Z. J.; Konstantinov, K.; Tournaire, Y.; Ng, S. H.; Wang, G. X.; Liu, H. K. Synthesis of Vanadium Pentoxide Powders with Enhanced Surface-Area for Electrochemical Capacitors. *J. Power Sources* **2006**, *162*, 1451–1454.
- (11) Warwick, M. E. A.; Roberts, A. J.; Slade, R. C. T.; Binions, R. Electric Field Assisted Chemical Vapour Deposition – a New Method for the Preparation of Highly Porous Supercapacitor Electrodes. *J. Mater. Chem. A* **2014**, *2*, 6115–6120.
- (12) Boukhalifa, S.; Evanoff, K.; Yushin, G. Atomic Layer Deposition of Vanadium Oxide on Carbon Nanotubes for High-Power Supercapacitor Electrodes. *Energy Environ. Sci.* **2012**, *5*, 6872–6879.

- (13) Reddy, R. N.; Reddy, R. G. Porous Structured Vanadium Oxide Electrode Material for Electrochemical Capacitors. *J. Power Sources* **2006**, *156*, 700–704.
- (14) Sudant, G.; Baudrin, E.; Dunn, B.; Tarascon, J.-M. Synthesis and Electrochemical Properties of Vanadium Oxide Aerogels Prepared by a Freeze-Drying Process. *J. Electrochem. Soc.* **2004**, *151*, A666–A671.
- (15) Rolison, D. R.; Dunn, B. Electrically Conductive Oxide Aerogels: New Materials in Electrochemistry. *J. Mater. Chem.* **2001**, *11*, 963–980.
- (16) Dong, W.; Sakamoto, J.; Dunn, B. Electrochemical Properties of Vanadium Oxide Aerogels and Aerogel Nanocomposites. *J. Sol-Gel Sci. Technol.* **2003**, *26*, 641–644.
- (17) Dong, W.; Rolison, D. R.; Dunn, B. Electrochemical Properties of High Surface Area Vanadium Oxide Aerogels. *Electrochem. Solid-State Lett.* **2000**, *3*, 457–459.
- (18) Huang, C.-M.; Hu, C.-C.; Chang, K.-H.; Li, J.-M.; Li, Y.-F. Pseudocapacitive Characteristics of Vanadium Oxide Deposits with a Three-Dimensional Porous Structure. *J. Electrochem. Soc.* **2009**, *156*, A667–A671.
- (19) Ghosh, A.; Ra, E. J.; Jin, M.; Jeong, H.-K.; Kim, T. H.; Biswas, C.; Lee, Y. H. High Pseudocapacitance from Ultrathin V_2O_5 Films Electrodeposited on Self-Standing Carbon-Nanofiber Paper. *Adv. Funct. Mater.* **2011**, *21*, 2541–2547.
- (20) Rauda, I. E.; Augustyn, V.; Saldarriaga-Lopez, L. C.; Chen, X.; Schelhas, L. T.; Rubloff, G. W.; Dunn, B.; Tolbert, S. H. Nanostructured Pseudocapacitors Based on Atomic Layer Deposition of V_2O_5 onto Conductive Nanocrystal-Based Mesoporous ITO Scaffolds. *Adv. Funct. Mater.* **2014**, *24*, 6717–6728.
- (21) Chen, Z.; Qin, Y.; Weng, D.; Xiao, Q.; Peng, Y.; Wang, X.; Li, H.; Wei, F.; Lu, Y. Design and Synthesis of Hierarchical Nanowire Composites for Electrochemical Energy Storage. *Adv. Funct. Mater.* **2009**, *19*, 3420–3426.
- (22) Chen, Z.; Augustyn, V.; Wen, J.; Zhang, Y.; Shen, M.; Dunn, B.; Lu, Y. High-Performance Supercapacitors Based on Intertwined CNT/ V_2O_5 Nanowire Nanocomposites. *Adv. Mater.* **2011**, *23*, 791–795.
- (23) Nagaraju, D. H.; Wang, Q.; Beaujuge, P.; Alshareef, H. N. Two-Dimensional Heterostructures of V_2O_5 and Reduced Graphene Oxide as Electrodes for High Energy Density Asymmetric Supercapacitors. *J. Mater. Chem. A* **2014**, *2*, 17146–17152.
- (24) Qu, Q. T.; Shi, Y.; Li, L. L.; Guo, W. L.; Wu, Y. P.; Zhang, H. P.; Guan, S. Y.; Holze, R. $V_2O_5 \cdot 0.6H_2O$ Nanoribbons as Cathode Material for Asymmetric Supercapacitor in K_2SO_4 Solution. *Electrochem. Commun.* **2009**, *11*, 1325–1328.

- (25) Conway, B. E.; Pell, W. G. Double-Layer and Pseudocapacitance Types of Electrochemical Capacitors and Their Applications to the Development of Hybrid Devices. *J. Solid State Electrochem.* **2003**, *7*, 637–644.
- (26) Lu, M.; Beguin, F.; Frackowiak, E. *Supercapacitors: Materials, Systems and Applications*; Wiley-VCH Verlag GmbH & Co. KGaA, 2013.
- (27) Sassin, M. B.; Chervin, C. N.; Rolison, D. R.; Long, J. W. Redox Deposition of Nanoscale Metal Oxides on Carbon for Next-Generation Electrochemical Capacitors. *Acc. Chem. Res.* **2013**, *46*, 1062–1074.
- (28) Peng, Y.; Chen, Z.; Wen, J.; Xiao, Q.; Weng, D.; He, S.; Geng, H.; Lu, Y. Hierarchical Manganese Oxide/Carbon Nanocomposites for Supercapacitor Electrodes. *Nano Res.* **2011**, *4*, 216–225.
- (29) Moreno-Castilla, C.; Ferro-Garcia, M. A.; Joly, J. P.; Bautista-Toledo, I.; Carrasco-Marin, F.; Rivera-Utrilla, J. Activated Carbon Surface Modifications by Nitric Acid, Hydrogen Peroxide, and Ammonium Peroxydisulfate Treatments. *Langmuir* **1995**, *11*, 4386–4392.
- (30) Chen, X.; Pomerantseva, E.; Gregorczyk, K.; Ghodssi, R.; Rubloff, G. Cathodic ALD V₂O₅ Thin Films for High-Rate Electrochemical Energy Storage. *RSC Adv.* **2013**, *3*, 4294–4302.
- (31) Østreng, E.; Nilsen, O.; Fjellvåg, H. Optical Properties of Vanadium Pentoxide Deposited by ALD. *J. Phys. Chem. C* **2012**, *116*, 19444–19450.
- (32) Musschoot, J.; Deduytsche, D.; Poelman, H.; Haemers, J.; Van Meirhaeghe, R. L.; Van den Berghe, S.; Detavernier, C. Comparison of Thermal and Plasma-Enhanced ALD/CVD of Vanadium Pentoxide. *J. Electrochem. Soc.* **2009**, *156*, P122–P126.
- (33) Baddour-Hadjean, R.; Golabkan, V.; Pereira-Ramos, J. P.; Mantoux, A.; Lincot, D. A Raman Study of the Lithium Insertion Process in Vanadium Pentoxide Thin Films Deposited by Atomic Layer Deposition. *J. Raman Spectrosc.* **2002**, *33*, 631–638.
- (34) Badot, J. C.; Ribes, S.; Yousfi, E. B.; Vivier, V.; Pereira-Ramos, J. P.; Baffier, N.; Lincot, D. Atomic Layer Epitaxy of Vanadium Oxide Thin Films and Electrochemical Behavior in Presence of Lithium Ions. *Electrochem. Solid-State Lett.* **2000**, *3*, 485–488.
- (35) Devine, C. K.; Oldham, C. J.; Jur, J. S.; Gong, B.; Parsons, G. N. Fiber Containment for Improved Laboratory Handling and Uniform Nanocoating of Milligram Quantities of Carbon Nanotubes by Atomic Layer Deposition. *Langmuir* **2011**, *27*, 14497–14507.

- (36) Domingo-García, M.; López Garzón, F. J.; Pérez-Mendoza, M. J. On the Characterization of Chemical Surface Groups of Carbon Materials. *J. Colloid Interface Sci.* **2002**, *248*, 116–122.
- (37) Amatucci, G. G.; Badway, F.; Du Pasquier, A.; Zheng, T. An Asymmetric Hybrid Nonaqueous Energy Storage Cell. *J. Electrochem. Soc.* **2001**, *148*, A930–A939.
- (38) Khomenko, V.; Raymundo-Piñero, E.; Béguin, F. Optimisation of an Asymmetric Manganese Oxide/Activated Carbon Capacitor Working at 2 V in Aqueous Medium. *J. Power Sources* **2006**, *153*, 183–190.
- (39) Chen, L.; Zhu, J. Metal Nanoparticle-Directed NiCo₂O₄ Nanostructure Growth on Carbon Nanofibers with High Capacitance. *Chem. Commun.* **2014**, *50*, 8253–8256.
- (40) Jeon, J.-W.; Sharma, R.; Meduri, P.; Arey, B. W.; Schaef, H. T.; Lutkenhaus, J. L.; Lemmon, J. P.; Thallapally, P. K.; Nandasiri, M. I.; McGrail, B. P.; Nune, S. K. In Situ One-Step Synthesis of Hierarchical Nitrogen-Doped Porous Carbon for High-Performance Supercapacitors. *ACS Appl. Mater. Interfaces* **2014**, *6*, 7214–7222.
- (41) Huang, Y.; Huang, Y.; Zhu, M.; Meng, W.; Pei, Z.; Liu, C.; Hu, H.; Zhi, C. Magnetic-Assisted, Self-Healable, Yarn-Based Supercapacitor. *ACS Nano* **2015**, *9*, 6242–6251.
- (42) Figueiredo, J. L.; Pereira, M. F. R.; Freitas, M. M. A.; Orfao, J. J. M. Modification of the Surface Chemistry of Activated Carbons. *Carbon* **1999**, *37*, 1379–1389.
- (43) Domingo-García, M.; López-Garzón, F. J.; Pérez-Mendoza, M. Effect of Some Oxidation Treatments on the Textural Characteristics and Surface Chemical Nature of an Activated Carbon. *J. Colloid Interface Sci.* **2000**, *222*, 233–240.
- (44) Moreno-Castilla, C.; López-Ramón, M. V.; Carrasco-Marín, F. Changes in Surface Chemistry of Activated Carbons by Wet Oxidation. *Carbon* **2000**, *38*, 1995–2001.
- (45) Moreno-Castilla, C.; Carrasco-Marín, F.; Maldonado-Hódar, F. J.; Rivera-Utrilla, J. Effects of Non-Oxidant and Oxidant Acid Treatments on the Surface Properties of an Activated Carbon with Very Low Ash Content. *Carbon* **1998**, *36*, 145–151.
- (46) Wang, X. J.; Li, H. D.; Fei, Y. J.; Wang, X.; Xiong, Y. Y.; Nie, Y. X.; Feng, K. A. XRD and Raman Study of Vanadium Oxide Thin Films Deposited on Fused Silica Substrates by RF Magnetron Sputtering. *Appl. Surf. Sci.* **2001**, *177*, 8–14.
- (47) Gotić, M.; Popović, S.; Ivanda, M.; Musić, S. Sol–gel Synthesis and Characterization of V₂O₅ Powders. *Mater. Lett.* **2003**, *57*, 3186–3192.
- (48) Mendialdua, J.; Casanova, R.; Barboux, Y. XPS Studies of V₂O₅, V₆O₁₃, VO₂ and V₂O₃. *J. Electron Spectrosc. Relat. Phenom.* **1995**, *71*, 249–261.

- (49) Sanchez, C.; Livage, J.; Lucazeau, G. Infrared and Raman Study of Amorphous V₂O₅. *J. Raman Spectrosc.* **1982**, *12*, 68–72.
- (50) Lee, H. Y.; Goodenough, J. B. Supercapacitor Behavior with KCl Electrolyte. *J. Solid State Chem.* **1999**, *144*, 220–223.
- (51) Augustyn, V.; Come, J.; Lowe, M. A.; Kim, J. W.; Taberna, P.-L.; Tolbert, S. H.; Abruña, H. D.; Simon, P.; Dunn, B. High-Rate Electrochemical Energy Storage through Li⁺ Intercalation Pseudocapacitance. *Nat. Mater.* **2013**, *12*, 518–522.
- (52) Lindström, H.; Södergren, S.; Solbrand, A.; Rensmo, H.; Hjelm, J.; Hagfeldt, A.; Lindquist, S.-E. Li⁺ Ion Insertion in TiO₂ (Anatase). 2. Voltammetry on Nanoporous Films. *J. Phys. Chem. B* **1997**, *101*, 7717–7722.
- (53) Liu, C.; Gillette, E. I.; Chen, X.; Pearse, A. J.; Kozen, A. C.; Schroeder, M. a; Gregorczyk, K. E.; Lee, S. B.; Rubloff, G. W. An All-in-One Nanopore Battery Array. *Nat. Nanotechnol.* **2014**, *9*, 1031–1039.
- (54) Ardizzone, S.; Fregonara, G.; Trasatti, S. “Inner” and “Outer” Active Surface of RuO₂ Electrodes. *Electrochim. Acta* **1990**, *35*, 263–267.
- (55) Liu, T.-C.; Pell, W. G.; Conway, B. E.; Roberson, S. L. Behavior of Molybdenum Nitrides as Materials for Electrochemical Capacitors. *J. Electrochem. Soc.* **1998**, *145*, 1882–1888.
- (56) Perera, S. D.; Liyanage, A. D.; Nijem, N.; Ferraris, J. P.; Chabal, Y. J.; Balkus, K. J. Vanadium Oxide Nanowire – Graphene Binder Free Nanocomposite Paper Electrodes for Supercapacitors: A Facile Green Approach. *J. Power Sources* **2013**, *230*, 130–137.
- (57) Shakir, I.; Ali, Z.; Bae, J.; Park, J.; Kang, D. J. Layer by Layer Assembly of Ultrathin V₂O₅ Anchored MWCNTs and Graphene on Textile Fabrics for Fabrication of High Energy Density Flexible Supercapacitor Electrodes. *Nanoscale* **2014**, *6*, 4125–4130.

CHAPTER 4. Intrinsic Limitations of Atomic Layer Deposition for Pseudocapacitive Metal Oxides in Porous Electrochemical Capacitor Electrodes

This chapter is based on a manuscript being prepared for submission as:

Daubert, J. S.; Wang, R.; Ovental, J. S.; Barton, H. F.; Rajagopalan, R.; Augustyn, V.;

Parsons, G. N. Intrinsic Limitations of Atomic Layer Deposition for Pseudocapacitive Metal Oxides in Porous Electrochemical Capacitor Electrodes

4.1 Abstract

By comparing the pseudocapacitive performance of ALD V_2O_5 in micro-, meso-, and macroporous carbon electrodes, we describe the fundamental limits to ALD in very fine pores for pseudocapacitive charge storage. Comparing experimental trends with an ALD coating model, we find that the thermal V_2O_5 ALD process using vanadium triisopropoxide (VTIP) and water is uniformly deposited into pores only when the pore diameter exceeds a critical diameter of 13 Å. By adding the ALD V_2O_5 layer onto activated carbon electrodes, we find that the capacity could be increased by 144% for carbon with micropores and macropores, whereas for carbon black powder containing only macropores (i.e. a low surface area resulting in a relatively small starting capacity) the ALD coating increased the capacity more than 40-fold. To understand the ALD coating limits, the pores of the carbon electrodes were modeled as a series of connected tubes, and the volume of V_2O_5 deposited determined experimentally was compared to the calculated deposition limit. Pores below this critical diameter were sealed and decreased the accessible volume for V_2O_5 deposition by more than half, decreasing the maximum capacity. The effect of the pore sealing by the ALD process on the capacitive response of the activated carbon based electrodes was also studied. This work highlights the intrinsic capabilities and limitations of coating microporous materials using ALD.

4.2 Introduction

Electrochemical capacitors are of great interest for storing energy generated from clean energy sources.¹⁻³ Activated carbon, with its high surface area, has traditionally been used to construct electrochemical capacitors, because it stores charge with an electrochemical double layer and exhibits a capacitance of 70-200 F/g.⁴⁻⁸ Electrochemical capacitors provide higher power density and longer lifespan than lithium ion batteries, but there is a need to increase their energy density to encourage widespread adoption. One approach to increase the charge storage capacity of electrochemical capacitors is through the addition of pseudocapacitive materials that undergo fast, reversible, Faradaic reactions that provide a constant capacitance over the operating potential, while still maintaining a high power density. In this work we explore the

incorporation of pseudocapacitive V_2O_5 into electrochemical capacitor electrodes constructed out of activated carbon using atomic layer deposition (ALD).

ALD consists of a vapor-phase self-limiting binary reaction sequence that is capable of depositing thin films into highly porous materials with no line-of-sight requirement, and thickness control that cannot be matched by other vapor-phase deposition techniques. ALD is of interest for energy storage, because it enables the modification of the porous materials that are currently being used in electrochemical capacitors and batteries.^{9,10} The different pseudocapacitive materials deposited for pseudocapacitors by ALD have included V_2O_5 ,^{11–15} RuO_2 ,^{16–19} Fe_2O_3 ,²⁰ NiO ,^{21,22} TiO_2 ,^{23–25} and Co_3O_4 .²⁶

In order to coat activated carbon using ALD an understanding of the complex network of the nanometer scale pores is necessary. Multiple groups have worked to model the diffusion and reaction of ALD precursors into small pores, focusing on parameters including the saturation dose,²⁷ exposure time,^{28,29} diffusion coefficient,^{30,31} and reactor pressure.³² Most of the models, however, focus on coating pores and particles that are micron scale, and not nanometer scale. Only a few groups have experimentally examined the limits of how deep and small a pore can be coated by ALD on the nanometer scale. Knez, et al. coated tobacco mosaic virus, with its well defined tubular structure with TiO_2 using titanium tetraisopropyl oxide and found the 4 nm wide inner hole of the virus was sealed off with an inner uncoated pore that was 1.0 to 1.5 nm in diameter.³³ Other work examining V_2O_5 ALD on carbon “onion” materials has shown that the V_2O_5 mass gain remains linear with increasing ALD cycles, whereas on activated carbon with large interior surface area, growth saturates after 100-200 ALD cycles.¹⁵ In previous work, we described details of V_2O_5 ALD using vanadium triisopropoxide (VTIP) and water to coat activated carbon, and we demonstrated that ALD deposits more V_2O_5 in mesoporous activated carbons (pores 2 to 50 nm in diameter) than in microporous carbons (pores less than 2 nm in diameter) of similar pore volume and surface area.¹¹

In general, Faradaic metal oxide thin films can store charge through pseudocapacitive and/or battery-type mechanisms, which can be differentiated by their kinetic behavior and the

variation of capacity with extent of charge storage. Pseudocapacitance gives rise to constant current over its voltage window, whereas battery-like response shows sharp, well defined, redox peaks.^{34,35} When adding pseudocapacitive materials to electrochemical capacitors it is necessary that it maintains a constant current response over its potential window, and that its capacity remains constant with varying charge/discharge rates. Vanadium oxide undergoes multiple Faradaic reactions, and has been shown to be pseudocapacitive with a rectangular cyclic voltammogram.^{11–13,36–43} In some cases, however, V₂O₅ has also been shown to exhibit sharp redox peaks with a decreased power density, that are not pseudocapacitive.^{14,15,44–46} Coating activated carbon with vanadium oxide can decrease the surface area and obstruct the electrochemical double layer, while also blocking pores within the carbon leading to charge diffusion resistance. This charge diffusion resistance can change the Faradaic response of the V₂O₅ from pseudocapacitive to battery-like.

In this study, we seek to understand the fundamental limits for coupling pseudocapacitive materials into porous carbon electrodes, including micro-, meso-, and macroporous materials. We therefore introduced carbon powders with distinctly defined pore volume and pore distribution into electrochemical capacitors electrodes and tested their performance after coating with various thicknesses of ALD V₂O₅. Comparing experimental trends with an ALD coating model, we thoroughly analyzed the effect of the pore structure on the V₂O₅ ALD. We conclude that the V₂O₅ ALD process used here is intrinsically limited where it can only deposit into pores that are above a critical diameter of 13 Å. The electrochemical charge storage properties of the electrodes were analyzed in a non-aqueous electrolyte using a three-electrode configuration. Carbon electrodes coated with thin layers of pseudocapacitive V₂O₅ retain capacitive behavior, whereas thicker V₂O₅ layers introduce Li⁺ diffusion limitations, resulting in a battery-like response. Our description of fundamental limitations of the V₂O₅ ALD process to create pseudocapacitive coatings in porous carbon provides important insight for advanced charge storage devices as well as basic understanding of general limitations of ALD in porous solids.

4.3 Experimental Section

Carbon powder and electrode preparation. The types of carbon powder studied were obtained in different ways. The “macro-CB” (CB refers to carbon black) carbon is Acetylene Black that was purchased from Alfa-Aesar, and the “micro-AC” (AC refers to activated carbon) is Porous Carbon that was purchased from ACS Material. The “meso-AC” carbon was synthesized as discussed previously.⁴⁷ The “macro-AC” was synthesized by adding furfuryl alcohol (FA) dropwise into p-toluenesulfonic acid monohydrate dissolved in tetrahydrofuran and allowed to polymerize. To this solution, polyethylene glycol (PEG) diacid (molecular weight 600 g/mol) was mixed in a weight ratio of 2:1 (PEG diacid: FA) and the polymers were blended. The polymer blend was then carbonized under argon atmosphere and activated using CO₂. Pore sizes were measured using a Quantachrome Autosorb-1C. Carbon powder (~25 mg) was degassed at 150°C for more than 4 hours before measurement of 20 adsorption and 20 desorption points between 0.05 and 0.995 P/P₀. Pore volume distributions were calculated in the AS1Win software package with a Barrett-Joyner-Halenda (BJH) desorption analysis.

To form carbon electrodes, the carbon powder (before ALD coating) was mixed with 5 wt.% acetylene carbon black (99.9%, Alfa Aesar) to increase the electrode conductivity, along with 10 wt.% polyvinylidene fluoride (PVDF) (Sigma Aldrich) as an electrode binder. The mixture was suspended into 1-methyl-2-pyrrolidinone (NMP) (99.5%, Sigma Aldrich) to form a slurry which was cast (~200 micron thick) onto stainless steel foil current collectors using a doctor blade. The electrodes were then dried at 120°C for 6 hours under vacuum to evaporate the NMP. The finished electrode area was ~1×1 cm² with a mass of ~1 mg.

ALD coating. For V₂O₅ coating, the carbon electrodes were placed flat on a metal sample holder and held down with metal clips to secure them in place during the ALD process. We were careful to have the clips contact only the current collector in order to protect the electrode from mechanical damage. The ALD was conducted in a custom-built viscous flow-tube ALD reactor as described previously.¹¹ The reactant carrier and purge gas was ultrahigh-purity nitrogen (99.999%, Arc3) that was further purified using a Gatekeeper inert gas purifier (rated

to <100 parts per trillion H₂O and O₂, Entegris) before flowing into the reactor. The reactor consisted of a stainless steel tube 10 cm in diameter connected to gas inlet and pumping ports by conflat flanges. A resistively heated jacket surrounding the system was used to achieve the desired temperature. A controlled temperature gradient was maintained along the entire gas flow path to prevent precursor condensation. The working pressure in the reactor during gas purge cycles was 1 Torr.

The V₂O₅ ALD process was conducted at 150 °C using vanadium triisopropoxide (VTIP) (96%, Alfa Aesar, kept at 45 °C with a vapor pressure of ~0.29 Torr)⁴⁸ and H₂O as co-reactants.¹¹ A typical V₂O₅ ALD cycle consisted of dosing VTIP by bubbling N₂ carrier gas through the VTIP to volatilize and deliver it to the reactor, followed by sealing the reactor to “hold” the reactor and allow the precursors to diffuse through the electrode, before-purging with nitrogen, dosing of water, “holding” the reactor to allow the water precursor to diffuse, and then purging with nitrogen before the next VTIP dose for the subsequent cycle. One ALD cycle (VTIP dose (hold)/N₂ purge/H₂O dose (hold)/N₂ purge) has a timing interval of 32(60)/100/0.2(60)/100 s, and the number of cycles was varied depending on the desired thickness of the thin film coating.

The thickness of the ALD films was measured using spectroscopic ellipsometry (J.A. Woollam Co. alpha-SE, using the CompleteEASE data analysis software package) on silicon monitor wafers that were placed in the reactor during ALD, and are accurate to within ±10%.

Annealing. The electrodes with and without ALD coating were annealed under air for 60 minutes with temperatures held between 200 and 300°C. X-ray photoelectron spectroscopy (XPS) (SPECS System with PHOIBOS 150 Analyzer) was used to analyze the composition of the V₂O₅ films on silicon. The spectra were calibrated based on the carbon 1s peak normalized at 284.5 eV. X-ray diffraction (XRD) (Rigaku SmartLab and Panalytical Empyrean, Cu K α source, 1.54 Å) was used to assess crystalline structure of the V₂O₅ films on silicon. Raman spectra of the V₂O₅ films on stainless steel were collected using a WITEC confocal Raman microscope system alpha300 M with a 532 nm laser source.

Capacitor characterization. Electrochemical measurements were carried out in a three-electrode cell using a BioLogic VMP3 potentiostat in an argon-filled glovebox, with oxygen and water levels <1 ppm. The electrolyte solution used was 1.0 M LiClO₄ in propylene carbonate (PC) and lithium metal foils were used as the counter and reference electrodes, all of which were purchased from Sigma Aldrich. Cyclic voltammetry was performed at scan rates from 1 to 200 mV/s using cutoff voltages at 4 and 2 V vs Li/Li⁺.

4.4 Results

Modeling ALD in carbon powders .Carbon powder is traditionally depicted as a spherical particle with series of internal pores of varying size that results in a very high surface area. Figure 4.1(a) shows a carbon particle with micropores, mesopores, and macropores (pores >500 Å in diameter), and Figure 4.1(b) illustrates how that particle may appear after coating with a saturating number of ALD cycles. In this picture, pores with lateral aperture less than a critical size, i.e. comparable to the molecular radius of the ALD precursor, are expected to not be accessible to ALD coating. Pores below a critical size become sealed off, and larger pores that are first coated with ALD can become sealed off when the inner pore becomes too narrow. The illustration of the carbon particle can be simplified and modeled as a series of narrowing pores, Figure 4.1(c), in which the pore diameter and volume can be adjusted to match the structure of different types of carbon powder. The figure highlights the features of a carbon model of narrowing pores: narrow pores below a critical diameter that are sealed and not coated with ALD, midsize pores that are initially coated with ALD films but become sealed when the inner pore reached the critical diameter, and larger pores that are coated with a conformal ALD coating.

The volume of V₂O₅ ($V_{V_2O_5}$) deposited in the carbon powder can be calculated by:

$$V_{V_2O_5} = \sum_{d_{pore}=0}^{\infty} V_{pore}(d_{pore}) \times \left(1 - \frac{d_{hole}^2}{d_{pore}^2}\right) \quad 4.1$$

where d_{pore} and $V_{pore}(d_{pore})$ are the pore diameter and the volume calculated from the experimental BJH desorption results (*vide infra*) as a function of d_{pore} , and d_{hole} is the diameter of the inner cylinder that is not filled with V_2O_5 . The value for d_{hole} is defined as:

$$d_{hole} = \begin{cases} d_{pore} & \text{if } d_{pore} < d_{critical} \text{ (the pore is empty and sealed),} \\ d_{critical} & \text{if } 2 l_{V_2O_5} > d_{pore} - d_{critical} \text{ (the pore is filled and sealed), or} \\ d_{pore} - 2 l_{V_2O_5} & \text{if } 2 l_{V_2O_5} < d_{pore} - d_{critical} \text{ (the pore is ALD coated)} \end{cases} \quad 4.2$$

where $d_{critical}$ is the critical diameter in which the ALD precursors cannot coat the carbon, and $l_{V_2O_5}$ is the thickness of ALD V_2O_5 deposited.

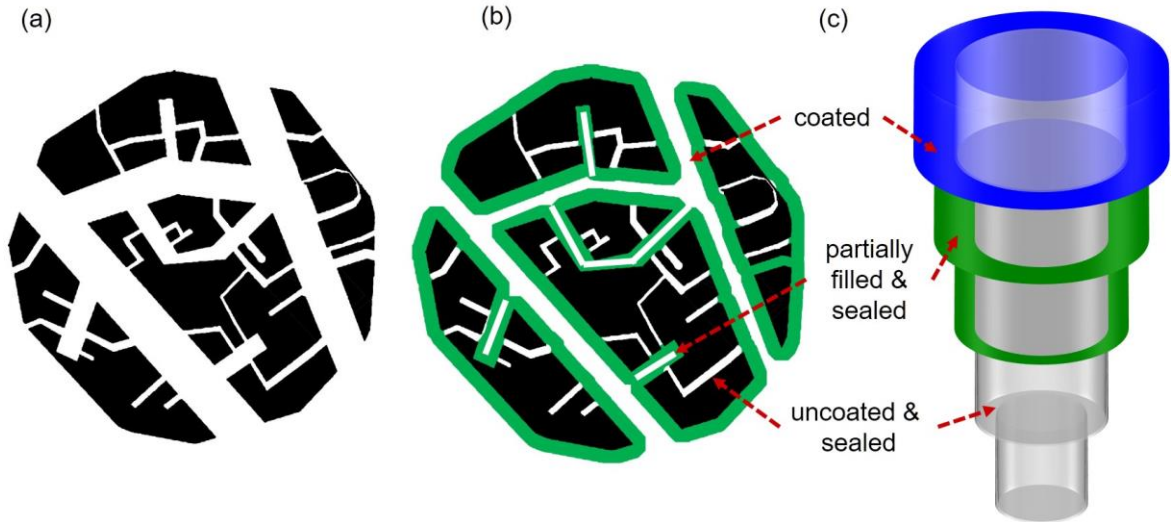


Figure 4.1. Illustration of a carbon particle (a) as formed; and (b) after being coated with pseudocapacitive material using ALD. After coating, the image highlights pores that are uncoated and sealed, pores that are partially filled and sealed, and pores that are internally coated. (c) A representative model for a carbon particle pore, depicted as a series of narrowing tubes coated with ALD. The coated, partially sealed and fully sealed portions are indicated in both (b) and (c).

Deposition of V_2O_5 ALD in carbon powders. In order to examine the effect of pore size on ALD pseudocapacitive layer formation, we evaluated four porous carbon substrates with different pore size, including three activated carbons and one carbon black powder. Before the carbon powders were fabricated into electrodes, their pore structure was determined using nitrogen absorption. The nitrogen isotherms are shown in Figure 4.2(a) and the cumulative pore volume, as calculated from the BJH desorption data, is shown in Figure 4.2(b). From the pore volume distribution, it can be seen that each carbon shows unique structure. One activated carbon has only micropores (micro-AC), another has both micro- and mesopores (meso-AC), and the third has both micro- and macropores (macro-AC). The carbon black has only macropores and does not have any micropores (macro-CB).

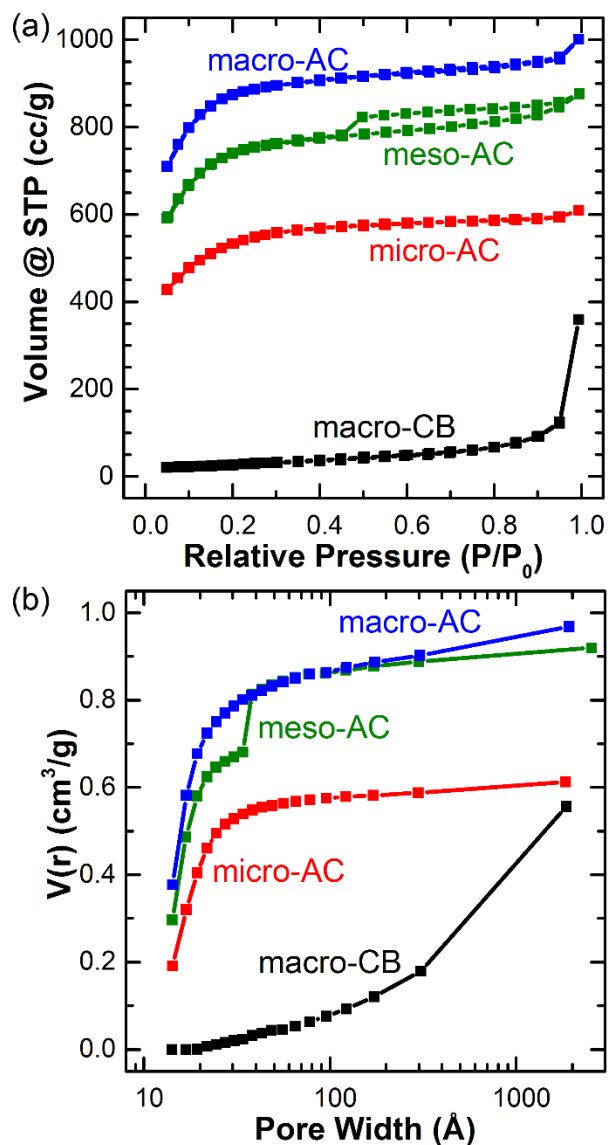


Figure 4.2. (a) Nitrogen isotherms and (b) cumulative pore volume of the carbon powders studied. The label “AC” corresponds to different activated carbons, and “CB” is a porous carbon black powder.

After the carbon powders were formed into electrodes they were coated with up to 300 \AA of V_2O_5 . The thickness was measured on a planar silicon wafer coated during the same ALD run. The volume of V_2O_5 deposited on the electrode, calculated from the measured mass change

after coating, is plotted in Figure 4.3 as a function of V_2O_5 thickness. For the micro-AC, meso-AC, and macro-AC samples, the volume of deposited V_2O_5 initially increases rapidly followed by a region with much less increase. The transition from rapid increase to a shallow, slow increase is expected when the pores within the particle become filled and the deposited film continues to grow on the external surface of the particle, adding a relatively small material volume for each growth cycle. Figure 4.3 also shows dashed lines determined from model calculations using the pore structure in Figure 4.1(c). One set of results, labeled “no pore sealing” shows the expected mass increase vs. number of ALD cycles for uniform ALD over the entire surface area within the pores. For each sample, the experimental result shows significantly less mass uptake, consistent with non-ideal ALD within the porous carbon. If a pore, hole, or trench is large enough to permit ALD precursor and reactant transport, growth can proceed under ALD conditions to uniformly coat the entire pore surface area. Uniform growth will decrease the pore opening diameter. Eventually, the diameter will reach a critical value (referred to as the critical pore diameter, $d_{critical}$) where the pore will be too small to permit reactant entry. Beyond this point, subsequent ALD cycles will seal the pore. Using the model pore shown in Figure 4.1, we calculated the expected mass change versus cycle number for various fixed values of $d_{critical}$. The other dashed curve in Figure 4.3 shows the expected V_2O_5 volume vs. thickness for $d_{critical} = 13 \text{ \AA}$ for each type of carbon powder. For each powder type, the trend in mass uptake is reasonably close to the model curves for $d_{critical} = 13 \text{ \AA}$. This value of the critical radius is also close to $d_{VTIP} = 9.6 \text{ \AA}$, the estimated molecular diameter of the VTIP ALD precursor used here.

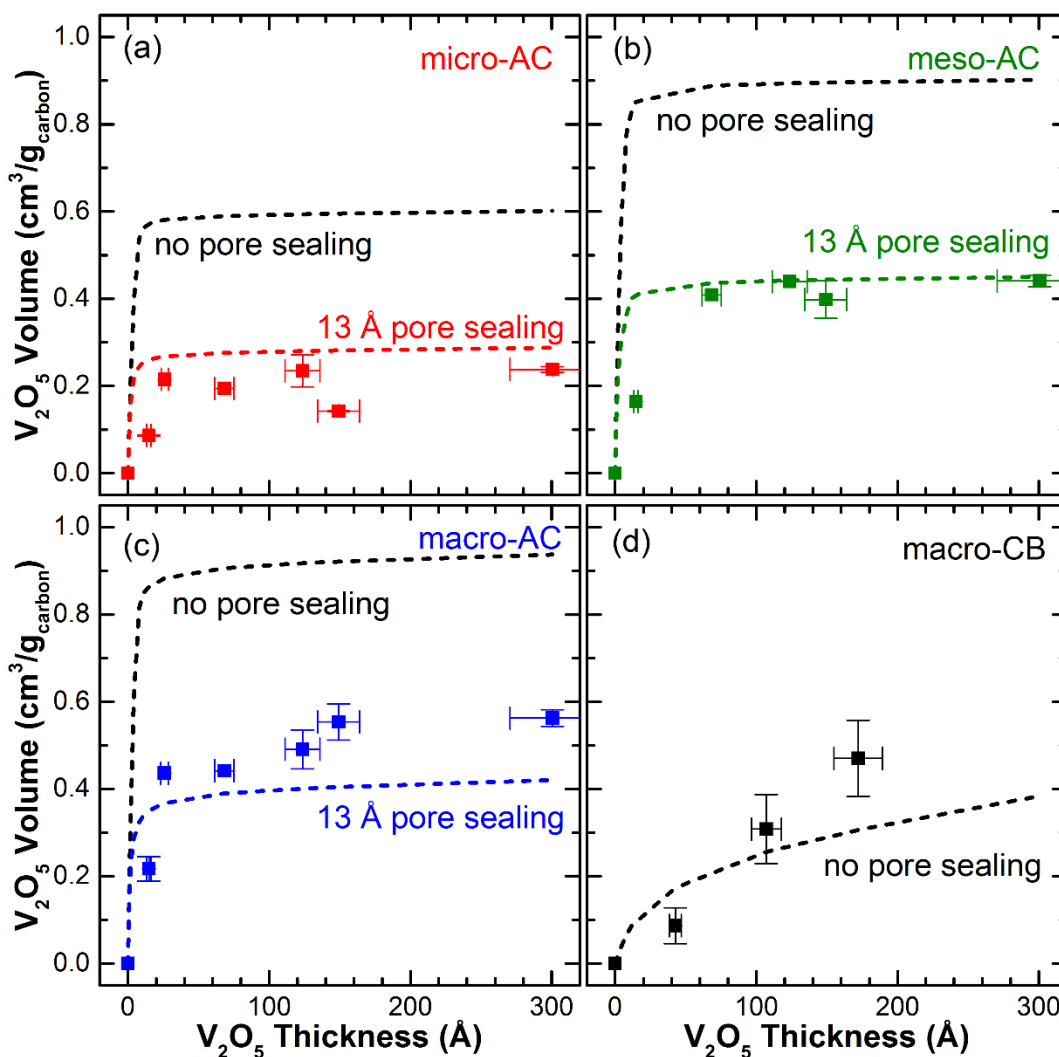


Figure 4.3. V_2O_5 volume gains of electrodes constructed from (a) micro-AC, (b) meso-AC, (c) macro-AC, and (d) macro-CB that were coated with varying thicknesses of V_2O_5 ALD. The dashed curves are the modeled volume gains with “no pore sealing” (representing the maximum amount of V_2O_5 based on the carbon’s pore volume), and the “13 \AA pore sealing” indicating the modeled V_2O_5 volume gain from depositing only in pores $> 13 \text{\AA}$ in diameter. Note: the macro-CB does not have any pores $< 13 \text{\AA}$ in diameter.

Effect of annealing on physical and electrochemical properties of ALD deposited V_2O_5 .

To understand the effect of post deposition processing on the ALD V_2O_5 films deposited on the carbon samples, a set of micro-AC electrodes were coated with 26 \AA of V_2O_5 and annealed

at 200°C, 250°C, and 300°C in air. This thickness of V_2O_5 ensures that a significant fraction of the pores remain unsealed, and allow access to the internal surface of the electrode. The electrochemical response of these samples was measured in a three electrode configuration, and the cyclic voltammograms performed at 2mV/s are shown in Figure 4.4. The electrode that was annealed at 300°C exhibited the highest capacity, and all further experiments were conducted after annealing the electrodes at 300°C. The electrodes were not annealed above 300°C to prevent degradation of the porous carbon and the PVDF binder.

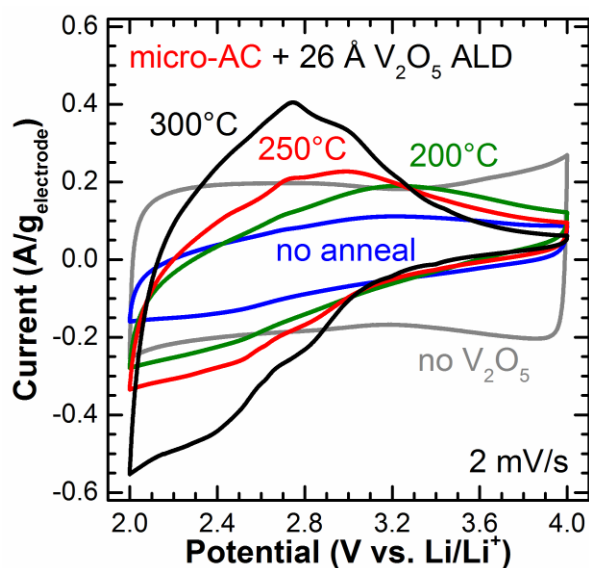


Figure 4.4. Cyclic voltammograms at 2mV/s of electrodes constructed out of micro-AC and coated with 26 Å of V_2O_5 ALD that were annealed at temperatures between 200°C and 300°C.

To further understand the effect of annealing, V_2O_5 thin films deposited on planar silicon surfaces under the same ALD conditions were analyzed as deposited at 150°C and after annealing at 300°C using XPS, XRD, and Raman spectroscopy. The results are shown in Figure 4.5. The XPS spectra of the as deposited vanadium oxide indicates the vanadium is in the 5+ oxidation state.^{13,49–51} There is minimal change (< 0.3 eV, which is below the error of

the XPS system) in the binding energy of the V 2p_{3/2} peak after annealing indicating that the vanadium is still in the 5+ oxidation state. The shoulder of the O 1s peak decreases slightly after annealing, indicating there has been -OH removal. The V₂O₅ is initially amorphous and does not have any XRD peaks, but after annealing it shows sharp peaks in the (001) and (002) planes indicating the V₂O₅ is now orthorhombic and oriented parallel with the substrate.^{49,52} The Raman spectra of the deposited V₂O₅ on planar stainless steel also indicates that it is amorphous, but after annealing the spectra is consistent with orthorhombic V₂O₅.^{49,52-55}

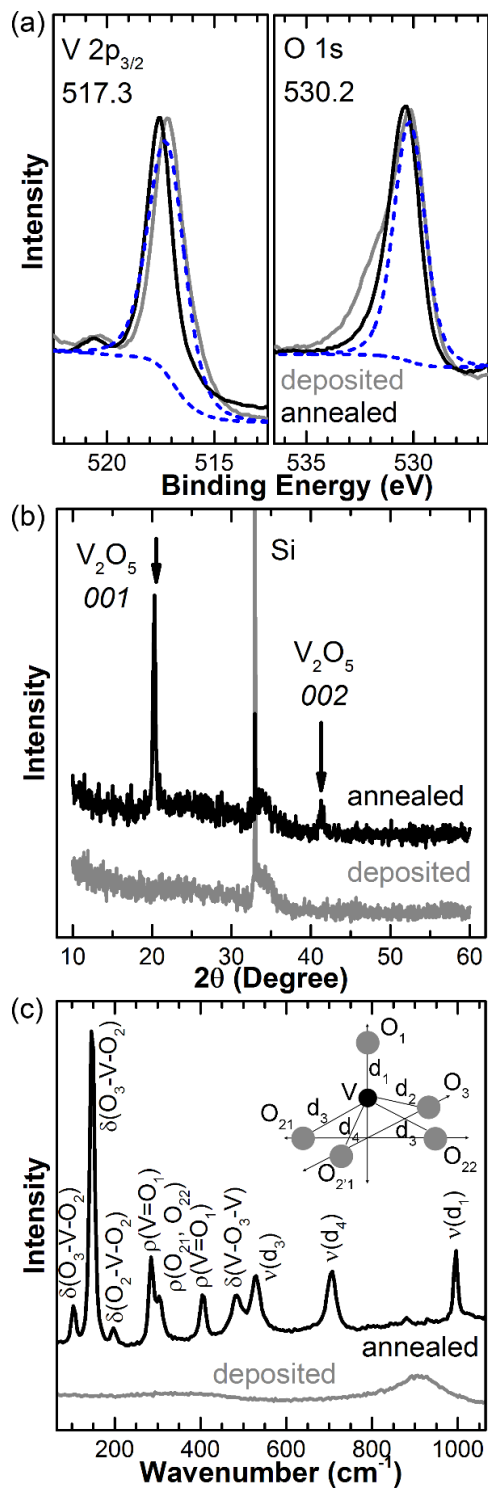


Figure 4.5. (a) XPS scans of V $2p_{3/2}$ and O $1s$ peaks, (b) XRD pattern, and (c) Raman spectra of V_2O_5 ALD as deposited at $150^\circ C$ and after annealing under air at $300^\circ C$.

Effect of V₂O₅ thickness on capacity and charge rate. Sets of electrodes constructed out of each type of carbon were analyzed by cyclic voltammetry using a non-aqueous Li⁺ electrolyte. For each carbon type, samples were prepared with different numbers of V₂O₅ ALD cycles and annealed at 300°C. Figure 4.6 shows cyclic voltammogram traces for each type of carbon as a function of V₂O₅ ALD thickness. For all of the carbon materials studied, the voltammetry results show that the V₂O₅ coating increases the charge storage capacity. The macro-AC and macro-CB show the largest increase in capacity, with a smaller change observed on the micro-AC and meso-AC samples. In addition, for each of the carbon samples, thicker V₂O₅ coatings lead to prominent redox peaks in the cyclic voltammogram traces. These features are associated with lithium intercalation into the crystalline V₂O₅ structure. During discharge the macro-CB +110 Å V₂O₅, the V₂O₅ first undergoes Li⁺ intercalation at 3.3 V vs. Li/Li⁺ to form a two phase region with both the α-V₂O₅ and ε-V₂O₅ phases, it then undergoes a Li⁺ intercalation again at 3.1 V to form the δ-V₂O₅ phase, before undergoing another Li⁺ intercalation at 2.2 V to form the γ-V₂O₅ phase.^{56,57}

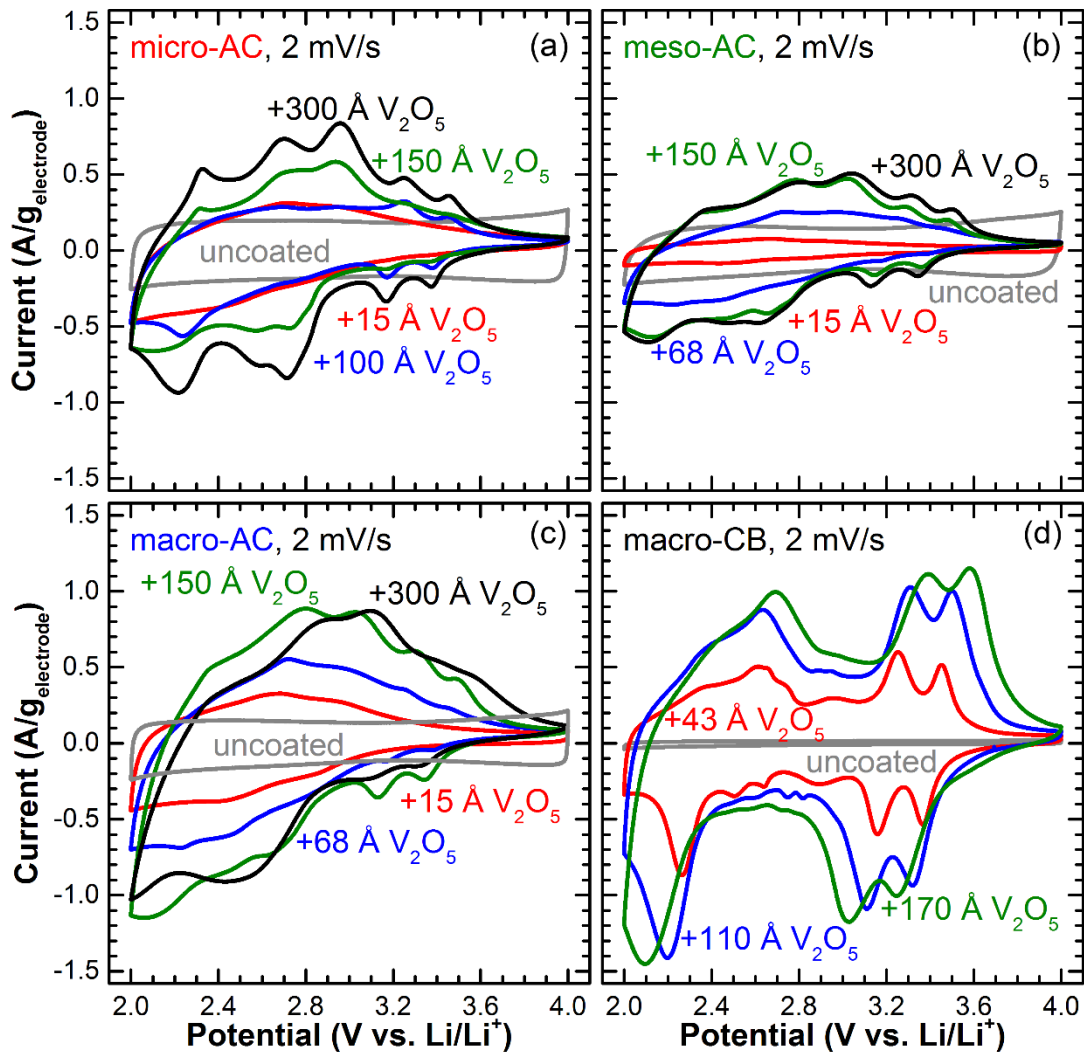


Figure 4.6. Cyclic voltammograms of (a) micro-AC, (b) meso-AC, (c) macro-AC, and (d) macro-CB electrodes coated with varying thicknesses of V_2O_5 ALD at 2 mV/s.

The capacity ($C/g_{\text{electrode}}$) of the carbon/ V_2O_5 structures was determined from the voltammogram curves for various thicknesses of V_2O_5 , and the results are shown in Figure 4.7 as a function of scan rate. For the uncoated carbon, as expected, the capacities of the activated carbons are larger than the carbon black. For the micro-AC and meso-AC carbons, the addition of V_2O_5 tends to initially reduce the electrode capacity, followed by an increase in energy storage for films $> 100 \text{ \AA}$, particularly at lower scan rates ($< 5 \text{ mV/s}$, corresponding to a

charge/discharge time of $> \sim 7$ mins). On the macro-AC, the capacity reached 406 C/g at 2 mV/s (with $t_{V_2O_5} = 150 \text{ \AA}$), an increase of 144% over the starting carbon. The macro-CB showed an even larger increase of more than 40-fold to 546 C/g at 2 mV/s (with $t_{V_2O_5} = 170 \text{ \AA}$). These values approach the value of 1000 C/g at 2 mV/s, measured on a planar stainless steel current collector, with $t_{V_2O_5} = 1100 \text{ \AA}$.

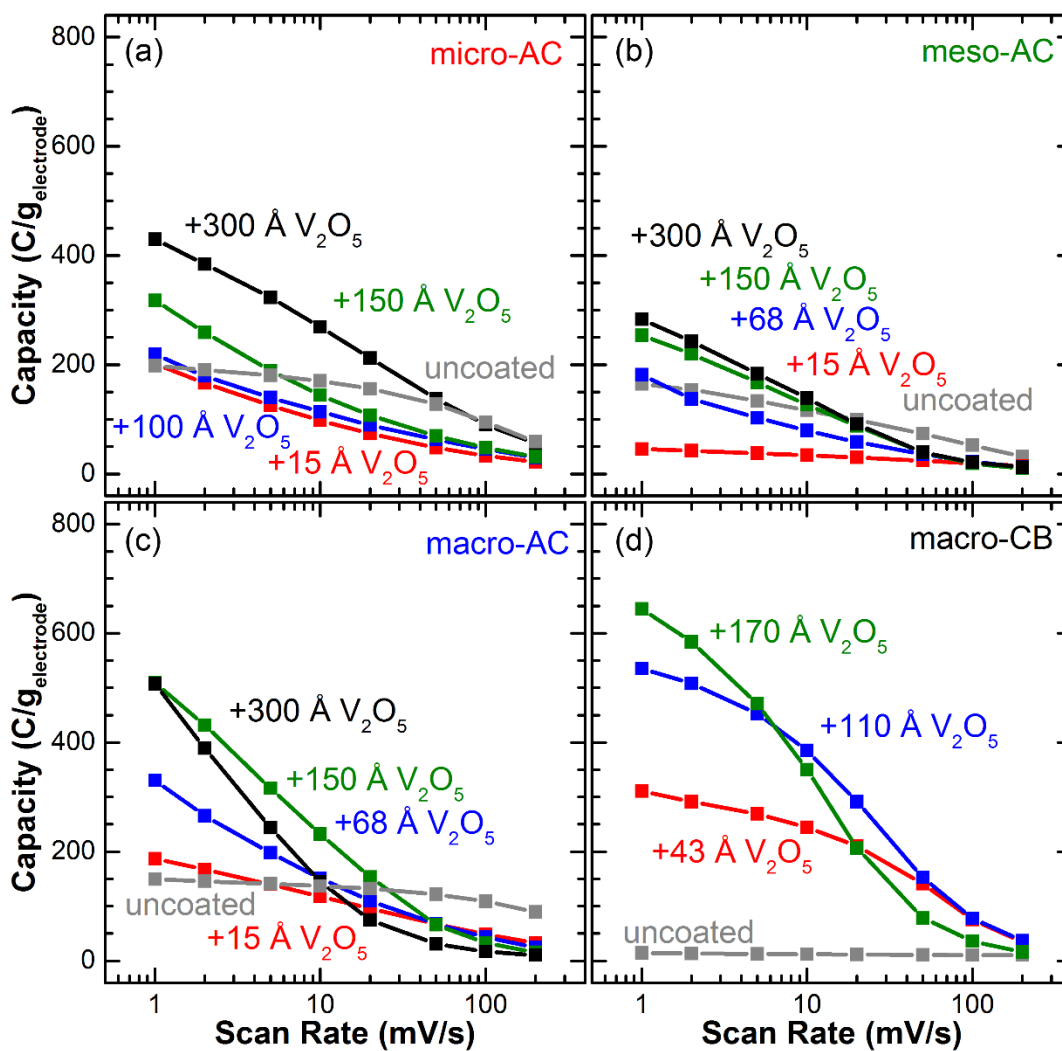


Figure 4.7. Capacity of (a) micro-AC, (b) meso-AC, (c) macro-AC, and (d) macro-CB electrodes that were cycled between 2-4 V vs. Li/Li⁺ at scan rates of 1 - 200 mV/s.

4.5 Discussion

Modeling carbon powder electrodes and deposition of V₂O₅. Because of the complex and irregular pore structure of porous carbon materials, the effect of adding pseudocapacitive layers, such as by ALD, has generally been difficult to model. As shown in Figure 4.1, Figure 4.2 and Figure 4.3, we modeled the pore structure in four types of carbon powders as a series of narrowing tubes coated with uniform pseudocapacitive V₂O₅. By quantifying the mass change after ALD and the known pore volume, we determined that for the ALD process studied here, pores were coated until the pore opening reached a critical diameter of 13 Å, after which the pores became sealed.^{11,33}

An ideal architecture for a pseudocapacitor electrode would optimize both gravimetric capacity (C/g) and areal capacity (C/cm²) by providing a large amount of accessible pseudocapacitive material, with only enough conductive carbon to maintain sufficient electron transport to and from the pseudocapacitive material. The high surface area (cm²/g_{carbon}) and pore volume (cm³/g_{carbon}) of activated carbon, combined with the uniform coating capability of ALD, provide a good basis for pseudocapacitor design. A key challenge, however, is to understand the limitations of the ALD process to maximize pseudocapacitance while minimizing the relatively slow battery-like response.

The macro-AC has a pore volume of 0.94 cm³/g_{carbon}, but with a critical pore sealing diameter of 13 Å, the accessible pore volume is reduced to only 0.42 cm³/g_{carbon}, which is less than 50% of the starting value. This “excess” carbon associated with the inaccessible volume adds mass with no corresponding pseudocapacitive V₂O₅. Thus, any inaccessible volume will tend to decrease the maximum attainable gravimetric capacity of the electrode, degrading the advantages of the activated carbon as a pseudocapacitor electrode platform.

Capacity of V₂O₅ coated carbon electrodes .The maximum capacity that can be obtained from coating electrodes constructed out of carbon powder can be calculated using:

$$Q_{max} = \frac{Q_{carbon} m_{carbon} + Q_{V_2O_5} V_{V_2O_5} \rho_{V_2O_5}}{m_{carbon} + V_{V_2O_5} \rho_{V_2O_5}} \quad 4.3$$

where the maximum gravimetric capacity (Q_{max}) is a function of the electrochemical double layer capacity of the carbon (Q_{carbon}), the capacity of the pseudocapacitive V_2O_5 ($Q_{V_2O_5}$), and the volume of V_2O_5 that can be deposited in the carbon ($V_{V_2O_5}$), which is dependent on the pore volume and structure of the carbon. The gravimetric capacity is determined using the mass of carbon (m_{carbon}) and the density of V_2O_5 ($\rho_{V_2O_5}$). The experimental capacity (Q_{exp}), maximum capacity with no pore sealing, and maximum capacity with 13 Å critical diameter ($d_{critical}$) pore sealing of the 4 types of carbon evaluated at 2 mV/s are listed in Table 4.1. The micro-AC and meso-AC, did not show a large increase in capacity from the addition of V_2O_5 , achieving only 30-35% of the maximum capacity expected with $d_{critical} = 13$ Å. The macro-AC and macro-CB carbons, however, approach 62 and 83%, respectively, of their maximum calculated value. This indicates that V_2O_5 is being utilized to provide a large increase in capacity of the electrodes.

Table 4.1. The experimental and maximum capacities of the carbons studied when coated with V_2O_5 .^a

Carbon	micro-AC +150 Å V_2O_5	meso-AC +150 Å V_2O_5	macro-AC +150 Å V_2O_5	macro-CB +170 Å V_2O_5
Q_{exp} (C/g)	210	198	406	546
Q_{max} (C/g)	740	780	800	660
Q_{max} with $d_{critical} = 13$ Å (C/g)	610	660	670	650
$Q_{exp} / Q_{max}(d_{critical} = 13$ Å) (%)	35	30	61	84

^aThe experimental capacities were measured at 2 mV/s. The maximum capacities are based off the experimental capacities at 2 mV/s of uncoated carbon electrodes and V_2O_5 that was deposited directly on a stainless steel current collector.

Charge storage mechanisms in V_2O_5 coated carbon electrodes. While the electrodes exhibited a large increase in capacity when coated with V_2O_5 , the cyclic voltammogram traces in Figure 4.6 show that the shape changed significantly from the uncoated electrodes. The

macro-AC coated with V_2O_5 have a much less rectangular voltammogram than the uncoated electrode. The macro-CB, however, has very large redox peaks due to lithium intercalation. The change in shape of the voltammogram trace indicates the electrodes are losing their capacitive behavior and the charge storage is becoming battery-like.

The decrease in charge storage capacity of the V_2O_5 coated electrodes with increasing scan rate (Figure 4.7) indicates that the kinetics of charge storage includes an electrolyte diffusion limited process. The normalized capacity as a function of scan rate is shown in Figure 4.8 for the macro-AC and the macro-CB electrodes annealed at 300°C . The uncoated electrodes retain 60-70% of their capacity when the scan rate increases from 1 mV/s to 200 mV/s. The ALD coating generally improves charge capacity, but relative to the uncoated carbon, they show a more significant capacity loss with increased scan rate. Specifically, the macro-AC (Figure 4.8 (a)) with 68 or 150 Å of ALD V_2O_5 retains only ~10% of their original capacity when the scan rate is increased from 1 to 200 mV/s. For the macro-CB (Figure 4.8(b)), the samples with 43 Å of V_2O_5 show similar normalized capacity retention as uncoated macro-CB at scan rates up to 20 mV/s, but capacity drops at faster scan rates. Macro-CB +170 Å V_2O_5 performs similarly to the coated macro-AC with only a ~10% capacity retention at fast scan rates. As a control, we measured the capacity of V_2O_5 deposited by ALD directly on planar stainless steel foil and found that these samples also showed capacity loss with increasing scan rate. For example, a sample with 200 Å of V_2O_5 on stainless steel exhibited a 50% capacity retention as the scan rate increased from 1-200 mV/s, which is similar to the performance of other types of V_2O_5 annealed at 300°C .^{14,58} The decrease in charge storage capacity at high scan rates indicates that the capacitive and diffusion limited charge storage kinetics of V_2O_5 coated electrodes needs to be elucidated.

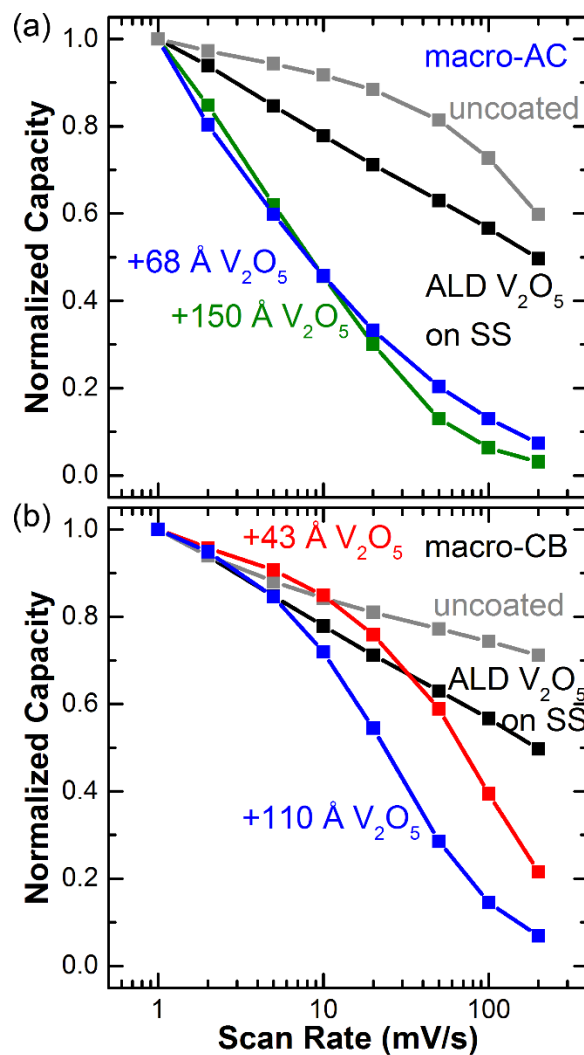


Figure 4.8. The normalized capacity of (a) macro-AC electrodes and (b) macro-CB electrodes with varying amounts of V₂O₅ deposited on them as a function of cyclic voltammetry scan rate. The normalized capacity of ALD V₂O₅ deposited directly on the stainless steel current collector is provided for comparison.

The capacitive contribution to the charge storage of an electrode can be quantitatively determined by analyzing the current response at a particular potential. A set of current vs. voltage data collected from cyclic voltammetry traces at various scan rates (ν) allows the current response to be separated into two components: i) a relatively fast capacitive component

that varies linearly with v ; and ii) a slower semi-infinite diffusion component that varies with $v^{1/2}$.^{11,14,59,60} Therefore the current (i) at a fixed potential (V) can be described as a combination of these two separate mechanisms:

$$i(V) = k_1(V) v + k_2(V) v^{1/2} \quad 4.4$$

where k_1 and k_2 are constants for a fixed potential. The constants were determined by linearizing the above equation, shifting the potentials so that the Li^+ intercalation occurs at constant potential for scan rates of 1-10 mV/s, and calculating the slope (k_1) and intercept (k_2) at discrete potentials over the entire sweep range of the cyclic voltammogram. As an example, the data in Figure 4.9(a) and (b) show results from macro-CB +43 Å V_2O_5 . Figure 9(a) shows the determination of k_1 and k_2 at 3 V. Figure 4.9(b) shows the experimental current response and the capacitive current from the k_1 fitting parameters scanned at 5 mV/s. Integrating the calculated capacitive current the macro-CB + 43 Å V_2O_5 gives a capacitive capacity of 235 C/g.

Using this approach, the capacitive capacity, which does not vary with scan rate, of each macro-CB sample coated with varying thicknesses of V_2O_5 ALD was determined, and the results are plotted as a function of V_2O_5 thickness in Figure 4.9(c). The uncoated macro-CB has a very small capacitive capacity, due to the low surface area of the base carbon. When macro-CB is coated with up to 110 Å of V_2O_5 in its macropores the capacity increases greatly due to the thin and capacitive V_2O_5 coating. When the V_2O_5 thickness on the macro-CB is increased to 170 Å, however, the V_2O_5 begins to exhibit diffusion limitations and the capacitive capacity decreases. Also shown in Figure 4.9(c) are results from the same analysis applied to the macro-AC coated with V_2O_5 ALD. The capacitive capacity of the macro-AC increases with increasing V_2O_5 thickness up to 150 Å of V_2O_5 . When the V_2O_5 thickness increases above 150 Å the capacitive capacity begins to decrease, which is consistent with electrolyte diffusion limitations being introduced by pore sealing during the ALD process and limiting the charge storage kinetics of the electrodes.

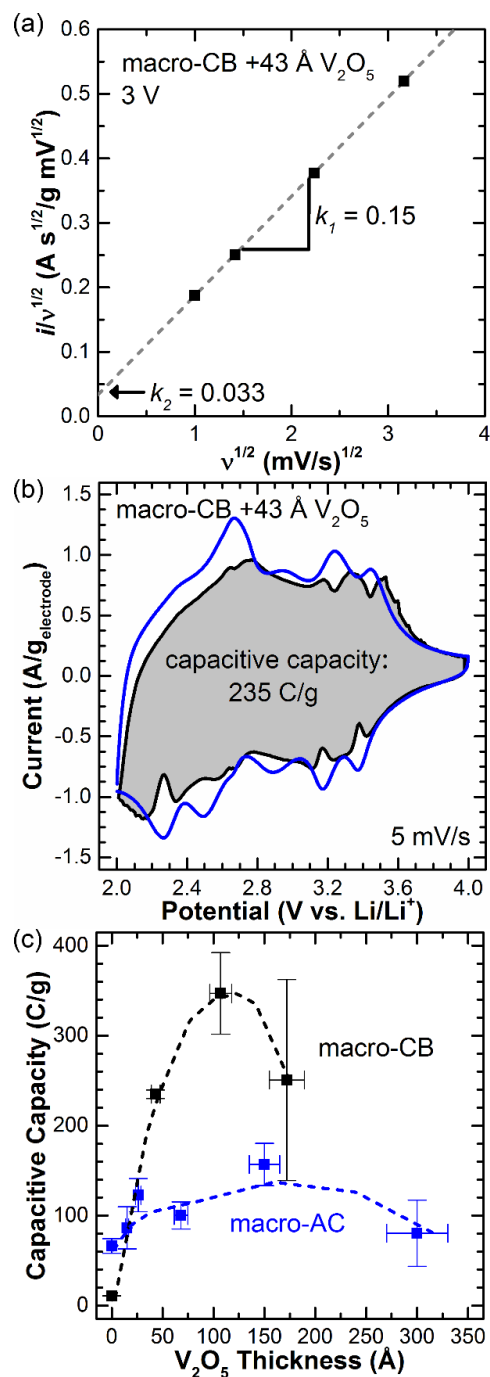


Figure 4.9. (a) Linearization of eqn. 4.4 for macro-CB +43 Å V₂O₅ at 3 V. (b) Cyclic voltammogram of macro-CB +43 Å V₂O₅ scanned at 5 mV/s, the current response calculated from eqn. 4.4, and the capacitive capacity of the electrode. (c) The capacitive capacity, which does not vary with scan rate, of the macro-CB and macro-AC electrodes as a function of V₂O₅ thickness.

4.6 Conclusions

By directly comparing four types of carbon powders with varying pore volumes, pore distributions and extent of pseudocapacitive ALD V_2O_5 coating, we find that small ($< 13 \text{ \AA}$) micropores become sealed, during the ALD process. This is due to intrinsic limitations of the molecular dimensions of the ALD reactants. Sealing of the pores decreased the accessible pore volume for V_2O_5 deposition by $> 50\%$, limiting the maximum achievable energy density for electrochemical capacitor electrodes constructed from activated carbon and coated with pseudocapacitive material.

Analysis of electrochemical charge storage showed that upon adding relatively thick layers ($\sim 150 \text{ \AA}$) of pseudocapacitive V_2O_5 , macroporous activated carbon (macro-AC) achieved a 144% increase in capacity, while the macroporous carbon black (macro-CB) has a 40-fold increase in capacity. This large increase, however, was accompanied by electrolyte diffusion limitations in the thick V_2O_5 that decreased the capacity of the electrodes at higher scan rates. This slower charge transport decreased the capacitive behavior and made the electrodes more battery-like, leading to an overall decrease in the electrode power density. Thin coatings of ALD V_2O_5 on the high surface area macroporous activated carbon enabled the electrodes to maintain better capacitive performance by minimizing diffusion limitations. Overall this work highlights the ability and inherent limitations of coating microporous materials using ALD, and provides insight into how starting pore structure affects the overall capability of carbon-based pseudocapacitor performance.

4.7 Acknowledgments

This material is based upon work supported by the Center for Dielectrics and Piezoelectrics I/UCRC under the National Science Foundation Grant Nos. IIP 1361571 and 1361503.

4.8 References

- (1) Yan, Y.; Li, B.; Guo, W.; Pang, H.; Xue, H. Vanadium Based Materials as Electrode Materials for High Performance Supercapacitors. *J. Power Sources* **2016**, *329*, 148–169.
- (2) Lokhande, V. C.; Lokhande, A. C.; Lokhande, C. D.; Kim, J. H.; Ji, T. Supercapacitive Composite Metal Oxide Electrodes Formed with Carbon, Metal Oxides and Conducting Polymers. *J. Alloys Compd.* **2016**.
- (3) Li, B.; Zheng, M.; Xue, H.; Pang, H. High Performance Electrochemical Capacitor Materials Focusing on Nickel Based Materials. *Inorg. Chem. Front.* **2016**, *3*, 175–202.
- (4) Béguin, F.; Presser, V.; Balducci, A.; Frackowiak, E. Carbons and Electrolytes for Advanced Supercapacitors. *Adv. Mater.* **2014**, *26*, 2219–2251, 2283.
- (5) Simon, P.; Gogotsi, Y. Materials for Electrochemical Capacitors. *Nat. Mater.* **2008**, *7*, 845–854.
- (6) Long, J. W.; Bélanger, D.; Brousse, T.; Sugimoto, W.; Sassin, M. B.; Crosnier, O. Asymmetric Electrochemical Capacitors—Stretching the Limits of Aqueous Electrolytes. *MRS Bull.* **2011**, *36*, 513–522.
- (7) Pandolfo, A. G.; Hollenkamp, A. F. Carbon Properties and Their Role in Supercapacitors. *J. Power Sources* **2006**, *157*, 11–27.
- (8) Gu, W.; Yushin, G. Review of Nanostructured Carbon Materials for Electrochemical Capacitor Applications: Advantages and Limitations of Activated Carbon, Carbide-Derived Carbon, Zeolite-Templated Carbon, Carbon Aerogels, Carbon Nanotubes, Onion-like Carbon, and Graphene. *WIREs Energy Env.* **2014**, *3*, 424–473.
- (9) Wen, L.; Zhou, M.; Wang, C.; Mi, Y.; Lei, Y. Nanoengineering Energy Conversion and Storage Devices via Atomic Layer Deposition. *Adv. Energy Mater.* **2016**, 1600468.
- (10) Wang, X.; Yushin, G. Chemical Vapor Deposition and Atomic Layer Deposition for Advanced Lithium Ion Batteries and Supercapacitors. *Energy Environ. Sci.* **2015**, *8*, 1889–1904.
- (11) Daubert, J. S.; Lewis, N. P.; Gotsch, H. N.; Mundy, J. Z.; Monroe, D. N.; Dickey, E. C.; Losego, M. D.; Parsons, G. N. Effect of Meso- and Micro-Porosity in Carbon Electrodes on Atomic Layer Deposition of Pseudocapacitive V₂O₅ for High Performance Supercapacitors. *Chem. Mater.* **2015**, *27*, 6524–6534.

- (12) Daubert, J. S.; Mundy, J. Z.; Parsons, G. N. Kevlar-Based Supercapacitor Fibers with Conformal Pseudocapacitive Metal Oxide and Metal Formed by ALD. *Adv. Mater. Interfaces* **2016**, *3*, 1600355.
- (13) Boukhalifa, S.; Evanoff, K.; Yushin, G. Atomic Layer Deposition of Vanadium Oxide on Carbon Nanotubes for High-Power Supercapacitor Electrodes. *Energy Environ. Sci.* **2012**, *5*, 6872–6879.
- (14) Rauda, I. E.; Augustyn, V.; Saldarriaga-Lopez, L. C.; Chen, X.; Schelhas, L. T.; Rubloff, G. W.; Dunn, B.; Tolbert, S. H. Nanostructured Pseudocapacitors Based on Atomic Layer Deposition of V_2O_5 onto Conductive Nanocrystal-Based Mesoporous ITO Scaffolds. *Adv. Funct. Mater.* **2014**, *24*, 6717–6728.
- (15) Fleischmann, S.; Jäckel, N.; Zeiger, M.; Krüner, B.; Grobelsek, I.; Formanek, P.; Choudhury, S.; Weingarth, D.; Presser, V. Enhanced Electrochemical Energy Storage by Nanoscopic Decoration of Endohedral and Exohedral Carbon with Vanadium Oxide via Atomic Layer Deposition. *Chem. Mater.* **2016**, *28*, 2802–2813.
- (16) Warren, R.; Sammoura, F.; Tounsi, F.; Sanghadasa, M.; Lin, L. Highly Active Ruthenium Oxide Coating via ALD and Electrochemical Activation in Supercapacitor Applications. *J. Mater. Chem. A* **2015**, *3*, 15568–15575.
- (17) Woo Kim, J.; Kim, B.; Won Park, S.; Kim, W.; Hyung Shim, J. Atomic Layer Deposition of Ruthenium on Plasma-Treated Vertically Aligned Carbon Nanotubes for High-Performance Ultracapacitors. *Nanotechnology* **2014**, *25*, 435404.
- (18) Yang, F.; Zhang, L.; Zuzuarregui, A.; Gregorczyk, K.; Li, L.; Beltrán, M.; Tollan, C.; Brede, J.; Rogero, C.; Chuvilin, A.; Knez, M. Functionalization of Defect Sites in Graphene with RuO_2 for High Capacitive Performance. *ACS Appl. Mater. Interfaces* **2015**, *7*, 20513–20519.
- (19) Gregorczyk, K. E.; Kozen, A. C.; Chen, X.; Schroeder, M. A.; Noked, M.; Cao, A.; Hu, L.; Rubloff, G. W. Fabrication of 3D Core–Shell Multiwalled Carbon Nanotube@ RuO_2 Lithium-Ion Battery Electrodes through a RuO_2 Atomic Layer Deposition Process. *ACS Nano* **2015**, *9*, 464–473.
- (20) Guan, C.; Liu, J.; Wang, Y.; Mao, L.; Fan, Z.; Shen, Z.; Zhang, H.; Wang, J. Iron Oxide-Decorated Carbon for Supercapacitor Anodes with Ultrahigh Energy Density and Outstanding Cycling Stability. *ACS Nano* **2015**, *9*, 5198–5207.
- (21) Chen, C.; Chen, C.; Huang, P.; Duan, F.; Zhao, S.; Li, P.; Fan, J.; Song, W.; Qin, Y. NiO/nanoporous Graphene Composites with Excellent Supercapacitive Performance Produced by Atomic Layer Deposition. *Nanotechnology* **2014**, *25*, 504001.

- (22) Guan, C.; Wang, Y.; Hu, Y.; Liu, J.; Ho, K. H.; Zhao, W.; Fan, Z.; Shen, Z.; Zhang, H.; Wang, J. Conformally Deposited NiO on a Hierarchical Carbon Support for High-Power and Durable Asymmetric Supercapacitors. *J. Mater. Chem. A* **2015**, *3*, 23283–23288.
- (23) Sun, X.; Xie, M.; Wang, G.; Sun, H.; Cavanagh, A. S.; Travis, J. J.; George, S. M.; Lian, J. Atomic Layer Deposition of TiO₂ on Graphene for Supercapacitors. *J. Electrochem. Soc.* **2012**, *159*, A364–A369.
- (24) Sun, X.; Xie, M.; Travis, J. J.; Wang, G.; Sun, H.; Lian, J.; George, S. M. Pseudocapacitance of Amorphous TiO₂ Thin Films Anchored to Graphene and Carbon Nanotubes Using Atomic Layer Deposition. *J. Phys. Chem. C* **2013**, *117*, 22497–22508.
- (25) Fisher, R. A.; Watt, M. R.; Konjeti, R.; Ready, W. J. Atomic Layer Deposition of Titanium Oxide for Pseudocapacitive Functionalization of Vertically-Aligned Carbon Nanotube Supercapacitor Electrodes. *ECS J. Solid State Sci. Technol.* **2014**, *4*, M1–M5.
- (26) Guan, C.; Qian, X.; Wang, X.; Cao, Y.; Zhang, Q.; Li, A.; Wang, J. Atomic Layer Deposition of Co₃O₄ on Carbon Nanotubes/carbon Cloth for High-Capacitance and Ultrastable Supercapacitor Electrode. *Nanotechnology* **2015**, *26*, 94001.
- (27) Gordon, R. G.; Hausmann, D.; Kim, E.; Shepard, J. A Kinetic Model for Step Coverage by Atomic Layer Deposition in Narrow Holes or Trenches. *Chem. Vap. Depos.* **2003**, *9*, 73–78.
- (28) Yanguas-Gil, A.; Elam, J. W. Self-Limited Reaction-Diffusion in Nanostructured Substrates: Surface Coverage Dynamics and Analytic Approximations to ALD Saturation Times. *Chem. Vap. Depos.* **2012**, *18*, 46–52.
- (29) Elam, J. W.; Routkevitch, D.; Mardilovich, P. P.; George, S. M. Conformal Coating on Ultrahigh-Aspect-Ratio Nanopores of Anodic Alumina by Atomic Layer Deposition. *Chem. Mater.* **2003**, *15*, 3507–3517.
- (30) Keuter, T.; Menzler, N. H.; Mauer, G.; Vondahlen, F.; Vaßen, R.; Buchkremer, H. P. Modeling Precursor Diffusion and Reaction of Atomic Layer Deposition in Porous Structures. *J. Vac. Sci. Technol. A Vacuum, Surfaces, Film.* **2015**, *33*, 01A104.
- (31) Fiorentino, G.; Vollebregt, S.; Tichelaar, F. D.; Ishihara, R.; Sarro, P. M. Impact of the Atomic Layer Deposition Precursors Diffusion on Solid-State Carbon Nanotube Based Supercapacitors Performances. *Nanotechnology* **2015**, *26*, 64002.

- (32) Poodt, P.; Mameli, A.; Schulpen, J.; Kessels, W. M. M. (Erwin); Roozeboom, F. Effect of Reactor Pressure on the Conformal Coating inside Porous Substrates by Atomic Layer Deposition. *J. Vac. Sci. Technol. A Vacuum, Surfaces, Film.* **2017**, *35*, 21502.
- (33) Knez, M.; Kadri, A.; Wege, C.; Gösele, U.; Jeske, H.; Nielsch, K. Atomic Layer Deposition on Biological Macromolecules: Metal Oxide Coating of Tobacco Mosaic Virus and Ferritin. *Nano Lett.* **2006**, *6*, 1172–1177.
- (34) Brousse, T.; Belanger, D.; Long, J. W. To Be or Not To Be Pseudocapacitive? *J. Electrochem. Soc.* **2015**, *162*, A5185–A5189.
- (35) Simon, P.; Gogotsi, Y.; Dunn, B. Where Do Batteries End and Supercapacitors Begin? *Science.* **2014**, *343*, 1210–1211.
- (36) Engstrom, A. M.; Doyle, F. M. Exploring the Cycle Behavior of Electrodeposited Vanadium Oxide Electrochemical Capacitor Electrodes in Various Aqueous Environments. *J. Power Sources* **2013**, *228*, 120–131.
- (37) Lao, Z. J.; Konstantinov, K.; Tournaire, Y.; Ng, S. H.; Wang, G. X.; Liu, H. K. Synthesis of Vanadium Pentoxide Powders with Enhanced Surface-Area for Electrochemical Capacitors. *J. Power Sources* **2006**, *162*, 1451–1454.
- (38) Warwick, M. E. A.; Roberts, A. J.; Slade, R. C. T.; Binions, R. Electric Field Assisted Chemical Vapour Deposition – a New Method for the Preparation of Highly Porous Supercapacitor Electrodes. *J. Mater. Chem. A* **2014**, *2*, 6115–6120.
- (39) Reddy, R. N.; Reddy, R. G. Porous Structured Vanadium Oxide Electrode Material for Electrochemical Capacitors. *J. Power Sources* **2006**, *156*, 700–704.
- (40) Dong, W. Electrochemical Properties of High Surface Area Vanadium Oxide Aerogels. *Electrochem. Solid-State Lett.* **2000**, *3*, 457–459.
- (41) Dong, W.; Sakamoto, J.; Dunn, B. Electrochemical Properties of Vanadium Oxide Aerogels and Aerogel Nanocomposites. *J. Sol-Gel Sci. Technol.* **2003**, *26*, 641–644.
- (42) Ghosh, A.; Ra, E. J.; Jin, M.; Jeong, H.-K. K.; Kim, T. H.; Biswas, C.; Lee, Y. H. High Pseudocapacitance from Ultrathin V₂O₅ Films Electrodeposited on Self-Standing Carbon-Nanofiber Paper. *Adv. Funct. Mater.* **2011**, *21*, 2541–2547.
- (43) Chen, Z.; Qin, Y.; Weng, D.; Xiao, Q.; Peng, Y.; Wang, X.; Li, H.; Wei, F.; Lu, Y. Design and Synthesis of Hierarchical Nanowire Composites for Electrochemical Energy Storage. *Adv. Funct. Mater.* **2009**, *19*, 3420–3426.

- (44) Huang, C.-M.; Hu, C.-C.; Chang, K.-H.; Li, J.-M.; Li, Y.-F. Pseudocapacitive Characteristics of Vanadium Oxide Deposits with a Three-Dimensional Porous Structure. *J. Electrochem. Soc.* **2009**, *156*, A667–A671.
- (45) Chen, Z.; Augustyn, V.; Wen, J.; Zhang, Y.; Shen, M.; Dunn, B.; Lu, Y. High-Performance Supercapacitors Based on Intertwined CNT/V₂O₅ Nanowire Nanocomposites. *Adv. Mater.* **2011**, *23*, 791–795.
- (46) Nagaraju, D. H.; Wang, Q.; Beaujuge, P.; Alshareef, H. N. Two-Dimensional Heterostructures of V₂O₅ and Reduced Graphene Oxide as Electrodes for High Energy Density Asymmetric Supercapacitors. *J. Mater. Chem. A* **2014**, *2*, 17146–17152.
- (47) Peer, M.; Qajar, A.; Rajagopalan, R.; Foley, H. C. Synthesis of Carbon with Bimodal Porosity by Simultaneous Polymerization of Furfuryl Alcohol and Phloroglucinol. *Microporous Mesoporous Mater.* **2014**, *196*, 235–242.
- (48) Badot, J. C.; Ribes, S.; Yousfi, E. B.; Vivier, V.; Pereira-Ramos, J. P.; Baffier, N.; Lincot, D. Atomic Layer Epitaxy of Vanadium Oxide Thin Films and Electrochemical Behavior in Presence of Lithium Ions. *Electrochem. Solid-State Lett.* **2000**, *3*, 485–488.
- (49) Wang, X. J.; Li, H. D.; Fei, Y. J.; Wang, X.; Xiong, Y. Y.; Nie, Y. X.; Feng, K. A. XRD and Raman Study of Vanadium Oxide Thin Films Deposited on Fused Silica Substrates by RF Magnetron Sputtering. *Appl. Surf. Sci.* **2001**, *177*, 8–14.
- (50) Gotić, M.; Popović, S.; Ivanda, M.; Musić, S. Sol–gel Synthesis and Characterization of V₂O₅ Powders. *Mater. Lett.* **2003**, *57*, 3186–3192.
- (51) Mendialdua, J.; Casanova, R.; Barbaux, Y. XPS Studies of V₂O₅, V₆O₁₃, VO₂ and V₂O₃. *J. Electron Spectros. Relat. Phenomena* **1995**, *71*, 249–261.
- (52) Chen, X.; Pomerantseva, E.; Gregorczyk, K.; Ghodssi, R.; Rubloff, G. Cathodic ALD V₂O₅ Thin Films for High-Rate Electrochemical Energy Storage. *RSC Adv.* **2013**, *3*, 4294–4302.
- (53) Julien, C.; Nazri, G. A.; Bergström, O. Raman Scattering Studies of Microcrystalline V₆O₁₃. *Phys. status solidi* **1997**, *201*, 319–326.
- (54) Abello, L.; Husson, E.; Repelin, Y.; Lucazeau, G. Vibrational Spectra and Valence Force Field of Crystalline V₂O₅. *Spectrochim. Acta Part A Mol. Spectrosc.* **1983**, *39*, 641–651.
- (55) Baddour-Hadjean, R.; Pereira-Ramos, J. P.; Navone, C.; Smirnov, M. Raman Microspectrometry Study of Electrochemical Lithium Intercalation into Sputtered Crystalline V₂O₅ Thin Films. *Chem. Mater.* **2008**, *20*, 1916–1923.

- (56) Cocciantelli, J. M.; Doumerc, J. P.; Pouchard, M.; Broussely, M.; Labat, J. Crystal Chemistry of Electrochemically Inserted $\text{Li}_x\text{V}_2\text{O}_5$. *J. Power Sources* **1991**, *34*, 103–111.
- (57) Delmas, C.; Cognacouradou, H.; Cocciantelli, J.; Menetrier, M.; Doumerc, J. The $\text{Li}_x\text{V}_2\text{O}_5$ System: An Overview of the Structure Modifications Induced by the Lithium Intercalation. *Solid State Ionics* **1994**, *69*, 257–264.
- (58) Jeyalakshmi, K.; Vijayakumar, S.; Purushothaman, K. K.; Muralidharan, G. Nanostructured Nickel Doped $\beta\text{-V}_2\text{O}_5$ Thin Films for Supercapacitor Applications. *Mater. Res. Bull.* **2013**, *48*, 2578–2582.
- (59) Liu, T. C.; Pell, W. G.; Conway, B. E.; Roberson, S. L. Behavior of Molybdenum Nitrides as Materials for Electrochemical Capacitors Comparison with Ruthenium Oxide. *J. Electrochem. Soc.* **1998**, *145*, 1882–1888.
- (60) Wang, J.; Polleux, J.; Lim, J.; Dunn, B. Pseudocapacitive Contributions to Electrochemical Energy Storage in TiO_2 (Anatase) Nanoparticles. *J. Phys. Chem. C* **2007**, *111*, 14925–14931.

CHAPTER 5. Kevlar®-Based Supercapacitor Fibers with Conformal Pseudocapacitive Metal Oxide and Metal formed by ALD

This chapter is based on a manuscript published as:

Daubert, J. S.; Mundy, J. Z.; Parsons, G. N. Kevlar-Based Supercapacitor Fibers with Conformal Pseudocapacitive Metal Oxide and Metal Formed by ALD. *Adv. Mater. Interfaces* **2016**, *3*, 1600355.

5.1 Abstract

Kevlar®, poly(p-phenylene terephthalamide) (PPTA), yarns were modified for use as flexible supercapacitor electrodes by coating them with a nanometer-scale film of conductive platinum metal and pseudocapacitive V_2O_5 using atomic layer deposition (ALD). The PPTA yarns were incorporated into a solid state supercapacitor through the use of a polyvinyl alcohol/lithium chloride gel electrolyte. Pseudocapacitive V_2O_5 films 11 nm thick provided up to a 5x increase in areal capacitance (18.4 mF cm^{-2}) over the Pt-only coated PPTA. Thicker films of V_2O_5 and wrapping the electrodes together into a single yarn resulted in decreased areal capacitance due to charge-transfer limitations. The work describes how ALD metal and metal oxide can be combined to add double layer and pseudocapacitive charge storage to mechanically robust PPTA creating unique multifunctional electronic fabric device systems.

5.2 Introduction

The development of flexible/stretchable electronics or “smart textiles” has spurred interest in developing flexible supercapacitors that are capable of powering the electronics and can be used in the same form factor.¹⁻³ Flexible supercapacitors can be classified as either electrochemical double layer capacitors (EDLCs) that store charge in a Helmholtz double layer, or pseudocapacitors that make use of reversible Faradaic surface redox reactions (i.e. pseudocapacitance). In order to achieve widespread adoption to power smart textiles, devices must have high areal capacitance, incorporate a robust current collector that maintains performance under repeated stress, be solid state to avoid the limitations of liquid electrolytes, and be formed from known fiber materials to simplify fabrication.

The efforts to produce flexible supercapacitors can be categorized by the type of current collectors used: flexible metal cores, carbon-based fibers, or the modification of traditional textile fibers or yarns. Within yarns, charge storage layers can be built into each fiber or be added to the external yarn surface after spinning. Table 5.1 presents recently published representative results for three types of fiber-based capacitors. Capacitance values are typically normalized by the lateral electrode area, i.e. the external cylindrical surface area of the fiber or

yarn structure. It is important to note, however, that the normalized capacitance will often depend on the yarn construction, i.e. fiber density, diameter and number of fibers in the yarn, and capacitive contribution from each fiber, making direct comparison difficult. Similar problems arise when normalizing by fiber volume, length or geometric area (i.e. the exposed size of a fabric “patch”).⁴⁻⁶ Comparisons based on mass or specific surface area are difficult, because active mass fraction is small and the specific surface area is difficult to quantify.

Table 5.1. Reported areal capacitance for various fiber-based supercapacitors.

Type of Fiber Substrate	Fiber Material	Conductive Component	Pseudo-capacitive Material	Fiber Surface Area Enhancement	Electrolyte	Capacitance per lateral surface area [mF cm ⁻²]	Reference
Metal Wire	Stainless Steel	Steel wire	MnO ₂	rGO	PVA-H ₃ PO ₄	411	Huang et al. ⁵
	Carbon Cloth	Carbon	ALD Co ₃ O ₄	CNT	H ₂ O-KOH	66 ^{a)}	Guan et al. ⁴
Carbon	rGO + Modified Cellulose	rGO	–	rGO/CNT	PVA-H ₃ PO ₄	177	Kou et al. ⁶
	Cotton Thread	CNT + Polypyrrole	MnO ₂	Nanostructured MnO ₂	PVA-H ₃ PO ₄	1490	Liu et al. ⁷
Common Textile	PPTA Fiber	Au	ZnO	Nanostructured ZnO	PVA-H ₃ PO ₄	2.4	Bae et al. ⁸
	PPTA Yarn	ALD Pt	ALD V ₂ O ₅	–	PVA-LiCl	18.4	this work

a) Reported as 416 mF per geometric cm², comprised of yarns with 0.1 cm² lateral surface area each

Table 5.1 shows reported capacitance per lateral fiber surface area for various fiber-based capacitors. For one case, the value for mF cm⁻² was estimated from the reported capacitance per geometric area and the given fiber size.⁴ To boost the capacitance per unit lateral area, researchers work to create fibers containing high surface area components⁶ or with high surface area nanostructured finishes,^{4,5,7,8} where the electrochemically active surface area can significantly exceed the lateral surface area. This point is reflected in the table values, where fibers with enhanced specific surface area show larger charge storage capacity compared to

cylindrical as-spun PPTA fibers reported here. Even with the smaller charge storage capacity, the use of as-prepared fibers may simplify capacitor fabrication and broaden options for capacitor integration.

Reports show that stainless steel,^{5,9-11} gold,¹² titanium,¹³ or platinum¹⁴ wire metal cores can be coated with various forms of carbon^{9,12} to form electrochemical double layer capacitors, or with pseudocapacitive TiO₂ nanotubes,¹³ polyaniline (PANI),^{10,14} Fe₂O₃,¹¹ and MnO₂⁵ to create supercapacitors. Many flexible supercapacitors utilize gel electrolytes formed by mixing polyvinyl alcohol (PVA) with ionic materials such as H₃PO₄,^{5,6,8,9,11-24} H₂SO₄,²⁵⁻²⁷ KOH,²⁸⁻³⁰ or LiCl.³¹⁻³³

Carbon-based fibers or cloth are often treated to increase the available specific surface area and increase conductivity as the basis for increasing the double-layer capacitance.^{6,16,17,20,25,34,35} Wet-spun rGO/CNT yarns have exhibited an areal capacitance of up to 177 mF cm⁻².⁶ Conductive polymers are also incorporated into the carbon materials to add pseudocapacitance.^{15,18,23,26,27} Researchers also study pseudocapacitive metal oxides including Co₃O₄,^{4,19} RuO₂,²⁹ and MnO₂,^{21,22,28,31,32,36} added to carbon-based fibers. The metal oxides are often incorporated into the fibers using liquid phase processes (i.e. electrodeposition, hydrothermal/solvothermal, sol-gel, spray deposition, or electroless),³⁷ but vapor phase processes (i.e. atomic layer deposition, ALD) can also be used to address issues of interfacial and surface chemistry at nanometer scale.³⁸ Under well-controlled conditions, the ALD process has the advantage of enabling conformal coating onto high surface area mesoporous carbon.³⁹ Using ALD Co₃O₄, carbon cloth modified with carbon nanotubes has produced estimated charge storage density of 66 mF cm⁻² on the carbon cloth when tested in a basic electrolyte.⁴ While flexible supercapacitors with carbon cores are able to provide high areal capacitance, the carbon fibers have not been commercialized for use in textiles.

Textile substrates are interesting for ALD because of its ability to coat the high aspect ratio materials at low processing temperatures.^{40,41} ALD has been used to make textiles, such as nonwoven nylon and polypropylene, conductive through the deposition of ZnO, tungsten, or

platinum.⁴²⁻⁴⁵ Several ALD materials have been studied for supercapacitors including V_2O_5 ,^{39,46,47} RuO_2 ,⁴⁸⁻⁵¹ Fe_2O_3 ,⁵² NiO ,^{53,54} TiO_2 ,⁵⁵⁻⁵⁷ and Co_3O_4 .⁴ In particular, V_2O_5 is of interest due to its higher theoretical pseudocapacitance than RuO_2 and has demonstrated capacitances of up to $1550 \text{ F g-V}_2\text{O}_5^{-1}$ when deposited on CNTs.⁴⁶ Most of the work involving pseudocapacitive materials via ALD has been performed on CNTs and graphene, but V_2O_5 has also been deposited on high surface area activated carbon for a 46% increase in capacitance.³⁹

A few researchers have explored capacitors formed directly on traditional textile fabrics, including cotton, lycra,⁵⁸ or Kevlar®. This approach offers unique opportunity to couple supercapacitor fabrication methodology with textile manufacturing. Double-layer capacitors have been formed by interweaving cotton with steel wires,⁵⁹ and cotton-based pseudocapacitors can be formed by the addition of active NiO and reduced graphene oxide.³³ An areal capacitance of 1490 mF cm^{-2} was reported for 0.3 mm thick cotton threads that were coated with high surface area CNTs, pseudocapacitive MnO_2 nanostructures, and polypyrrole.⁷

Kevlar®, or poly(p-phenylene terephthalamide) (PPTA), is particularly interesting because of its use in ballistic protection.^{60,61} Charge storage capacity has been added to PPTA fabrics by dip-coating the fabric in carbon nanotube ink,²⁴ and by sputter-coating with gold followed by hydrothermal growth of ZnO . The highest reported areal capacitance for PPTA based supercapacitors of 2.4 mF cm^{-2} was achieved using ZnO structures on PPTA fibers wound with Au-coated plastic wire.⁸ While ALD has previously been studied on PPTA,⁶² no previous reports show integration of pseudocapacitive ALD materials on PPTA textiles.

In this work, we report an integrated conductor/pseudocapacitor (Pt/V_2O_5) ALD approach to form PPTA-based supercapacitors using a solid PVA-LiCl gel electrolyte. We find capacitance values as high as 18.4 mF cm^{-2} for PPTA fiber-based capacitor devices without requiring significant surface area enhancement, while maintaining significant tensile strength of the starting PPTA material.

5.3 Experimental Section

Fiber materials: The base materials used for capacitor fabrication were PPTA yarns approximately 20 cm in length, extracted from a woven PPTA fabric. Each yarn consisted of 567 individual monofilament fibers with a diameter of 13 μm and a density of 1.44 g cm^{-3} . The PPTA textile (Style 1023, Barrday Inc.) was composed of 850 denier Kevlar® KM-2 yarns plain woven at 31 x 31 yarns per inch. The fabric was provided with spin finishes removed, and used as received.

ALD Coating: To form PPTA supercapacitors, PPTA yarn is first coated with a nanoscale thick layer of conductive metal using ALD to act as a current collector. For metal and metal oxide coating, the PPTA yarns were laid out straight on a flat metal sample holder with aluminum foil covering 1 cm of the ends of the PPTA, which kept them in place during the ALD process. ALD was performed in a custom-built viscous flow-tube ALD reactor. The reactant carrier and purge gas was ultrahigh-purity nitrogen (99.999%, Arc3) that was further purified using a Gatekeeper inert gas purifier (rated to <100 parts per trillion H_2O and O_2 , Entegris) before flowing into the reactor. The reactor consisted of a stainless steel tube 10 cm in diameter connected to gas inlet and pumping ports by conflat flanges. A resistively heated jacket surrounding the system was used to achieve the desired temperature. A controlled temperature gradient was maintained along the entire gas flow path to prevent precursor condensation. The working pressure in the reactor during gas purge cycles was 1 Torr.

Aluminum oxide (alumina, Al_2O_3) was deposited using ALD at 200 $^\circ\text{C}$ using trimethylaluminum (TMA) (98%, Strem Chemicals) and water (reagent grade, Ricco Chemical) as the co-reactants. A typical dosing scheme for the Al_2O_3 deposition was 0.5/30/0.5/30 s (TMA dose/ N_2 purge/ H_2O dose/ N_2 purge) for 25 cycles, resulting in a 3 nm thick film as measured on monitor silicon wafers using spectroscopic ellipsometry. Immediately following Al_2O_3 seed layer deposition, without breaking vacuum, platinum ALD was performed.

Pt films were deposited on the PPTA at 200 °C with 150 cycles of (methylcyclopentadienyl)trimethyl platinum (MeCpPtMe_3) (99%, Strem Chemicals) and ozone (O_3 , 11 wt. % in oxygen, generated by research-grade oxygen (99.999%, Arc3) flowing through an MKS Astex-AX8856 ozone generator) as co-reactants.⁴² MeCpPtMe_3 was contained in a stainless steel cylinder heated to approximately 60 °C. To promote flow of the low vapor pressure MeCpPtMe_3 into the reactor, before each dose, the pressure in the precursor vessel was reduced to ~250 mTorr by closing the N_2 carrier flow. The ALD chamber volume was then isolated from the vacuum pump and the MeCpPtMe_3 dosing valve was opened. After 8 s, the N_2 carrier flowed through the precursor line for 0.5 s, allowing the reactor pressure to increase to approximately 7 Torr. To promote reactant exposure for both MeCpPtMe_3 and O_3 , the reactor was sealed for a 5 s “hold” step to allow static vapor dosing and promote reactant diffusion into the PPTA yarn bulk. Thus, a typical ALD cycle scheme was pump down/ MeCpPtMe_3 dose (hold)/ N_2 purge/ O_3 dose (hold)/ N_2 purge with a timing of 15/8(5)/30/8(5)/30 s, respectively. Pt films were found to have a steady state growth of ~0.7 Å cycle⁻¹ at 200 °C as measured on silicon via x-ray reflectivity (XRR); thus, 150 cycles resulted in a 10 nm thick film. After the Pt deposition the PPTA yarns were taken out of the reactor and the aluminum foil removed. The ends of the PPTA yarns were then rewrapped with aluminum foil to cover 1 cm of the Pt coating from deposition of V_2O_5 for use as an electrical contact, and returned to the reactor.

The V_2O_5 ALD process was conducted at 150 °C using vanadium triisopropoxide (VTIP) (96%, Alfa Aesar, kept at 45 °C with a vapor pressure of ~0.29 Torr)⁶³ and H_2O as co-reactants.³⁹ A typical V_2O_5 ALD cycle consisted of dosing VTIP by bubbling N_2 carrier gas through the VTIP to volatilize and deliver it to the reactor, followed by sealing the reactor to “hold” the reactor and allow the precursors to diffuse through the PPTA yarn, before purging with nitrogen, dosing of water, “holding” the reactor to allow the water precursor to diffuse, and then purging with nitrogen before the next VTIP dose for the subsequent cycle. One ALD cycle (VTIP dose (hold)/ N_2 purge/ H_2O dose (hold)/ N_2 purge) has a timing interval of 64(60)/60/0.5(60)/60 s, and the number of cycles was varied between 100 and 500 depending

on the desired thickness of the V_2O_5 coating. The ALD growth rate of V_2O_5 on silicon wafers was determined to be $\sim 0.6 \text{ \AA cycle}^{-1}$.

Spectroscopic ellipsometry to measure the thickness of the Al_2O_3 and V_2O_5 films was conducted with a J.A. Woollam Co. alpha-SE using the CompleteEASE data analysis software package. A native SiO_2 layer of 20 \AA , as measured for each wafer, was also included in the optical model. Pt-ALD film thickness data were obtained via XRR using a Rigaku SmartLab diffractometer equipped with a $Cu \text{ K}\alpha$ source. XRR data were modeled using the Panalytical X'pert Reflectivity software package.

PPTA Characterization: The electrical properties of the PPTA were measured using a four probe device described previously.^{42,64} For each measurement, one PPTA yarn was twisted lengthwise 10 times to promote good contact between individual fibers. Scanning electron microscope (SEM) images were taken with a FEI Verios 460L.

The tensile strength of PPTA yarns was measured using an MTS Q-Test/5 Universal Testing Machine equipped with a 1000 lb load cell. Per ASTM D7269-08, pneumatic bollard-type clamps were used with 60 psi to prevent yarn slippage. A gauge length of 10 inches was used with a crosshead speed of 5 in per min. A U.S. Testing Twist Tester was used to insert 3 twist per in into each yarn.

Capacitor Fabrication and Characterization: The supercapacitors were tested in either an aqueous electrolyte (1 M potassium chloride (KCl, Acros)) or a gel electrolyte (PVA-LiCl). The PVA-LiCl gel electrolyte was prepared by dissolving 4 g of PVA (95% MW 95000, Acros) powder in 40 mL of distilled water at $\sim 95 \text{ }^\circ\text{C}$ with stirring. After the PVA was completely dissolved, 8.5 g of LiCl (99%, Acros) was slowly added into the PVA solution under vigorous stirring until it formed a homogeneous sticky solution. The solution was cooled at room temperature, and the solution became a clear and transparent gel. LiCl was used instead of H_3PO_4 , because V_2O_5 is known to dissolve in acidic conditions.

The PPTA electrodes were tested in both a 3-electrode and a symmetric capacitor configuration. The 3-electrode measurements were done in a H₂O-KCl electrolyte with single PPTA yarn, a platinum counter electrode, and a Ag/AgCl reference electrode. The symmetric capacitor measurements were completed without a reference electrode in either a dish filled with PVA-LiCl gel electrolyte into which the two PPTA yarns were submersed and separated by a porous separator, or with two PPTA yarns that had been dipped in PVA-LiCl gel electrolyte and wrapped together by hand to form a single yarn. The PPTA yarns were dried at 100 °C for 6 h after being covered in the PVA-LiCl electrolyte.

The supercapacitors were attached to a BioLogic VMP3 potentiostat with clips on the Pt coated ends of the electrodes for the electrochemical measurements. Cyclic voltammograms were collected at scan rates between 1 mV s⁻¹ and 200 mV s⁻¹ between -0.1 and 0.5 V vs. Ag/AgCl for the 3-electrode H₂O-KCl configuration, and 0 and 0.8 V for the symmetric PVA-LiCl configurations. In the symmetric configuration, the parallel electrodes ($C_{\text{electrode}}$) are considered to contribute equally to the measured cell capacitance (C_{cell}). The electrode capacitance is then given as

$$C_{\text{electrode}} = 2 C_{\text{cell}} = \frac{2}{\frac{dv}{dt} A (V_{\text{high}} - V_{\text{low}})} \frac{1}{2} \left\{ \int_{V_{\text{low}}}^{V_{\text{high}}} I(V) dV - \int_{V_{\text{high}}}^{V_{\text{low}}} I(V) dV \right\} \quad 5.1$$

where dv/dt is the scan rate, A is the area of each electrode in a symmetric cell, V_{high} and V_{low} are the limits of the sweep, and $I(V)$ is the total current. Electrochemical impedance spectroscopy (EIS) data was measured at the open circuit DC potential with a 10 mV amplitude AC from 100 kHz to 100 mHz.

5.4 Results

Figure 5.1 depicts the approach used here to produce PPTA based supercapacitors. The starting material was commercially available PPT A yarn consisting of 567 individual PPTA fibers, each 13 μm in diameter. The first step involved coating these yarns with conductive Pt by ALD.

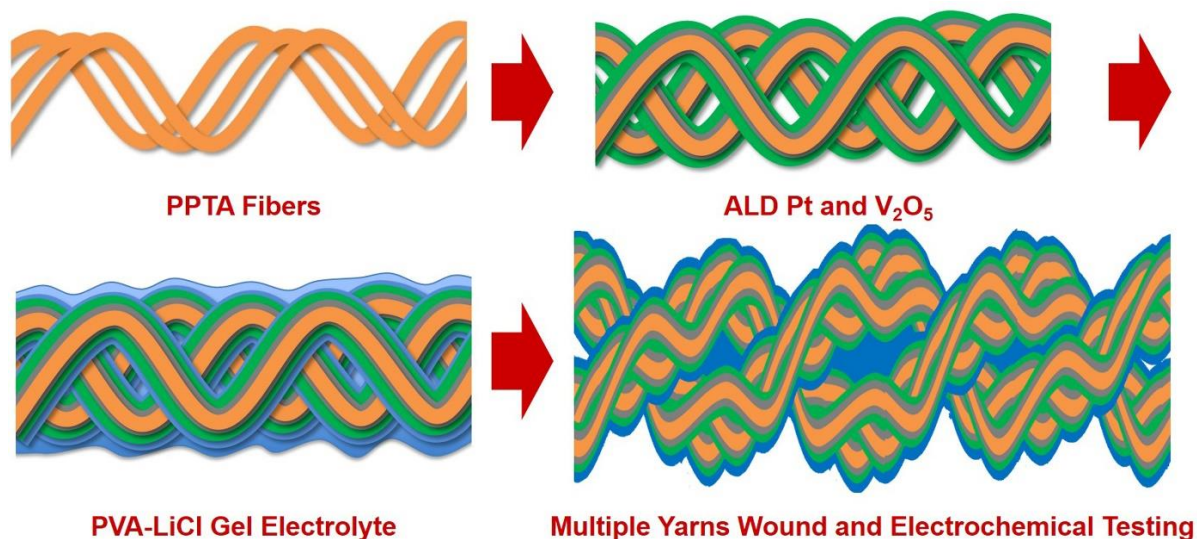


Figure 5.1. Schematic of PPTA supercapacitor construction and testing.

Initial tests of 150 cycles of Pt-ALD on neat PPTA produced no visible Pt film nucleation on the fiber, consistent with the measured negligible conductivity. Subsequently, we explored 3 nm ALD Al₂O₃ seed layers deposited on the PPTA to promote Pt nucleation on the PPTA fiber, similar to what had been previously investigated on nylon mats.⁴² The conductivity of the PPTA coated with a 3 nm Al₂O₃ seed layer and a 10 nm Pt film was 23,500 S cm⁻¹, indicating a coalesced Pt film had been achieved on the surface of the fibers. The pseudocapacitive V₂O₅ ALD films were then deposited on the coalesced Pt film. The combined Pt/V₂O₅ film increased the mass of the PPTA by less than 5%.

Scanning Electron Microscope images of 13 μm diameter PPTA fibers coated with ALD Pt and combined ALD Pt/V₂O₅ are shown in Figure 5.2a and 2b, respectively. Because of the conductive Pt, no additional metal coating was required for SEM imaging. The fiber surface shows a relatively smooth texture after both the Pt and V₂O₅ ALD coating. The knotted fibers show only limited evidence for peeling or delamination, demonstrating good coating flexibility and robustness. The arrows in Figure 5.2a and Figure 5.2b indicate features assigned to some shear-related cracking of the Pt or the V₂O₅ over-coating, respectively.

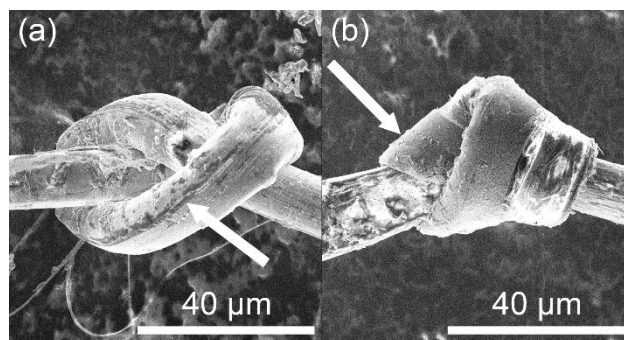


Figure 5.2. SEM image of individual PPTA fibers after coating with (a) ALD Pt; and (b) combined ALD Pt/V₂O₅. Fibers were knotted after ALD coating. Arrows indicate some evidence for minor sheer-related cracking of the ALD Pt and V₂O₅ in panels a and b, respectively.

The tensile strength of the Pt coated PPTA and combined Pt/V₂O₅ coated PPTA yarns are shown in Figure 5.3. The Pt coating with the Al₂O₃ seed layer resulted in a 24% decrease in the tensile strength, but the tensile strength was not further affected by the addition of the V₂O₅ coating, and overall the PPTA remains quite strong when compared to other textile materials. Similar decreases in tensile strength have been reported for Al₂O₃ coatings on PPTA.⁶²

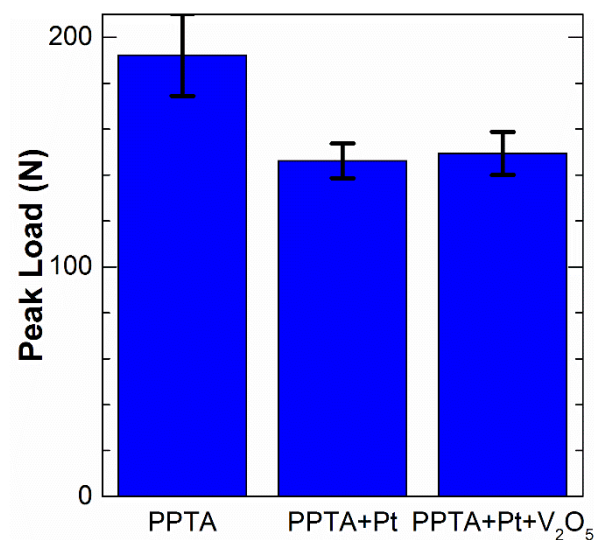


Figure 5.3. Tensile strength of PPTA, PPTA coated with Pt, and PPTA coated with Pt and V₂O₅.

After coating by ALD Pt, the fibers were then coated with ALD V₂O₅, then covered with PVA-LiCl gel electrolyte as described in the experimental section. The PPTA-based supercapacitors were tested in three configurations (Figure 5.4) to determine the performance. Specifically, they were tested in a three electrode configuration as a single yarn in aqueous electrolyte, or in a two electrode measurement as a pair of yarns in gel electrolyte. For some tests, two PPTA yarn electrodes are wound together to form two symmetric electrodes of a flexible supercapacitor, then analyzed in a two electrode structure while suspended in air. The capacitance values from the cyclic voltammetry scans at 2 mV s⁻¹ of PPTA electrodes coated with varying thickness ALD V₂O₅ coatings measured in each testing configuration are summarized in Table 5.2.

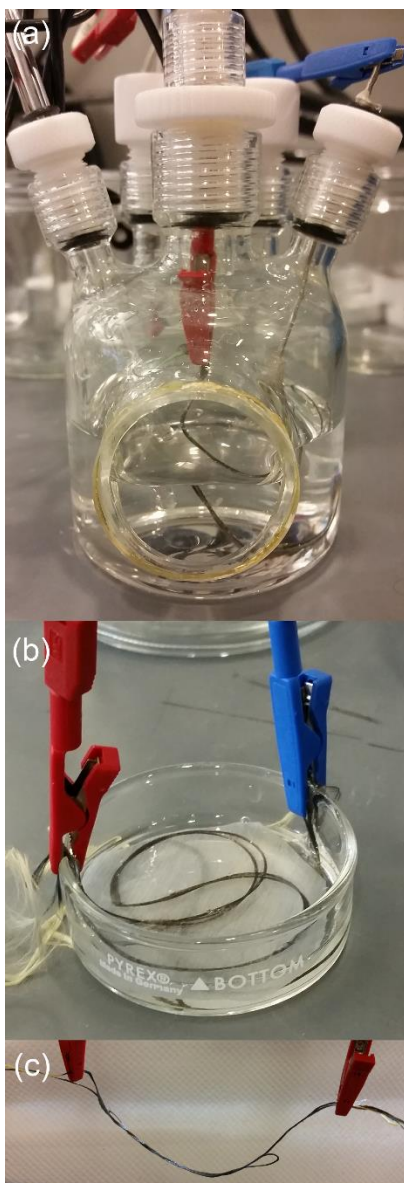


Figure 5.4. PPTA based supercapacitors were tested in (a) a single yarn in a 3-electrode configuration with a H₂O-KCl electrolyte; (b) a two-electrode configuration with two yarns in a PVA-LiCl gel electrolyte and a separator; and (c) a twisted pair of PPTA/Pt/V₂O₅ yarns coated with PVA-LiCl.

Table 5.2. Areal capacitance of varying thickness V_2O_5 films on PPTA electrodes at 2 mV s^{-1} .

V_2O_5 Thickness [nm]	Areal Capacitance [mF cm^{-2}]		
	$H_2O\text{-KCl}$	PVA-LiCl	Twisted yarn pair PVA-LiCl
0	2.7	3.7	-
7	-	-	0.6
11	3.8	18.4	3.1
15	-	-	3.6
24	-	12.4	-
38	-	7.4	4.7

The cyclic voltammetry scans of the supercapacitors at 2 mV s^{-1} in the 3-electrode $H_2O\text{-KCl}$ electrolyte are shown in Figure 5.5a. The Pt-coated PPTA exhibited a small capacitance, which is ascribed to an electrochemical double layer on the surface of the Pt. The PPTA that was then coated with V_2O_5 had a 41% increase over the Pt-coated PPTA.

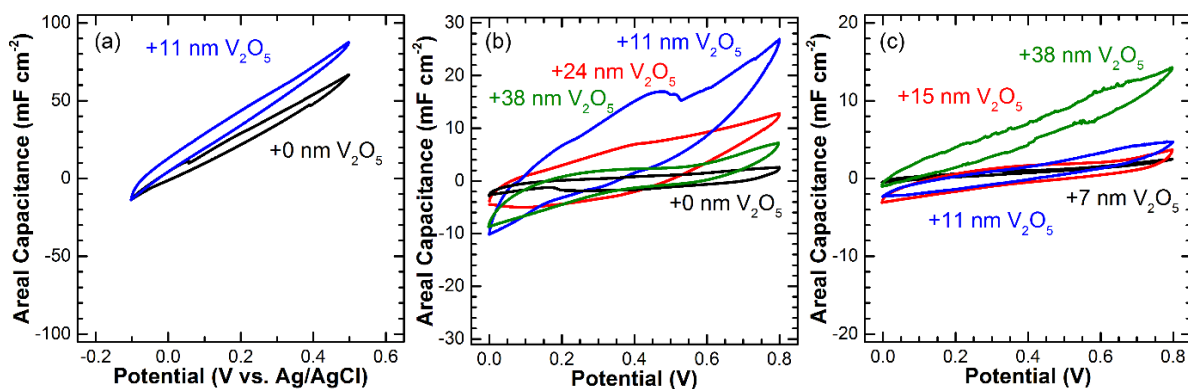


Figure 5.5. Cyclic voltammetry scans of V_2O_5 /Pt/PPTA supercapacitor yarns at 2 mV s^{-1} in (a) $H_2O\text{-KCl}$; and (b) PVA-LiCl. Panel (c) shows results for a twisted pair of PPTA/Pt/ V_2O_5 yarns in PVA-LiCl.

Figure 5.5b shows the cyclic voltammetry scans of PPTA supercapacitors tested in a PVA-LiCl electrolyte at 2 mV s^{-1} . The Pt-coated PPTA exhibited similar areal capacitance in the PVA-LiCl electrolyte as it did in the $H_2O\text{-KCl}$ electrolyte. PPTA coated with 11 nm of V_2O_5

had a capacitance of 18.4 mF cm^{-2} , which is a large increase over the V_2O_5 -coated PPTA tested in the $\text{H}_2\text{O-KCl}$ electrolyte, and a 5x increase in capacitance over the Pt-coated PPTA. PPTA that was then coated with 24 nm of V_2O_5 displayed a reduced capacitance when compared to the PPTA coated with 11 nm V_2O_5 , but still 3.3x more than the Pt-only coated PPTA. Finally PPTA that was coated with 38 nm of V_2O_5 had a still lower areal capacitance, but remains 2x the Pt coated PPTA.

The results of the cyclic voltammetry scans of the PPTA supercapacitors that were coated with PVA-LiCl and wound into a yarn are shown in Figure 5.5c. The PPTA only coated with Pt experienced shorting and did not exhibit a measureable capacitance when tested as a yarn. PPTA coated with 7 nm V_2O_5 eliminated the shorting, but exhibited only a small capacitance. PPTA coated with 11 nm V_2O_5 exhibited a large increase in capacitance, but the capacitance was lower than the PPTA that had been coated with the 11 nm of V_2O_5 and tested in PVA-LiCl. PPTA that was coated with 15 nm of V_2O_5 experienced a small increase in capacitance. PPTA that was then coated with 38 nm of V_2O_5 exhibited a higher areal capacitance than 15 nm V_2O_5 wound into a yarn, but lower capacitance than PPTA coated with 38 nm of V_2O_5 that was tested in PVA-LiCl.

All of the PPTA electrodes were tested at varying cyclic voltammetry scan rates from 1 to 200 mV s^{-1} , and the results are shown in Figure 5.6. The PPTA supercapacitors exhibited the largest capacitance at a 1 mV s^{-1} scan rate. The areal capacitance dropped with increasing scan rates. The PPTA coated with 11 nm of V_2O_5 and tested in PVA-LiCl experienced a 75% decrease in capacitance from 2 mV s^{-1} to 20 mV s^{-1} (Figure 5.6b). The PPTA with 38 nm of V_2O_5 coated with PVA-LiCl and wound into a yarn also experienced a 79% decrease in capacitance from 2 mV s^{-1} to 20 mV s^{-1} (Figure 5.6c). The supercapacitors maintained the same order of areal capacitance at both low and high scan rates as they did at 2 mV s^{-1} with V_2O_5 -coated PPTA performing better than Pt-only coated PPTA. The Pt-coated PPTA wound into a yarn (Figure 5.6c) exhibited shorting.

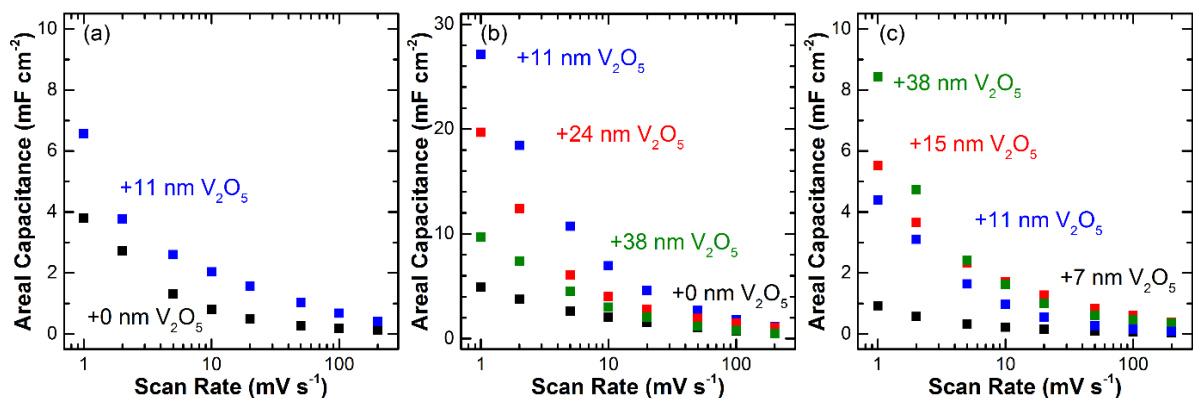


Figure 5.6. A summary of the areal capacitance as a function of cyclic voltammetry scan rate in (a) H₂O-KCl, (b) PVA-LiCl. Panel (c) shows results for a twisted pair of PPTA/Pt/V₂O₅ yarns in PVA-LiCl.

The PPTA coated with 11 nm of V₂O₅ was tested using electrochemical impedance spectroscopy (EIS) in each electrolyte configuration (Figure 5.7). The Nyquist plot of the PPTA tested in either the H₂O-KCl or PVA-LiCl shows the typical shape of a supercapacitor. There is a hump at low impedance from high frequency measurements related to charge-transfer resistance and double-layer capacitance, and a high impedance tail at low frequencies linked to charge storage in surface electrochemical reactions. The PPTA wrapped into a yarn, however, shows a very large impedance with no defined hump indicating different charge transfer behavior.

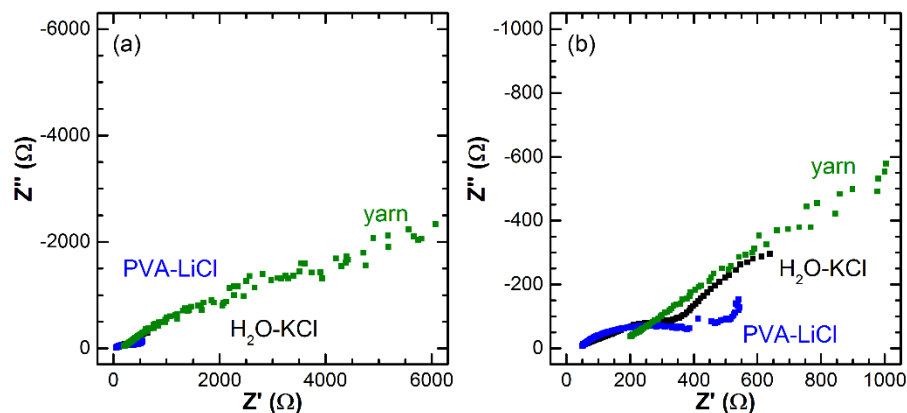


Figure 5.7. Nyquist plots of (a) PPTA coated with 11 nm of V_2O_5 , and (b) zoomed in view of the same data.

5.5 Discussion

Results presented here show that ALD metals and pseudocapacitive layers can be integrated into textiles to produce PPTA-based supercapacitors. The use of a 10 nm thick Pt ALD film on the PPTA yarns proved to be an effective current collector, because it made the PPTA highly conductive while maintaining the PPTA fiber size, mass, and tensile strength. The addition of a pseudocapacitive V_2O_5 ALD film on the Pt-coated PPTA yarns made them highly capacitive without significantly increasing yarn mass.

We first analyze the measured double layer capacitance for the Pt-coated PPTA fibers in PVA-LiCl and H_2O -KCl, then characterize the effect of adding the ALD V_2O_5 pseudocapacitive layer. The PPTA supercapacitors tested in PVA-LiCl electrolyte showed good voltammogram traces, whereas the more conductive H_2O -KCl showed a large slope consistent with shorting. We can use the fiber dimension and yarn construction to analyze the expected fiber capacitance in the PVA-LiCl electrolyte. Capacitance results in Figure 4b show a total double layer capacitance of 7.5 mF at 2 mV s^{-1} measured using 20 cm of PPTA yarn, comprised of 567 nearly cylindrical fibers with diameter of $13 \mu\text{m}$ each. The 7.5 mF measured capacitance corresponds to $\sim 160 \mu\text{F}$ per unit fiber specific surface area, or $\sim 3.8 \text{ mF per cm}^2$ yarn lateral

surface area. This capacitance is larger than 30 μF per unit specific surface area typically expected for a planar double layer.⁶⁵ The ALD Pt is known to experience island growth, which gives it a rough texture,^{42,66} and the relatively large capacitance likely results from an increase in surface area due to roughness and/or from pseudocapacitive oxygen sites on the Pt or within the underlying aluminum oxide. The measured capacitance also confirms that the ALD Pt process is able to sufficiently coat each fiber within the yarn structure to develop an electrically accessible charge double layer on the total fiber specific surface area, which is much larger than the lateral yarn surface area.

Results in Figure 5.5a and b show that adding pseudocapacitive V_2O_5 onto the Pt-coated PPTA increases the charge storage capacity. Similar to the double layer capacitors, the pseudocapacitor structures with ALD V_2O_5 showed slanted voltammogram traces in H_2O -KCl measured in the 3-electrode configuration (Figure 5.5a), consistent with poor charge/discharge rates, whereas the voltammograms were more regular and rectangular in PVA-LiCl measured using a separator (Figure 5.5b). In Figure 5.5b, the sample with 11 nm of V_2O_5 in PVA-LiCl at 2 mV s^{-1} showed a net capacitance of 35.2 mF, corresponding to $\sim 760 \mu\text{F}$ per unit fiber surface area, or $\sim 18.4 \text{ mF per cm}^2$ yarn lateral surface area, which is a 5x increase over the double layer capacitance measured in the same geometry without the pseudocapacitive V_2O_5 .

Similar to the double layer capacitance analysis, we can estimate the expected capacitance increase with the addition of V_2O_5 . Pseudocapacitive charge storage in V_2O_5 is expected to be as high as 1300 F g^{-1} . If the ALD V_2O_5 attains the bulk oxide density (3.357 g cm^{-3}), then deposition of 11 nm of V_2O_5 on each of the 567 fibers in the 20 cm long PPTA yarn would result in $\sim 4.8 \text{ mF per unit fiber specific surface area}$, or $\sim 116 \text{ mF per cm}^2$ yarn lateral surface area. In this case, the measured value is less than the highest value expected. Some capacitance loss is expected for a relatively thick V_2O_5 coating where the ions in the electrolyte are unable to diffuse into the bulk V_2O_5 during the voltage scan cycle. Reduced capacitance could also result if the net V_2O_5 thickness on the PPTA was less than measured on the silicon monitor wafers. However, previous studies of ALD metal oxide coatings on PPTA fibers show excellent correlation between thickness on the PPTA and planar monitor wafers.⁶² Full

pseudocapacitive charge storage in the V_2O_5 layer would also lead to linear increase in capacitance with oxide thickness. Increasing V_2O_5 thickness to 24 or 38 nm produced a decrease in charge storage capacity indicating the ions are only able to access part of the available oxide volume. We expect that increasing the oxide thickness in the regions between the fibers will block electrolyte transport, leading to an effective loss of accessible surface area and pseudocapacitive volume. Other studies report a similar decrease in capacitance with increasing oxide thickness and the capacitance loss was correlated with impeded ionic transport to the metal oxide.^{39,46}

We also find that winding the yarns into closely-coupled pairs led to a net decrease in the measured capacitance, which is also ascribed to a loss of ionic transport into the yarns (i.e. into the regions between the fibers) as the yarns are constricted upon winding. This is further supported by the EIS results in Figure 7 showing a very long high impedance tail for the twisted yarn pairs compared to the yarns measured with a separator in a less constricted geometry.

5.6 Conclusions

Common PPTA yarns can be used with PVA-LiCl electrolyte as a basis for a solid state flexible and mechanically strong supercapacitor charge storage device using a combination of ALD metal and ALD metal oxide to add conductive and pseudocapacitive layers, respectively. Results confirm that using ALD, nanoscale conductive and capacitive layers can be formed conformally on individual fibers within a complex yarn structure, producing a net electrochemically accessible surface area that substantially exceeds the external lateral surface area of the yarn itself.

The measured double layer capacitance on Pt-coated PPTA fibers reached 3.8 mF cm^{-2} , which is larger than expected for smooth fiber surfaces, likely due to surface roughness or pseudocapacitance from the underlying metal oxide deposited to promote Pt ALD nucleation. The charge storage in ALD V_2O_5 pseudocapacitor layers is as high as 18.4 mF cm^{-2} , which is less than expected from bulk charge storage density. We note, however, that this is the highest value reported for PPTA-based capacitors,^{8,24} and is commendable for capacitors formed from

common textiles, compared to other fiber systems that employ surface nanostructures or other high surface area treatments. The net capacitance tends to decrease with increasing V_2O_5 layer thickness, indicating loss of ionic species transport to the metal oxide. This is consistent with blocking effects of the oxide as it is formed by ALD in the regions between fibers within the yarn, and EIS results showing increased impedance when fibers are twisted into pairs.

Overall, the work shows that ALD metal and metal oxide can be used in combination to add double layer and pseudocapacitive charge storage to common woven textiles, including mechanically strong and resilient woven Kevlar, to create unique multifunctional flexible electronic fabric device systems.

5.7 Acknowledgments

This material is based upon work supported by the Center for Dielectrics and Piezoelectrics I/UCRC under the National Science Foundation Grant Nos. IIP 1361571 and 1361503.

5.8 References

- (1) Cai, X.; Peng, M.; Yu, X.; Fu, Y.; Zou, D. Flexible Planar/fiber-Architected Supercapacitors for Wearable Energy Storage. *J. Mater. Chem. C* **2014**, *2*, 1184–1200.
- (2) Yu, D.; Qian, Q.; Wei, L.; Jiang, W.; Goh, K.; Wei, J.; Zhang, J.; Chen, Y. Emergence of Fiber Supercapacitors. *Chem. Soc. Rev.* **2015**, *44*, 647–662.
- (3) Yang, P.; Mai, W. Flexible Solid-State Electrochemical Supercapacitors. *Nano Energy* **2014**, *8*, 274–290.
- (4) Guan, C.; Qian, X.; Wang, X.; Cao, Y.; Zhang, Q.; Li, A.; Wang, J. Atomic Layer Deposition of Co_3O_4 on Carbon Nanotubes/carbon Cloth for High-Capacitance and Ultrastable Supercapacitor Electrode. *Nanotechnology* **2015**, *26*, 94001.
- (5) Huang, Y.; Hu, H.; Huang, Y.; Zhu, M.; Meng, W.; Liu, C.; Pei, Z.; Hao, C.; Wang, Z.; Zhi, C. From Industrially Weavable and Knittable Highly Conductive Yarns to Large Wearable Energy Storage Textiles. *ACS Nano* **2015**, *9*, 4766–4775.
- (6) Kou, L.; Huang, T.; Zheng, B.; Han, Y.; Zhao, X.; Gopalsamy, K.; Sun, H.; Gao, C. Coaxial Wet-Spun Yarn Supercapacitors for High-Energy Density and Safe Wearable Electronics. *Nat. Commun.* **2014**, *5*, 3754.
- (7) Liu, N.; Ma, W.; Tao, J.; Zhang, X.; Su, J.; Li, L.; Yang, C.; Gao, Y.; Golberg, D.; Bando, Y. Cable-Type Supercapacitors of Three-Dimensional Cotton Thread Based Multi-Grade Nanostructures for Wearable Energy Storage. *Adv. Mater.* **2013**, *25*, 4925–4931.
- (8) Bae, J.; Song, M. K.; Park, Y. J.; Kim, J. M.; Liu, M.; Wang, Z. L. Fiber Supercapacitors Made of Nanowire-Fiber Hybrid Structures for Wearable/Flexible Energy Storage. *Angew. Chemie Int. Ed.* **2011**, *50*, 1683–1687.
- (9) Harrison, D.; Qiu, F.; Fyson, J.; Xu, Y.; Evans, P.; Southee, D. A Coaxial Single Fibre Supercapacitor for Energy Storage. *Phys. Chem. Chem. Phys.* **2013**, *15*, 12215–12219.
- (10) Fu, Y.; Wu, H.; Ye, S.; Cai, X.; Yu, X.; Hou, S.; Kafafy, H.; Zou, D. Integrated Power Fiber for Energy Conversion and Storage. *Energy Environ. Sci.* **2013**, *6*, 805–812.
- (11) Huang, Y.; Huang, Y.; Zhu, M.; Meng, W.; Pei, Z.; Liu, C.; Hu, H.; Zhi, C. Magnetic-Assisted, Self-Healable, Yarn-Based Supercapacitor. *ACS Nano* **2015**, *9*, 6242–6251.
- (12) Li, Y.; Sheng, K.; Yuan, W.; Shi, G. A High-Performance Flexible Fibre-Shaped Electrochemical Capacitor Based on Electrochemically Reduced Graphene Oxide. *Chem. Commun.* **2013**, *49*, 291–293.

- (13) Chen, T.; Qiu, L.; Yang, Z.; Cai, Z.; Ren, J.; Li, H.; Lin, H.; Sun, X.; Peng, H. An Integrated “Energy Wire” for Both Photoelectric Conversion and Energy Storage. *Angew. Chemie Int. Ed.* **2012**, *51*, 11977–11980.
- (14) Zhang, D.; Miao, M.; Niu, H.; Wei, Z. Core-Spun Carbon Nanotube Yarn Supercapacitors for Wearable Electronic Textiles. *ACS Nano* **2014**, *8*, 4571–4579.
- (15) Cai, Z.; Li, L.; Ren, J.; Qiu, L.; Lin, H.; Peng, H. Flexible, Weavable and Efficient Microsupercapacitor Wires Based on Polyaniline Composite Fibers Incorporated with Aligned Carbon Nanotubes. *J. Mater. Chem. A* **2013**, *1*, 258–261.
- (16) Chen, X.; Qiu, L.; Ren, J.; Guan, G.; Lin, H.; Zhang, Z.; Chen, P.; Wang, Y.; Peng, H. Novel Electric Double-Layer Capacitor with a Coaxial Fiber Structure. *Adv. Mater.* **2013**, *25*, 6436–6441.
- (17) Le, V. T.; Kim, H.; Ghosh, A.; Kim, J.; Chang, J.; Vu, Q. A.; Pham, D. T.; Lee, J.-H.; Kim, S.-W.; Lee, Y. H. Coaxial Fiber Supercapacitor Using All-Carbon Material Electrodes. *ACS Nano* **2013**, *7*, 5940–5947.
- (18) Lee, J. A.; Shin, M. K.; Kim, S. H.; Cho, H. U.; Spinks, G. M.; Wallace, G. G.; Lima, M. D.; Lepró, X.; Kozlov, M. E.; Baughman, R. H.; Kim, S. J. Ultrafast Charge and Discharge Biscrolled Yarn Supercapacitors for Textiles and Microdevices. *Nat. Commun.* **2013**, *4*, 1970.
- (19) Liu, B.; Tan, D.; Wang, X.; Chen, D.; Shen, G. Flexible, Planar-Integrated, All-Solid-State Fiber Supercapacitors with an Enhanced Distributed-Capacitance Effect. *Small* **2013**, *9*, 1998–2004.
- (20) Ren, J.; Bai, W.; Guan, G.; Zhang, Y.; Peng, H. Flexible and Weaveable Capacitor Wire Based on a Carbon Nanocomposite Fiber. *Adv. Mater.* **2013**, *25*, 5965–5970.
- (21) Ren, J.; Li, L.; Chen, C.; Chen, X.; Cai, Z.; Qiu, L.; Wang, Y.; Zhu, X.; Peng, H. Twisting Carbon Nanotube Fibers for Both Wire-Shaped Micro-Supercapacitor and Micro-Battery. *Adv. Mater.* **2013**, *25*, 1155–1159.
- (22) Xiao, X.; Li, T.; Yang, P.; Gao, Y.; Jin, H.; Ni, W.; Zhan, W.; Zhang, X.; Cao, Y.; Zhong, J.; Gong, L.; Yen, W.-C.; Mai, W.; Chen, J.; Huo, K.; Chueh, Y.-L.; Wang, Z. L.; Zhou, J. Fiber-Based All-Solid-State Flexible Supercapacitors for Self-Powered Systems. *ACS Nano* **2012**, *6*, 9200–9206.
- (23) Yu, D.; Goh, K.; Wang, H.; Wei, L.; Jiang, W.; Zhang, Q.; Dai, L.; Chen, Y. Scalable Synthesis of Hierarchically Structured Carbon Nanotube–graphene Fibres for Capacitive Energy Storage. *Nat. Nanotechnol.* **2014**, *9*, 555–562.

- (24) Gao, Y.; Sim, K.; Sun, S.; Chen, Z.; Song, J.; Yu, C. Crack-Insensitive Wearable Electronics Enabled Through High-Strength Kevlar Fabrics. *IEEE Trans. Components, Packag. Manuf. Technol.* **2015**, *5*, 1230–1236.
- (25) Meng, Y.; Zhao, Y.; Hu, C.; Cheng, H.; Hu, Y.; Zhang, Z.; Shi, G.; Qu, L. All-Graphene Core-Sheath Microfibers for All-Solid-State, Stretchable Fibriform Supercapacitors and Wearable Electronic Textiles. *Adv. Mater.* **2013**, *25*, 2326–2331.
- (26) Meng, Q.; Wang, K.; Guo, W.; Fang, J.; Wei, Z.; She, X. Thread-like Supercapacitors Based on One-Step Spun Nanocomposite Yarns. *Small* **2014**, *10*, 3187–3193.
- (27) Wang, K.; Meng, Q.; Zhang, Y.; Wei, Z.; Miao, M. High-Performance Two-Ply Yarn Supercapacitors Based on Carbon Nanotubes and Polyaniline Nanowire Arrays. *Adv. Mater.* **2013**, *25*, 1494–1498.
- (28) Xu, P.; Wei, B.; Cao, Z.; Zheng, J.; Gong, K.; Li, F.; Yu, J.; Li, Q.; Lu, W.; Byun, J.-H.; Kim, B.-S.; Yan, Y.; Chou, T.-W. Stretchable Wire-Shaped Asymmetric Supercapacitors Based on Pristine and MnO₂ Coated Carbon Nanotube Fibers. *ACS Nano* **2015**, *9*, 6088–6096.
- (29) Xu, J.; Wang, Q.; Wang, X.; Xiang, Q.; Liang, B.; Chen, D.; Shen, G. Flexible Asymmetric Supercapacitors Based upon Co₉S₈ Nanorod//Co₃O₄ @RuO₂ Nanosheet Arrays on Carbon Cloth. *ACS Nano* **2013**, *7*, 5453–5462.
- (30) Pang, H.; Zhang, Y.; Lai, W.-Y.; Hu, Z.; Huang, W. Lamellar K₂Co₃(P₂O₇)₂·2H₂O Nanocrystal Whiskers: High-Performance Flexible All-Solid-State Asymmetric Micro-Supercapacitors via Inkjet Printing. *Nano Energy* **2015**, *15*, 303–312.
- (31) Lu, X.; Yu, M.; Wang, G.; Zhai, T.; Xie, S.; Ling, Y.; Tong, Y.; Li, Y. H-TiO₂@MnO₂//H-TiO₂@C Core-Shell Nanowires for High Performance and Flexible Asymmetric Supercapacitors. *Adv. Mater.* **2013**, *25*, 267–272.
- (32) Yang, P.; Xiao, X.; Li, Y.; Ding, Y.; Qiang, P.; Tan, X.; Mai, W.; Lin, Z.; Wu, W.; Li, T.; Jin, H.; Liu, P.; Zhou, J.; Wong, C. P.; Wang, Z. Lin. Hydrogenated ZnO Core-Shell Nanocables for Flexible Supercapacitors and Self-Powered Systems. *ACS Nano* **2013**, *7*, 2617–2626.
- (33) Liu, L.; Yu, Y.; Yan, C.; Li, K.; Zheng, Z. Wearable Energy-Dense and Power-Dense Supercapacitor Yarns Enabled by Scalable Graphene-metallic Textile Composite Electrodes. *Nat. Commun.* **2015**, *6*, 7260.
- (34) Fu, Y.; Cai, X.; Wu, H.; Lv, Z.; Hou, S.; Peng, M.; Yu, X.; Zou, D. Fiber Supercapacitors Utilizing Pen Ink for Flexible/Wearable Energy Storage. *Adv. Mater.* **2012**, *24*, 5713–5718.

- (35) Chen, Z.; Qin, Y.; Weng, D.; Xiao, Q.; Peng, Y.; Wang, X.; Li, H.; Wei, F.; Lu, Y. Design and Synthesis of Hierarchical Nanowire Composites for Electrochemical Energy Storage. *Adv. Funct. Mater.* **2009**, *19*, 3420–3426.
- (36) Yu, D.; Goh, K.; Zhang, Q.; Wei, L.; Wang, H.; Jiang, W.; Chen, Y. Controlled Functionalization of Carbonaceous Fibers for Asymmetric Solid-State Micro-Supercapacitors with High Volumetric Energy Density. *Adv. Mater.* **2014**, *26*, 6790–6797.
- (37) Li, B.; Zheng, M.; Xue, H.; Pang, H. High Performance Electrochemical Capacitor Materials Focusing on Nickel Based Materials. *Inorg. Chem. Front.* **2016**, *3*, 175–202.
- (38) Guan, C.; Wang, J. Recent Development of Advanced Electrode Materials by Atomic Layer Deposition for Electrochemical Energy Storage. *Adv. Sci.* **2016**.
- (39) Daubert, J. S.; Lewis, N. P.; Gotsch, H. N.; Mundy, J. Z.; Monroe, D. N.; Dickey, E. C.; Losego, M. D.; Parsons, G. N. Effect of Meso- and Micro-Porosity in Carbon Electrodes on Atomic Layer Deposition of Pseudocapacitive V₂O₅ for High Performance Supercapacitors. *Chem. Mater.* **2015**, *27*, 6524–6534.
- (40) Brozena, A. H.; Oldham, C. J.; Parsons, G. N. Atomic Layer Deposition on Polymer Fibers and Fabrics for Multifunctional and Electronic Textiles. *J. Vac. Sci. Technol. A* **2016**, *34*, 10801.
- (41) Parsons, G. N.; Atanasov, S. E.; Dandley, E. C.; Devine, C. K.; Gong, B.; Jur, J. S.; Lee, K.; Oldham, C. J.; Peng, Q.; Spagnola, J. C.; William, P. S. Mechanisms and Reactions during Atomic Layer Deposition on Polymers. *Coord. Chem. Rev.* **2013**, *257*, 3323–3331.
- (42) Mundy, J. Z.; Shafiefarhood, A.; Li, F.; Khan, S. A.; Parsons, G. N. Low Temperature Platinum Atomic Layer Deposition on Nylon-6 for Highly Conductive and Catalytic Fiber Mats. *J. Vac. Sci. Technol. A* **2016**, *34*, 01A152.
- (43) Kalanyan, B.; Oldham, C. J.; Sweet, W. J.; Parsons, G. N. Highly Conductive and Flexible Nylon-6 Nonwoven Fiber Mats Formed Using Tungsten Atomic Layer Deposition. *ACS Appl. Mater. Interfaces* **2013**, *5*, 5253–5259.
- (44) Sweet, W. J.; Jur, J. S.; Parsons, G. N. Bi-Layer Al₂O₃/ZnO Atomic Layer Deposition for Controllable Conductive Coatings on Polypropylene Nonwoven Fiber Mats. *J. Appl. Phys.* **2013**, *113*, 194303.
- (45) Sweet, W. J.; Oldham, C. J.; Parsons, G. N. Conductivity and Touch-Sensor Application for Atomic Layer Deposition ZnO and Al:ZnO on Nylon Nonwoven Fiber Mats. *J. Vac. Sci. Technol. A* **2015**, *33*, 01A117.

- (46) Boukhalifa, S.; Evanoff, K.; Yushin, G. Atomic Layer Deposition of Vanadium Oxide on Carbon Nanotubes for High-Power Supercapacitor Electrodes. *Energy Environ. Sci.* **2012**, *5*, 6872–6879.
- (47) Rauda, I. E.; Augustyn, V.; Saldarriaga-Lopez, L. C.; Chen, X.; Schelhas, L. T.; Rubloff, G. W.; Dunn, B.; Tolbert, S. H. Nanostructured Pseudocapacitors Based on Atomic Layer Deposition of V_2O_5 onto Conductive Nanocrystal-Based Mesoporous ITO Scaffolds. *Adv. Funct. Mater.* **2014**, *24*, 6717–6728.
- (48) Warren, R.; Sammoura, F.; Tounsi, F.; Sanghadasa, M.; Lin, L. Highly Active Ruthenium Oxide Coating via ALD and Electrochemical Activation in Supercapacitor Applications. *J. Mater. Chem. A* **2015**, *3*, 15568–15575.
- (49) Woo Kim, J.; Kim, B.; Won Park, S.; Kim, W.; Hyung Shim, J. Atomic Layer Deposition of Ruthenium on Plasma-Treated Vertically Aligned Carbon Nanotubes for High-Performance Ultracapacitors. *Nanotechnology* **2014**, *25*, 435404.
- (50) Yang, F.; Zhang, L.; Zuzuarregui, A.; Gregorczyk, K.; Li, L.; Beltrán, M.; Tollan, C.; Brede, J.; Rogero, C.; Chuvilin, A.; Knez, M. Functionalization of Defect Sites in Graphene with RuO_2 for High Capacitive Performance. *ACS Appl. Mater. Interfaces* **2015**, *7*, 20513–20519.
- (51) Gregorczyk, K. E.; Kozen, A. C.; Chen, X.; Schroeder, M. A.; Noked, M.; Cao, A.; Hu, L.; Rubloff, G. W. Fabrication of 3D Core–Shell Multiwalled Carbon Nanotube@ RuO_2 Lithium-Ion Battery Electrodes through a RuO_2 Atomic Layer Deposition Process. *ACS Nano* **2015**, *9*, 464–473.
- (52) Guan, C.; Liu, J.; Wang, Y.; Mao, L.; Fan, Z.; Shen, Z.; Zhang, H.; Wang, J. Iron Oxide-Decorated Carbon for Supercapacitor Anodes with Ultrahigh Energy Density and Outstanding Cycling Stability. *ACS Nano* **2015**, *9*, 5198–5207.
- (53) Chen, C.; Chen, C.; Huang, P.; Duan, F.; Zhao, S.; Li, P.; Fan, J.; Song, W.; Qin, Y. NiO/nanoporous Graphene Composites with Excellent Supercapacitive Performance Produced by Atomic Layer Deposition. *Nanotechnology* **2014**, *25*, 504001.
- (54) Guan, C.; Wang, Y.; Hu, Y.; Liu, J.; Ho, K. H.; Zhao, W.; Fan, Z.; Shen, Z.; Zhang, H.; Wang, J. Conformally Deposited NiO on a Hierarchical Carbon Support for High-Power and Durable Asymmetric Supercapacitors. *J. Mater. Chem. A* **2015**, *3*, 23283–23288.
- (55) Sun, X.; Xie, M.; Wang, G.; Sun, H.; Cavanagh, A. S.; Travis, J. J.; George, S. M.; Lian, J. Atomic Layer Deposition of TiO_2 on Graphene for Supercapacitors. *J. Electrochem. Soc.* **2012**, *159*, A364–A369.

- (56) Sun, X.; Xie, M.; Travis, J. J.; Wang, G.; Sun, H.; Lian, J.; George, S. M. Pseudocapacitance of Amorphous TiO₂ Thin Films Anchored to Graphene and Carbon Nanotubes Using Atomic Layer Deposition. *J. Phys. Chem. C* **2013**, *117*, 22497–22508.
- (57) Fisher, R. A.; Watt, M. R.; Konjeti, R.; Ready, W. J. Atomic Layer Deposition of Titanium Oxide for Pseudocapacitive Functionalization of Vertically-Aligned Carbon Nanotube Supercapacitor Electrodes. *ECS J. Solid State Sci. Technol.* **2014**, *4*, M1–M5.
- (58) Yue, B.; Wang, C.; Ding, X.; Wallace, G. G. Polypyrrole Coated Nylon Lycra Fabric as Stretchable Electrode for Supercapacitor Applications. *Electrochim. Acta* **2012**, *68*, 18–24.
- (59) Jost, K.; Durkin, D. P.; Haverhals, L. M.; Brown, E. K.; Langenstein, M.; De Long, H. C.; Trulove, P. C.; Gogotsi, Y.; Dion, G. Natural Fiber Welded Electrode Yarns for Knittable Textile Supercapacitors. *Adv. Energy Mater.* **2015**, *5*, 1401286.
- (60) Jacobs, M. J. N.; Van Dingenen, J. L. J. Ballistic Protection Mechanisms in Personal Armour. *J. Mater. Sci.* **2001**, *36*, 3137–3142.
- (61) Lee, Y. S.; Wetzel, E. D.; Wagner, N. J. The Ballistic Impact Characteristics of Kevlar Woven Fabrics Impregnated with a Colloidal Shear Thickening Fluid. *J. Mater. Sci.* **2003**, *38*, 2825–2833.
- (62) Atanasov, S. E.; Oldham, C. J.; Slusarski, K. A.; Taggart-Scarff, J.; Sherman, S. A.; Senecal, K. J.; Filocamo, S. F.; McAllister, Q. P.; Wetzel, E. D.; Parsons, G. N. Improved Cut-Resistance of Kevlar® Using Controlled Interface Reactions during Atomic Layer Deposition of Ultrathin (<50 Å) Inorganic Coatings. *J. Mater. Chem. A* **2014**, *2*, 17371–17379.
- (63) Badot, J. C.; Ribes, S.; Yousfi, E. B.; Vivier, V.; Pereira-Ramos, J. P.; Baffier, N.; Lincot, D. Atomic Layer Epitaxy of Vanadium Oxide Thin Films and Electrochemical Behavior in Presence of Lithium Ions. *Electrochem. Solid-State Lett.* **2000**, *3*, 485–488.
- (64) Jur, J. S.; Sweet, W. J.; Oldham, C. J.; Parsons, G. N. Atomic Layer Deposition of Conductive Coatings on Cotton, Paper, and Synthetic Fibers: Conductivity Analysis and Functional Chemical Sensing Using “All-Fiber” Capacitors. *Adv. Funct. Mater.* **2011**, *21*, 1993–2002.
- (65) Conway, B. E. *Electrochemical Supercapacitors*; Springer US: Boston, MA, 1999.
- (66) Geyer, S. M.; Methaapanon, R.; Johnson, R.; Brennan, S.; Toney, M. F.; Clemens, B.; Bent, S. Structural Evolution of Platinum Thin Films Grown by Atomic Layer Deposition. *J. Appl. Phys.* **2014**, *116*, 64905.

CHAPTER 6. Corrosion Protection of Copper Using Al₂O₃, TiO₂, ZnO, HfO₂, and ZrO₂ Atomic Layer Deposition

This chapter is based on a manuscript published as:

Daubert, J. S.; Hill, G. T.; Gotsch, H. N.; Gremaud, A. P.; Ovental, J. S.; Williams, P. S.; Oldham, C. J.; Parsons, G. N. Corrosion Protection of Copper Using Al₂O₃, TiO₂, ZnO, HfO₂, and ZrO₂ Atomic Layer Deposition. *ACS Appl. Mater. Interfaces* **2017**, acsami.6b13571.

6.1 Abstract

Atomic layer deposition (ALD) is a viable means to add corrosion protection to copper metal. Ultrathin films of Al₂O₃, TiO₂, ZnO, HfO₂, and ZrO₂ were deposited on copper metal using ALD and their corrosion protection properties were measured using electrochemical impedance spectroscopy (EIS) and linear sweep voltammetry (LSV). Analysis of ~50 nm thick films of each metal oxide demonstrated low electrochemical porosity and provided enhanced corrosion protection from aqueous NaCl solution. The surface pretreatment and roughness was found to affect the extent of the corrosion protection. Films of Al₂O₃ or HfO₂ provided the highest level of initial corrosion protection, but films of HfO₂ exhibited the best coating quality after extended exposure. This is the first reported instance of using ultrathin films of HfO₂ or ZrO₂ produced with ALD for corrosion protection, and both are promising materials for corrosion protection.

6.2 Introduction

Copper is a common metal widely used in applications such as plumbing and heat exchangers.¹⁻⁶ While copper has a reasonable resistance to corrosion in liquid water, there is a finite corrosion rate, which decreases the life of the materials. The rate of copper corrosion is dependent on the water's temperature, pH, and solutes.^{3,4,6-9} The application of barrier coatings on copper is one method to reduce corrosion. There are many well-studied methods for applying corrosion protective coatings including chemical vapor deposition (CVD),^{10,11} self-assembled monolayers,¹² organic azoles,¹³ polymers,¹⁴ plasma,¹⁵ and electrochemical deposition.¹⁶ Recently, several groups have explored atomic layer deposition (ALD) as a means to form various metal oxide corrosion protection layers. For example, ALD Al₂O₃, TiO₂, and ZnO have been studied to protect metals including copper and stainless steel.¹⁷⁻³¹ In general, while the ALD coatings have been found to provide corrosion protection, the magnitude of corrosion protection has varied significantly between the reported results, in part due to differences in initial surface preparation. For example, Chai, et al. reported ALD Al₂O₃ layers 29.4 nm thick on mechanically and chemically polished copper and have corrosion

currents as low as $0.03 \mu\text{A}/\text{cm}^2$ and an impedance of $2 \times 10^6 \Omega/\text{cm}^2$ at 10 mHz.^{28,29} In another report, Mirhashemihaghighi, et al. deposited ALD Al_2O_3 layers 50 nm thick on mechanically polished and electropolished copper and found corrosion currents of $8 \times 10^{-5} \mu\text{A}/\text{cm}^2$ and impedances of $1 \times 10^8 \Omega/\text{cm}^2$.³⁰ The differences indicate that carefully polishing a copper surface can improve the corrosion protection of ALD coatings. For our studies, the effect of copper electropolishing is examined for some ALD coatings, but we primarily address the performance of various ALD coatings on as-received surfaces.

ALD is a vapor phase thin film deposition technique that is capable of depositing ultrathin, conformal films with subnanometer thickness control, and it is commonly used to form Al_2O_3 , TiO_2 , ZnO , HfO_2 and ZrO_2 , thin films of interest for corrosion protection.^{17-30,32} ALD is advantageous over other coating techniques, because of its ability to coat high aspect ratio materials with no line-of-sight requirement.

Alumina is the most readily studied ALD thin film for corrosion protection, because it has been shown to nucleate well on metals giving rise to low porosity that prevents the solution from accessing the metal.^{20-30,33} When copper is coated with Al_2O_3 barrier coatings and exposed to aqueous NaCl solution, the corrosion rate is markedly decreased compared to uncoated material, and the surface retains its original visual appearance.^{23,24,28-30} The long term corrosion protection of Al_2O_3 coatings, however, is known to be inhibited by its dissolution into water.^{20,22,27,33}

Titanium dioxide is also studied as a corrosion protection layer of metals.^{18-20,25,27,33} Titanium dioxide coatings deposited by ALD have been found to decrease the corrosion rate as well as shift the corrosion potential to be more positive than the base metal, indicating it provides corrosion resistance,^{18,19} and ALD TiO_2 has also been shown to prevent corrosion in alkaline conditions.³⁴ Titanium dioxide ALD, however, has issues during film nucleation on copper leading to high porosity and poor long term corrosion resistance.²⁷ The grain boundaries present in crystalline TiO_2 are also susceptible to species diffusion, which promote surface corrosion.²⁰

Relatively thick ZnO coatings on copper have also been shown to decrease corrosion current density.³⁵ ZnO deposited by ALD does not etch in alkaline conditions,³⁶ but suffers from dissolution in purified water.²⁷

Atomic layer deposition is also advantageous because it provides direct means to form laminated metal oxide films. For example, laminates of Al₂O₃ and TiO₂ have been studied on copper and stainless steel to combine the corrosion resistance of the TiO₂ and the low porosity of the Al₂O₃,^{17,20,27} and these structures show slower dissolution in water and improved corrosion protection and for copper compared to the single oxides.

Thin films of HfO₂ and ZrO₂ have been widely investigated for electronic dielectric applications, and some research teams have studied their capacity for surface corrosion protection, because of their strong dielectric properties. HfO₂ coatings have been shown to increase the impedance, indicating corrosion protection.^{37,38} ZrO₂ coatings are also of interest for corrosion protection, because they have been shown to increase the polarization potential, decrease the corrosion current density, and increase the impedance.^{39,40} The corrosion resistance of ALD HfO₂ and ZrO₂, however, has not been reported in detail.

In the present work, we use ALD to coat clean copper with a series of metal oxides including Al₂O₃, TiO₂, ZnO, HfO₂ and ZrO₂, and use atomic force microscopy (AFM) to examine the physical properties of the films, and electrochemical impedance spectroscopy (EIS) and linear sweep voltammetry (LSV) to characterize corrosion barrier properties. We find that all of the metal oxides provide enhanced corrosion protection, with Al₂O₃ and HfO₂ providing the greatest increase in impedance. Hafnium oxide provides a high level of corrosion protection even after a 21 day extended exposure to a NaCl solution.

6.3 Experimental Section

Substrate Preparation. Superconductive 101 copper sheets (99.99% McMaster-Carr) were cut into 16 mm by 24 mm by 1.2 mm coupons and cleaned in an ultrasonicator bath of acetone and rinsed with methanol to remove debris from the surface of the copper. To ensure the copper

maintained the surface texture produced during the manufacturing process, unless otherwise specified no additional mechanical or electrochemical polishing was performed before ALD coating. As shown in the AFM images in Figure 6.3, the starting copper surface had a root-mean-square (rms) roughness of 10 nm. To evaluate the effect of surface roughness, some samples were electropolished in 85% phosphoric acid at 1.4 V against a copper counter electrode for 5 min before being rinsed with deionized water, dried, and loaded into the ALD reactor. The rms roughness of the electropolished copper was 2.4 nm.

The copper coupons were coated using ALD in a home built viscous-flow, hot-wall type, ALD reactor operating with ultrahigh-purity nitrogen (99.999%, Arc3) reactant carrier and purge gas that was further purified using a Gatekeeper inert gas purifier (rated to <100 ppt H₂O and O₂, Entegris) before flowing into the reactor that was maintained between 1 and 2 Torr. Al₂O₃ was deposited using trimethyl-aluminum (TMA, 98% Strem Chemicals) and reagent grade H₂O (Ricca Chemical) at 150°C at a growth rate of 1.2 Å/cy, TiO₂ was deposited using titanium tetrachloride (TiCl₄, 99% Strem Chemicals) and H₂O at 150°C at a rate of 0.4 Å/cy, ZnO was deposited using diethylzinc (DEZ, 95% Strem Chemicals) and H₂O at 150°C at a rate of 2.5 Å/cy, HfO₂ was deposited using tetrakis(dimethylamido)hafnium (TDMAH, 99.99% Strem Chemicals) and H₂O at 150°C at a rate of 1.0 Å/cy, and ZrO₂ was deposited using tetrakis(dimethylamino)zirconium (TDMAZ, 99.99% Sigma Aldrich) and H₂O at 175°C at a rate of 1.1 Å/cy. A typical ALD cycle consisted of a 0.5 s ALD precursor dose, a 30 s N₂ purge, a 0.5 s H₂O dose, and a 30 s N₂ purge.

Film Characterization. AFM for surface topography analysis was conducted using a Digital Instruments Dimension 3000, with a Nanoscope IIIa controller and vibration shielded hood. Imaging was performed in intermittent contact mode. Image analysis was performed using built-in software functions to calculate the rms roughness of 1 μm² sites. The rms values of the copper varied ±50% between the sites scanned. The thickness of the ALD films was measured using spectroscopic ellipsometry (J.A. Woollam Co. alpha-SE, using the CompleteEASE data analysis software package) on monitor silicon wafers that were placed in the reactor during ALD, and are accurate to within ±10%.

Electrochemical Measurements. The backside of the coated copper coupon was removed with sandpaper to remove electrical resistances before being placed in a Princeton Applied Research flat corrosion cell (model K0235) with a 1 cm² working electrode, a platinum mesh counter electrode, and a 0.1 M sodium chloride electrolyte (99.5%, Sigma Aldrich). The cell was allowed to come to equilibrium (corrosion potential drift < 10 mV/h) before impedance measurements were taken. The impedance measurements were collected using a BioLogic VMP3 potentiostat with a perturbation of 10 mV over the frequency range from 100 kHz to 10 mHz. Ten points were collected per decade with 2 periods between each frequency measurement and 2 measurements per frequency. The impedance measurements at 10 mHz found to vary by $\pm 20\%$ between samples. The EIS data was then modeled using equivalent circuit models and curve fitting was performed using the ZSimpWin 3.21 software package. The fitted parameters have an uncertainty of $\pm 15\%$.

The LSV data was collected at a rate of 1 mV/s from -0.8 to 0.5 V versus a Ag/AgCl reference electrode. The corrosion potentials, corrosion currents, polarization resistances, and porosities were obtained from the polarization curves constructed using LSV, and were found to vary $\pm 20\%$ between samples. The polarization resistances were calculated using the Stern-Geary equation:^{24,28,30}

$$R_p = \frac{b_a b_c}{i_{corr} \ln(10)(b_a + b_c)} \quad 6.1$$

where b_a and b_c are the slopes of the anodic and cathodic branches of the Tafel plot.

The electrochemical porosity of the ALD films deposited of the copper were calculated by comparing R_p of the ALD coated copper using equation 2.5:^{24,28,30}

$$P = \left(\frac{R_p \text{ bare}}{R_p \text{ ALD}} \right) \times 10^{-\left(\frac{\Delta E_{corr}}{b_a} \right)} \times 100 \quad 6.2$$

Where ΔE_{corr} is the difference in the corrosion potentials from the polarization curve. Because this value is determined by the magnitude of the polarization resistance, the net electrochemical

porosity can be ascribed to ion transport through a continuous solid film, or due to charge flow through gaps or pinholes in the coating. Due to the variation in the measurements used in the calculation of the polarization resistances, the reported electrochemical porosities vary by $\pm 50\%$.

6.4 Results

Electrochemical impedance spectroscopy and linear sweep voltammetry analysis of varying thickness ALD films on copper. The results of bare copper and Al_2O_3 coatings of varying thickness tested using LSV and EIS are shown in Figure 6.1. The smooth shape of the polarization curves of the samples from LSV, with only a peak at the corrosion potential, indicates that the film is electrochemically inert. As the Al_2O_3 layer thickness increases, the corrosion potential shifts to more negative potential, indicating improved corrosion resistance, apparently saturating near 60 nm. The polarization curve for the 64 nm Al_2O_3 coating overlaps that from the 110 nm Al_2O_3 coating. Using the Tafel fit analysis described above, the polarization curves were used to calculate the corrosion current, polarization resistance, and porosity, and results are given in Table 6.1. The ALD Al_2O_3 layer led to a general decrease in corrosion current. Using the polarization resistances calculated for both the uncoated and the coated surfaces, the Stern-Geary equation (eq. 2.4) along with equation 2.5 shows that the electrochemical porosity of the Al_2O_3 coating decreased from 2.5% for 11 nm of Al_2O_3 to 0.1% for 110 nm Al_2O_3 .

The EIS results shown in the Bode plot in Figure 6.1b show that the Al_2O_3 coating add both increased corrosion resistance, as shown by the increased impedance near 10 mHz, and increased capacitance, as indicated by the increased phase angle near 100 Hz. The increase in capacitance is expected as compared to the copper native oxide.

Bode plots for TiO_2 and ZnO ALD films of varying thickness are shown in Figure 6.2 (a) and (b), respectively. Figure 6.2 (c) and (d) shows values for impedance at 10 mHz and the phase angle at 100 Hz collected from copper versus ALD film thickness for Al_2O_3 , TiO_2 , and ZnO . Thicker coatings of Al_2O_3 resulted in increased impedance, but the 110 nm Al_2O_3 coating did

not exhibit greater impedance than the 64 nm coating, consistent with the polarization curves, indicating that corrosion protection tends to saturate with increasing coating thickness. Alumina coatings between 29 nm and 110 nm on the copper all displayed a similar phase angle. A 40 nm coating of TiO₂ ALD showed an increase in impedance similar to that observed for Al₂O₃, but the increase in phase angle was lower. On the other hand, 50 to 200 nm coatings of ZnO ALD cause a smaller increase in impedance as Al₂O₃, but a small increase in phase angle that is similar to TiO₂.

In general, the correlation between the LSV and the EIS results indicates that Bode plots can be used as an indicator for the corrosion resistance of different thickness films or aging of films that are exposed to corrosive solutions.

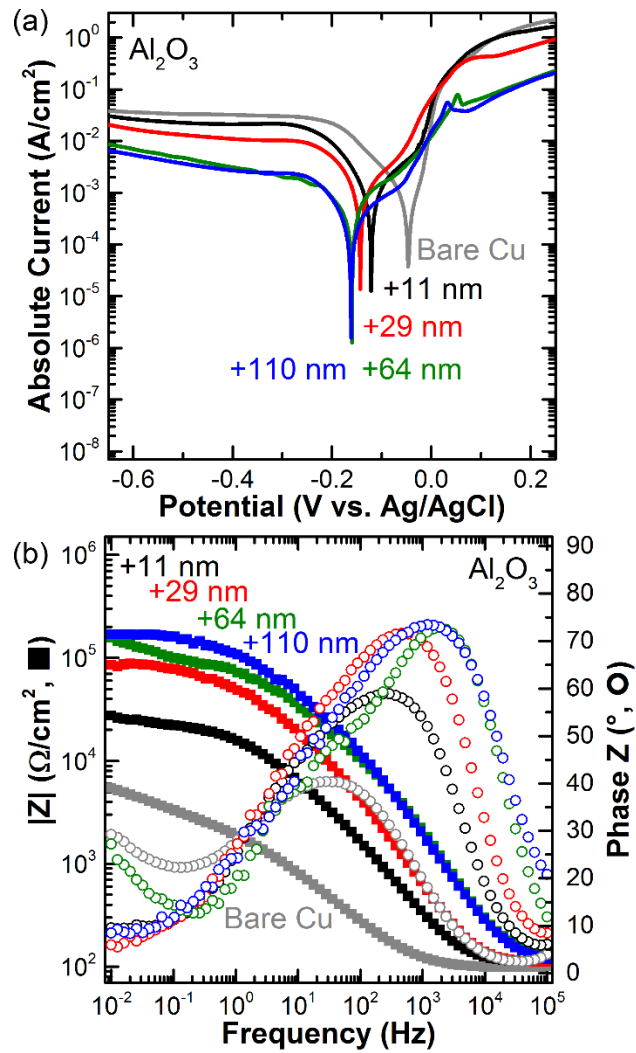


Figure 6.1. (a) Polarization curve and (b) Bode plot of bare copper and Al_2O_3 coatings of varying thickness on copper with impedance shown as closed squares and phase angle shown with open circles.

Table 6.1. Corrosion properties of Al₂O₃ films on varying thickness on copper obtained from LSV.

	E_{corr} (V vs. Ag/AgCl)	I_{corr} ($\mu\text{A}/\text{cm}^2$)	R_p (Ω/cm^2)	porosity (%)
Bare Cu	-0.046	1.28	1.5×10^4	100
+11 nm	-0.121	0.45	3.7×10^4	2.5
+29 nm	-0.143	0.83	2.7×10^4	1.6
+64 nm	-0.159	0.56	5.9×10^4	0.4
+110 nm	-0.162	0.11	1.9×10^5	0.1

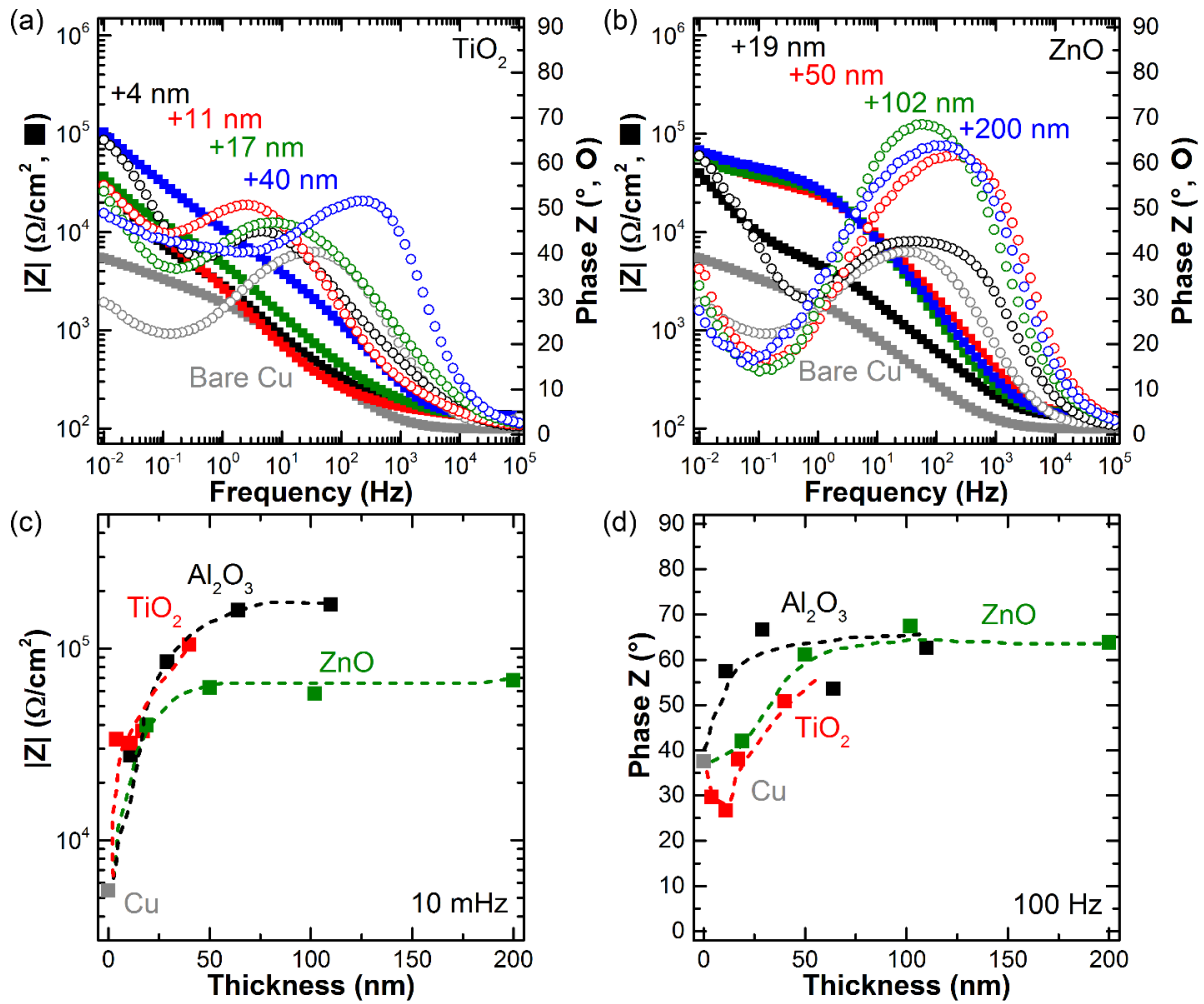


Figure 6.2. Bode plots for (a) TiO₂ and (b) ZnO films of varying thickness compared to uncoated copper with impedance shown as closed squares and phase angle shown with open circles. (c) Impedance at 10 mHz for bare copper and Al₂O₃, TiO₂, and ZnO films of varying thickness, and (d) phase angle at 100 Hz.

The effect of the copper surface on the electrochemical corrosion resistance was studied by electropolishing copper and coating it with 55 nm of Al₂O₃. The electrochemical corrosion protection properties improved significantly in comparison to the copper that had only been cleaned and coated with 64 nm of Al₂O₃, and are included in Table 6.4. The results, along with the decision to not electropolish all of the copper before the ALD coating, are elaborated on in the Discussion section.

Surface characterization of copper coated with 50 nm ALD films. The surface topography of copper coated with ~50 nm ALD films of Al₂O₃ (64 nm), TiO₂ (40 nm), ZnO (50 nm), ZrO₂ (60 nm), and HfO₂ (60 nm) was examined using AFM, and the results are presented in Figure 6.3. The bare copper has a similar rms surface roughness of 10 nm. While the thin films of Al₂O₃, ZnO, HfO₂, and ZrO₂ appear to have small nucleation sites, the rms for all of the samples remained low, between 7 and 15 nm, within the error of the rms measurements between scanned sites, and the ALD coatings retain the surface topography of the underlying copper. The TiO₂ surface, however, varies from the other coatings and is very rough with a rms roughness of 40 nm. The roughness of the TiO₂ is consistent with TiO₂ islands nucleating on the surface that grow to give a rough surface.²⁷ The TiO₂ film roughness, and its effect on the corrosion protection properties will be discussed in the Discussion section below.

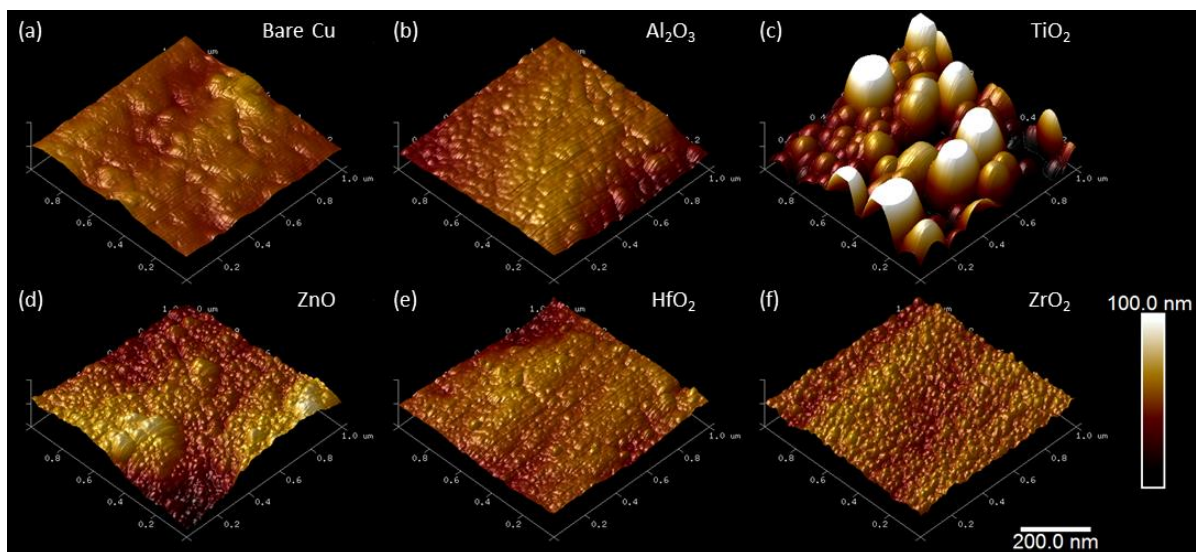


Figure 6.3. AFM images showing morphological differences between (a) bare Cu, (b) Al_2O_3 , (c) TiO_2 , (d) ZnO , (e) HfO_2 , and (f) ZrO_2 films.

Electrochemical properties of copper coated with 50 nm films. Copper coated with ~50 nm ALD films was measured using LSV and EIS. The polarization curves are shown in Figure 6.4, and were used to calculate the corrosion current, polarization resistance, and porosity of the ALD films shown in Table 6.2. All of the ALD films reduced the corrosion current by greater than 50%, with HfO_2 causing the largest decrease (83%). The ALD films all caused an increase in the polarization resistance between 170% (ZnO) and 515% (HfO_2). The porosities of all of the ALD films were below 2%, with the Al_2O_3 coating having the lowest porosity (0.4%) in part due to its large decrease in the corrosion potential, and ZnO having the highest porosity (1.8%) because of its relatively small increase in polarization resistance. The effect of the metal oxide on the observed corrosion resistance results will be examined in more detail in the Discussion below.

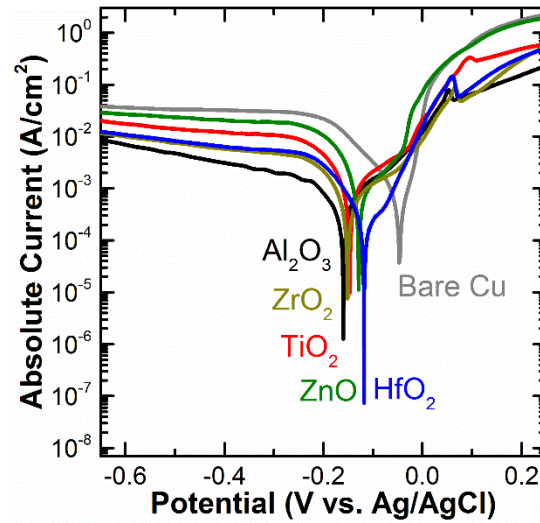


Figure 6.4. Polarization curves of ~50 nm films of Al₂O₃, TiO₂, ZnO, HfO₂, and ZrO₂ on copper.

Table 6.2. Corrosion properties of ~50 nm ALD films on copper obtained from LSV.

	E_{corr} (V vs. Ag/AgCl)	I_{corr} ($\mu\text{A}/\text{cm}^2$)	R_p (Ω/cm^2)	Porosity (%)
Bare Cu	-0.046	1.28	1.5×10^4	100
Al ₂ O ₃	-0.159	0.56	5.9×10^4	0.4
TiO ₂	-0.146	0.56	4.0×10^4	0.9
ZnO	-0.128	0.45	3.9×10^4	1.8
HfO ₂	-0.118	0.22	8.9×10^4	1.3
ZrO ₂	-0.151	0.42	6.3×10^4	0.5

Copper coated with 50 nm of ALD Al₂O₃, TiO₂, ZnO, HfO₂ or ZrO₂ was analyzed with EIS, and the results are shown in Figure 6.5. Films of Al₂O₃ and HfO₂ produce the largest increase in impedance, while films consisting of TiO₂, ZnO, and ZrO₂ show a smaller increase in impedance, similar to the increases in polarization resistance seen in LSV. The HfO₂ film shows the largest increase in the phase angle at 100 Hz, but Al₂O₃ shows a similar increase in phase angle at slightly higher frequencies. The TiO₂, ZnO, and ZrO₂ films all exhibit smaller changes in the phase angle, similar to the change in impedance, but are still higher than uncoated copper.

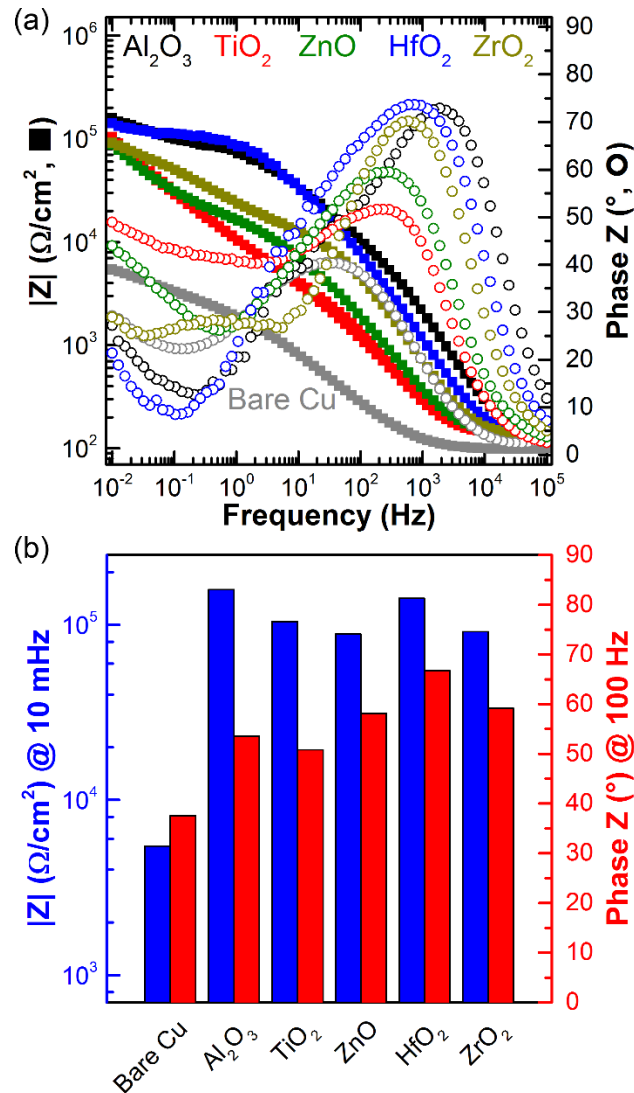


Figure 6.5. (a) Bode plot of ~50 nm films of Al₂O₃, TiO₂, ZnO, HfO₂, and ZrO₂ on copper with impedance shown as closed squares and phase angle shown with open circles, and (b) impedance at 10 mHz and phase at 100 Hz of the films.

Aging of coated copper. Figure 6.6 shows the Bode plots of copper coated with ~50 nm ALD thin films of Al₂O₃, TiO₂, ZnO, HfO₂, or ZrO₂ that were aged in 0.1 M NaCl for up to 90 h. Figure 6.7 shows the relative impedance at 10 mHz and relative phase angle at 100 Hz from EIS of the aged films compared to the initial impedance and phase angle. The bare copper

showed decreasing impedance and phase angle over time, consistent with corrosion of the copper. The HfO_2 and ZrO_2 films showed the smallest change in impedance and phase angle over time with both being practically unchanged after 90 h of exposure to the electrolyte, indicating the film was not affected by the NaCl solution. The ZnO , Al_2O_3 and TiO_2 films all exhibited an increase in impedance over time, indicating that the properties of the metal oxide films and the copper interface were changing from exposure to the electrolyte. LSV was not used to test the copper during aging, because the dc potential would alter the corrosion patterns.

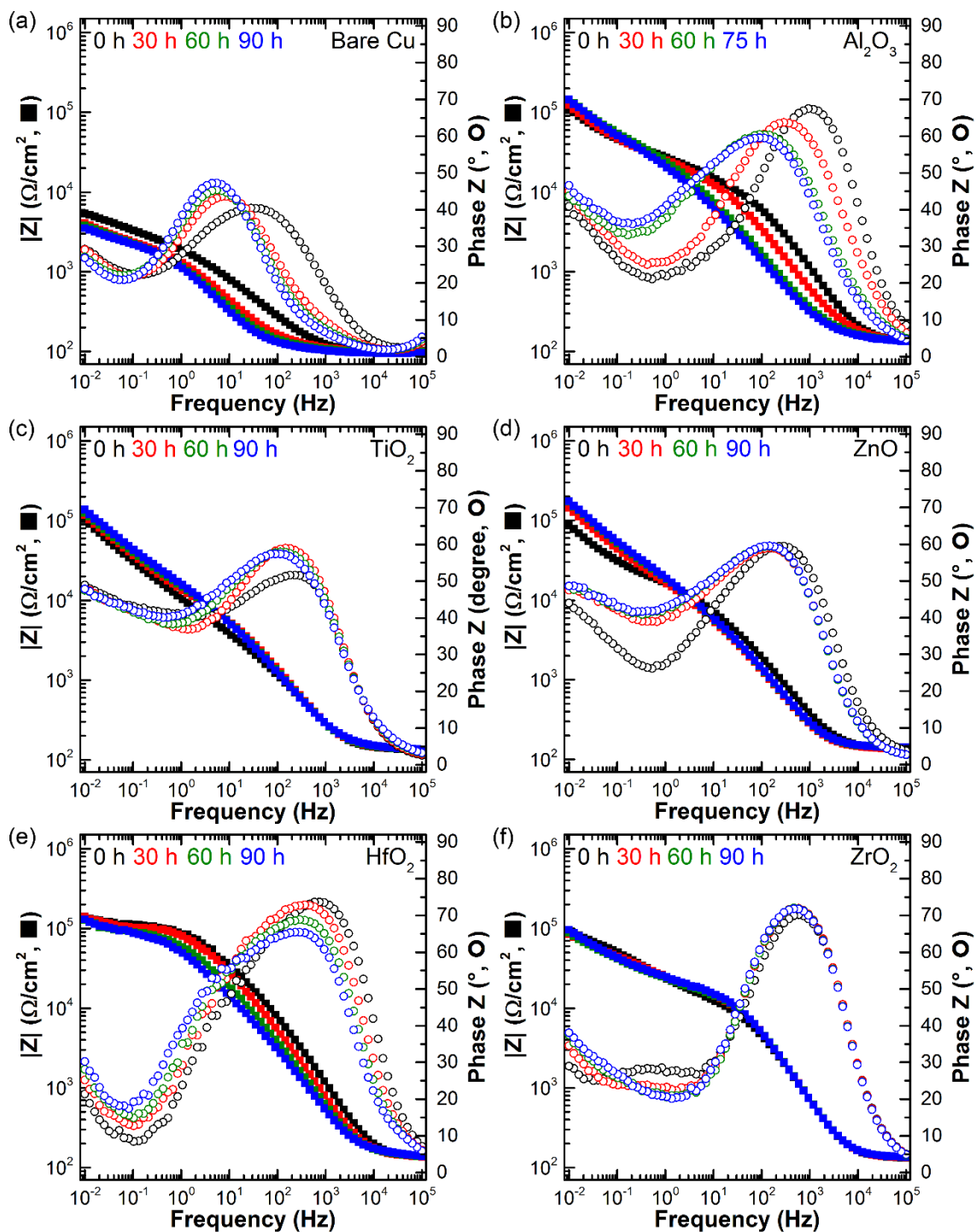


Figure 6.6. Bode plots of (a) uncoated copper and ~ 50 nm films of (b) Al_2O_3 , (c) TiO_2 , (d) ZnO, (e) HfO_2 , and (f) ZrO_2 on copper aged in 0.1 M NaCl for up to 90 h with impedance shown as closed squares and phase angle shown with open circles.

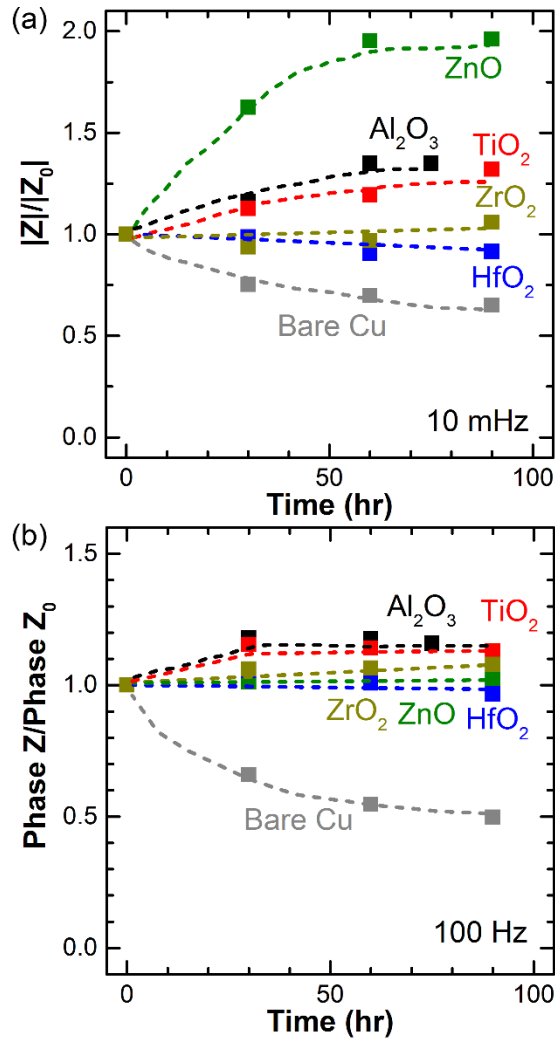


Figure 6.7. The (a) relative impedance at 10 mHz and (b) relative phase angle at 100 Hz of ~50 nm Al₂O₃, TiO₂, ZnO, HfO₂, ZrO₂ films on copper, and bare copper compared to the starting impedance and phase angle, respectively, during aging up to 90 h in electrolyte.

The extended corrosion protection properties of bare copper, Al₂O₃ coated copper, and HfO₂ coated copper from exposure to 0.1 M NaCl solution for 21 days were also measured. After the extended test the copper was removed from the solution, rinsed with deionized water, and dried before the surface roughness was examined with AFM. The images showing the morphological changes are shown in Figure 6.8. The surface of the bare copper changed significantly with newly formed grooves in the copper that indicate corrosion, and an increase

in the rms from 10 to 110 nm. The Al_2O_3 copper also showed visual signs of corrosion and an increase in the rms from 15 to 50 nm. The HfO_2 coated copper changed the least, still maintained a smooth appearance, and had the smallest increase in rms, from 9 to 34 nm.

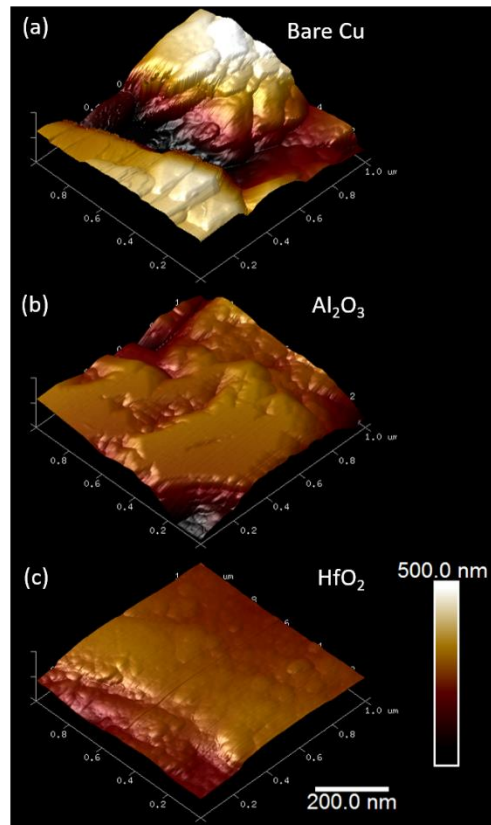


Figure 6.8. AFM images showing morphological differences in the surfaces of the (a) bare copper, (b) Al_2O_3 coated copper, and (c) HfO_2 coated copper after a 21 day exposure to 0.1 M NaCl.

The electrochemical corrosion resistance properties of the films after extended exposure to NaCl solutions were measured using EIS and the results are shown in Figure 6.9. The impedance and phase angle of the Al_2O_3 coated copper decreased significantly after extended exposure, indicating Al_2O_3 was no longer providing a large amount of corrosion protection.

The HfO₂ coated copper also showed a decrease in impedance and phase angle, albeit a much smaller decrease than the Al₂O₃ coated copper.

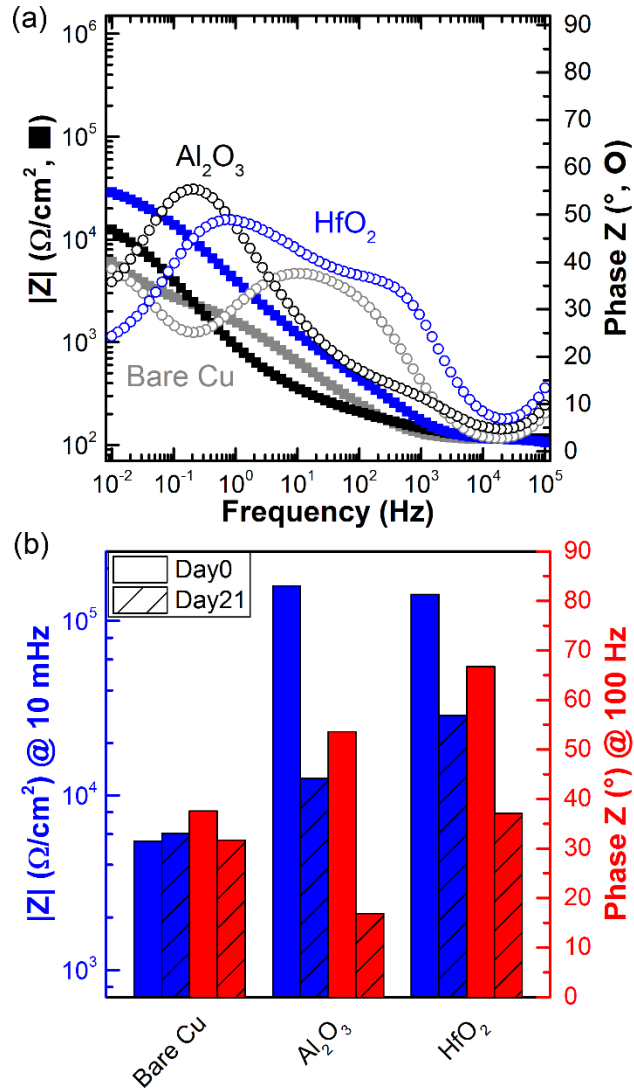


Figure 6.9. (a) Bode plots of bare copper, Al₂O₃ coated copper, and HfO₂ coated copper after a 21 day exposure to 0.1 M NaCl with impedance shown as closed squares and phase angle shown with open circles, and (b) a comparison of the impedance at 10 mHz and phase at 100 Hz of the films before and after the extended exposure.

6.5 Discussion

The LSV and EIS experiments of Al₂O₃ coatings on copper demonstrated that Al₂O₃ provides the corrosion protection of the as-received copper. Other studies that focused on LSV and EIS measurements of polished copper coated with Al₂O₃ in NaCl solutions, including Chai, et al. and Mirhashemihaghighi, et al., came to the same conclusion, but the reported values of corrosion current, corrosion potential, and impedance show some variation between studies for both the as-prepared and the Al₂O₃ coated copper.^{28–30} Table 6.3 compares the reported measurements of bare copper from those two studies, along with the results of this study for both as-cleaned and electropolished copper. The corrosion current of the bare copper varies by 2 orders of magnitude between studies, which can effect the calculated coating porosity.

Table 6.4 summarizes previous results and those obtained in this study using Al₂O₃ ALD corrosion protection layers. The reported impedance varies by 3 orders of magnitude, where improved results are ascribed to extensive polishing (mechanical, chemical, and/or electrochemical) used in these reports. The data shows that electropolishing the copper surface prior to exposure significantly improved the corrosion properties of the ALD Al₂O₃. The differences in surface preparation and changes in the native oxide that forms before ALD, has been further studied by Mirhashemihaghighi, et al.^{31,41} ALD coatings on rough surfaces tend to have a thicker, less uniform native oxide and are likely to have a higher porosity and lower capacitance, which likely causes the decrease in impedance values found in this work from the rough as-received copper surfaces. The use of as-received copper with limited surface preparation, however, can provide insight of how the ALD coatings will behave when applied to complex pieces of equipment (i.e. tubing or nozzles) that cannot be coated uniformly by other deposition techniques.

Table 6.3. Comparison of reported values obtained from LSV and EIS measurements of copper.

$ Z $ (Ω/cm^2 @ 10 mHz)	Max. Phase Z ($^\circ$)	E_{corr} (V vs. Ag/AgCl)	I_{corr} ($\mu\text{A}/\text{cm}^2$)	Reference
4×10^4	55°	-0.113	0.54	28,29
4×10^4	70°	-0.350	0.03	30
6×10^3	40°	-0.046	1.3	This work, cleaned
4×10^4	75°	-0.185	0.4	This work, electropolished

Table 6.4. Summary of reported results obtained from LSV and EIS measurements of Al_2O_3 coated copper.

Al_2O_3 Thickness (nm)	$ Z $ (Ω/cm^2 @ 10 mHz)	Freq. Phase Z $>85^\circ$ (Hz)	E_{corr} (V vs. Ag/AgCl)	I_{corr} ($\mu\text{A}/\text{cm}^2$)	Porosity (%)	Reference
29.4	2×10^6	$10^1 - 6 \times 10^3$	-0.048	0.03	1.4	28,29
50	1×10^8	$10^{-1} - 10^4$	-0.275	8×10^{-5}	0.01	30
64	2×10^5	Max. 75°	-0.159	0.6	0.4	This work, cleaned
55	4×10^5	Max. 75°	-0.163	0.07	0.08	This work, electropolished

In addition to Al_2O_3 , the TiO_2 and ZnO ALD films were found to improve the corrosion protection of the copper. When the impedance of varying thickness ALD films of TiO_2 and ZnO were compared to Al_2O_3 films, they also showed that 50 nm thick films are necessary to achieve high corrosion protection. The varying impedance of the < 50 nm films could be from the films having not fully coalesced over the copper, allowing the chloride solution to penetrate and corrode the copper. Increasing the film thickness to ~ 50 nm will improve uniformity by decreasing porosity and will provide a high level of corrosion protection. This is consistent with results we observe for initial corrosion resistance for thicker oxide films. Further increasing the film thickness above 50 nm for Al_2O_3 and ZnO did not increase the corrosion resistance of the coated copper or the capacitance of the films. Therefore, to compare different ALD thin films for their corrosion resistance, a film of 50 nm accurately represents the corrosion properties of the ALD material.

When all of the ~50 nm thick ALD films (Al_2O_3 , TiO_2 , ZnO , HfO_2 , and ZrO_2) were compared, they were all found to provide corrosion resistance when measured with LSV and EIS. Compared to the uncoated copper, all of the films resulted in lower corrosion potential and lower corrosion current when measured with LSV. The shape of the polarization curves remained similar before and after ALD, indicating the films are electrochemically active inert in the NaCl solution. The increase in impedance at low frequencies and phase angle at high frequencies of the 50 nm films indicates that the deposited films were more capacitive and of higher quality than the native oxide on the copper.^{29,30} The films all increased the phase angle at 100 Hz, but TiO_2 displayed the smallest increase in capacitance, possibly due to the film not being uniform thickness, as seen in the roughness of the coating that resulted from island growth.

According to the polarization curve, the HfO_2 provides the highest level of corrosion protection, because its low corrosion potential and large increase in polarization resistance indicates the largest decrease in the corrosion current. Overall, the EIS measurements of the films indicate that $64 \text{ nm Al}_2\text{O}_3 \approx 60 \text{ nm HfO}_2 > 56 \text{ nm ZrO}_2 > 40 \text{ nm TiO}_2 > 50 \text{ nm ZnO} \gg$ bare copper in terms of initial corrosion resistance and film quality.

The LSV and EIS measurements of the initial corrosion resistance of the films reached similar conclusions, indicating that EIS can be used as a non-destructive, *in-situ*, method to evaluate the corrosion protection properties of ALD films on copper during prolonged exposure. As shown in Figure 6.6, during prolonged exposure of up to 90 h in aqueous NaCl solution, both the HfO_2 and ZrO_2 films maintained their impedance at low frequencies and their high phase angle at high frequencies, indicating good corrosion protection, likely due in part to the amorphous nature of the oxides when deposited between 150°C and 175°C preventing solution from oxidizing the copper.^{42,43} The Al_2O_3 film, however, shows a shift in phase angle at high frequencies indicating that the coating is becoming less capacitive. This confirms that the Al_2O_3 , while being amorphous when deposited at 150°C should prevent the solution from corroding the copper,⁴⁴ is degrading, likely due to dissolution, and results in less corrosion protection of the metal in aqueous solutions. The ZnO films also show an increase in

impedance over time, which could be a result of the ZnO, which is crystalline when deposited with ALD at 150°C,⁴⁵ having grain boundaries in which the chloride solution can penetrate to the copper surface. Titanium dioxide also experienced an increase in impedance over time, and while TiO₂ is amorphous when deposited using ALD at 150°C,⁴⁶ its poor nucleation on the copper leads to high porosity in which the solution can oxidize the copper.

After the 21 day extended exposure to the NaCl solution the scans of the bare copper and the Al₂O₃ coated copper showed signs of significant corrosion. The HfO₂ coated copper, while being rougher than before the exposure to the solution, still had a smooth appearance. The EIS results of the Al₂O₃ film indicate that nearly all of the Al₂O₃ dissolved into the solution and was providing minimal corrosion protection of the copper. The HfO₂ coated copper, however, had an impedance that remained comparable to the initial impedance of the ZnO and ZrO₂ films, indicating the HfO₂ was still provided a high level of corrosion protection.

To understand the electrolyte, ALD film, and copper electrochemical system, it can be modeled using the diagram and equivalent circuit shown in Figure 4.1, respectively. In the circuit, R_{NaCl} is the resistance of the NaCl electrolyte, and Q_{film} is the capacitance of the film using a constant phase element capacitance, and R_{film} is the pore resistance of the ALD film. Also in the circuit, Q_{int} is the capacitance of the interface between the ALD film and the copper using a constant phase element, R_{int} is the resistance of the interface, and W_{int} is the Warburg admittance to describe the mass diffusion in the system. The copper with native oxide was modeled using the same circuit.⁴⁷⁻⁴⁹

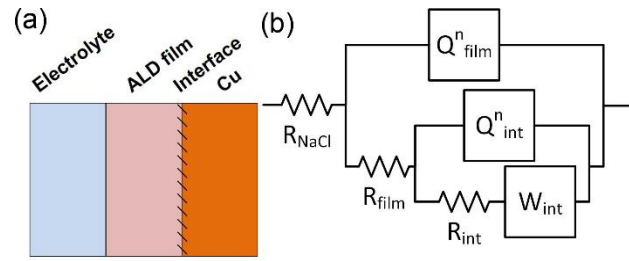


Figure 6.10. (a) Diagram of the test setup; and (b) the equivalent circuit used to model the impedance results.

The fitting parameters obtained for the ~50 nm films using the model in Figure 4.1 (b) are listed in Table 6.5. The Q_{film} values decrease from the ALD films, and are lowest for Al_2O_3 and HfO_2 . Similar decreases in Q_{film} values have been seen for other ALD films that provide high levels of corrosion resistance.^{29,30} The n_{film} parameters are highest for the HfO_2 and ZrO_2 films, which exhibited the largest phase angle at high frequencies. High n values are typical of a smooth substrate with a coating with a strong capacitive feature.³⁰ The bare copper had the lowest n_{film} , consistent with the small phase angle exhibited at high frequencies.

Table 6.5. Fitted Equivalent Circuit Model Parameters of ~50 nm ALD Films on Copper

	R_{NaCl} (Ω/cm^2)	Q_{film} ($\text{S s}^n/\text{cm}^2$)	n_{film}	R_{film} (Ω/cm^2)	Q_{int} ($\text{S s}^n/\text{cm}^2$)	n_{int}	R_{int} (Ω/cm^2)	W_{int} ($\text{S s}^{1/2}/\text{cm}^2$)
Bare Cu	103	1.5×10^{-5}	0.81	1.5×10^3	2.8×10^{-5}	0.76	3.1×10^3	9.0×10^{-4}
Al_2O_3	134	3.7×10^{-7}	0.89	9.5×10^3	5.3×10^{-6}	0.65	1.8×10^4	4.2×10^{-5}
TiO_2	133	2.8×10^{-6}	0.85	1.6×10^3	1.4×10^{-5}	0.61	7.2×10^3	3.0×10^{-5}
ZnO	134	2.1×10^{-6}	0.84	5.4×10^3	3.5×10^{-6}	0.79	8.4×10^3	5.3×10^{-5}
HfO_2	133	2.9×10^{-7}	0.92	2.1×10^4	1.0×10^{-6}	0.76	8.1×10^4	7.5×10^{-5}
ZrO_2	131	4.8×10^{-7}	0.92	9.4×10^3	2.0×10^{-5}	0.50	9.3×10^4	9.3×10^{-4}

^aOn the basis of the quality of the data fits, uncertainties are estimated to be $\pm 15\%$ of the value given.

The polarization resistance can be calculated from the fitting parameters for pore resistance and film resistance from the model ($R_p = R_{\text{film}} + R_{\text{int}}$).^{29,50} Figure 6.11 shows the change in the polarization resistance of the different ~50 nm films during prolonged exposure to the electrolyte. The bare copper starts with, and maintains, the lowest polarization resistance. The

Al₂O₃, TiO₂, and ZnO films all experience an increase in the polarization resistance over the 90 hour measurement time, consistent with the impedance observed at 10 mHz (Figure 6.7 (a)). The HfO₂ film exhibits a decrease in impedance over time, but maintains the highest impedance even after 90 h in the highly corrosive NaCl solution. The fitted resistance parameters for the ZrO₂ films, however, indicate the films undergo a larger decrease in impedance over time. This indicates that ZrO₂ is less protective than HfO₂ in this environment, even though in Figure 6.6 (e) and (f), both ZrO₂ and HfO₂ show similar trends in impedance over time. This decrease in the fitted resistance for the ZrO₂ films could be a mathematical artifact from the model fitting, because the Warburg admittance of the ZrO₂ films decreases over time, while maintaining relatively constant for the other films. Due to the heavy corrosion of the copper and dissolution of the ALD films that were exposed to the solution for 21 days, the model used in Figure 4.1 has uncertainties in the fitted parameters $\gg 15\%$, and are not comparable to the films that were only exposed for up to 90 h.

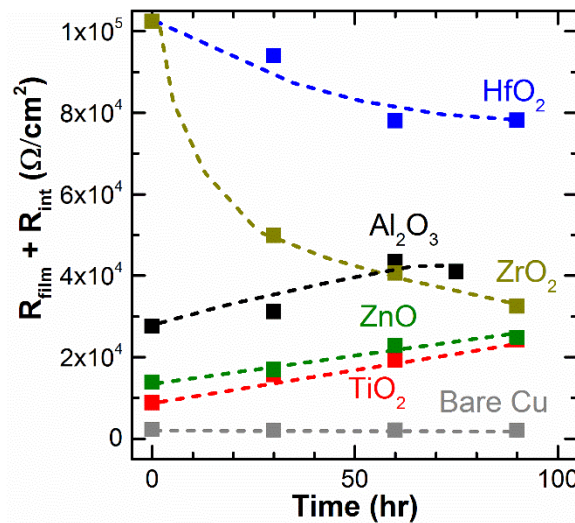


Figure 6.11. Polarization resistance of ~50 nm films during exposure to 0.1 M NaCl solution calculated from model fitting parameters.

6.6 Conclusions

ALD can be used to deposit thin films of metal oxides on copper to provide corrosion protection from corrosive chloride solutions. Ultrathin films of Al_2O_3 , TiO_2 , ZnO , HfO_2 , and ZrO_2 were deposited on copper metal using ALD, and corrosion resistance was characterized using electrochemical measurements (EIS and LSV). All ALD layers showed significant protection of the copper. While 10-25 nm thick films of Al_2O_3 , TiO_2 , and ZnO provide varying levels of corrosion resistance, thicker films (50 nm or thicker) showed better performance with lower electrochemical porosity. Significantly increasing the thickness above 50 nm was not found to provide increased corrosion resistance. Films of Al_2O_3 and HfO_2 provided the highest initial corrosion resistance as measured using EIS, but the quality of the Al_2O_3 film degraded over time from a 21 day exposure to NaCl solution, and no longer protected the copper from corrosion. HfO_2 provided the largest increase in polarization resistance and decrease in corrosion current when measured with LSV. The HfO_2 films also maintained the overall smoothness of the copper after 21 days, and continued to provide significant electrochemical corrosion protection. The properties of the ZrO_2 showed minimal change in performance after exposure to NaCl for 90 h. This is the first reported use of thin films of HfO_2 and ZrO_2 deposited on copper using ALD for corrosion protection, and their anticorrosion properties are promising and could be of interest for further study.

6.7 Acknowledgments

The authors acknowledge funding from the U.S. Navy under contract N00253-16-C-0002.

6.8 References

- (1) Lee, S.-H.; Kim, J.-G.; Koo, J.-Y. Investigation of Pitting Corrosion of a Copper Tube in a Heating System. *Eng. Failure Anal.* **2010**, *17*, 1424–1435.
- (2) Lu, B.; Meng, W. J.; Mei, F. Experimental Investigation of Cu-Based, Double-Layered, Microchannel Heat Exchangers. *J. Micromech. Microeng.* **2013**, *23*, 035017.
- (3) Sobue, K.; Sugahara, A.; Nakata, T.; Imai, H.; Magaino, S. Effect of Free Carbon Dioxide on Corrosion Behavior of Copper in Simulated Water. *Surf. Coat. Technol.* **2003**, *169–170*, 662–665.
- (4) Boulay, N.; Edwards, M. Role of Temperature, Chlorine, and Organic Matter in Copper Corrosion by-Product Release in Soft Water. *Water Res.* **2001**, *35*, 683–690.
- (5) Armanious, A.; Johannsen, K. Alternative Methods for Copper Corrosion Studies in Household Plumbing Systems. *Mater. Corros.* **2012**, *63*, 438–444.
- (6) Farooqi, O. E.; Asce, M.; Loganathan, G. V.; Edwards, M. A.; Bosch, D.; Lee, J.; Scardina, P. Copper Pinhole Failures: Plumbing Susceptibility and Management. *J. Water Resour. Plan. Manag.* **2009**, *135*, 227–236.
- (7) Jeon, B.; Sankaranarayanan, S. K. R. S.; van Duin, A. C. T.; Ramanathan, S. Atomistic Insights into Aqueous Corrosion of Copper. *J. Chem. Phys.* **2011**, *134*, 234706.
- (8) Pehkonen, S. O.; Palit, A.; Zhang, X. Effect of Specific Water Quality Parameters on Copper Corrosion. *Corrosion* **2002**, *58*, 156–165.
- (9) Feng, Y.; Siow, K.-S.; Teo, W.-K.; Tan, K.-L.; Hsieh, A.-K. Corrosion Mechanisms and Products of Copper in Aqueous Solutions at Various pH Values. *Corrosion* **1997**, *53*, 389–398.
- (10) Lau, K. H.; Sanjurjo, A.; Wood, B. J. Aluminum and Alumina Coatings on Copper by Chemical Vapor Deposition in Fluidized Bed Reactors. *Surf. Coat. Technol.* **1992**, *54–55*, 234–240.
- (11) Sanjurjo, A.; Wood, B. J.; Lau, K. H.; Tong, G. T.; Choi, D. K.; McKubre, M. C. H.; Song, H. K.; Church, N. Titanium-Based Coatings on Copper by Chemical Vapor Deposition in Fluidized Bed Reactors. *Surf. Coat. Technol.* **1991**, *49*, 110–115.
- (12) Yamamoto, Y.; Nishihara, H.; Aramaki, K. Self-Assembled Layers of Alkanethiols on Copper for Protection Against Corrosion. *J. Electrochem. Soc.* **1993**, *140*, 436–443.

- (13) Brusic, V.; Frisch, M. A.; Eldridge, B. N.; Novak, F. P.; Kaufman, F. B.; Rush, B. M.; Frankel, G. S. Copper Corrosion With and Without Inhibitors. *J. Electrochem. Soc.* **1991**, *138*, 2253–2259.
- (14) Tallman, D. E.; Spinks, G.; Dominis, A.; Wallace, G. G. Electroactive Conducting Polymers for Corrosion Control. *J. Solid State Electrochem.* **2002**, *6*, 73–84.
- (15) Lin, Y.; Yasuda, H. Effect of Plasma Polymer Deposition Methods on Copper Corrosion Protection. *J. Appl. Polym. Sci.* **1996**, *60*, 543–555.
- (16) Patil, S.; Sainkar, S. R.; Patil, P. P. Poly(o-Anisidine) Coatings on Copper: Synthesis, Characterization and Evaluation of Corrosion Protection Performance. *Appl. Surf. Sci.* **2004**, *225*, 204–216.
- (17) Marin, E.; Lanzutti, A.; Guzman, L.; Fedrizzi, L. Corrosion Protection of AISI 316 Stainless Steel by ALD Alumina/titania Nanometric Coatings. *J. Coatings Technol. Res.* **2011**, *8*, 655–659.
- (18) Shan, C. X.; Hou, X.; Choy, K.-L. Corrosion Resistance of TiO₂ Films Grown on Stainless Steel by Atomic Layer Deposition. *Surf. Coat. Technol.* **2008**, *202*, 2399–2402.
- (19) Shan, C. X.; Hou, X.; Choy, K.-L.; Choquet, P. Improvement in Corrosion Resistance of CrN Coated Stainless Steel by Conformal TiO₂ Deposition. *Surf. Coat. Technol.* **2008**, *202*, 2147–2151.
- (20) Matero, R.; Ritala, M.; Leskelä, M.; Salo, T.; Aromaa, J.; Forsén, O. Atomic Layer Deposited Thin Films for Corrosion Protection. *Le J. Phys. IV* **1999**, *9*, 1340–1344.
- (21) Potts, S. E.; Schmalz, L.; Fenker, M.; Díaz, B.; Światowska, J.; Maurice, V.; Seyeux, A.; Marcus, P.; Radnóczy, G.; Tóth, L.; Kessela, W. M. M. Ultra-Thin Aluminium Oxide Films Deposited by Plasma-Enhanced Atomic Layer Deposition for Corrosion Protection. *J. Electrochem. Soc.* **2011**, *158*, C132–C138.
- (22) Díaz, B.; Härkönen, E.; Maurice, V.; Światowska, J.; Seyeux, A.; Ritala, M.; Marcus, P. Failure Mechanism of Thin Al₂O₃ Coatings Grown by Atomic Layer Deposition for Corrosion Protection of Carbon Steel. *Electrochim. Acta* **2011**, *56*, 9609–9618.
- (23) Díaz, B.; Światowska, J.; Maurice, V.; Seyeux, A.; Normand, B.; Härkönen, E.; Ritala, M.; Marcus, P. Electrochemical and Time-of-Flight Secondary Ion Mass Spectrometry Analysis of Ultra-Thin Metal Oxide (Al₂O₃ and Ta₂O₅) Coatings Deposited by Atomic Layer Deposition on Stainless Steel. *Electrochim. Acta* **2011**, *56*, 10516–10523.
- (24) Díaz, B.; Härkönen, E.; Światowska, J.; Maurice, V.; Seyeux, A.; Marcus, P.; Ritala, M. Low-Temperature Atomic Layer Deposition of Al₂O₃ Thin Coatings for Corrosion

- Protection of Steel: Surface and Electrochemical Analysis. *Corros. Sci.* **2011**, *53*, 2168–2175.
- (25) Marin, E.; Lanzutti, A.; Paussa, L.; Guzman, L.; Fedrizzi, L. Long Term Performance of Atomic Layer Deposition Coatings for Corrosion Protection of Stainless Steel. *Mater. Corros.* **2015**, *66*, 907–914.
- (26) Mirhashemihaghighi, S.; Światowska, J.; Maurice, V.; Seyeux, A.; Zanna, S.; Salmi, E.; Ritala, M.; Marcus, P. Corrosion Protection of Aluminium by Ultra-Thin Atomic Layer Deposited Alumina Coatings. *Corros. Sci.* **2016**, *106*, 16–24.
- (27) Abdulagatov, A. I.; Yan, Y.; Cooper, J. R.; Zhang, Y.; Gibbs, Z. M.; Cavanagh, A. S.; Yang, R. G.; Lee, Y. C.; George, S. M. Al₂O₃ and TiO₂ Atomic Layer Deposition on Copper for Water Corrosion Resistance. *ACS Appl. Mater. Interfaces* **2011**, *3*, 4593–4601.
- (28) Chai, Z.; Li, J.; Lu, X.; He, D. Use of Electrochemical Measurements to Investigate the Porosity of Ultra-Thin Al₂O₃ Films Prepared by Atomic Layer Deposition. *RSC Adv.* **2014**, *4*, 39365–39371.
- (29) Chai, Z.; Liu, Y.; Li, J.; Lu, X.; He, D. Ultra-Thin Al₂O₃ Films Grown by Atomic Layer Deposition for Corrosion Protection of Copper. *RSC Adv.* **2014**, *4*, 50503–50509.
- (30) Mirhashemihaghighi, S.; Swiatowska, J.; Maurice, V.; Seyeux, A.; Klein, L. H.; Harkonen, E.; Ritala, M.; Marcus, P. Electrochemical and Surface Analysis of the Corrosion Protection of Copper by Nanometer-Thick Alumina Coatings Prepared by Atomic Layer Deposition. *J. Electrochem. Soc.* **2015**, *162*, C377–C384.
- (31) Mirhashemihaghighi, S.; Światowska, J.; Maurice, V.; Seyeux, A.; Klein, L. H.; Salmi, E.; Ritala, M.; Marcus, P. Interfacial Native Oxide Effects on the Corrosion Protection of Copper Coated with ALD Alumina. *Electrochim. Acta* **2016**, *193*, 7–15.
- (32) Hausmann, D. M.; Gordon, R. G. Surface Morphology and Crystallinity Control in the Atomic Layer Deposition (ALD) of Hafnium and Zirconium Oxide Thin Films. *J. Cryst. Growth* **2003**, *249*, 251–261.
- (33) Correa, G. C.; Bao, B.; Strandwitz, N. C. Chemical Stability of Titania and Alumina Thin Films Formed by Atomic Layer Deposition. *ACS Appl. Mater. Interfaces* **2015**, *7*, 14816–14821.
- (34) Hu, S.; Shaner, M. R.; Beardslee, J. A.; Lichterman, M.; Brunschwig, B. S.; Lewis, N. S. Amorphous TiO₂ Coatings Stabilize Si, GaAs, and GaP Photoanodes for Efficient Water Oxidation. *Science* **2014**, *344*, 1005–1009.

- (35) Spathis, P.; Poullos, I. The Corrosion and Photocorrosion of Zinc and Zinc Oxide Coatings. *Corros. Sci.* **1995**, *37*, 673–680.
- (36) Sun, K. G.; Li, Y. V.; Saint John, D. B.; Jackson, T. N. pH-Controlled Selective Etching of Al₂O₃ over ZnO. *ACS Appl. Mater. Interfaces* **2014**, *6*, 7028–7031.
- (37) Esplandiu, M. J.; Patrino, E. M.; Macagno, V. A. Characterization of Hafnium Anodic Oxide Films: An AC Impedance Investigation. *Electrochim. Acta* **1995**, *40*, 809–815.
- (38) Badawy, W. a.; Al-Kharafi, F. M. Electrochemical Behaviour of Naturally Passivated Hafnium in Aqueous Solutions of Different pH. *J. Mater. Sci.* **1999**, *34*, 2483–2491.
- (39) Li, H.; Liang, K.; Mei, L.; Gu, S.; Wang, S. Corrosion Protection of Mild Steel by Zirconia Sol-Gel Coatings. *J. Mater. Sci. Lett.* **2001**, *51*, 1081–1083.
- (40) Li, Q.; Zhong, X.; Hu, J.; Kang, W. Preparation and Corrosion Resistance Studies of Zirconia Coating on Fluorinated AZ91D Magnesium Alloy. *Prog. Org. Coat.* **2008**, *63*, 222–227.
- (41) Mirhashemihaghighi, S.; Światowska, J.; Maurice, V.; Seyeux, A.; Klein, L. H.; Salmi, E.; Ritala, M.; Marcus, P. The Role of Surface Preparation in Corrosion Protection of Copper with Nanometer-Thick ALD Alumina Coatings. *Appl. Surf. Sci.* **2016**, *387*, 1054–1061.
- (42) Kukli, K.; Ritala, M.; Sajavaara, T.; Keinonen, J.; Leskelä, M. Atomic Layer Deposition of Hafnium Dioxide Films from Hafnium Tetrakis(ethylmethanamide) and Water. *Chem. Vap. Deposition.* **2002**, *8*, 199–204.
- (43) Cho, G. Y.; Noh, S.; Lee, Y. H.; Ji, S.; Hong, S. W.; Koo, B.; An, J.; Kim, Y.-B.; Cha, S. W. Properties of Nanostructured Undoped ZrO₂ Thin Film Electrolytes by Plasma Enhanced Atomic Layer Deposition for Thin Film Solid Oxide Fuel Cells. *J. Vac. Sci. Technol. A.* **2016**, *34*, 01A151.
- (44) Zhang, L.; Jiang, H. C.; Liu, C.; Dong, J. W.; Chow, P. Annealing of Al₂O₃ Thin Films Prepared by Atomic Layer Deposition. *J. Phys. D. Appl. Phys.* **2007**, *40*, 3707–3713.
- (45) Yamada, A.; Sang, B.; Konagai, M. Atomic Layer Deposition of ZnO Transparent Conducting Oxides. *Appl. Surf. Sci.* **1997**, *112*, 216–222.
- (46) Aarik, J.; Aidla, A.; Uustare, T.; Sammelselg, V. Morphology and Structure of TiO₂ Thin Films Grown by Atomic Layer Deposition. *J. Cryst. Growth* **1995**, *148*, 268–275.
- (47) Brizuela, F.; Procaccini, R.; Ceré, S.; Vázquez, M. Anodically Grown Films on Copper and Copper–nickel Alloys in Slightly Alkaline Solutions. *J. Appl. Electrochem.* **2006**, *36*, 583–590.

- (48) Trachli, B.; Keddami, M.; Takenouti, H.; Srhiri, A. Protective Effect of Electropolymerized 3-Amino 1,2,4-Triazole towards Corrosion of Copper in 0.5 M NaCl. *Corros. Sci.* **2002**, *44*, 997–1008.
- (49) Valcarce, M. B.; De Sánchez, S. R.; Vázquez, M. A Comparative Analysis of Copper and Brass Surface Films in Contact with Tap Water. *J. Mater. Sci.* **2006**, *41*, 1999–2007.
- (50) Liu, C.; Bi, Q.; Leyland, A.; Matthews, A. An Electrochemical Impedance Spectroscopy Study of the Corrosion Behaviour of PVD Coated Steels in 0.5 N NaCl Aqueous Solution: Part II. *Corros. Sci.* **2003**, *45*, 1257–1273.

APPENDICES

APPENDIX A: Supporting Information for Chapter 3. Effect of Meso- and Micro-Porosity in Carbon Electrodes on Atomic Layer Deposition of Pseudocapacitive V₂O₅ for High Performance Supercapacitors

This appendix is the supporting information from a manuscript published as:

Daubert, J. S.; Lewis, N. P.; Gotsch, H. N.; Mundy, J. Z.; Monroe, D. N.; Dickey, E. C.; Losego, M. D.; Parsons, G. N. Effect of Meso- and Micro-Porosity in Carbon Electrodes on Atomic Layer Deposition of Pseudocapacitive V₂O₅ for High Performance Supercapacitors. *Chem. Mater.* **2015**, *27*, 6524–6534.

A.1 Figures

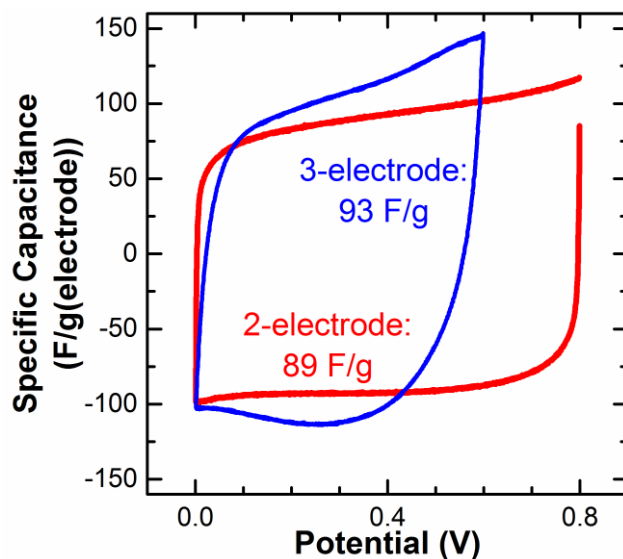


Figure A.1. Comparison of G60 electrodes in a measured using cyclic voltammetry in a 3-electrode and 2-electrode configuration. There is no significant difference in the performance of the electrodes.

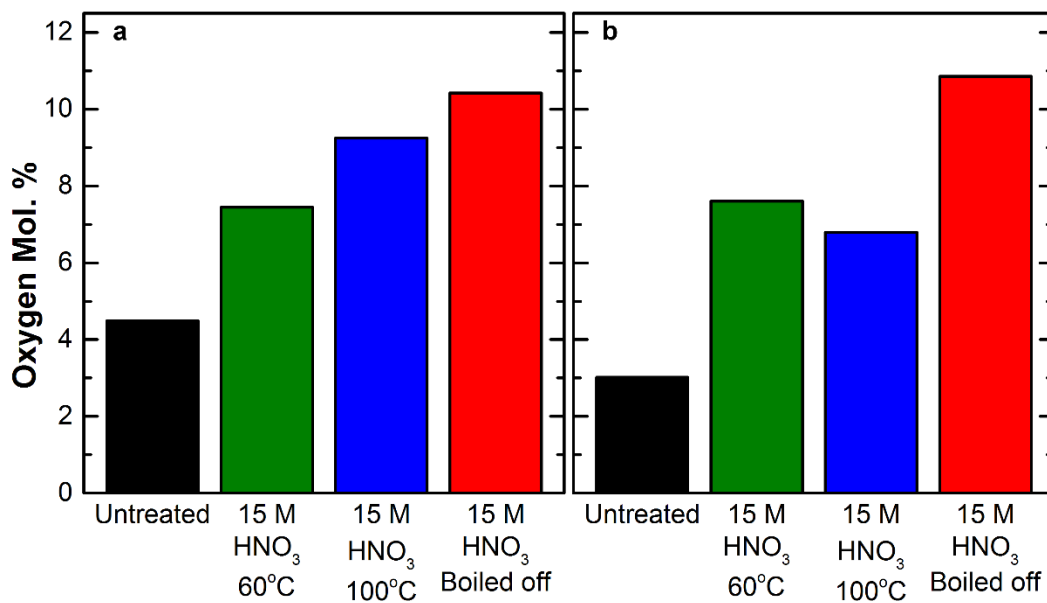


Figure A.2. Elemental analysis by EDS of (a) G60 and (b) Supra carbon shows more oxygen in the carbon after the acid treatment consistent with the IR results.

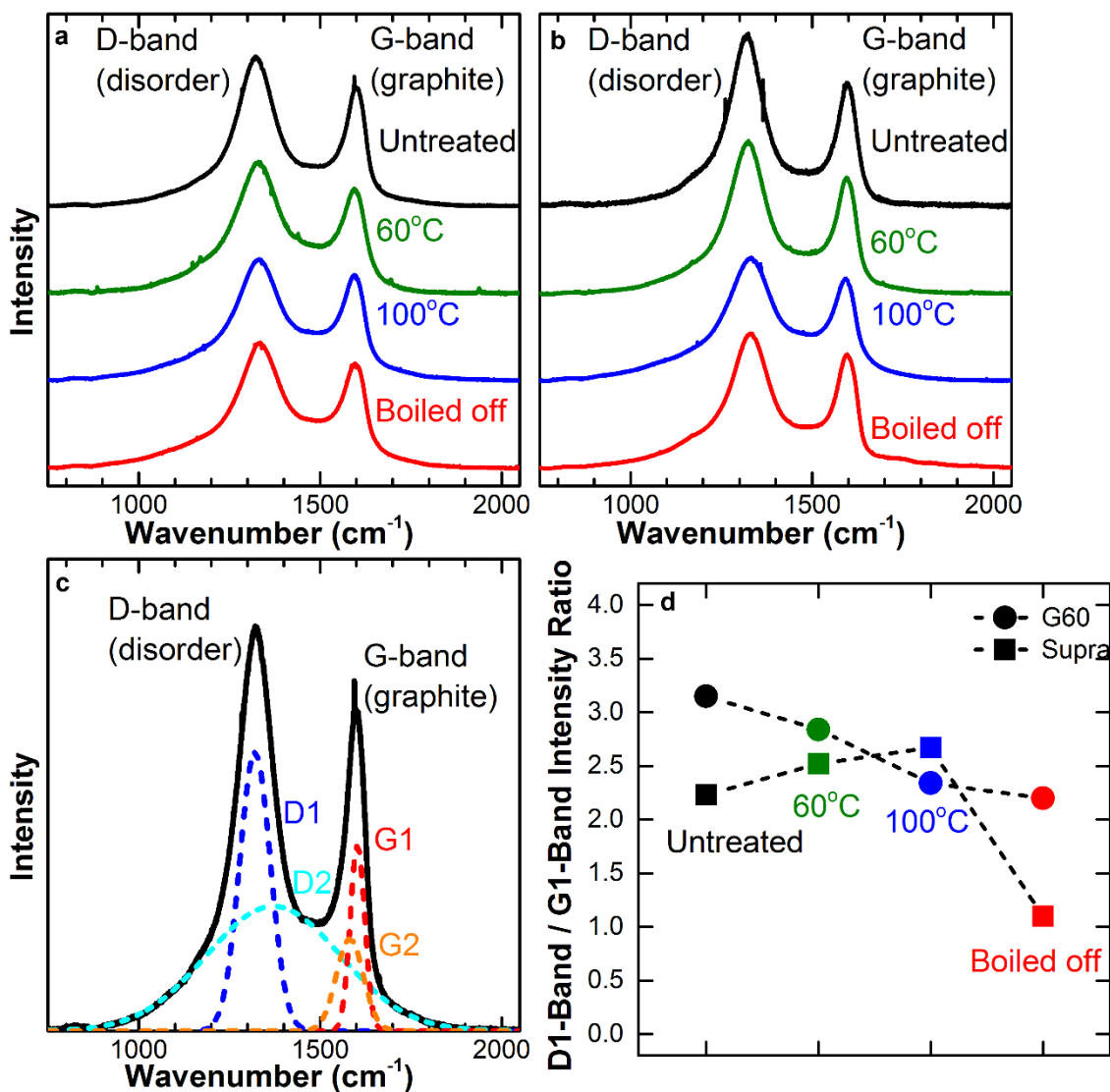


Figure A.3. Raman spectra of (a) G60 and (b) Supra. (c) Band fitting for untreated G60 is shown; and (d) the comparison of the peaks is shown for all samples. The carbon powders were measured with a Raman spectrometer after different acid treatments to identify the disorder (D) and graphitic (G) nature of the powder.¹ The deconvolution of the Raman spectra shows that for the G60 powder, the high temperature acid treatment tends to decrease the relative intensity of the D-band (i.e. increasing graphic structure) whereas the Supra shows a relative increase in the D-band. However, these changes are small, and we do not see significant trends in electrode performance for these changes in D- and G- mode intensity.

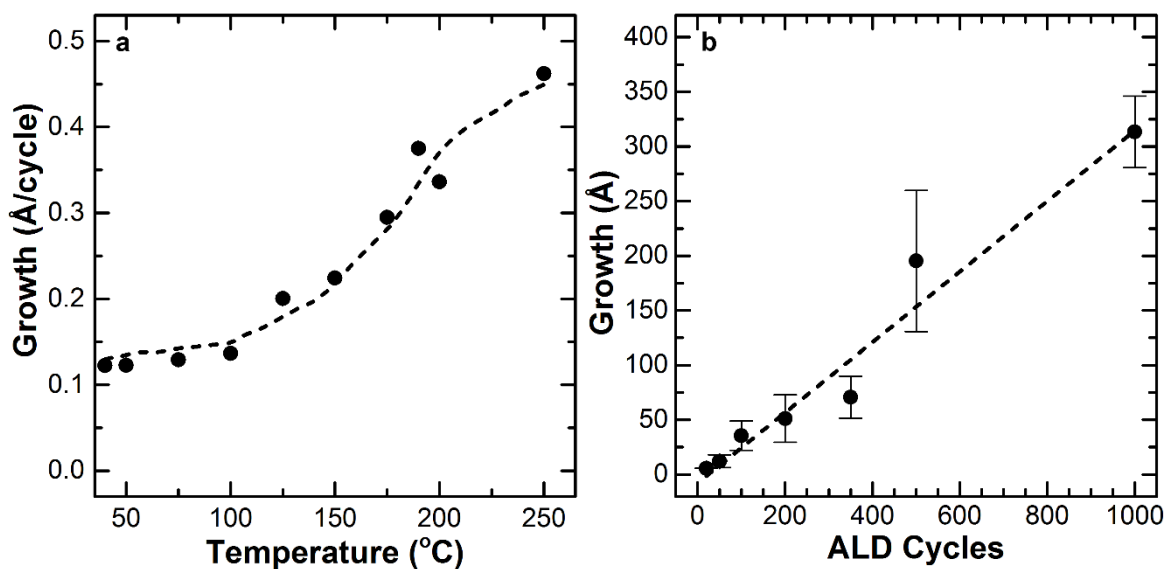


Figure A.4. (a) V_2O_5 growth per cycle at varying temperatures; and (b) growth with cycle number at 150°C. Film thickness was determined from ellipsometry. The ALD temperature window and growth rate are consistent with previous reports.²

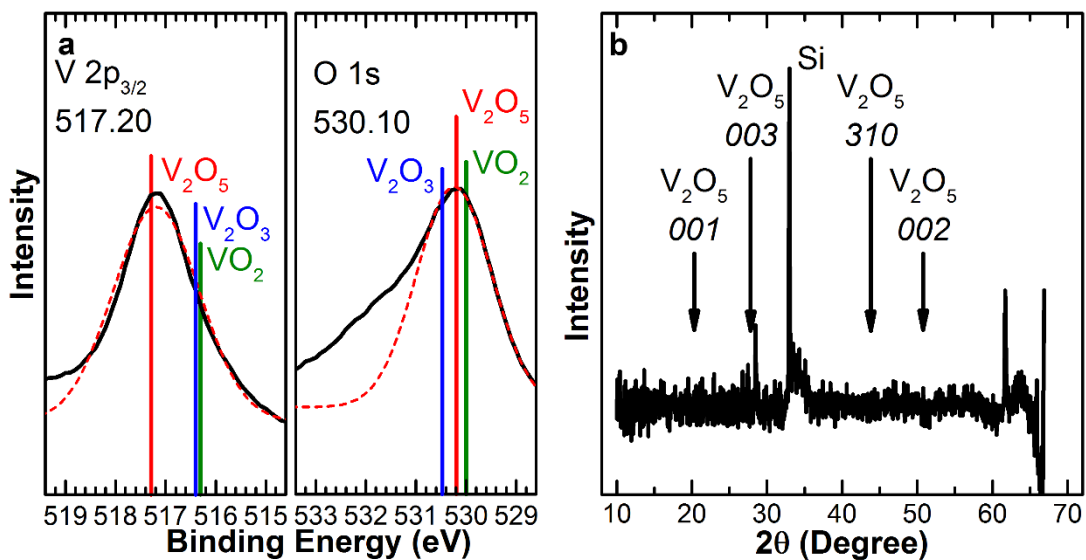


Figure A.5. (a) XPS and (b) XRD (b) of 400 Å vanadium oxide films deposited at 175°C on Si indicate the vanadium oxide deposited is amorphous V_2O_5 .³⁻⁶

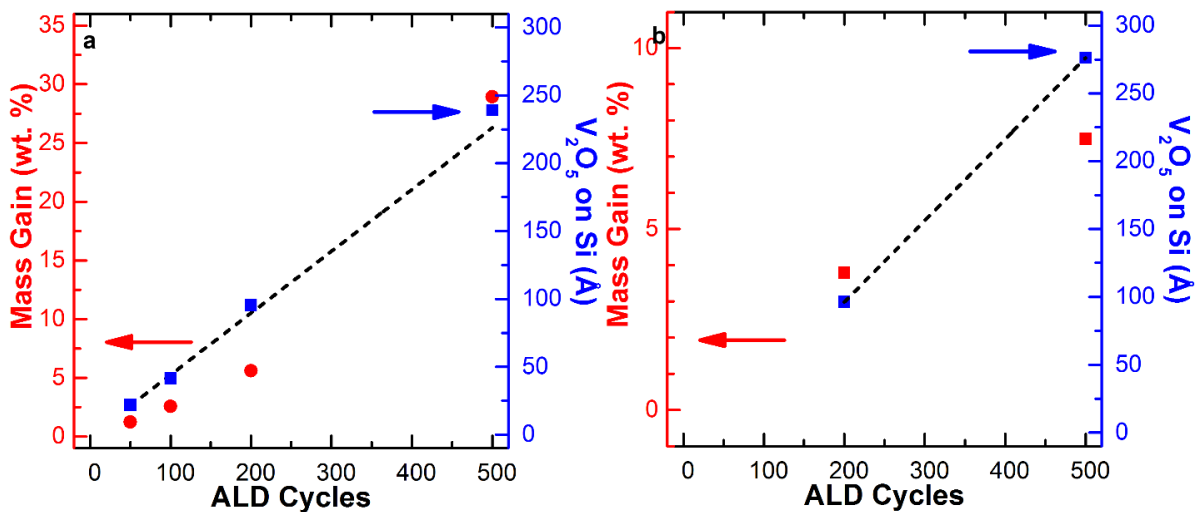


Figure A.6. Mass gain of (a) G60 and (b) Supra powder that was treated with boiling nitric acid as a function of ALD cycles of V₂O₅ at 150°C and the corresponding thickness of V₂O₅ measured on monitor Si wafers. The resulting linear increase in mass gain fits for G60 carbon fits in the with the linear film growth seen on monitor silicon wafers. Similar trends were also seen for the limited number of Supra powder coated. The G60 and Supra carbons displayed different mass gains after similar number of ALD cycles. The variation could be a result of the Supra carbon powder that was coated having a surface area that was only about 1/3 of that of the G60 carbon powder that was coated. We would expect different carbon powders to have a linear mass gain as well, but with a different slope, which would vary as a result of different pore size distribution and surface area of the carbons.

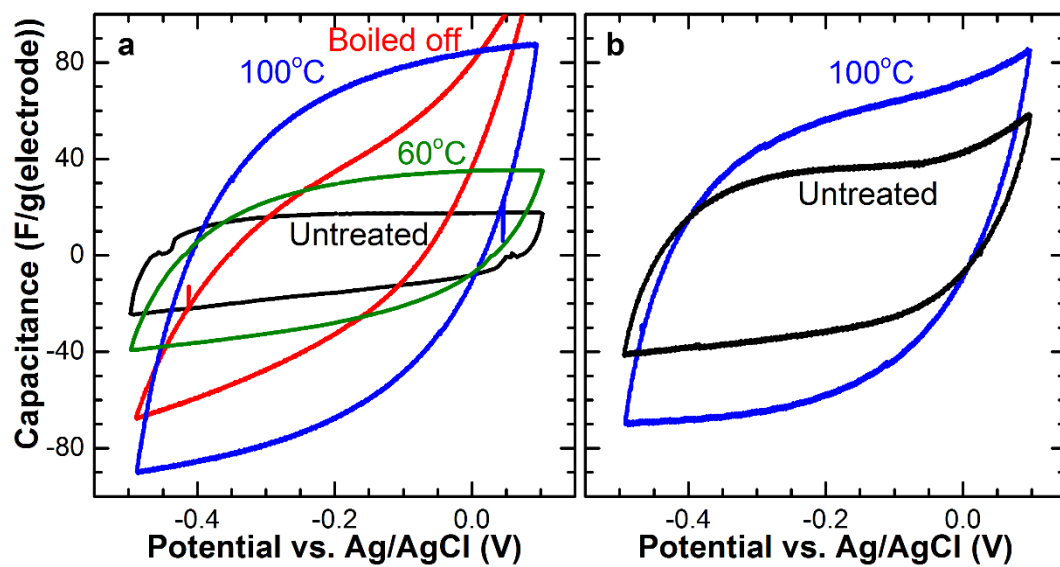


Figure A.7. Effect of acid treatment on capacitance measured in a 3-electrode cell on (a) G60 and (b) Supra in 1 M KCl reported at a scan rate of 200 mV/s.

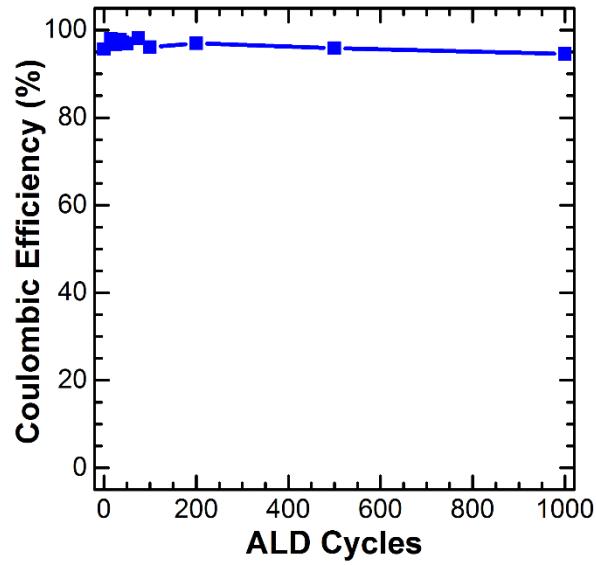


Figure A.8. Coulombic efficiency of V_2O_5 coated G60 electrodes as a function of ALD cycles charged/discharged from 0.0 to 0.8 V at a rate of 5 A/g(capacitor).

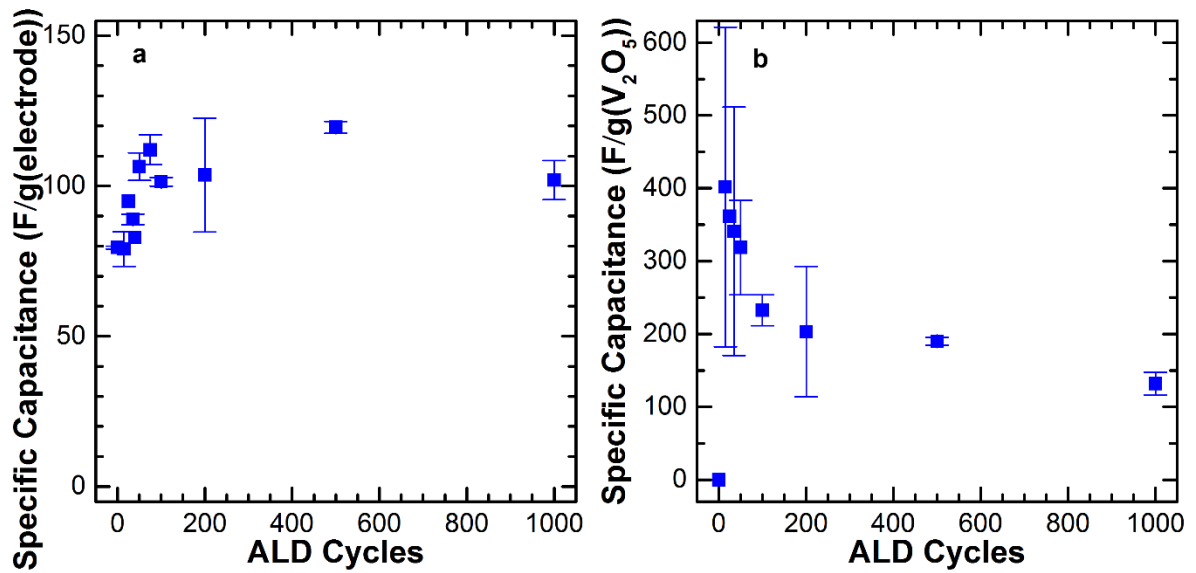


Figure A.9. EIS model results of G60 electrodes coated with V_2O_5 . (a) specific capacitance and (b) specific capacitance of deposited V_2O_5 .

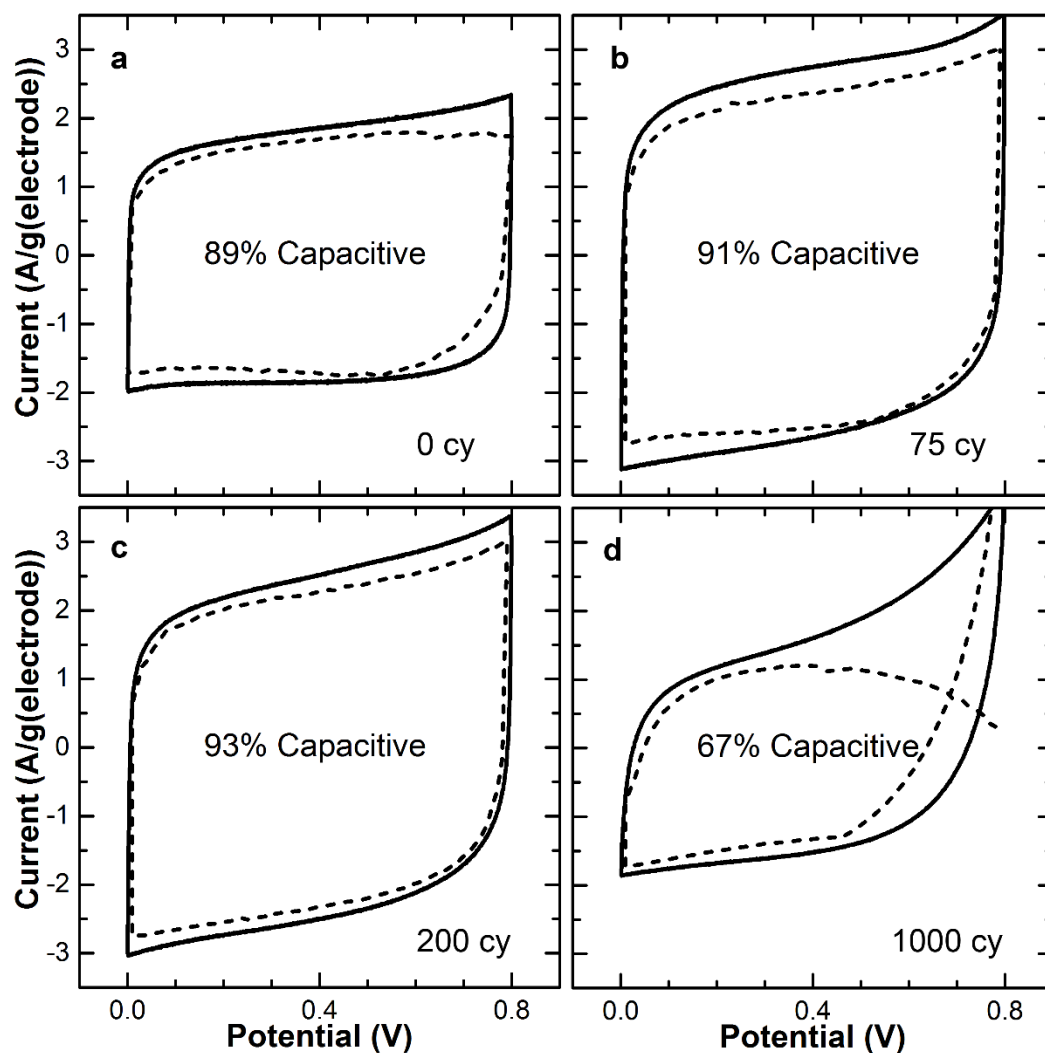


Figure A.10. Current response during cyclic voltammetry from either capacitive processes (varies with ν) or diffusion processes (varies with $\nu^{-1/2}$) in the G60 EC coated with V_2O_5 ALD: (a) 0 cycles; (b) 75 cycles; (c) 200 cycles; and (d) 1000 cycles according to the relationship $i(V) = k_1\nu + k_2\nu^{1/2}$, where k_1 and k_2 are constants at a particular sweep rate. The capacitive current (dashed line) represents 67 to 93% of the total current (solid line).^{7,8}

A.2 References

- (1) Shimodaira, N.; Masui, A. Raman Spectroscopic Investigations of Activated Carbon Materials. *J. Appl. Phys.* **2002**, *92*, 902–909.
- (2) Chen, X.; Pomerantseva, E.; Gregorczyk, K.; Ghodssi, R.; Rubloff, G. Cathodic ALD V_2O_5 Thin Films for High-Rate Electrochemical Energy Storage. *RSC Adv.* **2013**, *3*, 4294–4302.
- (3) Boukhalifa, S.; Evanoff, K.; Yushin, G. Atomic Layer Deposition of Vanadium Oxide on Carbon Nanotubes for High-Power Supercapacitor Electrodes. *Energy Environ. Sci.* **2012**, *5*, 6872–6879.
- (4) Wang, X. J.; Li, H. D.; Fei, Y. J.; Wang, X.; Xiong, Y. Y.; Nie, Y. X.; Feng, K. A. XRD and Raman Study of Vanadium Oxide Thin Films Deposited on Fused Silica Substrates by RF Magnetron Sputtering. *Appl. Surf. Sci.* **2001**, *177*, 8–14.
- (5) Gotić, M.; Popović, S.; Ivanda, M.; Musić, S. Sol–gel Synthesis and Characterization of V_2O_5 Powders. *Mater. Lett.* **2003**, *57*, 3186–3192.
- (6) Mendialdua, J.; Casanova, R.; Barbaux, Y. XPS Studies of V_2O_5 , V_6O_{13} , VO_2 and V_2O_3 . *J. Electron Spectros. Relat. Phenomena* **1995**, *71*, 249–261.
- (7) Liu, T.-C.; Pell, W. G.; Conway, B. E.; Roberson, S. L. Behavior of Molybdenum Nitrides as Materials for Electrochemical Capacitors. *J. Electrochem. Soc.* **1998**, *145*, 1882–1888.
- (8) Rauda, I. E.; Augustyn, V.; Saldarriaga-Lopez, L. C.; Chen, X.; Schelhas, L. T.; Rubloff, G. W.; Dunn, B.; Tolbert, S. H. Nanostructured Pseudocapacitors Based on Atomic Layer Deposition of V_2O_5 onto Conductive Nanocrystal-Based Mesoporous ITO Scaffolds. *Adv. Funct. Mater.* **2014**, *24*, 6717–6728.

APPENDIX B. Co-Authored Publications

B.1 Solvate Structures and Spectroscopic Characterization of LiTFSI Electrolytes

A Raman spectroscopic evaluation of numerous crystalline solvates with lithium bis(trifluoromethanesulfonyl)imide (LiTFSI or $\text{LiN}(\text{SO}_2\text{CF}_3)_2$) has been conducted over a wide temperature range. Four new crystalline solvate structures— $(\text{PHEN})_3:\text{LiTFSI}$, $(2,9\text{-DMPHEN})_2:\text{LiTFSI}$, $(\text{G3})_1:\text{LiTFSI}$ and $(2,6\text{-DMPy})_{1/2}:\text{LiTFSI}$ with phenanthroline, 2,9-dimethyl[1,10]phenanthroline, triglyme, and 2,6-dimethylpyridine, respectively—have been determined to aid in this study. The spectroscopic data have been correlated with varying modes of $\text{TFSI}^- \cdots \text{Li}^+$ cation coordination within the solvate structures to create an electrolyte characterization tool to facilitate the Raman band deconvolution assignments for the determination of ionic association interactions within electrolytes containing LiTFSI. It is found, however, that significant difficulties may be encountered when identifying the distributions of specific forms of TFSI^- anion coordination present in liquid electrolyte mixtures due to the wide range of $\text{TFSI}^- \cdots \text{Li}^+$ cation interactions possible and the overlap of the corresponding spectroscopic data signatures.

*Seo, D. M.; Boyle, P. D.; Sommer, R. D.; Daubert, J. S.; Borodin, O.; Henderson, W. A. Solvate Structures and Spectroscopic Characterization of LiTFSI Electrolytes. *J. Phys. Chem. B* **2014**, *118*, 13601–13608.

B.2 Electrolyte Solvation and Ionic Association VI. Acetonitrile-Lithium Salt Mixtures: Highly Associated Salts Revisited*

Molecular dynamics (MD) simulations of acetonitrile (AN) mixtures with LiBF_4 , LiCF_3SO_3 and LiCF_3CO_2 provide extensive details about the molecular- and mesoscale-level solution interactions and thus explanations as to why these electrolytes have very different thermal phase behavior and electrochemical/physicochemical properties. The simulation results are in full accord with a previous experimental study of these $(\text{AN})_n\text{-LiX}$ electrolytes. This computational study reveals how the structure of the anions strongly influences the ionic association tendency of the ions, the manner in which the aggregate solvates assemble in solution and the length of time in which the anions remain coordinated to the Li^+ cations in the solvates which result in dramatic variations in the transport properties of the electrolytes.

*Borodin, O.; Han, S.-D.; Daubert, J. S.; Seo, D. M.; Yun, S.-H.; Henderson, W. A. Electrolyte Solvation and Ionic Association: VI. Acetonitrile-Lithium Salt Mixtures: Highly Associated Salts Revisited. *J. Electrochem. Soc.* **2015**, *162*, A501–A510.